

# **Experimental Investigation of the steady state and transient operation of Diesel Engines fuelled by high percentage biodiesel blends**

THESIS

submitted in partial fulfillment of the requirements  
for the degree of Doctor of Philosophy in Mechanical Engineering  
of the Department of Mechanical Engineering  
University of Thessaly

BY

DIMITRIOS N. TZIOURTZIOUMIS \*



Dipl. Mechanical Engineer,  
University of Thessaly  
Born on 25<sup>th</sup> February 1986  
in Thessaloniki

Supervising Committee  
Prof. A. M. Stamatelos, supervisor  
Assoc. Prof. H. Stapountzis  
Prof. C. Papadimitriou

Volos, June 2012

---

\* "Alexander S. Onassis" Public Benefit Foundation

# Contents

1.	Introduction – Aim and Objectives of this Thesis.....	10
2.	Literature search on the effect of Biodiesel on engine performance, emissions and DPF operation ....	14
2.1	Literature review – common rail diesel engines with biodiesel .....	14
2.1.1	Engine power and efficiency .....	15
2.1.2	NO <sub>x</sub> emissions.....	16
2.1.3	Particulate matter and smoke opacity .....	16
2.2	Evolution of the modern diesel injection systems.....	17
2.2.1	Injection system dynamics .....	18
2.2.2	Transient engine performance .....	19
2.3	Combustion characteristics .....	19
2.4	Diesel Particulate Filter performance – Soot oxidation reactivity .....	20
2.5	Diesel spray atomization characteristics .....	21
2.5.1	Droplets collision and coalescence .....	21
2.5.2	Droplet breakup.....	22
2.5.3	Breakup models.....	23
3.	Experimental layout and procedure with the common rail engine .....	25
3.1	Engine data .....	25
3.2	Engine management system information and maps .....	26
3.3	Active regeneration procedure.....	33
3.3.1	General Overview of Regeneration Strategies .....	33
3.3.2	Engine maps description .....	33
3.4	Properties of tested fuels .....	40
3.5	Test equipment and procedure .....	41
4.	Experimental results with the common rail engine .....	43
4.1	Effect of B70 on engine performance and fuel consumption .....	43
4.2	Effect of B70 fuel on the Injection system parameters.....	48
4.3	Effect of B70 on the pollutant emissions .....	49
4.4	Conclusions.....	51
5.	Dynamic effects and transient performance in common rail injection systems .....	52
5.1	Engine instrumentation and injection system .....	52
5.2	Test fuels .....	53
5.3	ECU operating maps.....	53
5.4	Results and discussion.....	54
5.4.1	Injection system dynamics at characteristic operating points .....	54
5.4.2	Transient results .....	58
5.5	Suggested engine improvements .....	63
5.6	Conclusions.....	65
6.	Experimental layout and test procedure with the single cylinder Diesel engine .....	67
6.1	The injection process in a PLN injection system .....	67
6.2	Experimental setup .....	68
6.2.1	Engine test equipment and injection system .....	68
6.2.2	Equipment for indicator diagrams.....	73

6.2.3	Properties of fuels and blending .....	76
6.2.4	Experimental procedure .....	76
6.3	Results and Discussion .....	76
6.3.1	Calculation of injection timing advance in a PLN injection system .....	76
6.3.2	Cycle-to-cycle variation.....	79
6.3.3	Combustion characteristics.....	79
6.3.4	Soot emissions.....	81
6.3.5	Energy balance .....	83
6.4	Conclusions.....	84
7.	Investigation of the effect of biodiesel blends on the performance of a fuel additive-assisted diesel filter regenerations system .....	86
7.1	Experimental.....	86
7.1.1	Filter loading test protocol.....	90
7.1.2	Transient regeneration experiments .....	92
7.2	Effect of B20 blend on regeneration behavior .....	106
7.3	Model and reaction scheme employed.....	121
7.4	Filter geometry and model input data .....	121
7.5	Tuning of kinetics parameters .....	121
8.	Impact of biodiesel on fuel system components durability .....	124
8.1	Introduction.....	124
8.2	Fuel filter plugging .....	127
8.3	Common Rail injector wear .....	128
8.4	Pressure regulator replacement .....	133
8.5	Common Rail high pressure pump replacement .....	133
9.	Experimental investigation of the effect of biodiesel blends on the characteristics of fuel sprays .....	136
9.1	Introduction.....	136
9.2	Influence of fuel properties on droplet diameter.....	136
9.3	Diesel spray dynamics .....	137
9.4	Laser Doppler Velocimetry overview .....	137
9.5	Test equipment and procedure .....	137
9.6	Test fuels .....	141
9.7	Results and discussion.....	141
9.8	Conclusions.....	153
10.	Conclusions.....	155
11.	References .....	157

© Δημήτριος Τζιουρτζιούμης

Η έγκριση της διδακτορικής διατριβής από το Τμήμα Μηχανολόγων Μηχανικών της Πολυτεχνικής Σχολής του Πανεπιστημίου Θεσσαλίας δεν υποδηλώνει αποδοχή των απόψεων του συγγραφέα (Ν. 5343/32 Άρθρο 202 παρ. 2).

# Ευχαριστίες

Στη διάρκεια εκπόνησης της παρούσας Διδακτορικής Διατριβής σημαντικός αριθμός ανθρώπων συνεργάστηκαν και πρόσφεραν την βοήθεια τους υποστηρίζοντας τη διεξαγωγή της έρευνας με διάφορους τρόπους. Είμαι ευγνώμων σε όλους. Στο σημείο αυτό θεωρώ υποχρέωση μου να απευθύνω θερμές ευχαριστίες στους παρακάτω:

- Τον επιβλέποντα της παρούσας Διατριβής, Δρ. Αναστάσιο Σταματέλλο, για την εμπιστοσύνη με την οποία με περιέβαλε από τα φοιτητικά μου χρόνια και την αμέριστη επιστημονική και ανθρώπινη καθοδήγηση που με προσέφερε στην αντιμετώπιση πάσης φύσεως προβλημάτων που ανέκυψαν στις διάφορες φάσεις της παρούσας Διατριβής. Του είμαι πραγματικά ευγνώμων γιατί δημιούργησε τις προϋποθέσεις για την πραγματοποίηση της εργασίας αυτής.
- Τα μέλη της συμβουλευτικής επιτροπής Δρ. Κώστα Παπαδημητρίου και Δρ. Ερρίκο Σταπουντζή για τις χρήσιμες παρατηρήσεις και υποδείξεις τους στις διάφορες φάσεις της εργασίας. Επιπλέον, θα ήθελα να ευχαριστήσω τον Δρ. Ερρίκο Σταπουντζή για την καθοδήγηση και τις λεπτομερείς παρατηρήσεις του κατά τη μελέτη της επίδρασης του αυξανόμενου ποσοστού biodiesel στα χαρακτηριστικά ψεκασμού εγχυτήρων Diesel χαμηλής (10 bar) και υψηλής πίεσης (210 bar) (κατανομές ταχυτήτων και διαμέτρων σταγονιδίων), καθώς επίσης και για την ευγενή παραχώρηση εύκολης πρόσβασης και χρήσης της συσκευής Laser Doppler Velocimetry-1D component για τα αντίστοιχα πειράματα.
- Τον Καθηγητή Δρ. Νικόλαο Πελεκάση, τον Αναπληρωτή Καθηγητή Δρ. Αναστάσιο Σταμάτη, τον Αναπληρωτή Καθηγητή του ΑΠΘ Δρ. Γρηγόριο Κολτσάκη και τον Επίκουρο Καθηγητή του Τ.Ε.Ι. Λάρισας Δρ. Ονούφριο Χαραλάμπους για την ευγενή αποδοχή τους να είναι μέλη της εξεταστικής επιτροπής και τις εκτενείς παρατηρήσεις τους.
- Τους προπτυχιακούς και μεταπτυχιακούς φοιτητές του Ε.Θ.Θ.Μ. Φώτη Μπουρουτζήκα για την ανεκτίμητη βοήθεια του στο στήσιμο των πειραματικών διατάξεων (Ruggerini RF91 DI Diesel engine) και στη μελέτη των φαινομένων που ανέκυψαν κατά τις διάφορες φάσεις της έρευνας, τον μεταπτυχιακό φοιτητή Δημήτριο Τσοκόλη για την συνεργασία κατά την ανάπτυξη της αυτοματοποιημένης διαδικασίας επεξεργασίας των δυναμοδεικτικών μετρήσεων. Τον προπτυχιακό φοιτητή Γιάννη Χατζηνάκη και τον Erasmus προπτυχιακό φοιτητή Remi Staub για την συμβολή τους στην διεξαγωγή των πειραμάτων στην περιοχή των ψεκασμών μιγμάτων diesel με διάφορα ποσοστά biodiesel και τέλος την Δρ. Μηχανολόγο Μηχανικό Ολυμπία Ζώγου για την ομαλή συνεργασία που είχαμε όλα αυτά τα χρόνια. Θα πρέπει να σημειωθεί ότι η έγκαιρη και επιτυχής περαίωση της εργασίας έγινε εφικτή χάρη στην συνεισφορά και την ομαδική συνεργασία ,υπό την καθοδήγηση του επιβλέποντος, των μελών του Εργαστηρίου.
- Την Εταιρεία PSA Peugeot-Citroen για την ευγενή προσφορά του σύγχρονης τεχνολογίας common rail κινητήρα Diesel (DW10 ATED) και του λογισμικού διαχείρισης της ECU του κινητήρα (INCA software) τα οποία αποτέλεσαν τα κεντρικά εργαλεία στην διεξαγωγή των πειραμάτων κατά το 1<sup>ο</sup> μέρος της Διατριβής.

- Την εταιρεία IBIDEN Co. Ltd για την ευγενή προσφορά των κεραμικών φίλτρων που χρησιμοποιήθηκαν στην διεξαγωγή των μετρήσεων.
- Την εταιρεία Rhodia Electronics & Catalysis για την παροχή του διαλύματος του καταλυτικού προσθέτου.
- Την εταιρεία Lion Hellas και ειδικά τον διευθυντή ανταλλακτικών κ Σπύρο Σταμπολή για την παροχή καινούριας αντλίας υψηλής πίεσης Common Rail με σημαντικά μειωμένο κόστος.
- Τον κ. Αναστάσιο Δαφερέρα (ΕΤΕΠ του Τμήματος) για την ανεκτίμητη συμβολή του στο σχεδιασμό και κατασκευή των πολύπλοκων διατάξεων που χρησιμοποιήθηκαν στις διάφορες πειραματικές διατάξεις, καθώς και τον κ. Αθανάσιο Βέργο (ΕΤΕΠ του Τμήματος) ο οποίος συνεργάστηκε σε διάφορες μηχανουργικές εργασίες.

**Ειδικές ευχαριστίες:** Η παρούσα Διδακτορική Διατριβή ενισχύθηκε οικονομικά από το Κοινωφελές Ίδρυμα Αλέξανδρος Σ. Ωνάσης στα πλαίσια χορήγησης υποτροφίας Διδακτορικών Σπουδών Εσωτερικού κατά το χρονικό διάστημα 2009-2011.



# Acknowledgments

With undertaking my PhD, a variety of people helped and supported me in various ways. In this section, I would like to acknowledge those mentioned below and express my gratitude to them.

My supervisor, Dr. Anastassios Stamatelos, for his confidence from the first years of my undergraduate studies and his invaluable support in all phases of this work. Through, these years, he guided me, contributed in every bit of this work and offered his thoughtful advice and knowledge in the field of Mechanical Engineering. I am grateful to him because he generated the conditions for the completion of this work.

The members of the supervising committee, Dr. Costas Papadimitriou and Dr. Hericos Stapountzis for his guidance during the study of the phenomena and issues that came during the various phases of this work. Further acknowledgments should be given to Dr. Hericos Stapountzis for his contribution to the study of the effect of the increased biodiesel blending ratio on diesel injectors' injection characteristics, the profitable discussions during the analysis of the results and the kind supply of the Laser Doppler Velocimetry 1D-component for the measurements of the velocity and droplet diameters distributions.

Dr. Nikolaos Pelekasis, Dr. Anastassios Stamatis, Dr. Grigoris Koltsakis of the Mechanical Engineering Faculty, AUTH, and Dr. Onoufrios Haralampous of the Technological Education Institute of Larissa, for their valuable advice and remarks.

My colleagues in the Lab. undergraduate students, Fotis Bouroutzikas, Giannis Hatzinakis and Erasmus student Remi Staub, and a post graduate student, Dimitris Tsokolis, for his invaluable help to the preparation of the experimental devices and the useful discussions during the study of the phenomena and finally Dr. Mechanical Engineer Olympia Zogou for the smooth collaboration during the various phases of this work.

Ing. Anastassios Dafereras, support staff of the Department, for his invaluable contribution during the design and construction of the electronic parts of experimental devices employed in this work and Mr. Athanasios Vergos for the smooth cooperation and support during various technical works.

The companies PSA Peugeot-Citroen for the supply of a modern HDi Diesel engine and engine management data, Ibiden Co. Ltd for the supply of Diesel filters and Rhodia Electronics & Catalysis for the supply of fuel additives employed in the loading and regeneration experiments.

**Special acknowledgements:** This PhD Thesis was financially supported by "Alexander S. Onassis" Public Benefit Foundation under a doctoral scholarship (2009-2011). The initial motivation for the work stemmed from our participation in the collaborative R&D project "RIP A6-Production of biofuels in Thessaly", with financial support from the Hellenic General Secretariat of Research and Technology, with EU funds.

## Abstract

In Greece, biodiesel, in the form of Fatty Acid Methyl Esters (FAME), is produced since 2005 and currently mixed in the Diesel fuel at about 5.5% vol., this percentage being slowly but steadily increasing. The production capacity of existing biodiesel factories in Greece can supply the required quantities to increase the biodiesel blending percentage up to 15%, provided that the necessary vegetable oil and recycled oil quantities should become available and prices be favorable. According to Greek legislation, at least 30% of the raw material must be domestically produced. This need is covered mainly by recycled cooking oils and only secondarily by energy crops in Northern Greece. The production of biodiesel from local factories in Greece was regulated by means of distributing an annual quantity of biodiesel among the factories, based on an algorithm that is modified every year. Automotive manufacturers allow running of modern diesel powered passenger cars on blends of biodiesel up to B20-B30, provided that certain additional maintenance measures are taken, including more frequent fuel and oil filter changes, along with inspection of engine oil level and the fuel lines and injection system components for possible leaks. In order to ensure customer's acceptance, standardization and quality assurance are key factors for the market introduction of biodiesel as transport fuel. This PhD thesis examines the effect of biodiesel fuel on performance, efficiency, emissions and injection system durability of conventional and modern Diesel engines under steady state and transient operating conditions.

These include a better understanding of the engine ECU operation with a high biodiesel (FAME) blend in modern common-rail injection Diesel engine, the study of the biodiesel combustion analyzing the captured indicator graphs, the investigation of the filter regeneration behavior by means of the infrared thermography on a small filter module and in-house computational tool and the study of biodiesel atomization and injection characteristics by means of the Laser Doppler Velocimetry technique.

In the first part of the Thesis, a better understanding of the engine ECU operation with a high biodiesel (FAME) blend in modern common-rail injection Diesel engines is attempted. This understanding is applied to the explanation of the observed effects on the engine performance and emissions characteristics with this engine category. The results are compared to the relatively scarce works reported in the specialized literature for the specific engine category and high blending ratios. Also, the effect of biodiesel blends in the transient fuel system and engine operation is examined. Furthermore, the effect of prolonged engine operation at a high biodiesel blend on the fuel system and the engine components is investigated.

In the second part of the Thesis, the effect of low percentage biodiesel blends on the diesel filter loading and regeneration behavior of a conventional, single cylinder Diesel engine with low pressure injection system is presented. A fuel additive is employed in order to perform filter regeneration at relatively low exhaust temperatures. The effect of the biodiesel on the filter regeneration is further investigated by means of infrared thermography on a small filter module and in-house computational tool. In addition, the effect of biodiesel on injection characteristics is investigated by means of Laser Doppler Velocimetry technique.

The results enhance our understanding of the engine ECU behavior with the high percentage biodiesel blends. Certain modifications to engine ECU maps and control parameters are proposed and discussed, aimed at improvement of transient performance of modern engines run on high percentage biodiesel blends. However, a high pressure pump failure that was observed after prolonged engine operation with the B70 blend, hints to the use of more conservative biodiesel blending in fuel that should not exceed 30% for common rail engines.

The observed benefits as regards the DPF extend also to the faster evolution of regeneration and the lower overall filter wall temperatures with favorable effects on the filter durability.

## Nomenclature

A	pre-exponential factor of reaction rate expression, [mole/(m <sup>3</sup> s)]
A/F	air to fuel ratio
A <sub>p</sub>	plunger area, [mm <sup>2</sup> ]
(A/F) <sub>st</sub>	stoichiometric air to fuel ratio
B	bulk modulus, [Pa]
b <sub>sp</sub>	fuel delivery per stroke (fuel consumption), [mm <sup>3</sup> /st.]
c	speed of sound, [m/s]
d <sub>j</sub>	diameter of the undistributed jet, [μm]
E	activation energy, [J/mole]
E <sub>str</sub>	fuel energy input per stroke, [J/st]
H <sub>u</sub>	lower heating value, [MJ/kg]
m	mass, [kg]
m <sub>f</sub>	fuel mass flow rate, [kg/s]
m <sub>fr</sub>	mass flow rate, [kg/s]
Oh	Ohnesorge number, [-]
p	injection pressure, [bar]
P	engine power [kW]
r	rate of reaction, [mole/(m <sup>3</sup> s)]
R	universal gas constant, [8.3144 J/(moleK)]
Re	Jet Reynolds number, [-]
t	time, [s]
T	temperature, [K]
u	plunger velocity, [m/s]
<u>v</u>	relative velocity of the ambient gas, [m/s]
V	volume of compressed fuel, [m <sup>3</sup> ]
We	Jet Weber number, [-]
y	oxygen molar fraction, [-]

## Greek letters

β	coefficient of volume thermal expansion, [K <sup>-1</sup> ]
η <sub>th</sub>	thermal efficiency, [%]
θ	crank shaft angle, [deg]
λ	lambda = (A/F)/(A/F) <sub>st</sub> [-]
μ	dynamic viscosity, [Pa s]
ρ	density, [kg/m <sup>3</sup> ]
ρ <sub>0</sub>	density at 15°C, [kg/m <sup>3</sup> ]
σ	surface tension, [N/m]
ψ	fractional extent of the catalytic additive oxidation, [-]

## Abbreviations

AMD	Area Mean Diameter, [μm]
BM	isentropic Bulk Modulus, [Pa]
b <sub>mep</sub>	brake mean effective pressure, [bar]
b <sub>sf</sub>	brake specific fuel consumption, [g/kWh]



CA	Crank Angle, [deg]
COV	Coefficient of Variation
DI	Direct Injection
DoE	Design of Experiment
DPF	Diesel Particulate Filter
ECU	Engine Control Unit
EGR	Exhaust Gas Recirculation
FAME	Fatty Acid Methyl Ester
HSDI	High Speed Direct Injection (engine)
imep	indicated mean effective pressure, [bar]
ITA	Injection Timing Advance
LTTE	Laboratory of Thermodynamics and Thermal Engines
NOP	Nozzle Opening Pressure
PM	Particulate Matter
PN	Particle Number
PWM	Pulse Width Modulation
SMD	Sauter Mean Diameter, [ $\mu\text{m}$ ]
TGA	Thermo-Gravimetric Analysis
UEGO	Universal Exhaust Gas Oxygen (sensor)
VMD	Volume Mean Diameter
VOF	Volatile Organic Fraction

## 1. Introduction – Aim and Objectives of this Thesis

According to the ambitious Vision Paper of the Biofuels Research Advisory Council [1], the European Union could replace 25% of its transportation fuels by biofuels until 2030. Due to the specific fuel balances existing in the European Fleet, that make Europe a net exporter of gasoline and importer of Diesel fuel it is estimated that this target would be most probably realized mainly by biodiesel (75% biodiesel-vs-25% bioethanol) [2]. In Greece, biodiesel, in the form of Fatty Acid Methyl Esters (FAME), is produced since 2005 and currently mixed in the Diesel fuel at about 5.5% vol., this percentage being slowly but steadily increasing. The production capacity of existing biodiesel factories in Greece can supply the required quantities to increase the biodiesel blending percentage up to 15%, provided that the necessary vegetable oil and recycled oil quantities should become available and prices be favorable. According to Greek legislation, at least 30% of the raw material must be domestically produced. This need is covered mainly by recycled cooking oils and only secondarily by energy crops in Northern Greece. The production of biodiesel from local factories in Greece was regulated by means of distributing an annual quantity of biodiesel among the factories, based on an algorithm that is modified every year. The total quantity of biodiesel that is mixed in the Diesel fuel in Greece is relatively low during the last years, compared to the total production capacity of the 14 local factories that amounts to 800,000 m<sup>3</sup>. Besides the annual fluctuations, there is an overall increasing trend in the local factories' production and the percentage of raw materials locally produced in Greek energy crops. Total Biodiesel production in Greece was about 164,000 m<sup>3</sup> in 2010 and 132,000 m<sup>3</sup> in 2011. This corresponds to an overall blending ratio of about 5-7%. Figure 1.1 presents the biodiesel production in Greece during the last 6 years.

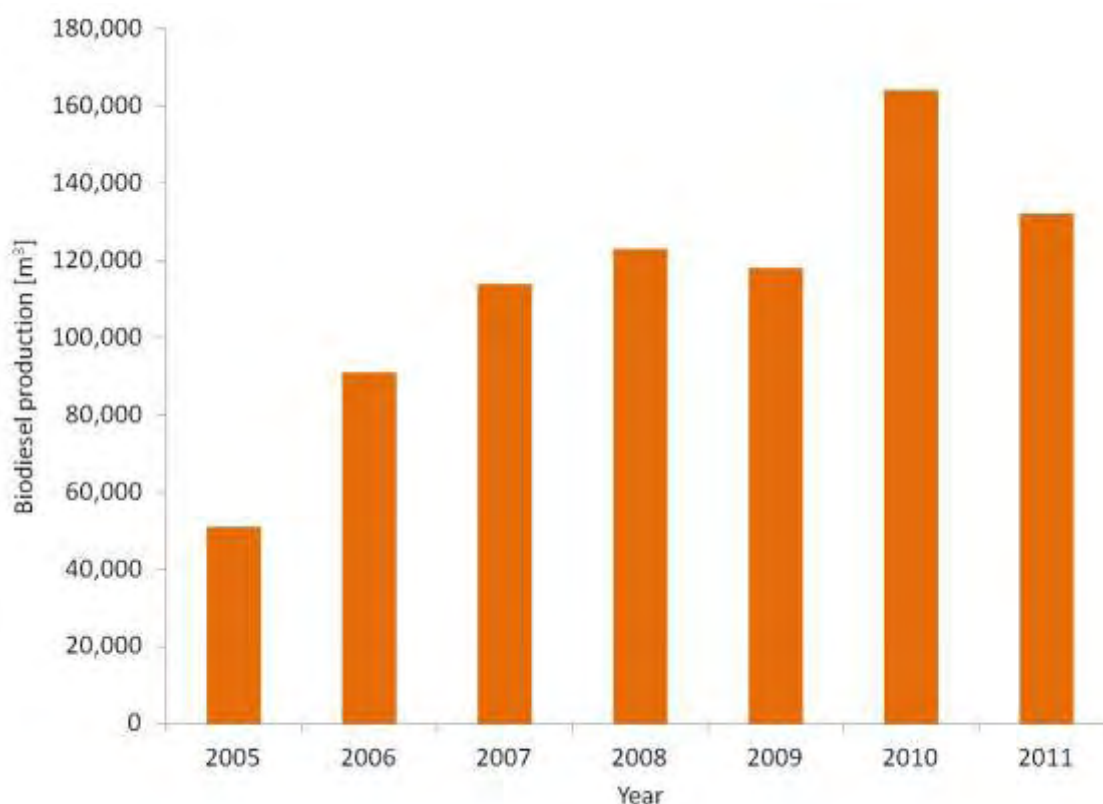


**Figure 1.1.** Biodiesel production in Greece during the last 6 years, from 2005 to 2011.

Biodiesel production in Greece started in 2005 with a total production of 51,000 m<sup>3</sup>. After that, a sharp increase was followed, reaching the values of 91,000 m<sup>3</sup>, 114,000 m<sup>3</sup> and 123,000 m<sup>3</sup> in 2006, 2007 and 2008 respectively. In 2009, the last year before the economic crisis, the total biodiesel production was about 118,000 m<sup>3</sup> and amounted to 4.1% of the total Diesel fuel consumption of 2,837,350 m<sup>3</sup>. On the other hand, the steady long-term increase of fuel prices, along with the severe taxation of fuel in Greece would make extremely profitable to produce biodiesel in small units operated by local farmers in Thessaly, to fuel their agricultural machinery.

Nowadays, automotive manufacturers allow running of modern diesel powered passenger cars on blends of biodiesel up to B20-B30, provided that certain additional maintenance measures are taken, including more frequent fuel and oil filter changes, along with inspection of engine oil level and the fuel lines and injection system components for possible leaks. In order to ensure customer's acceptance, standardization and quality assurance are key factors for the market introduction of biodiesel as transport fuel.

According to a common statement by the diesel fuel injection systems manufacturer's association [3], diesel fuel specifications (EN 590 in Europe, D6751 in the USA), should be regularly updated to allow for the gradually increasing percentage of biodiesel mixing (currently 5% but soon to be extended to 7%+3%). In this way, the injection system's components are to be protected from possible secondary effects of fatty acid methylesters that include fuel leakage or filter plugging due to the softening, swelling or hardening and cracking of some elastomers and displacement of deposits from diesel operation, corrosion of aluminium or zinc parts in fuel injection equipment due to free methanol residues, filter plugging or corrosion of fuel injection equipment due to residues of FAME process chemicals, corrosion of fuel injection equipment or filter plugging due to hydrolysis of FAME by free water residues – bacterial growth, filter plugging or injector coking due to corrosion of non-ferrous metals by free glycerine residues, filter plugging – lacquer formation by soluble polymers in hot areas due to the precipitation of deposits, generation of excessive local heat in rotary distributor or supply pumps, due to the high viscosity of the biodiesel [4]. Also, further oxidation stability improvements are considered essential to the increase of biodiesel blending percentages above 20%. Resistance to oxidative degradation during storage is an increasingly important issue for biodiesel [5, 6].

The effects of biodiesel blends on the operation, performance and emissions of Diesel engines have been studied by a vast amount of published and unpublished research work, since 1980 [4, 7, 8]. The combustion of biodiesel in engines equipped with pump–line–nozzle fuel systems normally results in advancement of the start of injection and combustion, due to differences in chemical and physical properties of the fuels. Unit injector or common rail injection system – equipped engines do not exhibit the same behavior [9, 10].

As a general trend, combustion of biodiesel blends reduces CO, HC and particulate emissions, both in older technology and modern diesel engines, depending also on the specific quality of biodiesel employed [11]. In addition to legislated pollutants, biodiesel is known to significantly reduce several unregulated pollutant species.

As a general conclusion from the study of the specialized literature, one could say that the published research on the performance and emissions of modern, common rail injection engines with medium-to-high percentage of biodiesel blending is limited. This observation was the main motivation factor for the first part of this thesis.

As a second conclusion from the literature search, the published research on the performance of Diesel Particulate Filters installed on engines run on biodiesel blends is also limited. This observation was the main motivation factor for the second part of this thesis.

Overall, it should be emphasized that the production and use of biodiesel in Thessaly, that was the main motivating force behind this thesis and the associated research work of the Laboratory, remains a valid option today, in view of the increasing fuel prices, the significant fuel needs of the agricultural operations and the resulting good profitability of energy crops. The use of low –to- medium percentage biodiesel blends is expected to be a workable choice both for the common rail engines of modern agricultural tractors and the wide variety of older equipment that is and will be in use for many years to come.

Based on the above reasoning and strategy, this thesis was designed to consist of two parts:

In the first part, a better understanding of the engine ECU operation with a high biodiesel (FAME) blend in modern common-rail injection Diesel engines is attempted. This understanding is applied to the explanation of the observed effects on the engine performance and emissions characteristics with this engine category. The results are compared to the relatively scarce works reported in the specialized literature for the specific engine category and high blending rates [11-13]. Also, the effect of biodiesel blends in transient fuel system and engine operation is examined. Furthermore, the effect of prolonged engine operation at a high biodiesel blend on the fuel system and the engine components is investigated.

In the second part of this thesis, we focus on the effect of low percentage biodiesel blends on the diesel filter loading and regeneration behavior of a conventional, single cylinder engine with low pressure injection system. A fuel additive is employed in order to perform filter regeneration at relatively low exhaust temperatures. The effect of the biodiesel on the filter regeneration is further investigated by means of infrared thermography on a small filter module and in-house computational tools. In addition, the effect of biodiesel on injection characteristics is investigated by means of Laser Doppler Velocimetry technique.

The following diagram gives an overview of the contents of this PhD thesis and helps understanding the research strategy employed.

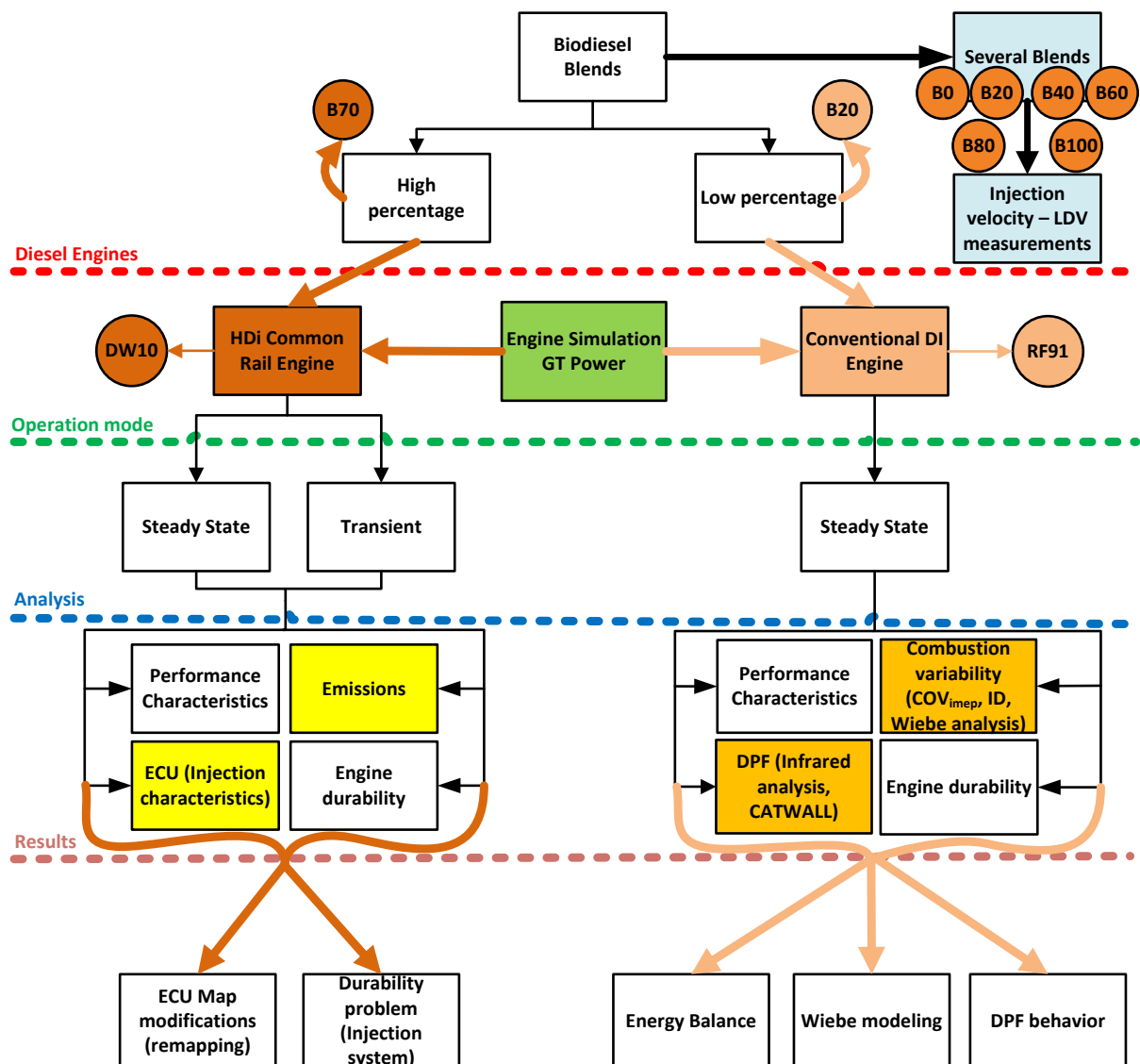


**Figure 1.2.** Thesis investigation strategy – Two type of diesel engines (modern and conventional) running on different operation modes, using high and low biodiesel blends in order to investigate corresponding operation variables.

The most important novelties of this thesis are the following:

- (i) The effect of the use of a high percentage biodiesel blend – B70 – on the injection control, performance, emissions and durability of a modern, high pressure injection, common rail Diesel engine is studied and adds to the limited published research results in this subject.
- (ii) The effect of the use of medium percentage of biodiesel blends – B20, B40 – on the performance, injection, combustion and especially on the Diesel Particulate filter loading and regeneration behavior is assessed by novel experimental methods, assisted by modeling.

## 2. Literature search on the effect of Biodiesel on engine performance, emissions and DPF operation

### 2.1 Literature review – common rail diesel engines with biodiesel

Rapeseed biodiesel is in use in Germany since the early eighties. Its use has been progressively increasing in Europe and North America during the following years, adding different plant oils in the biodiesel mixture. An initial review of the specialized literature regarding the effects on engine performance and emissions, published by [7], soon became obsolete. The last decade was marked by an impressive expansion of international interest on biofuels, supported by a highly ambitious position by the European Union [1, 14]. However, a certain slowdown in the expansion of the use of biofuels is observed after 2008, that is due to skepticism about possible side effects on the prices of foodstuff [15], as well as the need to better study the plant-to-wheel efficiency and sustainability of biofuel production and use. Despite the slower increase of biofuels penetration in the market, the specialized research literature continues to expand. The interest is shifted to the third generation biofuels which employ low-priced agricultural by-products for their production [16].

An inclusive literature review on the general subject of the effect of biodiesel on engine performance and emissions, that covered more recent work done during the last decade was first presented in [8]. As regards the effects of biodiesel blends on CO and THC emissions, most researchers agree to a significant decrease when substituting conventional diesel fuel with biodiesel fuels. A review by EPA [17], pointed to a 70% mean reduction in THC levels and about 50% in CO when the engine is fuelled by pure biodiesel instead of conventional diesel. The reasons proposed to explain this decrease included the oxygen content of the biodiesel itself, the higher cetane number of biodiesel which reduces combustion delay, the higher final distillation point of diesel fuel (THC emissions), as well as the advance in injection and combustion timing. Nevertheless, further, significant research work with modern, common rail Diesel engines is necessary in order to better understand the effects of biodiesel blends on the injection, combustion and emissions of ultra-low emitting engines. Especially with the EURO-4 and EURO-5/6 engines, equipped with diesel particulate filters, which are now on the European vehicle fleet, it is necessary to study in depth the effect of biodiesel on the operation of the different filter [18] and regeneration technologies and engine durability effects due to oil dilution from post-injection [19-21].

NO<sub>x</sub> and Particulate Matter (PM) emissions are the main concern for modern Diesel engines, due to the high temperature, lean, diffusion flame of the Diesel combustion chamber. NO<sub>x</sub> and PM emissions of modern Diesel engines are very close to the legislated standards, which are becoming increasingly stringent [22]. For example, Euro 5 legislation reduces NO<sub>x</sub> and PM emissions of passenger cars from 0.25 and 0.025 g/km up to 0.18 and 0.005 g/km, respectively, in the NEDC [23]. Moreover, EURO-5/6 legislation additionally checks particle number emissions. A solid particle number (PN) emission limit of  $6 \times 10^{11}$  km<sup>-1</sup> becomes effective at the Euro 5b/6 stage for all categories of diesel vehicles (M, N1, N2). The PN limit must be met in addition to the PM mass emission limits. PN emissions are measured over the NEDC test cycle using the PMP method [24]. The same limit will be applied to Direct Injection (FSI) gasoline vehicles. Number-based PN limits are significantly more stringent than the respective mass-based PM limits and reflect the well-established knowledge of the more severe health effects of nanoparticles with very low total mass, compared to larger micron-sized particles that make up for the larger part of the total particulate mass emitted by modern engines. [25, 26]. An improved understanding of the pollution reduction potential of biodiesel in modern Diesel engines would help car manufacturers to better adapt

their engines to the use of higher percentages of biodiesel, compromising between efficiency and cost. Also, it could suggest that local authorities further promote biodiesel use in urban areas with numerous diesel powered vehicles as a possible means of improving air quality.

As regards diesel-powered cars and light commercial vehicles, Euro 5 emissions reduction requirements, effective until Euro 6 comes into force (2014), apply stringent limits for NO<sub>x</sub> emissions (80 mg/km) and particulate matter (4.5 mg/km). Starting from 2012, each manufacturer must adhere to an average CO<sub>2</sub> emissions limit equivalent to 130 g/km for all new passenger cars registered in the EU. The remaining 10 g/km reduction necessary to meet the proposed 120 g/km target for the whole car industry by 2012, (average current levels: 160 g/km), is to be achieved partly by the increased use of sustainable biofuels. On 23 April 2009, the European Union adopted the Renewable Energy Directive (RED) which includes a 10% target for the use of renewable energy in road transport fuels by 2020 [27]. The same target is shared by Brazil, Japan and Indonesia. China's target for 2020 is 5%. U.S. aims at a 30% for 2030. Scepticism about the positive impact of biofuels has escalated recently. The observed trade-offs between food, animal feed and fuels and their impact on agricultural markets led to a debate over the role of biofuels in the 2007-08 food-prices crisis that is slowing down the -initially more ambitious- legislative steps.

According to a common statement by the diesel fuel injection systems manufacturer's association [28], diesel fuel specifications (EN 590 in Europe, D6751 in the USA) should be regularly updated to allow for the gradually increasing percentage of biodiesel blending. In this way, the injection system's components are to be protected from possible secondary effects of fatty acid methylesters that include fuel leakage or filter plugging due to the softening, swelling or hardening and cracking of elastomers and displacement of deposits, corrosion of aluminium or zinc parts in fuel injection equipment due to free methanol residues or residues of FAME process chemicals, free glycerine, generation of excessive local heat in rotary pumps, due to the high viscosity of the biodiesel [4]. Also, further oxidation stability improvements are considered essential to the increase of biodiesel blending percentages above 20%. Resistance to oxidative degradation during storage is an increasingly important issue for biodiesel [5, 6]. Although no more than 20% biodiesel is normally blended in the fuel, the use of higher percentage blends has been tested and several research papers [29-31] have been published on the effect on the steady state engine performance and emissions. On the other hand, transient characteristics and fuel system's dynamics are certainly affected by the use of high percentage biodiesel blends and this needs further investigation.

### **2.1.1 Engine power and efficiency**

Biodiesel possesses a reduced gross heating value (on a mass basis) compared to diesel fuel. This holds true (to a lesser extent) also per unit volume and results in higher volume fuel consumption whenever diesel fuel is substituted by biodiesel. Thus, when the engine is tested on the test bench, maximum power is reduced unless the maximum fuel pump delivery per stroke is increased to compensate for the lower heating value reduction. Although the reported rated power reduction range at about 8% for B100 and by analogy to lower blends, there exist some variation around these percentages among different engines and researchers [32-36] (experimental errors are frequent in the measurement of fuel consumption in various cycles). In older injection systems on the other hand, the higher viscosity, which reduces the back flow across the piston clearance of the injection pump, may further compensate the loss in heating value. In addition, the higher bulk modulus and sound velocity of biodiesel [37-39], together with its higher viscosity [40], lead to an advanced start of injection. This, jointly with cetane number increase, may slightly advance the start of combustion, which sometimes may increase the power output.

Engine thermal efficiency, as calculated from brake-specific fuel consumption, is normally employed to compare the performance of different fuels, taking aside the effect of the difference in their Lower Heating Value. Most researchers observed no significant change in thermal efficiency when using biodiesel [8, 41]. However, thermal efficiency with alternative fuels should always be calculated with the necessary accuracy: that is, the heating value of the fuel must be measured, along with the fuel density, in the case of volumetric fuel flow rate measurement. Fuel density changes with temperature should also be taken into account [42].

### 2.1.2 NO<sub>x</sub> emissions

Most of the literature reviewed in [8] shows either a slight NO<sub>x</sub> emissions increase with biodiesel blends, or no important effect at all. Increase in NO<sub>x</sub> in older technology engines is mainly attributed to the advancement in injection derived from the physical properties of biodiesel (viscosity, density, compressibility, speed of sound). The effect of the physical properties of biodiesel on the injection advance (with respect to the start of injection with diesel fuel) has been widely proved in older technology engines. When biodiesel is injected, the pressure rise produced by the pump propagates more quickly towards the injectors due to its higher sound velocity. In addition, the higher viscosity reduces leakages in the pump leading to an increase in the injection line pressure. Therefore, a quicker and earlier needle opening is observed with respect to diesel fuel.

Nowadays, the injection cartographies are optimized by engine designers as a function of the NO<sub>x</sub>-soot trade-off [8]. Delaying injection can reduce the NO<sub>x</sub> emissions level, increasing of course PM emissions [14]. Leung et al. [43] proposed that other injection parameters, in combination with injection timing, should be modified in order to eliminate the expected NO<sub>x</sub> emissions increase without any penalty in PM reductions.

The effect of the increased oxygen availability on NO<sub>x</sub> emissions has also been examined by various researchers. Lapuerta et al. [8] concluded that the oxygen content of biodiesel could not cause any increase in NO formation because diffusion combustion occurs mainly in regions with oxygen-fuel ratio around the stoichiometric one, which is 2.81 for biodiesel with C:H ratio of 1.87 and 3.58 for a standard diesel fuel with C:H ratio 1.82. They argue that internal oxygen in the fuel molecule is not enough to compensate this difference.

### 2.1.3 Particulate matter and smoke opacity

The literature search made by [8] concludes that almost the majority of authors report a noticeable decrease in PM emissions with the use of biodiesel blends as fuel. However, this reduction in the solid fraction of the particulate (black carbon), is usually accompanied by an increase in the soluble organic fraction (SOF). Such an increase could be due to the lower volatility of the unburned hydrocarbons from biodiesel combustion, which favors their condensation and adsorption on the particles surface. Yamane et al. [44] carried out optical visualizations of the fuel jet and found that evaporation and air-mixing are slower with biodiesel. The following factors are reported to explain the particulate reduction by use of biodiesel: The oxygen content of the biodiesel molecule, which promotes combustion even in fuel-rich regions, the lower stoichiometric A/F of biodiesel combustion, which reduces the probability of fuel-rich regions. Also, the non-existence of aromatics in biodiesel fuels and the zero sulfur content of most biodiesel fuels, which prevents sulfate formation. Finally, it is known that biodiesel, despite its higher average distillation temperature, demonstrates a lower final boiling point. That is, heavy distillates that are unavoidably present in small quantities in Diesel fuel, are absent in biodiesel due to its natural origin. The



absence of such heavy hydrocarbons unable to vaporize, (soot precursors), reduces soot emissions [8, 45-47].

## 2.2 Evolution of the modern diesel injection systems

The variety of reported trends in the effect of biodiesel fuel blends on Diesel engine combustion can be mainly attributed to the variety of existing, older and modern fuel injection systems, especially for diesel passenger cars. Starting from the pre-chamber and swirl-chamber engines where the combustion was initiated at rich blend conditions in the pre-chamber and continued later in the main chamber, where the partially burned blend was injected, equipped with glow plugs for the preheating of the pre-chamber and rotary type fuel pumps, that distribute at 130-150 bar the fuel to the pressure-operated injectors, with the increased particulate emissions in transient operation, technology shifted during the nineties to the Direct Injection Diesel engines, with a distributor pump with increased injection pressure levels (180-250 bar) and some electronic parts. Thus, the passenger diesel cars acquired the well-known fuel economy, reliability, lower cylinder head thermal loading, lack of preheaters etc, advantages of the DI engines traditionally employed in trucks and buses. However, they also took their disadvantages, like the increased noise levels, and the difficulties to attain the increasingly stringent particulate and NO<sub>x</sub> emissions standards.

Modern passenger car diesel engines are of the common rail, high pressure direct injection technology. A rotary pump supplies the common rail with high pressure (1300-2000 bar) fuel. The injectors are fed by this rail, controlled by an electric valve, based on ECU signals. These engines are more quiet and cleaner as regards emissions, especially during acceleration, due to the improved control of combustion, by means of dividing injection in pilot injection, main injection and also possibly post-injection (when necessary for exhaust temperature increase to induce regeneration of the diesel filter).

Diesel engine emissions are known to be affected by fuel quality, engine operation temperature, combustion chamber type and technology, fuel injection system technology, engine operation point and operation conditions. During the last fifteen years, engine exhaust emission standards in Europe, measured according to the NEDC (New European Driving Cycle), evolved from Euro 1 (1993 – CO < 3.16 g/km, HC+NO<sub>x</sub>< 1.13 g/km, particulate < 0.16 g/km) to Euro 5 (2009 - CO < 0.5 g/km, (HC+NO<sub>x</sub>)< 0.23 g/km, NO<sub>x</sub> < 0.18 g/km, particulate < 0.005 g/km) and beyond (EURO 6, 2014). Especially the NO<sub>x</sub> and particulate standards are extremely stringent – the latter require the use of a particulate filter as standard equipment in modern diesel passenger cars.

Fuel quality improves, with gradually diminishing sulfur content (e.g. EN-590: 1996: 0.05 %, 2005: 50 ppm, 2009:10 ppm). Also, the cetane index is increasing and the use of additives assisting emissions reduction is tolerated.

Injection pressure in common rail systems can be controlled irrespective of engine rpm, and stays constant during the injection phase. The accurate control of injector opening and closing by the microcomputer, allows for a wide range of possibilities for tailoring the injection and combustion curve by the engine manufacturer. The injected fuel quantity can be divided in separate parts, as the pilot injection which reduces engine noise due to self-ignition of the initial injected quantity, as well as the NO<sub>x</sub> formation. This small quantity of fuel (1 - 4 mm<sup>3</sup>) allows for a more regular combustion, with a gradual increase of temperature and pressure in the combustion chamber. The microcomputer control of all injection parameters, based on previously defined maps that are saved in the ECU memory, allow the optimization of steady state and transient engine operation.

The high pressure pump has been designed to supply significant fuel quantities with respect to the engine needs. The surplus quantity returns to the tank by means of a leak orifice that is controlled by the

pressure regulator. The pressure regulator controls the rail pressure, based on the engine speed and load. The required pressure value is computed by the ECU and confirmed based on the information fed back by the rail pressure sensor. Rail pressure varies between 280 bar (low load) and 1400 bar (high load), or even more, up to 2000 bar [48].

The injection pressure control loop is based on the determination, by the ECU, based on rpm and load, of the target value of the injection pressure. This value is fed to the pressure regulator. The actual rail pressure is fed back to the ECU to complete the control loop. The activation time of the injector solenoid valve varies between 200 - 1200  $\mu$ s.

In contrast with older injection systems, the ECU determines independently the injected fuel quantity and injection advance. The injected fuel quantity is determined by the ECU, by means of a combination of rail pressure and injection duration. The regulation of the fuel quantity is based on the estimation by the ECU, based on the respective sensors' signals and the rail pressure signal and the respective maps, of the required fuel quantity and the respective duration of injectors' current.

The rail pressure significantly affects the injected fuel quantity per degree Crank Angle, as well as the degree of atomization of the fuel. The injector opening duration, the injector needle lift and the number and diameter of injection orifices are the main factors determining the fuel delivery per stroke.

The engine ECU takes into account the following sensor's signals:

- throttle position
- cooling water temperature
- fuel temperature
- engine speed and crankshaft position
- ambient absolute pressure and intake manifold pressure
- vehicle speed
- activation of braking and clutch decoupling contact
- intake air mass flow rate and temperature.
- EGR valve position
- compressor boost pressure.

The ECU takes additionally into account the respective engine operating mode, i.e. engine startup (additional fuel delivery for startup), engine idle (idle fuel flow rate), normal operation, cold start, acceleration fuel enrichment etc.

An important sensor for the operation with biodiesel fuel blends is the fuel temperature sensor, normally of the CTN type, usually placed on the rail or on the fuel return circuit. This sensor's signal allows the ECU to correct the injected fuel quantity, to make up for the fuel viscosity decrease with temperature.

### **2.2.1 Injection system dynamics**

Dynamic fuel phenomena in common rail system components can cause sensible injection perturbations. The wave propagation phenomena following each injection event cause pressure oscillations that affect the injected fuel quantity [49]. The rail pressure is affected by the system dynamics due to the finite volume capacity of the rail. Most researchers investigated the injection pressure fluctuations and dynamic effects on multiple injection common rail system operation by means of test-bench experiments. Experiments carried out in a Bosch injector test bench showed that a proper control of the solenoid valve allowed drastically reducing the variability of the pilot pulses [50]. Ubertini [51] presented a physical model

that takes into account the geometry of the rail and the fuel properties, to simulate pressure fluctuations immediately upstream the CR injector. He concluded that the pressure oscillation frequency is a function of the rail's main dimensions and the speed of sound.

### **2.2.2 Transient engine performance**

Transient engine performance is increasingly studied during the last three decades, dating back to the classical works by Watson and Janota [52], Horlock and Winterbone [53]. Nowadays, experimental and computational studies of performance, emissions, injection characteristics and turbocharger parameters during transient operation using pure diesel but even biodiesel blends appear in various published works. Wijetunge et al. [18] studied the dynamic behavior of a high speed direct injection diesel engine equipped with CVT (continuously variable transmission) and VGT (variable geometry turbine) under steady state and transient operating conditions. They analyzed the changes of boost pressure, EGR and valve position and their effect on emissions, reporting deviations between transient and steady-state HC emissions. In the same manner the transient responses of different types of VGT were investigated by [54]. A detailed study on the transient modeling of common rail diesel engines has been presented in [55, 56]. The authors investigated diesel engine transient operation by means of experiments and simulation codes on an HSDI turbocharged diesel engine equipped with VGT.

In the common rail, high pressure direct injection engines, a rotary pump supplies the rail with high pressure fuel. The injectors are fed by the rail based on ECU signals. These engines are cleaner, especially during acceleration, due to the improved control of combustion by means of dividing injection in pilot injection, main injection and possibly post-injection, to induce regeneration of the diesel filter. Injection pressure in common rail systems can be controlled irrespective of engine speed and stays constant (on the average) during the injection phase. Accurate control of injector opening and closing by the microcomputer, allows for a wide range of possibilities for tailoring the injection and combustion curve.

The capabilities of microcomputer control are increasingly exploited by the engine manufacturers, as the detailed analysis of the common rail injection and combustion is increasing our understanding of the phenomena involved and the effect of the fuel properties on the process. The surplus fuel quantity supplied by the pump returns to the tank by means of a leak orifice that is controlled by the pressure regulator, controlling the rail pressure, based on the engine speed and load. The required pressure levels are computed by the ECU and confirmed based on the information fed back by the rail pressure sensor. Rail pressure varies between 280 bar (low load) and 1400 bar (high load), or even more, up to 2000 bar [48].

## **2.3 Combustion characteristics**

Several researchers investigated the effect of biodiesel blends on combustion characteristics such as peak cylinder pressure, pressure rise rate, combustion duration, heat release rate, by conducting experiments on direct injection diesel engines.

Zhang et al. [57] and McDonald et al. [58] investigated the combustion characteristics of direct injection diesel engines using blends of methyl, isopropyl and winterized methyl ester of soybean oil with diesel fuel. They found that all fuel blends had similar combustion behavior except of ignition delay which was shorter than diesel. In other study, Senatore et al. [36] concluded that, with rapeseed oil methyl ester as a fuel, heat release always takes place in advance, injection starts earlier and exhaust gas temperature is higher.

Sihna and Agarwal [59] investigated the combustion characteristics in a direct injection diesel engine running with diesel and rice bran oil methyl ester blend (B20). Tests were performed at different loads ranging from no load to 100% at constant engine speed. They found that the overall combustion

characteristics were quite similar for biodiesel blend B20 and B0. However, in the case of B20, the combustion starts earlier, the Ignition delay is lower and the combustion duration is slightly longer. Heat release analysis showed lower heat release rate during premixed combustion phase in case of B20 which was responsible for lower peak cylinder pressure and pressure rise rate. Further analysis indicated faster burn of 10% and slower burn of 90% of fuel using B20 blend.

The effects of pure rapeseed methyl ester (B100) and different diesel/RME (B20, B50) blends on cylinder pressure, emissions, engine efficiency and net heat release rate were presented by [10]. They found that the ignition delay was reduced while the initial uncontrolled premixed combustion phase was increased in case biodiesel blends. The advanced combustion resulted in the reduction of smoke, HC and CO. Fuel consumption was increased in case of blends due to lower LHV while engine efficiency was not affected.

## **2.4 Diesel Particulate Filter performance – Soot oxidation reactivity**

As already mentioned, the use of a DPF is absolutely necessary in Diesel cars following Euro 4. The drawback to using DPF aftertreatment technology is the increased backpressure from the stored soot and the fuel economy penalty associated with the regeneration. Filter durability may be also an issue here. Knowledge of soot reactivity in the DPF and the kinetics of soot oxidation are important in achieving optimal control and long durability of these devices.

Previous studies have shown improved DPF performance with the use of biodiesel blended fuels [60-64]. One such study measured two parameters used to gauge the performance of a DPF: balance point temperature and regeneration rate [61]. The balance point temperature is the temperature at which the rate of oxidation of stored soot is equivalent to rate of soot accumulation. They found the balance point temperature to be 45 °C lower for B20, when compared with B0, for the CDPF used in that study. The second parameter of interest, regeneration rate, is a measure of how quickly the DPF can be fully regenerated. Williams et al. [61] found improvements in the rate of DPF regeneration rate with the use of biodiesel.

The oxidative reactivity of diesel particulate is an important factor affecting diesel particulate filter regeneration behavior. While few studies have examined fuel property effects on soot reactivity, several studies have analyzed soot chemistry and morphology as they relate to the behavior of biodiesel-derived soot oxidation [61-63]. One study investigated the soot particles' structure at different percentages of a complete combustion and cites three PM properties that are important to reactivity: the number of edge sites (amorphous structure), the number of surface oxygen groups and the amount of volatile matter within the soot [62]. Based on this analysis, they proposed an oxidation progression model that explains the difference in oxidation rate of biodiesel blend-derived soot compared with conventional diesel soot. It concluded that surface oxygen sites, which are more prevalent in biodiesel soot, are the primary cause of more rapid soot oxidation. In the same manner, Müller et al. [65] investigated the oxidative reactivity of particulate matter from different sources and found that the internal nanostructure controlled the particle oxidative reactivity. It should be mentioned that engine operating conditions affect the nanostructure of the particles and hence the particle oxidative reactivity. Zhu et al. [66] found that the particulate appeared to have amorphous structure at low engine loads and graphitic structures at high engine loads. Particulate composition is another important factor affecting particle oxidative reactivity. Volatile matter such as hydrocarbons that filled the micro pores on the particulate is a source of further micro pore development and hence creating a variation in particle reactivity [67].

Fuel-borne catalysts, such as cerium [68], iron and platinum based compounds, have been proven to assist in DPF regeneration (by normal Diesel fuel) by increasing the reactivity of particulate matter. The

alkali metals that can result from the production of biodiesel are well known to catalyze carbon oxidation and may act as a fuel-borne catalyst. Although recent fuel quality surveys typically shown undetectable levels of alkali metals in the fuel [61], sodium and potassium can be present because of the catalyst used for transesterification.

Several researchers investigated the oxidation properties of particulates from biodiesel and diesel fuel and calculated, using TGA analysis, the oxidation kinetic parameters. Several researchers [69-75] adopt the use of the following modified form of the Arrhenius expression for diesel and biodiesel soot burning on the filter wall with exhaust gas oxygen:

$$-\frac{dm}{dt} = Ae^{-E/RT}m^n \quad [2.1]$$

where  $m$  is the actual mass of sample under oxidation,  $t$  is the time,  $A$  is the frequency factor,  $E$  is the activation energy,  $R$  is the molar gas constant,  $T$  is the soot layer temperature,  $n$  is the reaction order. For soot oxidation the reaction order is assumed equal to 1.

Lu, Cheung and Huang [76], using the modified Arrhenius expression, found that the activation energy is respectively in the range of 142-175, 76-127 and 133-162 kJ/mole for Ultra Low Sulfur Diesel, B100 and Low Sulfur Diesel particulate samples. It is obvious that diesel soot has higher activation energy than biodiesel soot. In the literature, the activation energy of biodiesel and diesel soot varies from 88 kJ/kmol and 108 kJ/mole [77] to 160 kJ/mole and 129 kJ/mole [78] for B100 and B0 soot respectively. Although the activation energies are not the same, the oxidation rates of biodiesel soot are always higher than those of diesel soot [62, 76-78].

## 2.5 Diesel spray atomization characteristics

The sprays of diesel engines are known to have a high penetration with low spreading rates and atomization is often due to impingement of the fuel jet on the piston crown. Because of the high velocities, short injection durations and the density of liquid, measurements of droplet diameter, flux and particularly relative velocity are not available in sufficient detail to quantify the characteristics of the spray as it develops in time and distance and to identify the spatial extent, over which atomization occurs in the spray [79].

### 2.5.1 Droplets collision and coalescence

Because of the dense nature of the droplet concentration in the region immediately downstream of the injector, droplet collision and coalescence is a frequent event. The collision and coalescence of fuel engine sprays is of great interest since it will affect the droplet size, number density and velocity of the droplet essentially influencing the structure of the spray and altering engine performance and as a consequence fuel emissions. Depending on the drops velocity and configuration of the spray, as well as the physical properties of the fluid, collision can lead to various outcomes, such as bouncing collision, due to the presence of an interesting air film, permanent or temporary coalescence, which occurs when the kinetic energy exceed the value of stable coalescence, followed by disruption of fragmentation [80, 81]. The number of droplets resulting from disruption remains the same whereas fragmentation is the outcome of catastrophic breakup into numerous small droplets. Droplet coalescence is the phenomenon where two droplets can approach each other with a distance smaller than a critical value depending on the droplet properties and its environment.

There are significant studies in which droplet collision and coalescence is directly related to spray combustion applications such as the experimentations carried out by [80, 82] on propanol and hexadecane liquids, however these were mainly observational studies. Jiang et al. [83] carried out the most detailed investigation of collision behavior involving hydrocarbon droplets, with studies involving fuels from heptanes to hexadecane. Orme [81] demonstrated that collision dynamics and outcome for the hydrocarbon droplets can be significantly different and much more complex than collision of water droplets due to the difference in physical properties.

Generally collision needs to be incorporated in the numerical description of dense spray configurations. Indeed the numerical results of Martinelli et al. [84] predicted a much smaller mean droplet diameter of  $7\mu\text{m}$  than the  $42\mu\text{m}$  measured by [85] and he explained that the main reason for this major discrepancy was because droplet coalescence was neglected. This also demonstrates that in the presence of collision and coalescence phenomena, the droplet size is less dependent on the initial conditions.

### 2.5.2 Droplet breakup

The atomization of liquids has many important applications such as internal combustion engines and atomization quality is crucial to ensure good combustion efficiency and low emissions of pollutants. As a result, numerous interesting studies on droplet breakup phenomena from [86-93] have been reported for several decades and literature on this physical process is quite abundant.

The atomization process is generally divided into two stages. First, primary droplet breakup process defines the initial conditions for the spray, affecting mixing rates, secondary breakup and collisions. Early observation [86] showed that liquid fuel leaving the nozzle is broken up into shreds and small ligaments by aerodynamic forces and instabilities developing at the liquid/gas interface. These ligaments are quickly broken into drops by the surface tension of the fuel.

Then the secondary breakup where the large drops produced in primary atomization are further disintegrated into smaller droplets due to the strong shear forces imposed on the droplets, due to high relative velocities between the gas and spray phase. Primary followed by secondary breakup is likely to be a phenomenon occurring in dense sprays. The transformation of an initial liquid jet into a multitude of small liquid droplets will increase the surface area per unit volume of liquid and as a result the evaporation rate and it will lead to a significant shortening of the droplet lifetime, [94]. The relative velocities of the droplet are significantly reduced during secondary breakup (between 30 and 70% deceleration, depending on droplet size) due to large drag coefficients due to droplet deformation [92] significantly reducing droplet penetration.

Breakup regimes transitions depend largely on the ratio of disruptive aerodynamic force to surface tension forces, represented by the Weber number and the ratio between the liquid viscous and the surface tension forces, represented by a dimensionless group known as Ohnesorge number [91]. Weber and Ohnesorge numbers are expressed as follows:

$$We_j = \frac{\rho_g V_j^2 d_j}{\sigma} \quad [2.2]$$

$$Oh = \frac{\mu_l}{\sqrt{\rho_l \sigma d_j}} = \frac{[(\rho_l / \rho_g) We_j]^{1/2}}{Re_j} \quad [2.3]$$

The higher the Weber number, the larger the deforming external pressure forces are, compared to the restoring surface tension forces. In the absence of such disruptive forces, surface tension tends to pull the

liquid into the form of a sphere. The Ohnesorge number accounts for the influence of liquid viscosity on droplet breakup. At low Oh numbers, droplet deformation becomes significant at We of roughly 1, and droplet breakup occurs at We of around 10-12, with a critical Weber number taken to be generally of the order of 12, with bag, multimode, and shear breakup regimes observed progressively at larger Weber number. With increasing Oh, however, higher values of We are needed in order to trigger breakup, because the high viscous forces hinder droplet deformation which are the first stage towards the breakup process.

### 2.5.3 Breakup models

Reitz and Diwakar [95] proposed a method called WAVE method for calculating droplet breakup and found that the droplet size downstream of the injector was influenced by the competition between collision and coalescence. They had some success in predicting the experimental measurements made notably by Hiroyasu and Kadota [85]. O'Rourke and Amsden [96] presented an alternative model for droplet breakup, the so called TAB model. This model is based on an analogy, suggested by Taylor, between an oscillating and distorting droplet and a spring mass system. The TAB model is mostly valid at low drop We number and possesses several advantages over the Reitz and Diwakar breakup model, enumerated by O'Rourke and Amsden, such that there is not a unique critical Weber number for breakup, the effects of liquid viscosity are included, which can significantly affect the oscillations of the small droplets. Also, the model predicts the state of oscillation and distortion of the droplets and gives drop sizes that are more in agreement with experimental data of liquid jet breakup [97]. Finally, the model does not need to input the spray angle since the spray angle is automatically calculated by the TAB method, unlike the Reitz and Diwakar model but on the other hand, the TAB models needs more constants.

O'Rourke and Amsden demonstrated that one major limitation of the TAB model is that only one oscillation mode can be kept tracked of, while many such modes exist in reality. Some improvements were also introduced concerning the atomization process introducing a 'hybrid' model based on the TAB and the WAVE model [98]. Indeed, it has been established that the TAB model underestimates the tip penetration, resulting in fast evaporation and fuel rich regions close to the nozzle while the WAVE model overestimates it [99] and the simultaneous choice of both models has a physical meaning since for large diameter drops, near the nozzle exit, the model of unstable wave propagation on a liquid surface may be more relevant, while in the later stages of the injection process, the computation of break-up with the TAB analogy seems to be more appropriate for smaller drops [99]. The WAVE and TAB models are the most used secondary breakup models in CFD simulations. Ibrahim et al. [100] introduced the droplet deformation and breakup model (DDB) which provided a better agreement with experimental data compared with the TAB model since the breakup criteria has been modified. Indeed, the assumption in the TAB model that the breakup criterion is the amplitude of oscillations of the drops equals the drop radius has been proven to be unrealistic following [89] publication, who suggested that breakup occurs at different sizes for different Weber numbers.

The model suggested by [100] is applicable for breakup regimes whose  $We > 20$ . The DDB models match well the experimental penetration data at low temperature, while the three models under predict the droplet size and, at high temperature, the DDB model shows the highest penetration rate suggesting that it is more appropriate for simulating the spray dynamics for small engine like conditions and the WB model is more suitable for large engines, while the TAB model is estimated to be completely inadequate. The TAB and WB models underestimate the spray cone angle at low temperature, whereas the DDB overestimates it, but at higher temperature it gives accurate predictions, whereas WB and TAB calculate lower values.

## **PART 1**

### **EXPERIMENTS WITH A COMMON RAIL, HPDI ENGINE**

The first part of this thesis comprises engine bench tests with a 2.0 liter, common rail, high pressure injection passenger car Diesel engine fuelled by B70 biodiesel blend. The results are compared to the respective results of baseline tests with standard EN 590 Diesel fuel. Engine performance and CO, THC and NO<sub>x</sub> emissions were measured. Also, indicative particulate sampling was made with a simplified, undiluted exhaust sampler. Aim of this study was to better understand how the Engine Control Unit (ECU) responds to the different fuel quality. A series of characteristic operation points for engine testing is selected to better serve this purpose. Data acquisition of the engine ECU variables was made through the INCA software and the ETAS/MAC-2 interface. Also, additional data acquisition based on external sensors was carried out by means of LabVIEW software.

The results enhance our understanding of the engine ECU behavior with the high percentage biodiesel blends. Also, they are compared to what is known from the related literature for the behavior of common rail Diesel engines with biodiesel blends.

Having improved understanding on how the engine's electronic control unit (ECU) and fuel system responds to different fuel properties, emphasis is shifted to the fuel system dynamics and the engine's transient response. A series of characteristic transient operation points was selected for the tests. Data acquisition of all monitored engine ECU variables was made by means of INCA software/ ETAS Mac2 interface. Additional data acquisition regarding engine performance was based on external sensors. The results indicate significant differences in fuel system dynamics and transient engine operation with the B70 blend at high fuel flow rates. Certain modifications to engine ECU maps and control parameters are proposed and discussed, aimed at improvement of transient performance of modern engines run on high percentage biodiesel blends.

However, a high pressure pump failure that was observed after prolonged engine operation with the B70 blend, hints to the use of more conservative biodiesel blending in fuel that should not exceed 30% for common rail engines.



### 3. Experimental layout and procedure with the common rail engine

#### 3.1 Engine data

The experimental data employed in this chapter were obtained in-house on the 2.0 L, 4 cylinder, turbocharged, common rail, direct injection, Diesel engine installed on one of the test benches of the Laboratory of Thermodynamics and Thermal Engines, Figure 3.1. Also, another set of test data was made available by the engine manufacturer. The engine bench is equipped with a Froude-Consine eddy current dynamometer which is digitally controlled by Texcel 100, and a PWM engine throttle actuator. The engine is equipped with a Bosch common rail fuel injection system which enables up to three injections per cycle and provides a 1350 bar maximum rail pressure. The exhaust gas recirculation (EGR) valve and the injection parameters are controlled via the engine's electronic control unit (ECU), which is shown in Figure 3.2.

**Table 3.1.** Engine technical specifications.

Engine type	HDI turbocharged engine
Cylinders	4, in-line
Bore	85 mm
Stroke	88 mm
Displacement	1997 cm <sup>3</sup>
Rated power /rpm	80 kW/4000 rpm
Rated torque/rpm	250 Nm/2000 rpm
Compression ratio	18:1
ECU version	Bosch EDC 15C2 HDI
Diesel filter	IBIDEN SiC filter



**Figure 3.1.** DW10ATED engine test bench (left) and group of Exhaust gas analyzers (right). DW10 HDi Diesel engine, eddy current dynamometer and exhaust system are presented.

The data acquisition of the engine ECU variables was carried out via ETAS/MAC 2 interface and INCA software. Furthermore, additional data based on external sensors was achieved by means of NI Data Acquisition cards and LabVIEW software.

These include pressures (by piezo-resistive transducers) and temperatures (by K-type thermocouples) at various points along the engine intake and exhaust line, fuel and air flowrate, A/F control purposes by means of an UEGO sensor. Sampling of exhaust gas is led to a pair of THC analyzers, Figure 3.1 , (JUM HFID 3300A), CO, CO<sub>2</sub> (Signal Model 2200 NDIR) and NO<sub>x</sub> (Signal Model 4000 CLD) analyzers. The main specifications of the engine are given in Table 3.1.

### 3.2 Engine management system information and maps

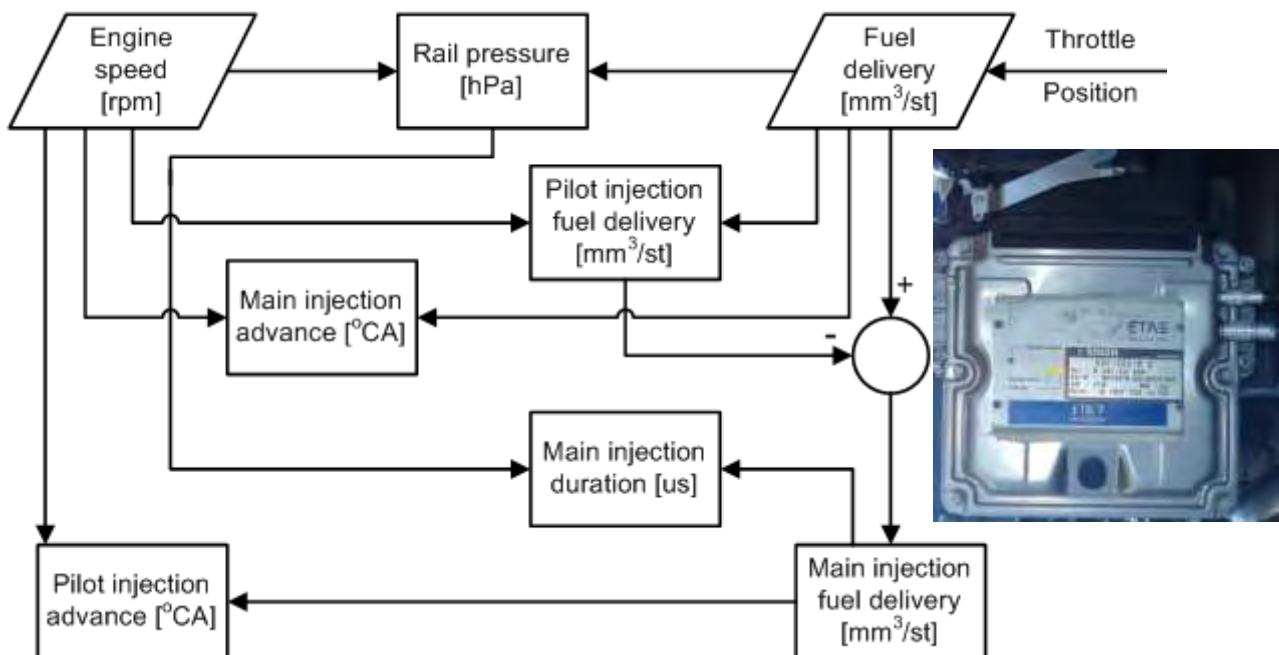


**Figure 3.2.** ECU flowchart for the calculation of the main injection parameters (common rail injection system).

The engine management system relies on maps stored in the ECU for the calculation of several engine control parameters. These parameters are calculated successively, as shown in the flow chart of Figure 3.2.

Common rail pressure [hPa] as function of engine speed and fuel delivery per stroke, Figure 3.3.

- Injector opening duration [ $\mu$ s] as function of rail pressure and fuel delivery per stroke. The injection system enables up to three injections per cycle, pilot, main and post injection, Figure 3.4.
- Pilot injection fuel delivery [ $\text{mm}^3/\text{stroke}$ ] as function of engine speed and total fuel delivery, Figure 3.5.
- Pilot injection advance [ $^\circ\text{CA}$ ] as function of engine speed and fuel delivery per stroke, Figure 3.6.
- Main injection advance [ $^\circ\text{CA}$ ] (with pilot injection) as function of engine speed and fuel delivery per stroke, Figure 3.7.

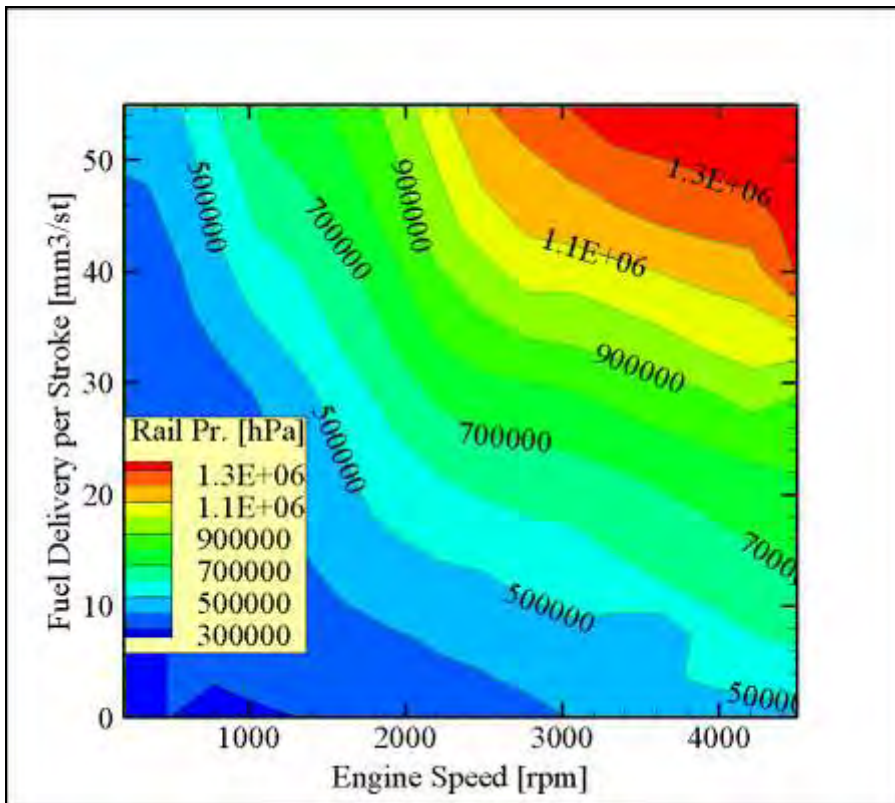


**Figure 3.3.** Common Rail pressure as function of engine speed and fuel delivery per stroke.

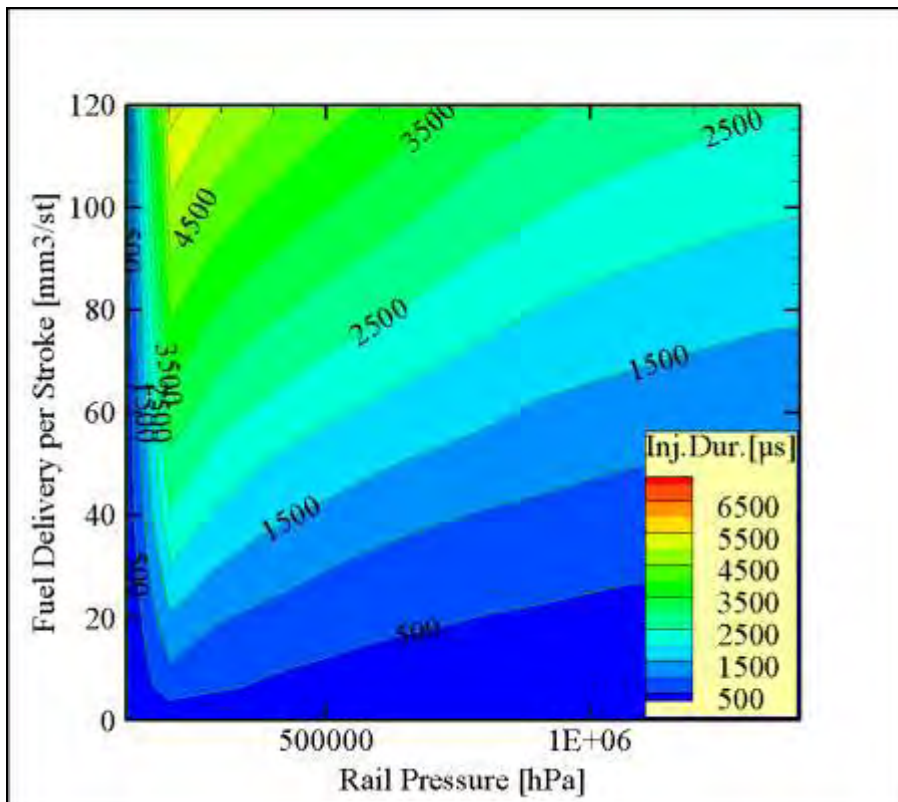


**Figure 3.4.** Injector opening duration [µs] as function of rail pressure and fuel delivery per stroke (pilot, main and post-injection).

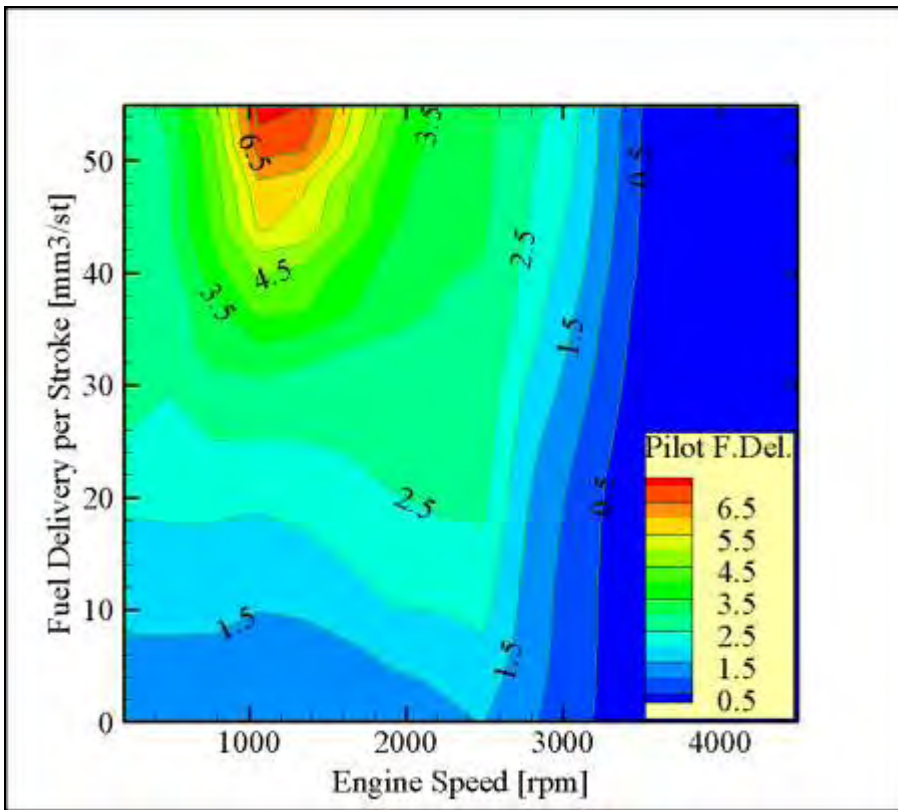


**Figure 3.5.** Pilot injection fuel delivery [mm<sup>3</sup>/stroke] as function of engine speed and total fuel delivery.

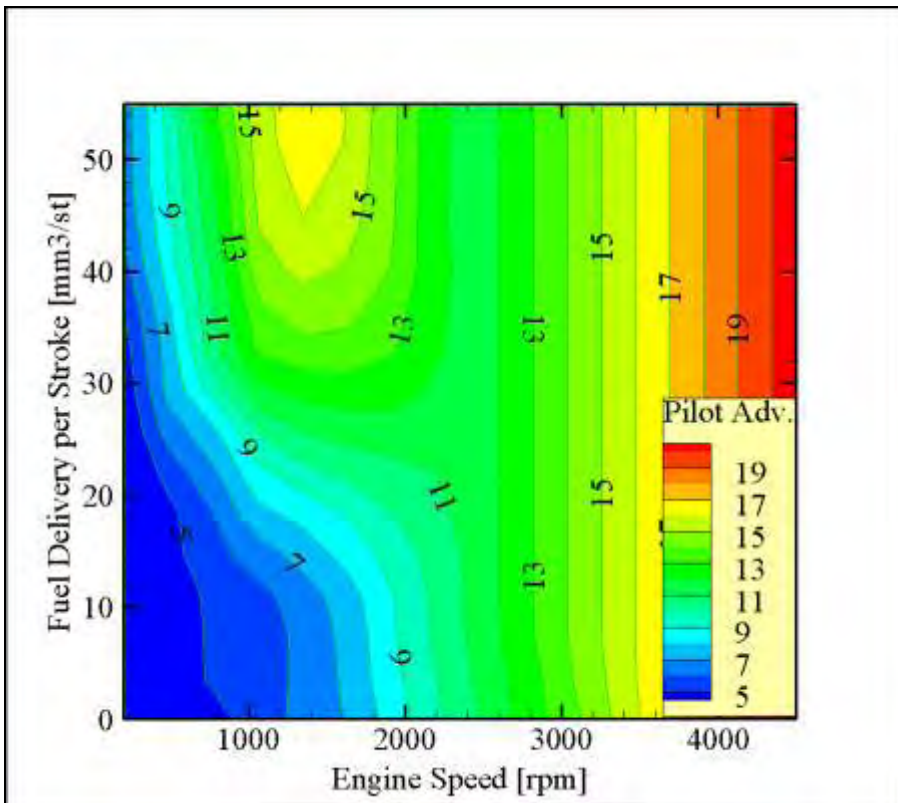


**Figure 3.6.** Pilot injection advance [°CA] as function of engine speed and fuel delivery per stroke.

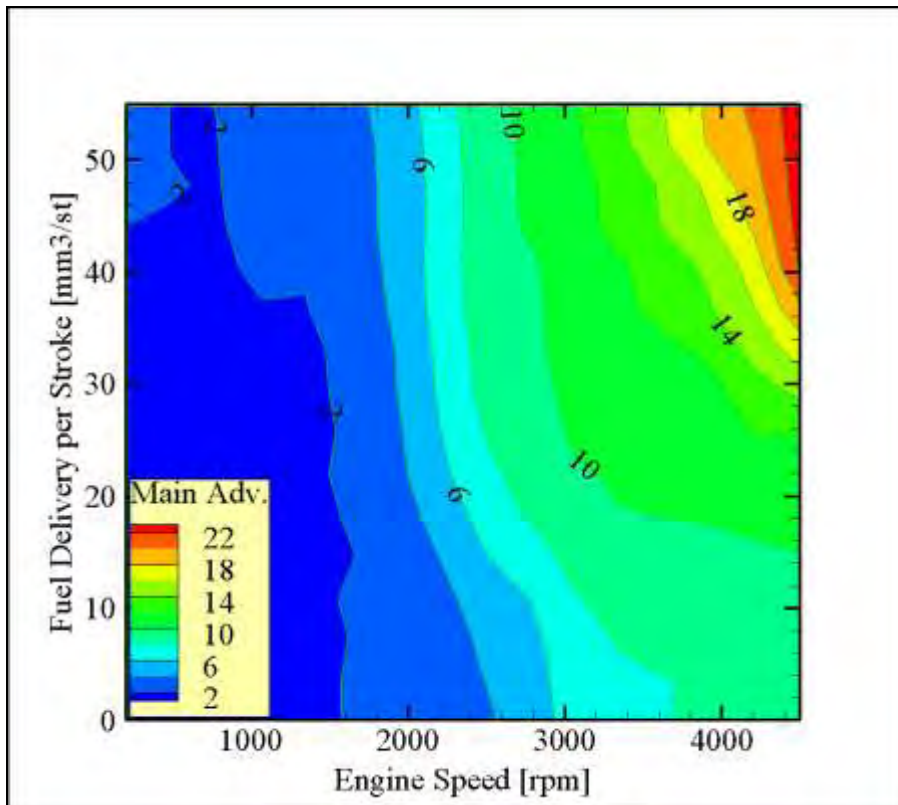


**Figure 3.7.** Main injection advance [°CA] (with pilot injection) as function of engine speed and fuel delivery per stroke.

Data acquisition of the engine ECU variables, which are presented in Figure 3.9, was made through the INCA software, which may record several hundreds of ECU variables. The following variables were regularly recorded (with a time step of 100 ms) during our measurements:

- Engine speed
- Pedal position
- Water temperature
- EGR valve position
- Throttle valve position
- Turbo valve position
- Intake air temperature
- Intake pressure (set point and measured)
- Air mass flow (set point and measured)
- Fuel temperature
- Fuel pressure (set point and measured)
- Fuel mass delivery per cycle, Injection advance (pilot)
- Injection advance (main)
- Injection duration (pilot, main and post injection)

Also, additional data acquisition based on external sensors was carried out by means of LabVIEW software for the following quantities:

- Engine Speed
- Engine Torque
- Cooling water inlet and outlet temperatures
- Fuel mass flow rate
- Air flow rate
- A/F ratio
- Compressor boost pressure
- Turbo in pressure
- Temperatures and pressures at various points in engine inlet and exhaust lines, including oxidation catalyst and Diesel filter.

Figure 3.10 presents LabVIEW's front panel, including the additional measured variables.

The specific engine is equipped with a 1<sup>st</sup> generation common rail system based on a CP1 Bosch high pressure pump (1350 bar). The pump is connected to the camshaft and therefore driven with half the engine speed. It has 3 radial pistons (pump plungers) and its maximum power consumption at nominal engine speed and maximum discharge pressure reaches 3.5 kW. The pump signal contains three sinus waves with different phase. The main signal frequency is three times the frequency of the pump (i.e. the frequency of the half engine speed).

The required rail pressure is regulated through a pressure valve, which in this case is embodied in the high pressure pump. The fuel flow rate supplied by the pump is proportional to the engine speed. In the specific type of 1<sup>st</sup> generation common rail system, (without fuel flow regulation at the suction side) a significant quantity of compressed fuel is forced to expand and return to the tank at low load operation points. This process leads to a significant heating of the fuel [101].

The injectors are responsible for injecting fuel into the combustion chamber. The amount of injected fuel and injection time are controlled by the ECU through signals sent to the electromagnet. This electromagnet controls the opening and closing of the valve in the injector. First there is a pilot injection and then a main injection. Since the valve in the injector is closed very quickly, a so-called water hammer is formed in the injector pipe.

The water hammer is created when a valve is closed quickly in a pipe. There is an initial pressure  $p_0$  and an initial velocity  $v$  in the pipe. Suddenly the valve is closed, which creates a pressure wave that travels toward the main rail. The fluid between the wave and the valve will be at rest but the fluid between the wave and the rail will still have the initial velocity  $v$ . When the wave reaches the main rail the whole pipe will have the pressure  $p_0 + \Delta p$ , but the pressure in the rail will still be  $p_0$ .

This imbalance of pressure makes the fuel flow from the pipe back to the rail with the velocity  $v$  and a new pressure wave is created and it travels toward the valve end of the pipe. When the wave reaches the end, the fluid is still flowing. The pressure at this point will be less than the initial value,  $p_0 - \Delta p$ . This leads to a rarefied wave of pressure in the other direction. When this wave reaches the rail, the pipe will have a pressure less than that in the rail. There is an imbalance in pressure again and the process repeats itself in a periodic manner.

The result is an oscillation which is damped because of viscous effects. First when an injection occurs the valve opens and as a result there is a pressure drop. Then the valve is closed quickly and the water hammer phenomenon appears. Because of the pilot and the main injection the pressure signal gets an appearance

of two damped oscillations after each other. An extensive description of the CR system working principles is reported in [101].

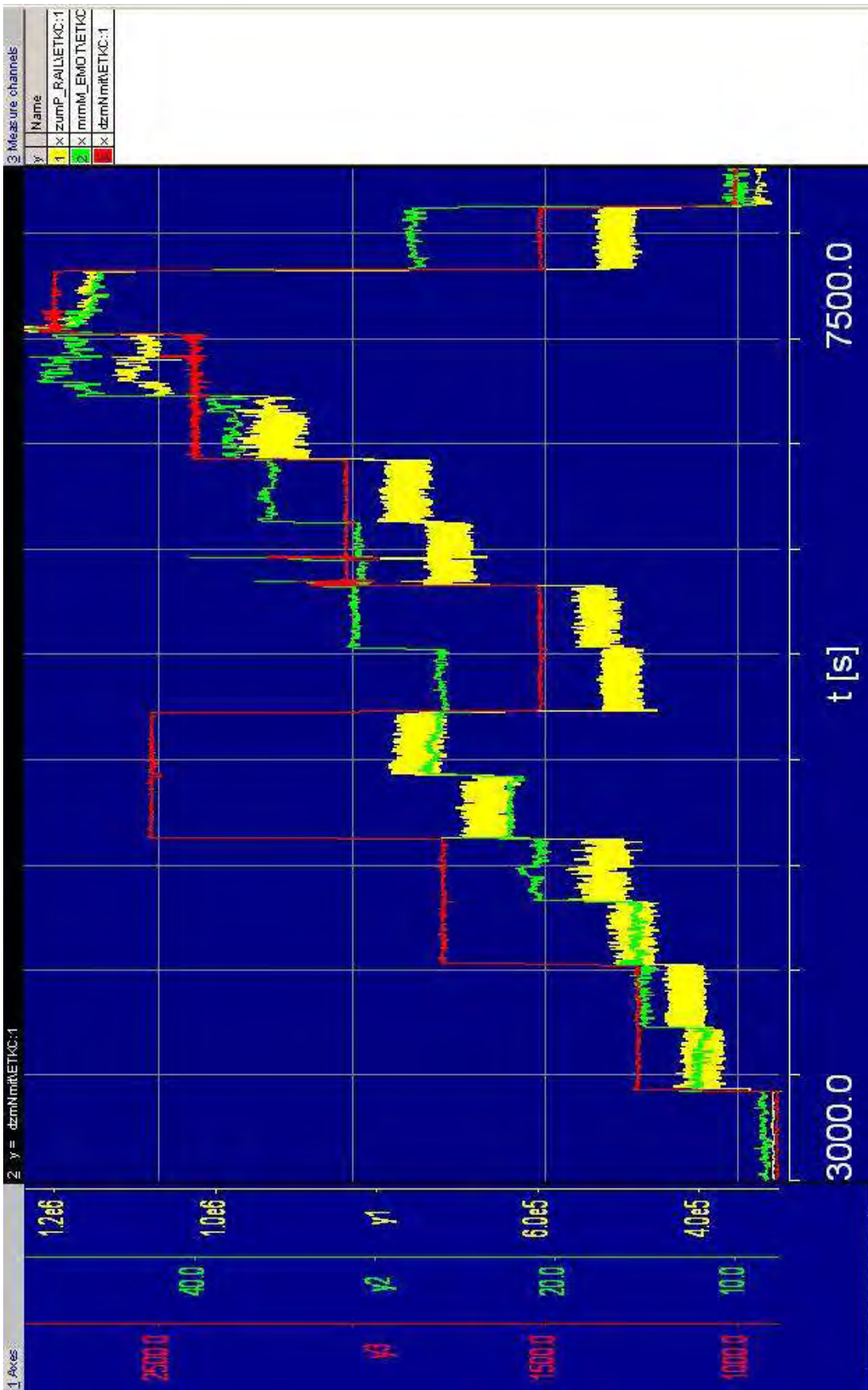


Figure 3.8. INCA Software – Post processing stored measurements.

dzmNmit	Engine speed	0 [1/min]
fgmFGAKT	Vehicle speed	23.34 [km/h]
anmPWG	Pedal Position	3.22 [%]
ldmVERB	Fuel Consumption	0.000 [l/h]
anmUBT	Batery Voltage _Filtered Value	14143.5 [mV]
anmWTF	Water Temperature	80.6 [Grad C]
fpmPC_On	Post injection Actuation	0 [-]
fpmNE_ME_W	Fuel mass flow during post injection	0.00 [mm <sup>3</sup> ]
fpmME_HE	Reduction of Nominal injection due to Post injection	0.00 [mm <sup>3</sup> ]
fpoAB_NEFP	Injection advance	0.0000 [Grad KW]
ehmFARS	EGR Valve Position	5.00 [%]
ehmFLDK	Throttle Valve position	5.60 [%]
ehmFLDS	Turbo Valve Position	15.00 [%]
anmLTF	Intake Air Temperature	34.0 [Grad C]
ldmP_Llin	Intake Pressure (measured)	1031.00 [hPa]
ldmP_Lsoll	Intake Pressure (Set point)	1270.00 [hPa]
armM_List	Air mass flow (measured)	3276.00 [mg/Hub Luft]
armM_Lsoll	Air mass flow (Set Point)	582.00 [mg/Hub Luft]
anmKTF	Fuel Temperature	74.1 [Grad C]
zumP_RAIL	Fuel Pressure (measured)	5500 [hPa]
zumPQsoll	Fuel Pressure (Set Point)	450000 [hPa]
mrmM_EMOT	Fuel mass delivery per Cycle	74.10 [mm <sup>3</sup> ]
zuoAB_VE1k	Injection Advance (Pilot)	0.00 [Grad KW]
zuoAB_Hek	Injection Advance (Nominal)	-0.02 [Grad KW]
zuoAD_HE	injection duration (main injection)	1144.00 [μs]
zuoAD_NE	injection duration (post injection)	0.00 [μs]
zuoAD_VE1	injection duration (pilot injection)	384.00 [μs]

Figure 3.9. INCA SOFTWARE - Stored ECU variables.

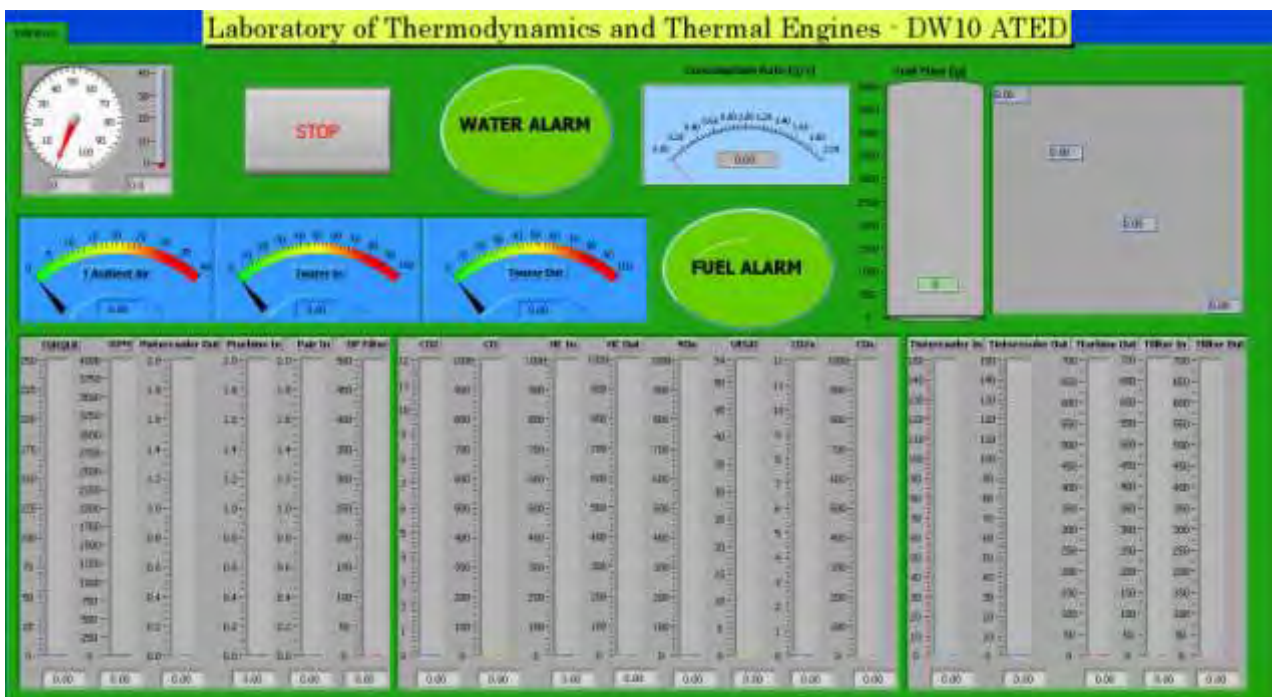


Figure 3.10. LabVIEW software front panel.



### 3.3 Active regeneration procedure

#### 3.3.1 General Overview of Regeneration Strategies

The DPF strategies structure was designed to control the DPF regeneration. This regeneration is triggered by an intelligent system that globally monitors the state of the filter and generates a certain number of actions:

- EGR cut
- Electrical consumers activation (vehicle application only)
- Intake air temperature control (vehicle application only)
- Post-injection activation
- Change of pilot and main injections timings

Globally speaking the ECU strategies use sensors such as intake air temperature, ambient temperature, engine water temperature, DOC inlet and outlet temperatures and ambient absolute pressure.

To effectively apply post-injection, appropriate water and intake air temperatures are required. When these conditions are achieved, 2 levels of post-injection are available:

- level 1 aims at lighting the catalyst off
- level 2 shall generate exhaust gas temperature levels that can regenerate the DPF

Each post-injection level uses 4 specific maps: post-injection timing, post-injection quantity, main injection quantity reduction, boost pressure. Set points use the following parameters:

- engine speed (dzmNmit in rpm)
- global system fuel quantity (mrmM\_EMOT in mm<sup>3</sup>/str)
- current engine fuel quantity (ldmM\_E in mm<sup>3</sup>/str)

#### 3.3.2 Engine maps description

##### ➤ Post-injection Activation

##### Description

To activate post-injection a special wire (leading to a switch) on the engine wiring loom is required in order to simulate a regeneration request. To authorize this action label fpwPC\_on value needs to be changed: it shall be set to 1 to activate it by the switch or set to 0 to activate it by the ECU manager (on a vehicle).

Once the regeneration request is done, post-injection cannot be authorized until water and intake air temperatures have reached appropriate levels according to the fpwMAWTFKL curve.

##### Control means

Measurement channel: fpmPC\_ON

This channel helps checking the activation state of post-injection out:

fpmPC\_ON = 0: means there is no active regeneration request

= 4: a regeneration is requested but post injection is not authorized yet

= 5: post-injection activation conditions are fulfilled and post-injection is therefore authorized

### ➤ Effective Post-injection

#### Description

Post-injection is only used in a defined engine map area depending on engine speed and load. On the DW12 application post-injection is currently activated from 1000 rpm and 9 mm<sup>3</sup>/str of global fuel quantity (emot – image of the pedal position).

Post-injection area:

- ✓ fpwLimREmo = hysteresis upper threshold for fuel quantity: No available in our ECU model
- ✓ fpwLimLEmo = hysteresis lower threshold for fuel quantity (EDC 15 C2: fpwLimLEmot)
- ✓ fpwLimRN = hysteresis upper threshold for engine speed: No available in our ECU model
- ✓ fpwLimLN = hysteresis lower threshold for engine speed (EDC 15 C2: fpwLimN)

#### Control means

Measurement channels:

- ✓ fpmAD\_Naon (binary) : bit 3 = 0 means that post-injection is effectively applied
- ✓ fpmMA\_CAR = (time) counter of effective post-injection.

### ➤ Post-injection levels

#### Description

As previously mentioned there exist 2 different levels of post-injection. A transition strategy is used to switch from one level to the other. The post-injection level applied depends on the catalyst temperature levels (upstream DOC = AT1 probe, downstream DOC = AT2 probe). Transition is made according to the fpwSN2cTKL curve.

#### Control means

Measurement channels:

- ✓ fpmAT1= measured DOC inlet temperature
- ✓ fpmAT2= measured DOC outlet temperature
- ✓ fpmHyste gives information about the post-injection level and authorization for transition
  - = 0 the system is currently in level 1 (DOC temperature too low)
  - = 1 temperature levels could allow to switch to level 2 but the system is either in level 1 or the operating conditions are outside the post-injection area
  - = 9 the system is in level 2 and post-injection is effective.

### ➤ Post-injection maps

#### Description

When post-injection is activated, EGR is cut (the chosen position values are fpwIEGRAG for the EGR valve and fpwIEGRDK for the throttle). Then injection timings are changed for pilot (fpwABVE\_KF) and/or main (fpwABHE\_KF).

Each post-injection level uses the same batch of maps:

- ✓ fpwNMEBPC1(2\*) = post-injection timing
- ✓ fpwNMEDPC1(2\*) = post-injection quantity
- ✓ fpwNMEDMI1(2\*) = main injection quantity reduction
- ✓ fpwNMETP1(2\*) = boost pressure

\*: the number (1 or 2) corresponds to the post-injection level

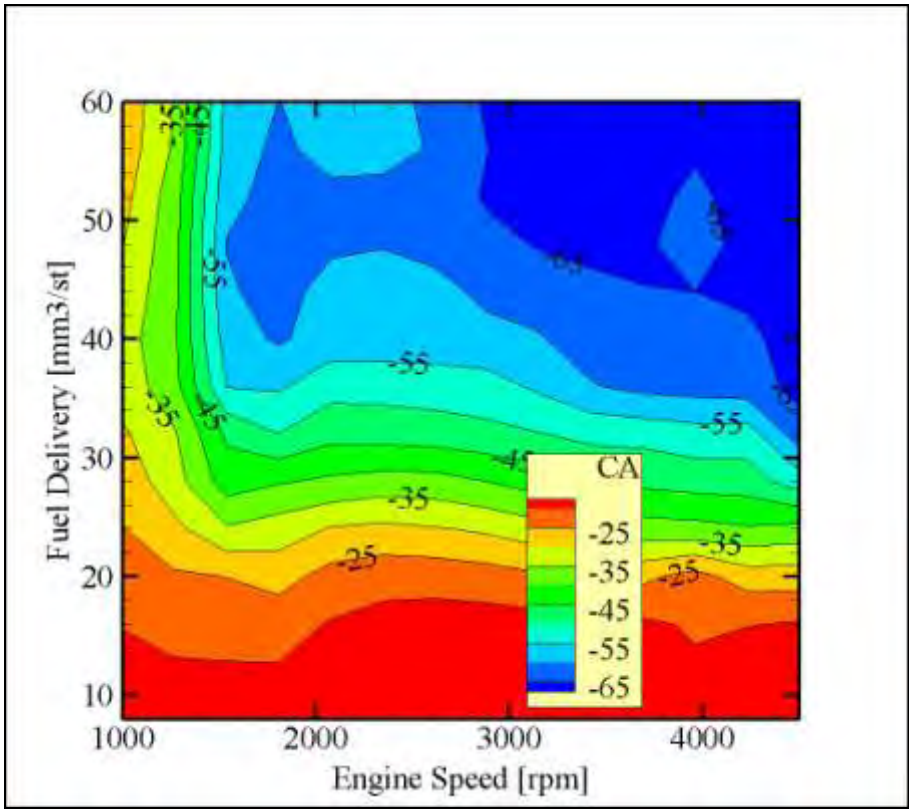


Figure 3.11. Post injection timing during level 1.

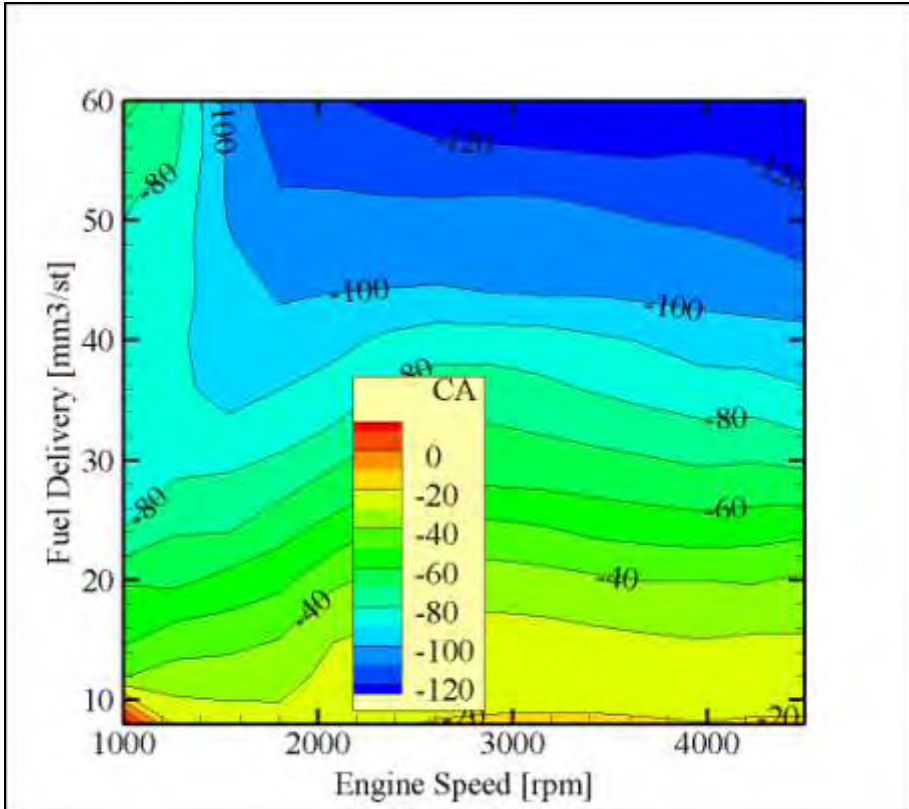


Figure 3.12. Post injection timing during level 2.

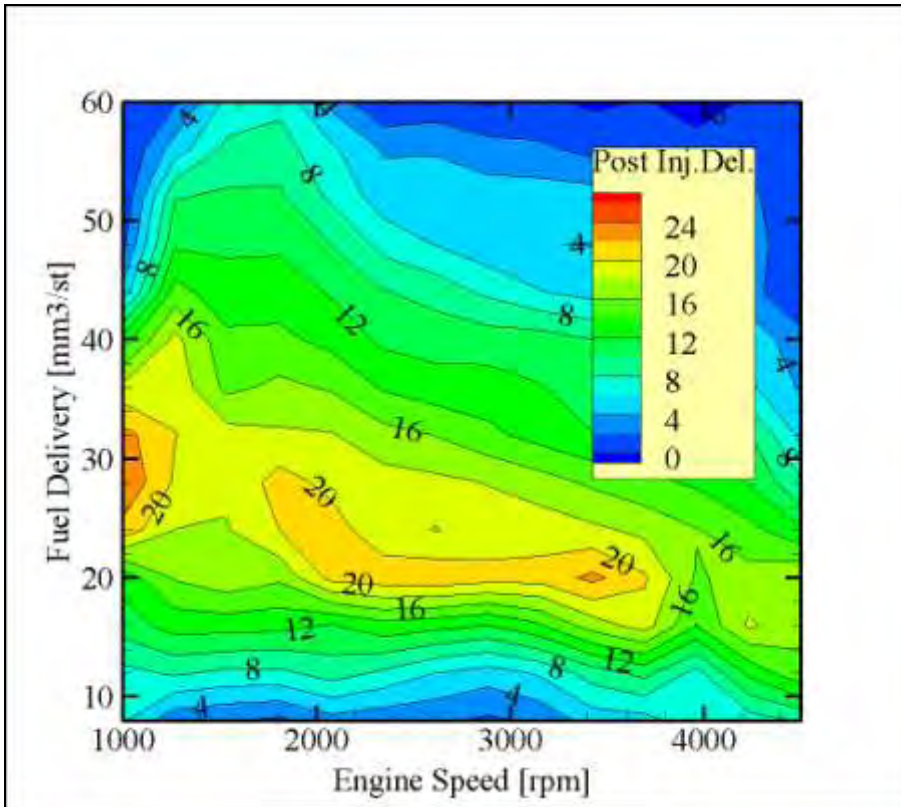


Figure 3.13. Post injection quantity during level 1.

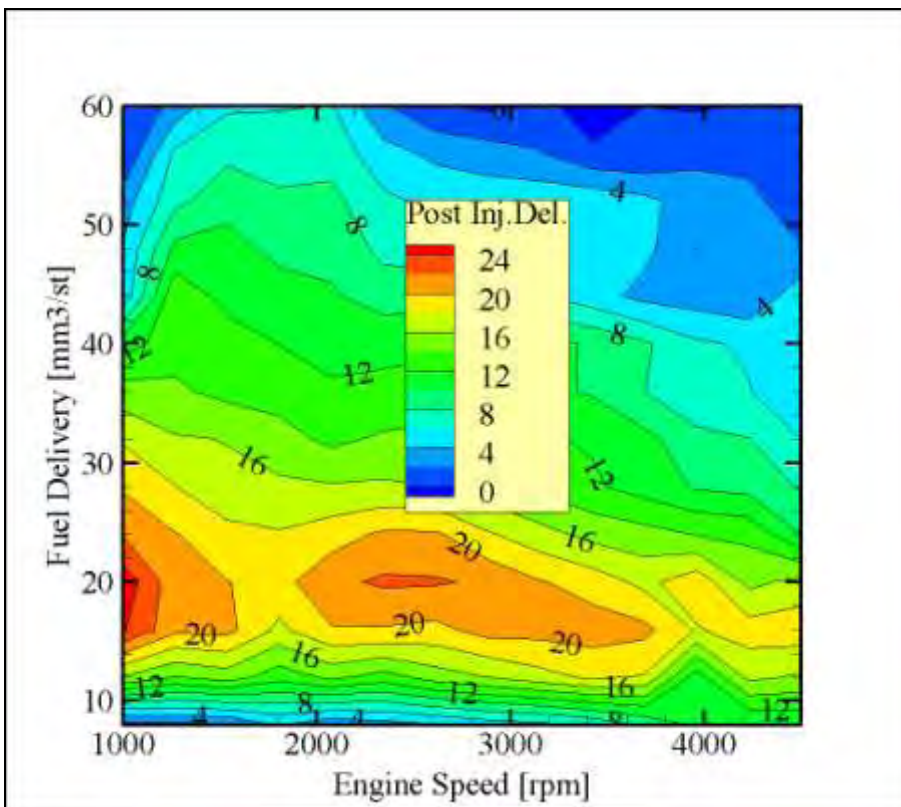
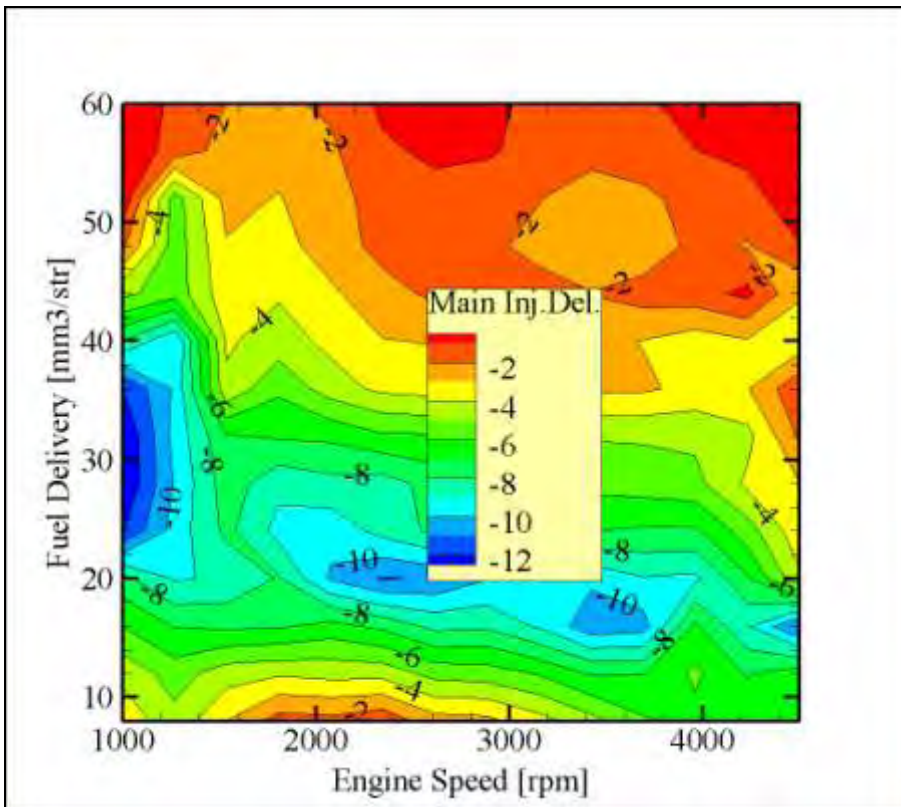
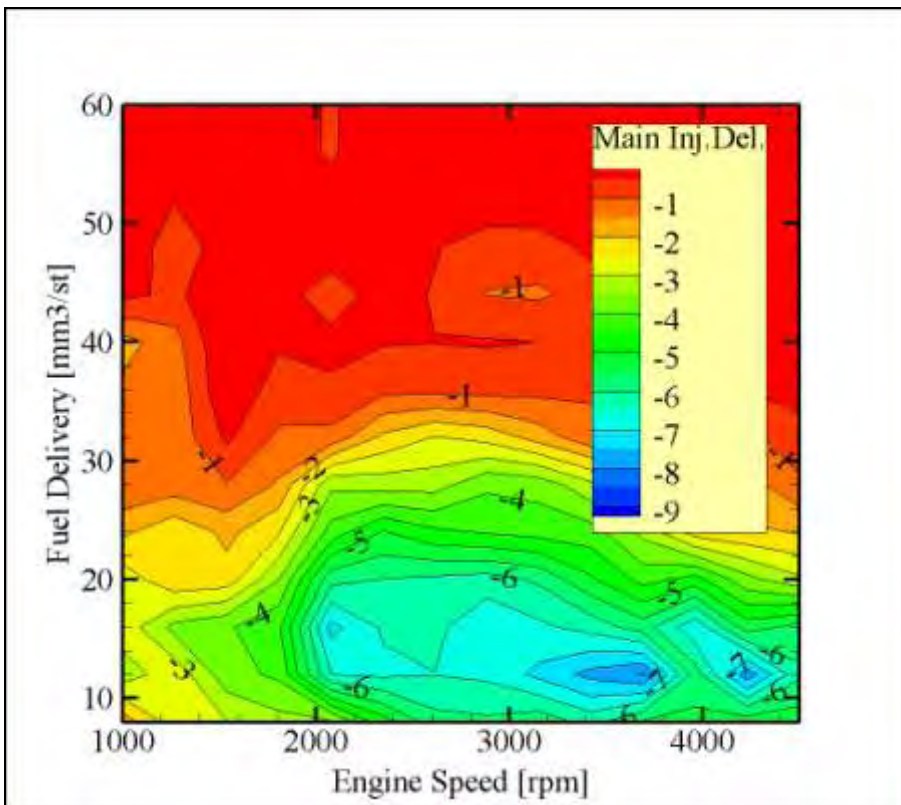


Figure 3.14. Post injection quantity during level 2.



**Figure 3.15.** Main injection quantity reduction during level 1.



**Figure 3.16.** Main injection quantity reduction during level 2.

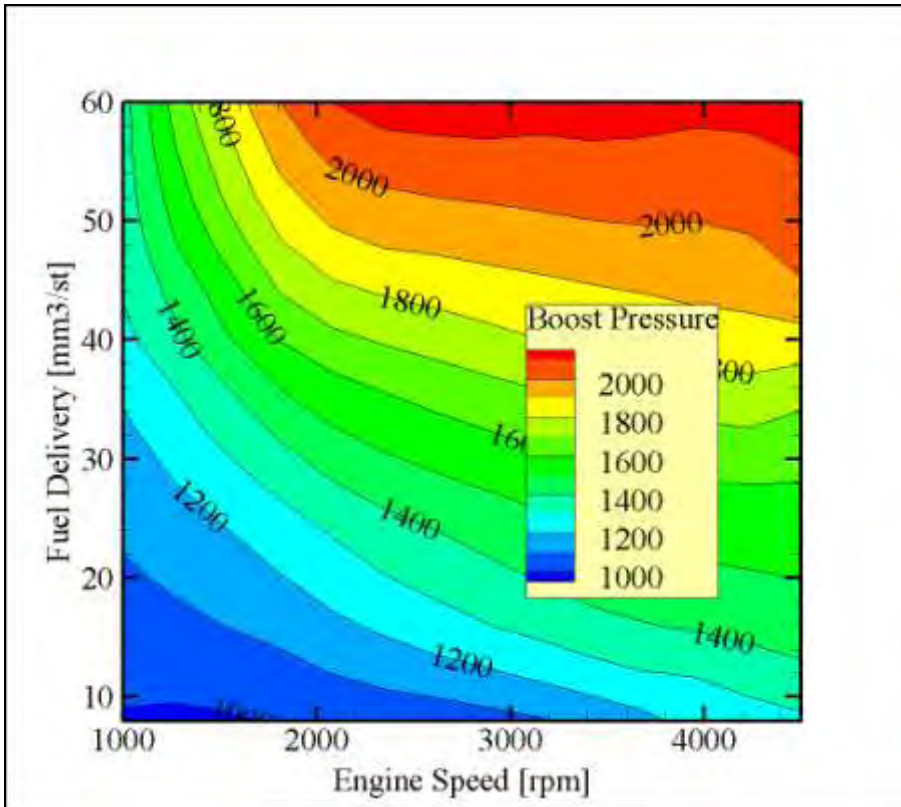


Figure 3.17. Boost pressure during level 1.

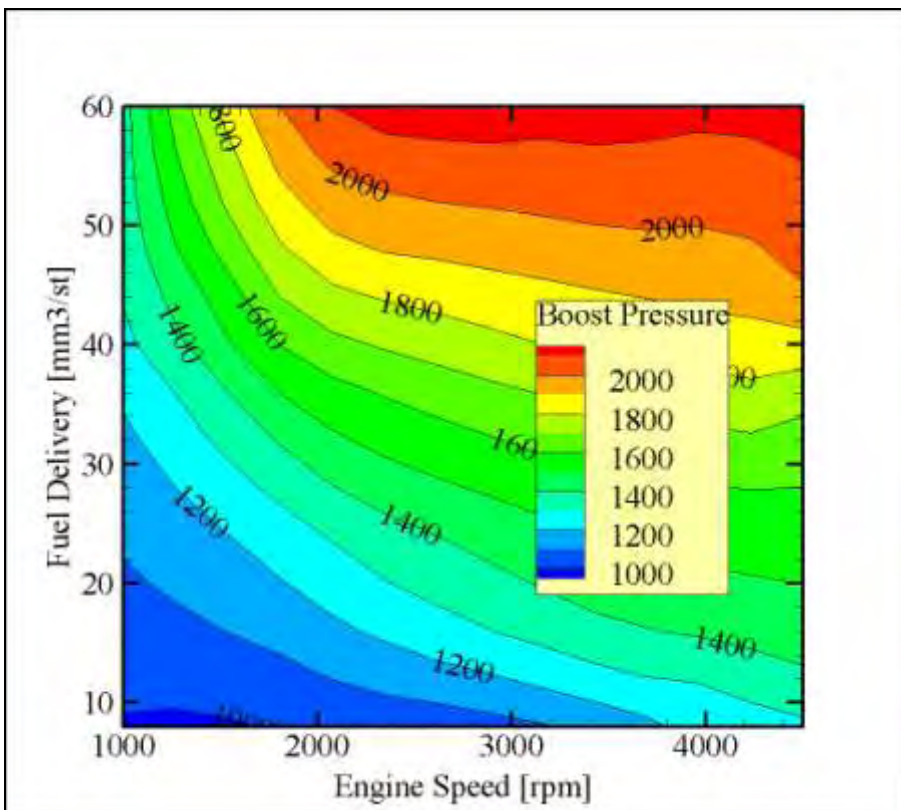


Figure 3.18. Boost pressure during level 2.

## Control Means

Measurement channels:

- ehmfARS : EGR valve PWM command value
- ehmFLDK : EGR throttle PWM command value
- fpmABVEk1 : pilot injection timing correction
- zumAB\_VE : pilot injection timing
- fpmABHEk1 : main injection timing correction
- zuoAB\_HEk : main injection timing
- fpoAB\_NEFP : post injection timing
- fpmNE\_ME\_W : post injection quantity
- fpmME\_HE : main injection reduction quantity
- IdmP\_Llin : measured boost pressure

### ➤ Intake Air Heater and Intercooler throttle control

#### Description

This function is normally controlled by a special strategy that is only active on the vehicle. A manual control of these throttles shall therefore be used on an engine dyno.

Intercooler control:

- ✓ fpwRAS\_off = throttle position when the regeneration request is stopped
- ✓ fpwRAS\_on = throttle position when the regeneration request is activated

Intake Air Heater control:

- ✓ fpwRAA\_off = throttle position when the regeneration request is stopped
- ✓ fpwRAA\_on = throttle position when the regeneration request is activated

#### Control means

Measurement channels:

- ✓ ehmFLDK : Intercooler throttle PWM command value
- ✓ ehmFRAA : Intake Air Heater throttle PWM command value

EDC 16 C3 post injection procedure is summarized in the following flowchart:

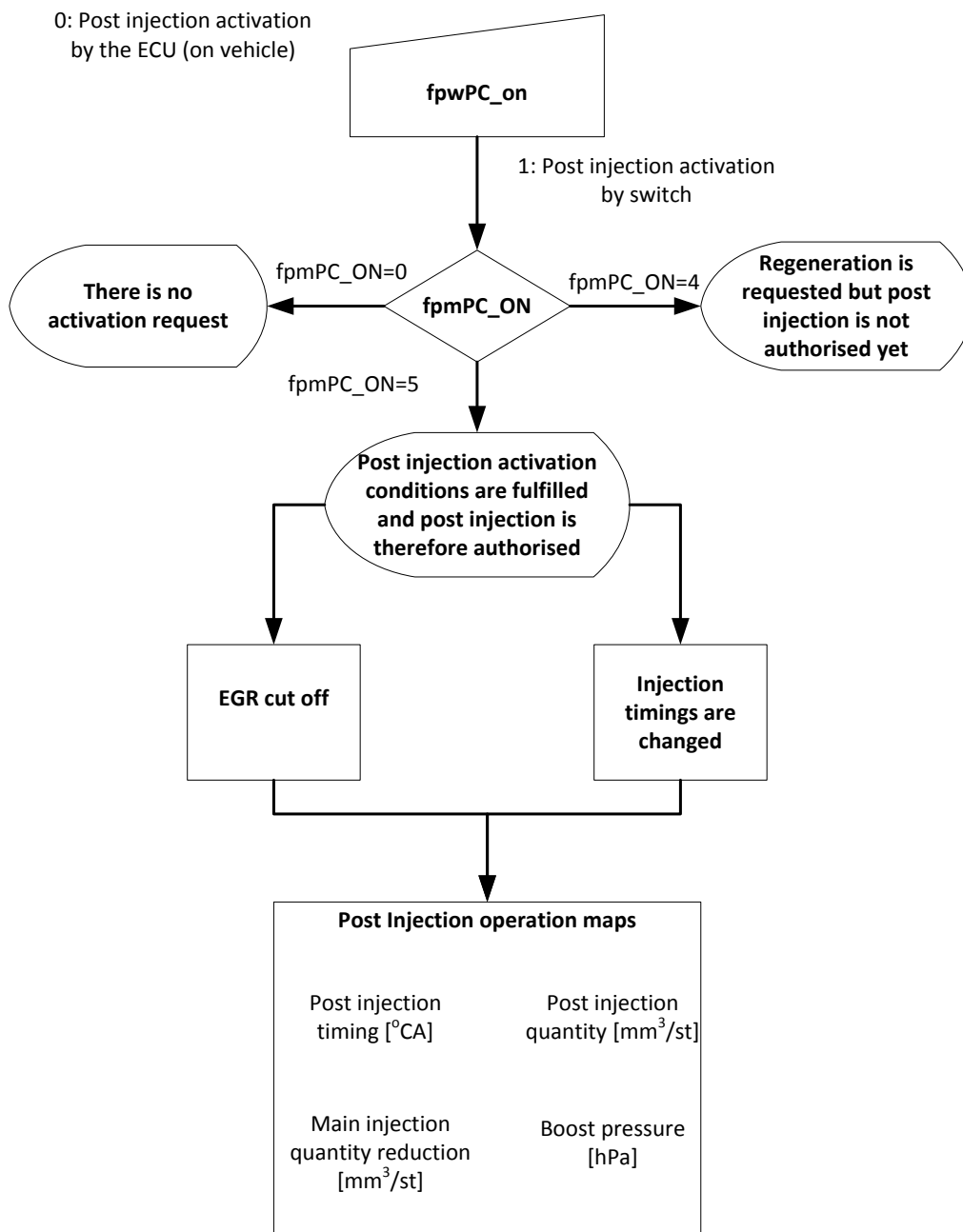


**Figure 3.19.** ECU operation during DPF regeneration. Post injection activation flow chart.

### 3.4 Properties of tested fuels

The fuels under investigation are pure Diesel (0% biodiesel), and a blend of 70 vol. % Biodiesel in pure Diesel. Throughout this part of the thesis the tested fuels were denoted as B0 and B70, respectively. B0 conforms to European standard EN 590. The biodiesel employed in the measurements is a fatty acid methyl ester produced by 40% rapeseed oil, 30% soybean oil and 30% recycled cooking oils. It was supplied by ELIN biofuels SA (Volos factory) and conforms to EN-14214:2003 specifications [102]. A comparison between the tested fuels is given in Table 3.2, along with the corresponding range of variation of each parameter in the different fuel types used in Europe and North America [103, 104]. Unfortunately, the exact methyl esters profile of the tested biodiesel was not available. However, since the fatty acid profile of biodiesel is identical to that of the parent oil, an approximate profile corresponding to the above parent oil mixing percentages can be estimated based on the indicative methyl esters profiles discussed in [105]. Based on



the additional assumption that our recycled cooking oils are composed of sunflower and palm oil, we estimated an approximate methyl ester profile consisting of 12% C16:0, 5% C18:0, 40% C18:1, 36% C18:2 and 7% C18:3. Based on this profile, the stoichiometric (A/F) of our pure biodiesel is calculated to 12.48.

**Table 3.2.** Comparison of the range of variation of the main fuel properties, between biodiesel and diesel fuel. Properties of the specific fuels employed in this study are also included in separate columns.

Specifications / ranges	Biodiesel (range)	Diesel (range)	Our case Biodiesel (FAME)	Our case Diesel
Density (15 °C) [kg/m <sup>3</sup> ]	860–895	815–845	865	825
Viscosity (40 °C) [cSt]	3.5–5.5	2–3.5	4.7	2.5
Cetane number	45–65	40–55	55	50
Cold filter plugging point [°C]	-5 to 10	-25 to 0	-3	-12
Gross heating value [MJ/kg]			40.3	46.1
Lower heating value [MJ/kg]	36.5–38	42.5–44	37.7	43.3
Water content [mg/kg]	0–500		330	-
Acid number [mg KOH/g]	0–0.60		0.16	-
Sulfur content [ppm]		10–500		50
Iodine number g iodine/100g			117	-

### 3.5 Test equipment and procedure

The experimental work [106] was made on the 2.0 l., 4 cylinder, 4-stroke, turbocharged, intercooled Diesel engine connected to a Froude - Consine eddy current dynamometer with Texcel 100 direct digital controller and a PWM engine throttle actuator. The main specifications of the engine are given in Table 3.1. The engine is equipped with a Bosch common rail fuel injection system which enables up to three injections per cycle and provides a 1350 bar maximum rail pressure. The injection system parameters and exhaust gas recirculation (EGR) are controlled via the engine's electronic control unit (ECU). ETAS/MAC 2 interface and the INCA software interface were used for the data acquisition of the engine ECU variables.

Also, additional data acquisition was carried out by means of external sensors, NI Data acquisition cards and LabVIEW software. These sensors include piezo-resistive transducers for pressures and K-type thermocouples for temperatures at various points along the engine inlet and exhaust line, fuel and air flow rate and an UEGO sensor for A/F control purposes. Sampling of exhaust gas is led to a pair of THC analyzers (JUM HFID 3300A), CO, CO<sub>2</sub> (Signal Model 2200 NDIR) and NO<sub>x</sub> (Signal Model 4000 CLD) analyzers.

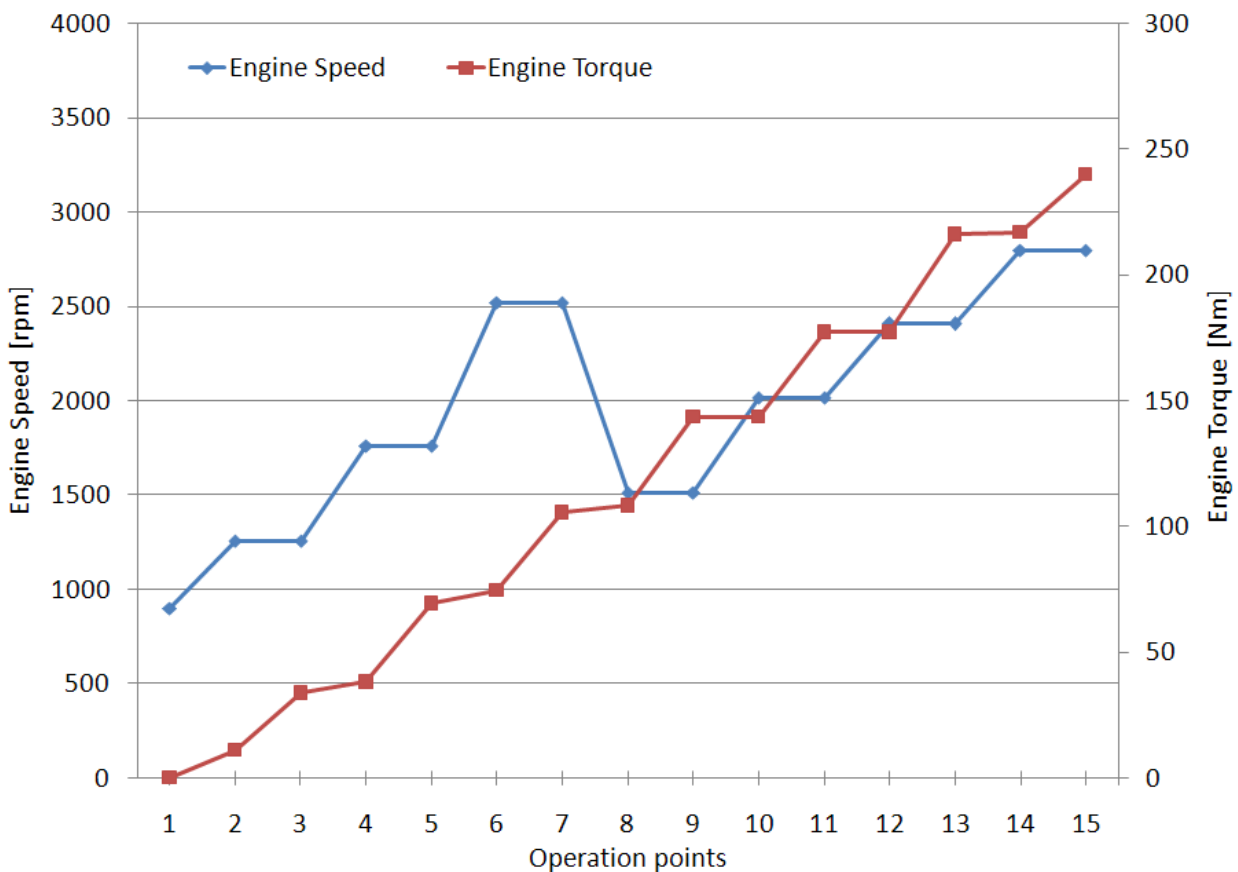


**Figure 3.20.** Sequence of operation points selected for the comparison of fuels.

Data acquisition directly on the engine ECU was possible through the INCA software. The following variables were regularly recorded (with a time step of 100 ms) during our measurements: Engine speed, Pedal position, Water temperature, EGR valve position, Throttle valve position, Turbo valve position, Intake air temperature, Intake pressure (set point and measured), Air mass flow (set point and measured), Fuel temperature, Fuel pressure (set point and measured), Fuel mass delivery per cycle, Injection advance (pilot), Injection advance (main), Injection duration (pilot, main and post injection). Additionally external sensors and LabVIEW software, was used to record the following quantities: Engine Speed, Engine Torque, Cooling water inlet and outlet temperatures, Fuel mass flow rate, Air flow rate, A/F ratio, Compressor boost pressure, Turbo in pressure, temperatures and pressures at various points in engine inlet and exhaust lines, including oxidation catalyst and Diesel filter.

A sequence of steady state operation points was selected as shown in Figure 3.20. The set of operation points was selected to cover the full extent of the engine operation map (from low speed – low load to high speed- high load), and thus study also engine operation that is not represented in the legislated cycles (e.g. NEDC), which usually focus to the lower left quadrant of speed – load regime. The specific sequence of operation points was programmed in the dyno controller (Test Sequence Editor). The transition time between each two successive points was set to 5 seconds. As regards secondary effects of the use of the B70 biodiesel blend, during the tests with B70, we noticed fuel leaks due to the loosening of the fitting of the elastic pipe which leads fuel returns to the fuel tank. Additionally, high fuel temperatures were measured in the fuel return line, and we had to install a counter-flow heat exchanger (water-to-fuel) for return line cooling, by means of 20°C water from the supply. This effect is already reported by other researchers with injection systems based on rotary supply or distributor pumps [4].

## 4. Experimental results with the common rail engine<sup>†</sup>

### 4.1 Effect of B70 on engine performance and fuel consumption

As already reported in the experimental section, the dyno controller was programmed to attain the same operation points for both alternative fuels used. However, the real engine performance was slightly affected as shown in Figure 4.1. Small differences in engine torque are observed, that fall within the statistical variability of engine performance. The results are presented below in the form of line graphs, where the horizontal axis contains always the numbers of the 15 operation points of the sequence of Figure 3.20. Thus, the lines connecting the 15 values of each variable in the graphs are not representing any intermediate operation points. They are just connecting the points to allow the simultaneous presentation of the variation of more, related variables in one graph, which could not easily be done with a bar chart.

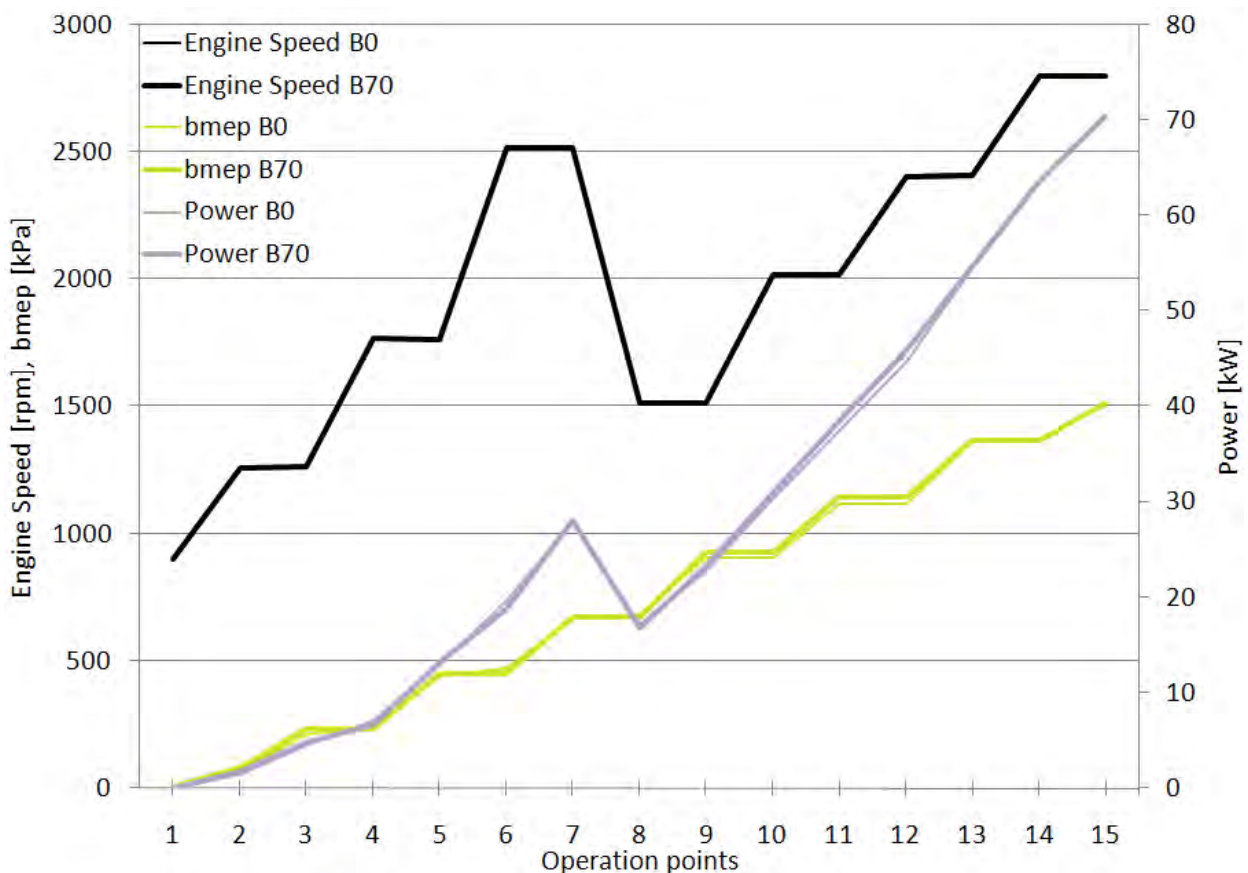


**Figure 4.1.** Comparison of engine speed, bmep, power with Diesel fuel and B70 blend at the 15 operation points of the cycle.

The most marked difference in the performance of the engine fuelled by B70 is the increase in fuel delivery per stroke, for the respective operation points, as presented in Figure 4.2. There exists only one

<sup>†</sup> Part of this chapter was published in: Proceedings of the Institution of Mechanical Engineers, Vol. 223 Part D: J. Automobile Engineering, 685-701, 2009 (DOI: 10.1243/09544070JAUTO1094).

operation point where we observe a decrease of fuel consumption with B70. This could be possibly due to a significant difference in engine efficiency and turbocharger speed at this low load operation point with EGR.

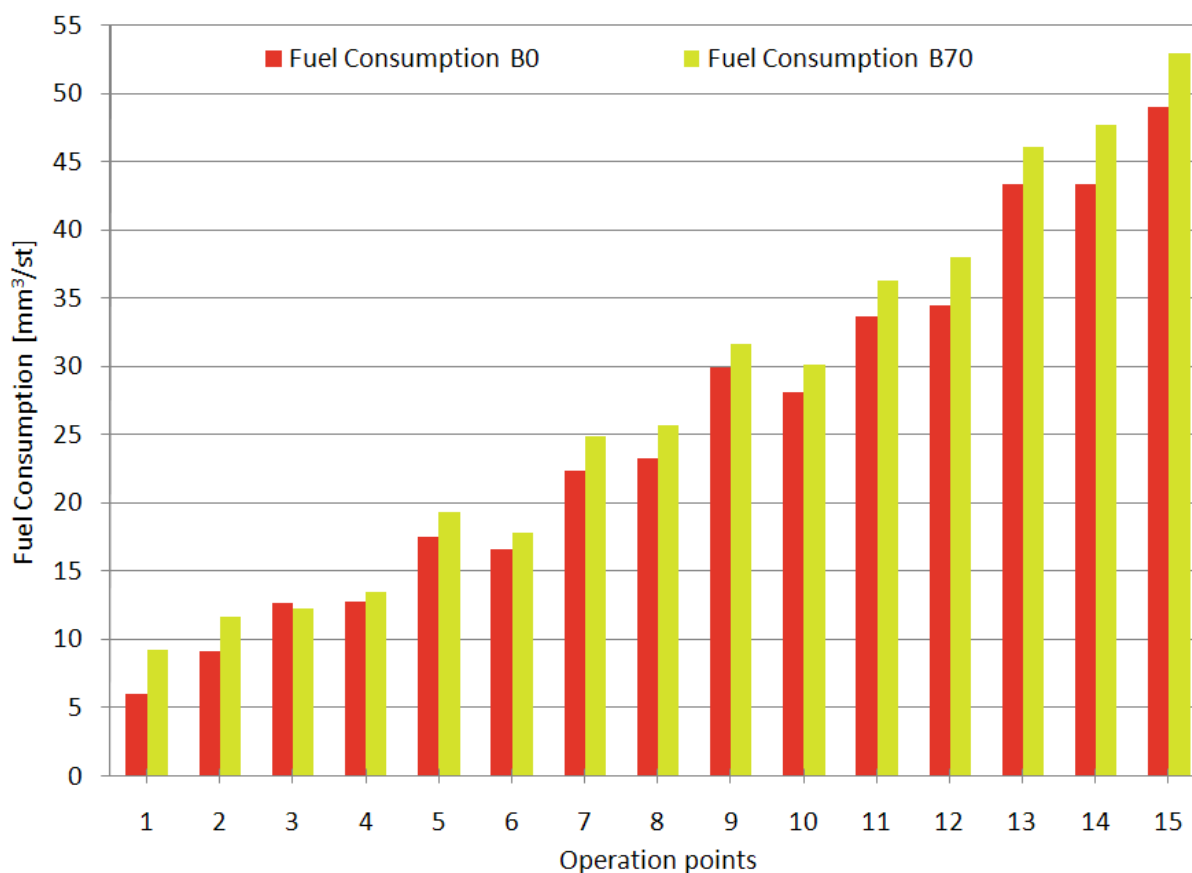


**Figure 4.2.** Fuel consumption ( $b_{sp}$ ) increase with B70 –vs- Diesel fuel at the 15 operation points of the cycle.

The increase in fuel delivery per stroke is expected, as already mentioned. Additional fuel mass is required in order to produce the same power per cycle burning a blend with lower heating value (see Table 4.1). Gross heating value of the two fuels was measured in a Parr 1261 Oxygen Bomb. The results are presented in Table 4.1.

**Table 4.1.** Results of Gross heating value measurements with the bomb calorimeter.

Diesel EN590	Gross heating value [MJ/kg]	Mean Gross heating value [MJ/kg]	Mass of H <sub>2</sub> O in exhaust gas per kg of fuel	Lower heating value [MJ/kg] (computed)
1	46.0434	46.2276	1.17	43.30
2	46.2124			
3	46.4261			
Biodiesel EN 14214	Gross heating value [MJ/kg]	Mean Gross heating value [MJ/kg]	Mass of H <sub>2</sub> O in exhaust gas per kg of fuel	Lower heating value [MJ/kg] (computed)
1	40.1051	40.2913	1.04	37.69
2	40.4928			
3	40.2761			

According to the results of the above Table, the lower heating value of the B70 blend is 37.7 MJ/kg, whereas the respective value for the Diesel fuel is 43.3 MJ/kg.

In order to calculate the fuel energy input per stroke, we additionally need to take into account fuel density, which is also a function of fuel temperature.

$$\rho_f = \frac{\rho_0}{1 + \beta \Delta t} \quad [4.1]$$

The coefficient of thermal expansion of biodiesel is assumed  $\beta = 8.3 \text{ E-4 [1/K]}$  [107]. The coefficient of thermal expansion of Diesel fuel is assumed  $\beta = 11 \text{ E-4 [1/K]}$  [108], and  $\rho_0$  is the reference density at 15°C (Table 3.2).

Based on the above, the fuel energy input per stroke is given by the equation:  $E_{str} = \rho_f H_u b_{sp}$  [4.2]

If we apply this equation, e.g. at operation point 15, the fuel energy input per stroke for the Diesel fuel is 1692.6 J/stroke, whereas the respective value for the B70 blend is 1689.6 J/stroke. Thus, the required fuel energy input per stroke to produce the same engine power, is almost equal for the two alternative fuels. This implies also that engine efficiency is not modified from the shift to the biodiesel blend. The results of detailed calculations of engine efficiency for all operation points are included in Figure 4.5 below.

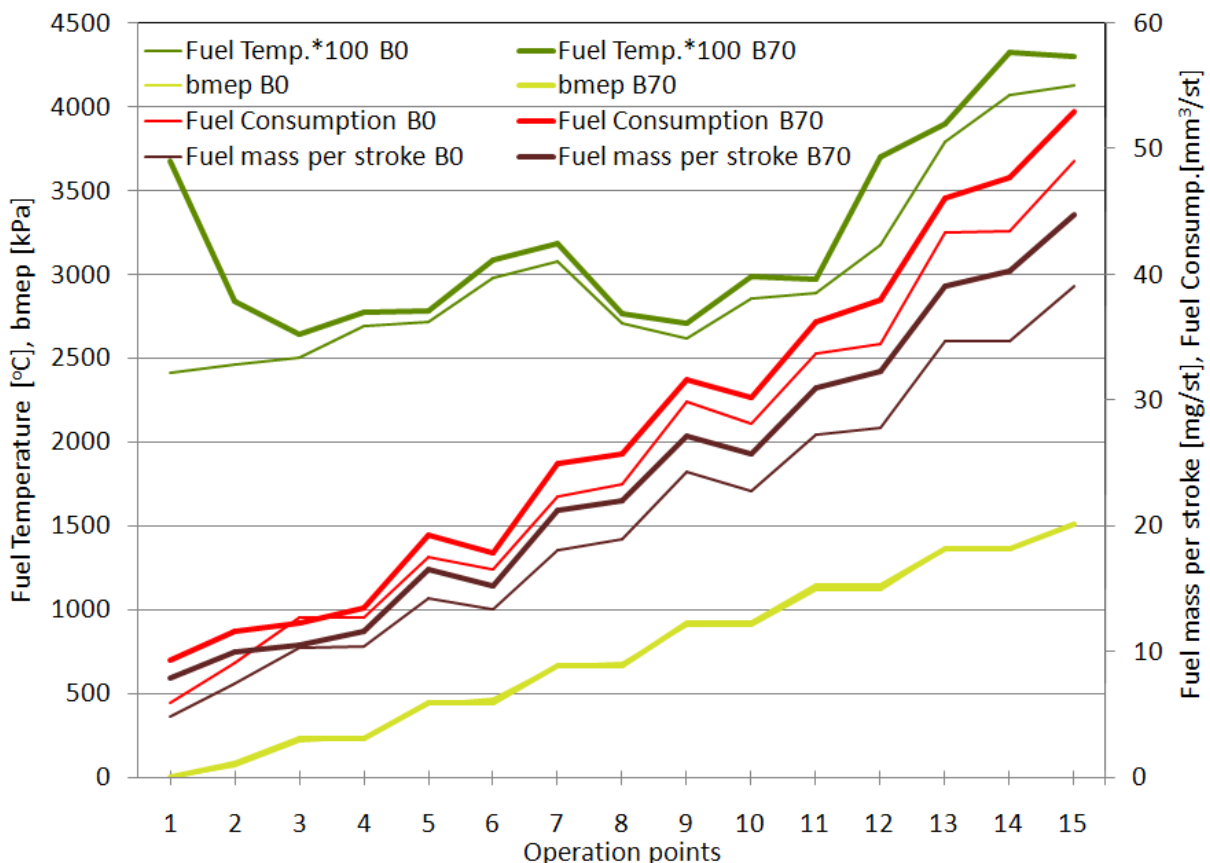


**Figure 4.3.** Comparison of fuel delivery per stroke, fuel temperature, bmep and fuel mass per stroke for B0 and B70 at the 15 points of the cycle.

The above remarks suggest that the engine is forced to burn a higher B70 fuel quantity in order to produce the same torque at each operating point. Next step is to see if this change in fuel quantity also affects A/F ratio and  $\lambda$ . To this end, one must take into account that a Diesel engine is expected to draw

approximately the same air quantity (mass) for a given engine speed and load. Since, as explained above, the engine needs to draw a higher fuel mass per stroke to account for the lower energy content of B70, it is expected that A/F will be lower with the B70 fuel at all operating points. This is confirmed in Figure 4.4. As seen by a comparison, in this figure, of A/F calculated based on the air and fuel mass flowrate measured by the ECU sensors (pink lines) and the respective A/F measured directly by means of the UEGO sensor (dashed lines), there should be made slight modifications in the UEGO calibration curve for EN-590 Diesel fuel exhaust gas, to cope for the B70 blend exhaust gas.

Stoichiometry calculations based on the above mentioned methyl ester profile, produce a value for the stoichiometric A/F for our biodiesel sample of  $(A/F)_{st}=12.48$ . This reduction in stoichiometric A/F with respect to Diesel fuel, is mainly due to the oxygen content of the biodiesel molecules, and not to the difference in C:H ratio, which remains approximately the same with biodiesel [104]. Based on this calculation, the stoichiometric A/F ratio of the B70 mixture we employed in our tests is estimated to be  $(A/F)_{st}=13.08$ . The lambda values shown in Figure 4.4 (lambda is the ratio of A/F to  $(A/F)_{st}$ ), are calculated based on the ECU measurements (air and fuel mass flowrate).

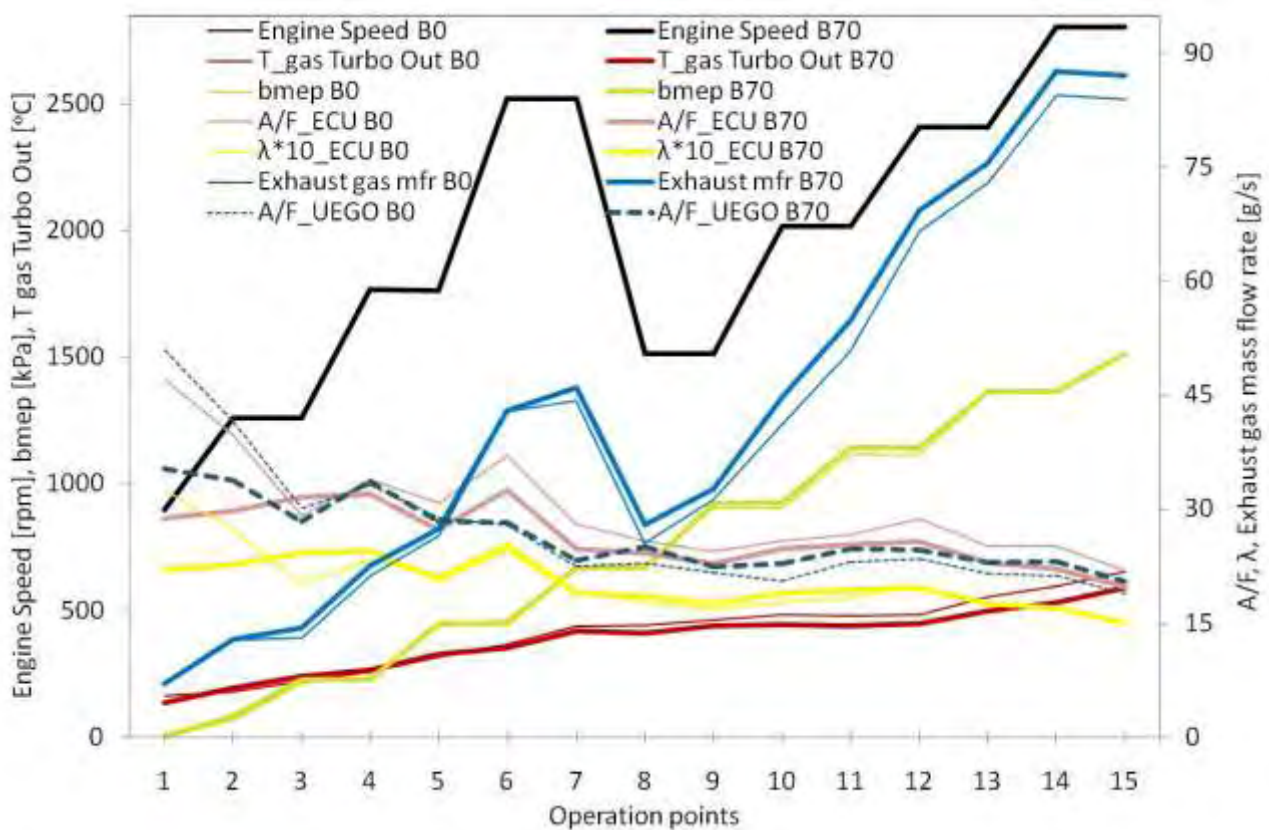


**Figure 4.4.** Differences in A/F, lambda, exhaust gas temperatures and mass flow rates at the 15 points of the cycle.

According to this figure, A/F (calculated based on ECU signals, as mentioned above) is reduced overall with the B70 biodiesel blend. On the other hand, lambda ( $\lambda$ ) is higher with the B70 blend in the medium-to-high loads, whereas it is lower at low loads. As regards exhaust gas temperature levels, they are reduced with the B70 blend in the medium-to-high load engine regime. A similar behavior is reported in [109]. This fact deserves some additional discussion. The differences in A/F should be partly related to the shifted operation points of the turbocharger, which affects exhaust temperature at turbine exit. It is interesting to see if the engine draws the same levels of air mass flow rate in the case of the B70 fuel. The exhaust gas

mass flow rate, calculated based on the ECU measurements, is also presented in Figure 4.4. The increase in fuel mass flow rate with B70 is accompanied by a decreased A/F ratio with this blend. Overall, the exhaust gas mass flow rate is increased in the medium-to-high loads. This implies that the turbocharger's operation point is shifted and this gives an explanation to the observed lower turbine out temperature.

The effect of biodiesel on engine efficiency is another issue of interest here. A detailed calculation of engine efficiency was made according to the following procedure:

$$\eta_{th} = \frac{P}{\dot{m}_f H_u} = \frac{1}{bsfc H_u} \quad [4.3]$$

Fuel mass is calculated based on fuel volume flow rate as measured by the ECU, taking into account the variable fuel density as function of fuel temperature, as measured by the ECU. The results are employed in the calculation of brake specific fuel consumption and thermal efficiency values presented in Figure 4.5.

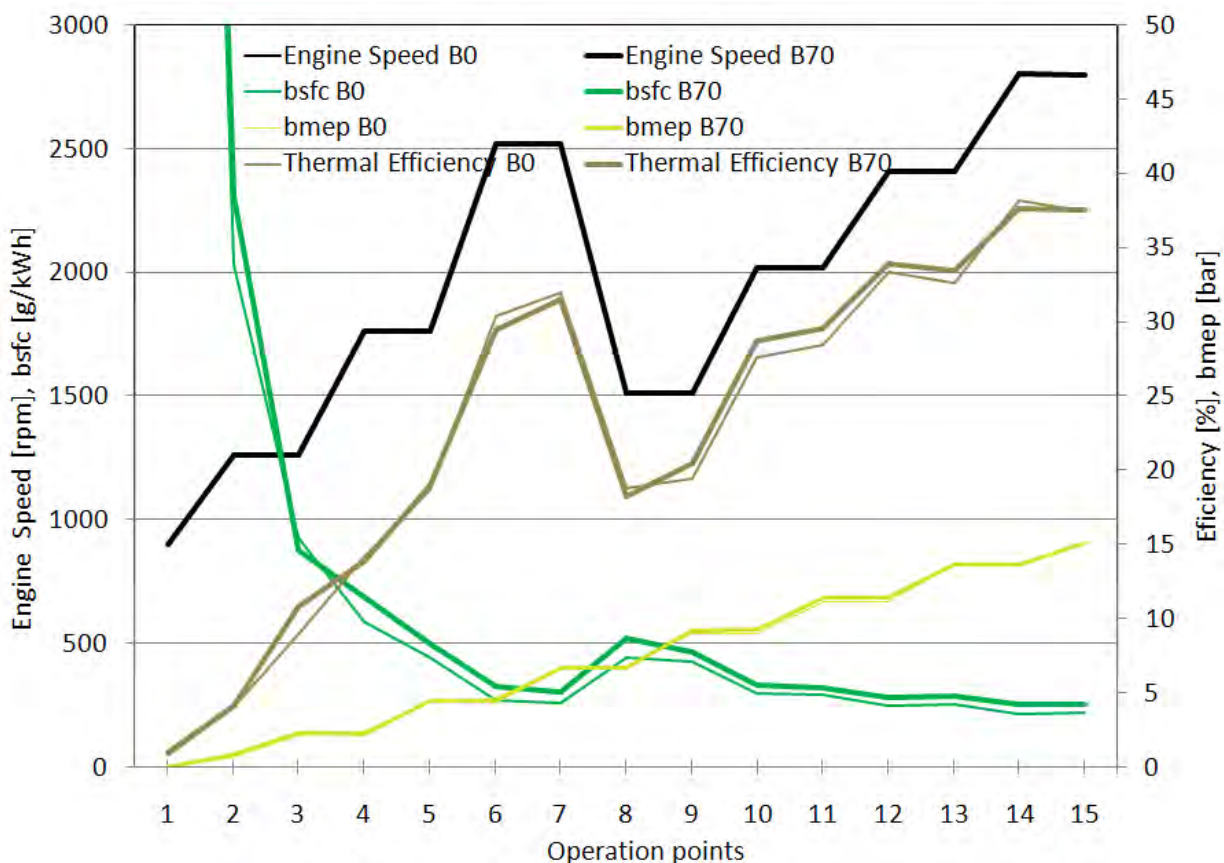


**Figure 4.5.** Differences in bsfc, bmep and engine efficiency at the 15 points of the cycle.

To obtain the same torque and power output for both tested fuels, the brake specific fuel consumption was higher for the B70 blend in inverse proportion to the lower heating value per volume of fuel, this leading to similar thermal efficiencies.

It should be mentioned here that the highest load selected for the comparison of the two fuels was less than the maximum torque. The reason for this selection lies to a certain reduction in the maximum torque that was observed with the B70 blend (240 instead of 250 Nm). This reduction is explained by the fact that the maximum fuel delivery per stroke of about 55 mm<sup>3</sup>/st. in the engine ECU maps, does not suffice for the case of fuelling with B70 (Figure 4.3) due to its lower heating value.

Obviously, the ECU does not have the possibility of detecting the difference in fuel properties. At high load conditions, the request by the accelerator of more torque increases the fuel delivery per stroke to the limits of the ECU's cartography. In order to keep the same maximum torque with biodiesel blends, an extension of the limits of the fuel delivery map would suffice, since an adequate margin of A/F exists. Moreover, if it would become possible to trace the biodiesel percentage in the fuel by some kind of sensor, additional improvements would be possible in the ECU maps, to further improve performance with the biodiesel blends [110].

## 4.2 Effect of B70 fuel on the Injection system parameters

The effect of B70 blend on the main fuel injection system parameters is presented in Figure 4.6.

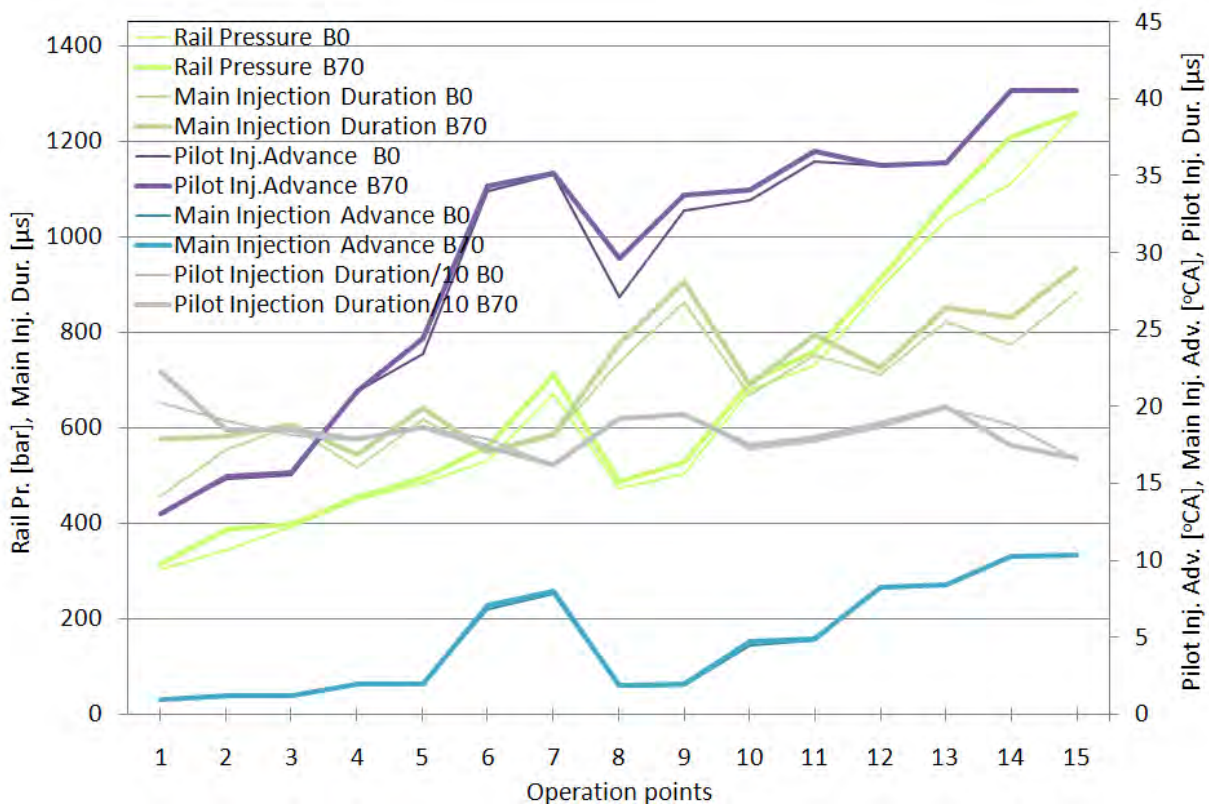


**Figure 4.6.** Differences in fuel injection parameters (common rail pressure, pilot and main injection advance, pilot and main injection duration) at the 15 points of the cycle.

As shown in Figure 4.6, the main injection advance and the pilot injection time were not affected by the use of the biodiesel blend. That is, as expected for a common rail fuel injection system [8, 9], the difference of the speed of sound in biodiesel does not affect the start of the main injection.

On the other hand, the rail pressure, pilot injection advance and main injection time are increased with the B70 blend. This is explained by the algorithm of calculation of these variables by the ECU, along with the ECU cartography: Rail pressure is mapped in the ECU as function of engine speed and fuel delivery per stroke. Since biodiesel has a lower heating value than pure diesel, more fuel needs to be injected into the engine cylinder which causes the higher fuel delivery and thus increased rail pressures for the B70 fuel blend. The increase in pilot injection advance and main injection time was caused by the effect of the increased fuel delivery, as calculated by the ECU based on the maps of Figures 3.3 to 3.7.



### 4.3 Effect of B70 on the pollutant emissions

The effect of the B70 fuel blend on the engine HC and CO emissions is presented in Figure 4.7. The reduction of CO emissions is quite observable in the figure, especially at high loads. It is in line with the reported results of the literature. On the other hand, the effect of B70 fuel on THC emissions is less pronounced, and is mainly seen at low to medium loads. Again, this is in line with what is reported in the literature for common rail Diesel engines [41].

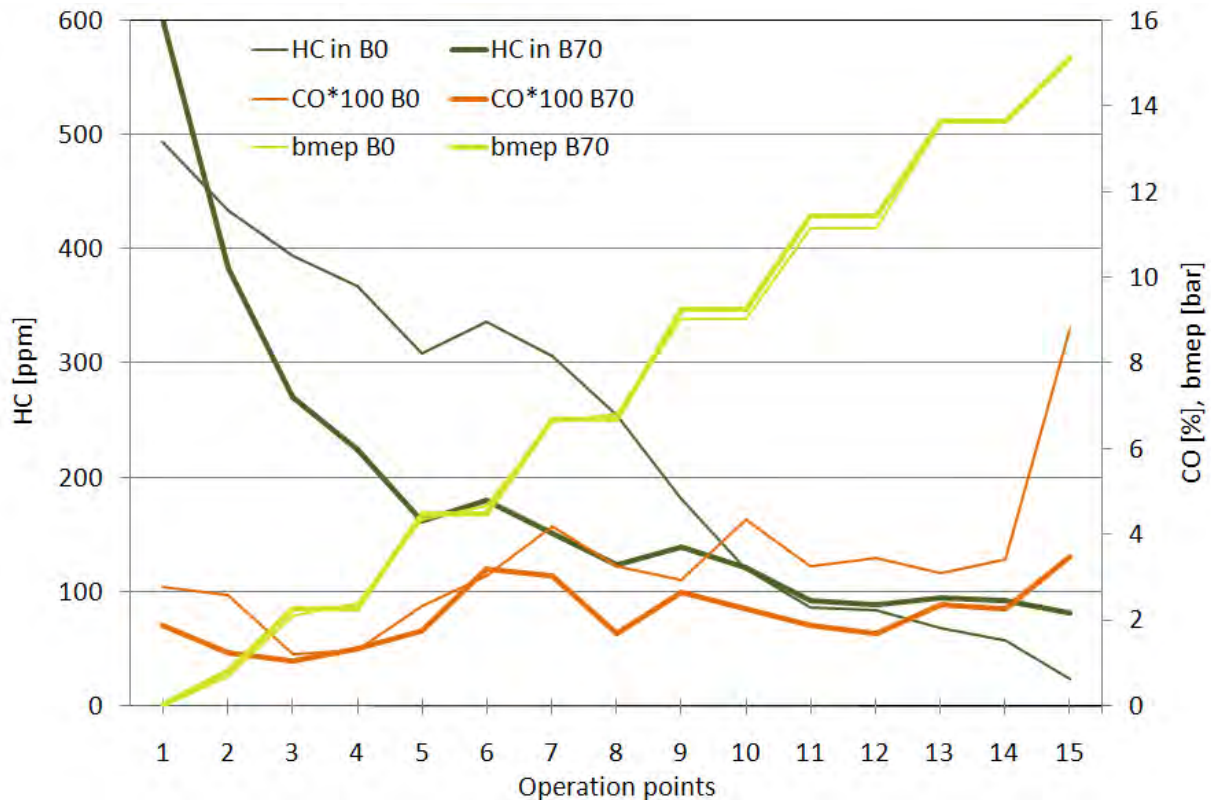


**Figure 4.7.** Differences in HC and CO emissions between B70 and B0 at the 15 points of the cycle.

The effect of the B70 blend on the  $\text{NO}_x$  emissions, is significantly more complicated, but again in line with what is reported in the literature [7, 111, 112]. According to the results presented in Figure 4.8, there is a general trend of somewhat increased  $\text{NO}_x$  emissions in most part of the engine performance map. However, there exist certain operation points at medium –to- high engine loads, where  $\text{NO}_x$  emissions are reduced with the B70 blend. These points would correspond to high speed driving of the Diesel-powered passenger car equipped with the specific engine. In Figure 4.8, an attempt is made to correlate the observed variations in  $\text{NO}_x$  emissions with respective variation in fuel injection parameters and A/F. It can be seen that the operation points with increased  $\text{NO}_x$  emission with the B70 are generally characterized by a significant increase by the ECU of the pilot injection advance which points to an earlier start of combustion, in which case  $\text{NO}_x$  is expected to rise somewhat.

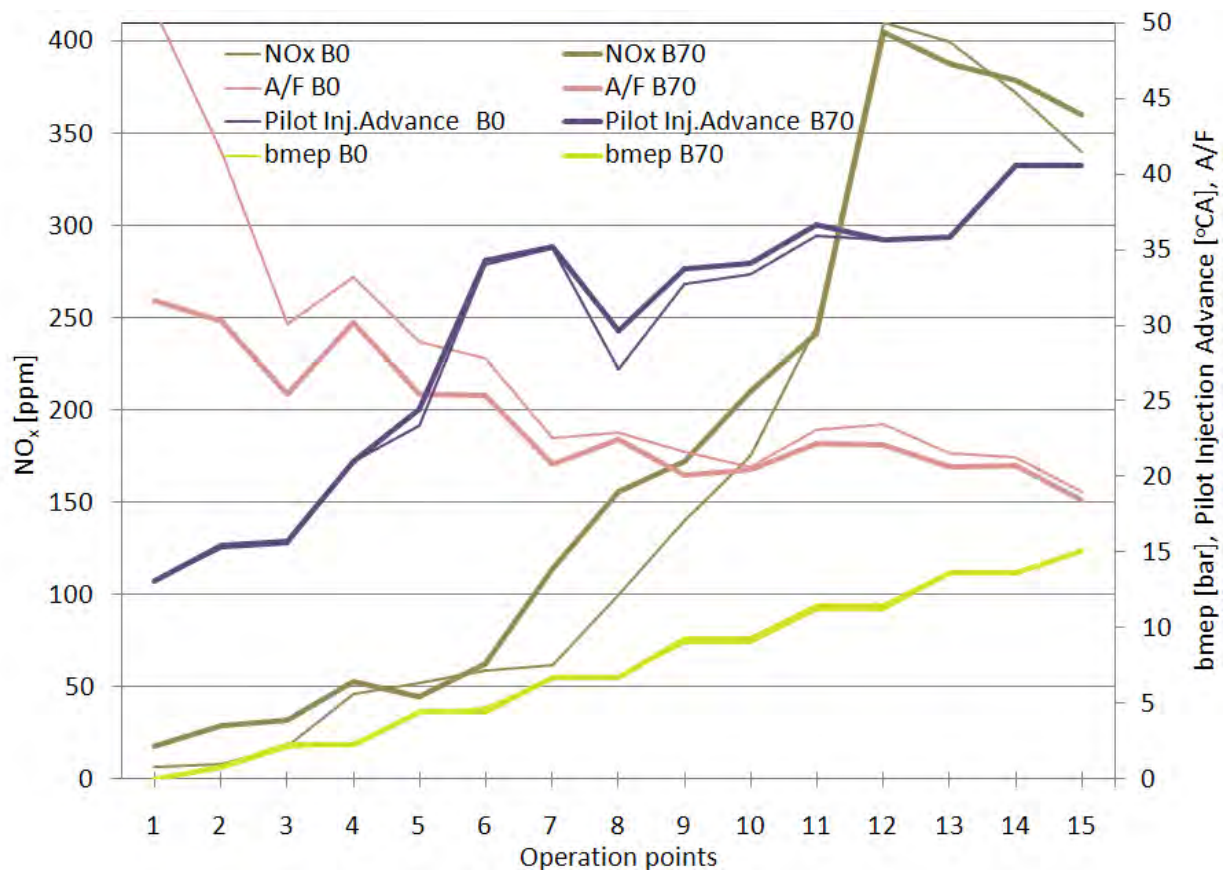


**Figure 4.8.** Differences in NO<sub>x</sub> emissions between B70 and B0 at the 15 points of the cycle.



**Figure 4.9.** Comparison of particulate samples (undiluted exhaust gas upstream filter passing through a Pallflex 47mm filter during the total cycle. Left: Diesel fuel. Right: B70 biodiesel blend.

Finally, although we did not carry out the legislated particulate sampling from diluted exhaust gas, the samples taken from undiluted gas very close to the exhaust line in 47mm filters, one for each cycle, are comparatively presented in Figure 4.9 just for a qualitative comparison. The lower blackening of the filter in the B70 case is apparent, along with the characteristic yellowish color of the B70 particulate, which implies a higher SOF content. These observations, which are in accordance with the literature [11, 12, 113-116], can be mainly explained by the oxygen content of the biodiesel molecule, which enables more complete

combustion and promotes the oxidation of the already formed soot. In addition the lower stoichiometric need of air in case of biodiesel blend combustion reduces the probability of fuel – rich regions in the non – uniform fuel – air blend.

#### 4.4 Conclusions

- The specialized literature is relatively sparse regarding the effect of fuelling modern, common rail diesel engines by high biodiesel content fuel blends. This study contributes to this area, by presenting comparative test results with a common rail, high pressure injection, passenger car diesel engine fuelled by B70 versus normal diesel fuel.
- A sequence of 15 steady state engine operation points was selected as representative of the engine operation map. This test sequence was programmed in the controller of the eddy current dynamometer and the most important engine performance and emissions characteristics were recorded, with the engine fuelled by B70 and alternatively, by pure Diesel fuel.
- The biodiesel employed in the tests was a FAME based on 40% rapeseed oil, 30% soybean oil and 30% waste cooking oils as raw material, supplied by a local factory.
- Engine tests performed under low, medium and high load conditions have shown a sharp reduction in CO and HC emissions upstream catalyst, with the use of the B70 blend.
- The effect of the decreased heating value of the biodiesel (despite its slightly increased density) in the brake specific fuel consumption increase was confirmed by the measurements. Engine efficiency was not generally observed to change with biodiesel combustion.
- As expected, decreased air to fuel ratio values were measured with the B70 at all operation points. On the other hand, lambda was observed to increase at the medium-to-high load range.
- The effect of the B70 blend on the main fuel injection parameters (common rail pressure, pilot and main injection advance and time) was measured and explained based on the maps stored in the ECU of the engine.
- A significant increase of the fuel temperatures was observed with the B70 blend. It was necessary to install a heat exchanger in the fuel return line, in order to keep fuel at acceptable temperatures (less than 50 °C).
- The effect of the B70 on NO<sub>x</sub> emissions was less pronounced and more complex. NO<sub>x</sub> reduction was only observed at medium-to-high loads. Again, this can be explained based on the modification by the ECU of certain fuel injection parameters for the B70 combustion.
- Reduced PM emissions and smoke opacity was observed by a qualitative comparison of the soot collected on Pallflex filters from undiluted exhaust gas sampled directly from the exhaust line for the total duration of each test. Again, this is in line with what is known from the literature.
- The discussion improves understanding of how the common rail injection engine responds to the biofuel blend, as compared to the reference fuel, based on the injection control flowchart.

## 5. Dynamic effects and transient performance in common rail injection systems<sup>‡</sup>

Comparative steady state engine bench tests of a 2.0 liter, common rail, high pressure injection passenger car (HSDI) diesel engine fuelled by a B70 biodiesel blend have been presented in a previous paper [117]. The results compared well to the limited information reported in the literature for the specific engine category [55]. Later on, the tests were extended to cover selected transient operation points, as well as dynamic effects on the fuel system. The results are presented in this chapter, aiming at a better understanding of the effect of high biodiesel blends on the transient operation and the fuel system's dynamics of an HSDI Diesel engine.

### 5.1 Engine instrumentation and injection system

Facilities to monitor and control engine variables are installed on a DW10 ATED, 2.0 l, 4-cylinder, direct injection, common rail diesel engine, installed on an engine test bench at the Laboratory of Thermodynamics and Thermal Engines. The engine is coupled to a Froude-Consine eddy current dynamometer with Texcel 100 direct digital controller and a PWM engine throttle actuator [106]. The main data for the engine and injection system are given in Table 5.1.

**Table 5.1.** Engine and injection system technical data.

Engine type	HSDI turbocharged diesel engine
Engine model	DW10 ATED
Number of cylinders	4, in line
Bore	85 mm
Stroke	88 mm
Rated power	80 kW, 4000 rpm
Rated torque	250 Nm, 2000 rpm
Compression ratio	18:1
Injection system	CP1 Bosch high pressure pump (1350 bar)
Injector body and nozzle	Bosch with five injector nozzle holes
ECU version	Bosch EDC 15C2 HDI
Diesel filter	IBIDEN SiC filter

The main injection system's parameters, along with the EGR and waste gate valve positions are controlled via the engine's electronic control unit (ECU). ETAS hardware and the INCA software interface were used to access engine ECU operating variables and maps. Also, additional data acquisition of pressures, temperatures, A/F, fuel and flow rates, based on external sensors was carried out by means of NI

---

<sup>‡</sup> Part of this chapter was published in: ECOS 2011, 24th International Conference on Efficiency, Cost, Optimization, Simulation and Environmental Impact of Energy Systems, July 4- 7 2011, Novi Sad, Serbia and Effects of a 70% biodiesel blend on the fuel injection system operation during steady-state and transient performance of a common rail diesel engine Energy Conversion and Management, 2012, 60: p.56-67, doi:10.1016/j.enconman.2011.10.028

Data acquisition hardware and software. The exhaust gas analysis system consists of a group of analyzers for measuring THC (JUM HFID 3300A), CO, CO<sub>2</sub> (Signal Model 2200) and NO<sub>x</sub> (Signal Model 4000 CLD).

**Table 5.2.** Properties of the specific fuels employed in this study [117].

Specifications / ranges	Our case Biodiesel (FAME)	Our case Diesel
Density (15 °C) [kg/m <sup>3</sup> ]	865	825
Viscosity (40 °C) [cSt]	4.7	2.5
Cetane number	55	50
Cold filter plugging point [°C]	-3	-12
Gross heating value [MJ/kg]	40.3	46.2
Lower heating value [MJ/kg]	37.7	43.3
Water content [mg/kg]	330	-
Acid number [mg KOH/g]	0.16	-
Sulfur content [ppm]	-	50
Iodine number [g iodine/100g]	117	-

## 5.2 Test fuels

The fuels under investigation are pure diesel EN 590 (0% biodiesel), and a blend of 70 vol. % biodiesel in pure diesel. Throughout this thesis the tested fuels were denoted as B0 and B70, respectively. The biodiesel employed was a fatty acid methyl ester produced by 40% rapeseed oil, 30% soybean oil and 30% recycled cooking oils. It was supplied by ELIN biofuels SA (Volos factory) and conforms to EN14214:2008 [118] specifications. Tested fuels properties are listed in Table 5.2.

## 5.3 ECU operating maps

In order to better understand the variation of the specific engine's behavior with biodiesel blends, the mapping of the basic operating parameters in the engine ECU is to be discussed first. The main maps that are stored in the ECU are summarized below. It should be mentioned that the basic injection maps, including pilot and main injection were presented in [117]. They are employed in the calculation of the following variables: (i) fuel delivery (mm<sup>3</sup>/stroke) as a function of engine speed and measured intake air mass flow. (ii) air mass flow rate (mg/stroke) and waste gate valve fraction (%) as function of engine speed and fuel delivery (Figure 5.1). Data acquisition of the engine ECU variables was made through the INCA software, which may record hundreds of ECU variables.

The following variables were regularly recorded during the tests: Engine speed, Pedal position, Water temperature, EGR valve position, Throttle valve position, Turbo valve position, Intake air temperature, Intake pressure (set point and measured), Air mass flow (set point and measured), Fuel temperature, Fuel pressure (set point and measured), Fuel mass delivery per cycle, Injection advance (pilot), Injection advance (main), Injection duration (pilot, main and post injection).

Additional data acquisition based on external sensors was carried out for the following quantities: Engine Speed, Engine Torque, Cooling water inlet and outlet temperatures, Fuel mass flow rate, Air mass flow rate, A/F ratio, Compressor boost pressure, Turbine inlet pressure, temperatures and pressures at various points in engine inlet and exhaust lines, including oxidation catalyst and diesel filter.

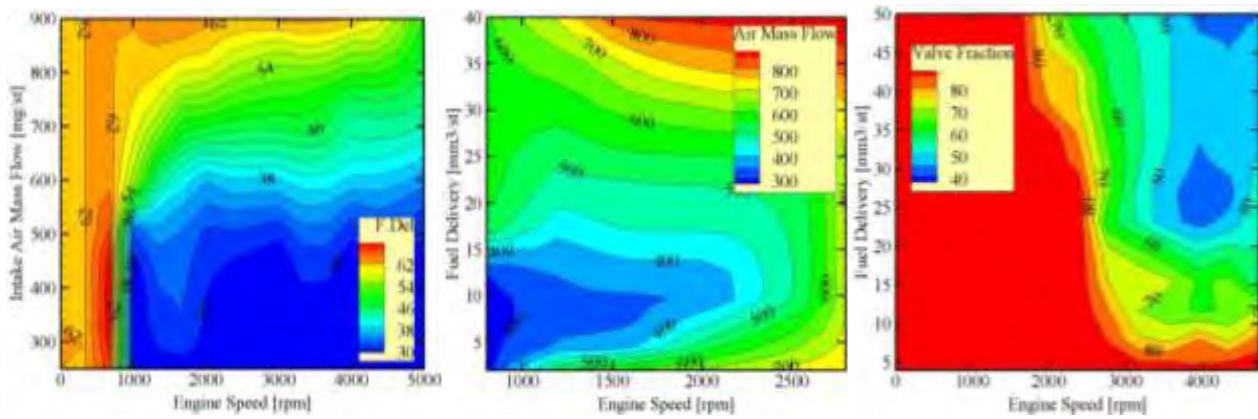


**Figure 5.1.** Smoke limited fuel delivery ( $\text{mm}^3/\text{st}$ ) as a function of engine speed and intake air mass flow (left), air mass flow rate ( $\text{mg}/\text{st}$ ) (middle) and waste gate valve fraction (%) as a function of engine speed and fuel delivery (right).

A sequence of steady state operation points was selected to cover a wide range of the engine operation map (from low speed-low load to high speed-high load). The sequence of operation points was programmed in the dyno controller (Test Sequence Editor). The transition time between each two successive points was set to 5 seconds. Details of the steady state testing are given in [117].

## 5.4 Results and discussion

Typical steady state performance of the injection system is presented here by means of examining in detail three characteristic operation points, namely, (1250 rpm-40 Nm), (2500 rpm-70 Nm) and (3600 rpm-130 Nm). The injection system's dynamics was investigated for a characteristic period of 400 ms. The variation of fuel injection parameters, fuel consumption, engine speed, turbocharger parameters (inlet manifold pressure, inlet air mass flow, turbo valve position) and EGR valve position for the tested fuels at specific operation points is presented in this section.

### 5.4.1 Injection system dynamics at characteristic operating points

The effect of the engine speed on the peak –to- peak amplitude and fluctuation frequency of the rail pressure signal for both tested fuels is presented in Figures 12.2 to 12.4. Some characteristic values of data acquisition parameters are presented in Table 5.3. It should be mentioned in this context that the ECU modifies its acquisition rate according to operating conditions and type of engine parameter. Fuel consumption and injection duration (pilot, main and post) have the same acquisition rate of 50 Hz, irrespective of the engine operating conditions. On the other hand, the acquisition rate of variables closely correlated to the engine cycle like the rail pressure, injection advance (pilot and main), throttle, EGR and wastegate valve position, intake manifold pressure and intake air mass flow, is varying as function of engine speed (see Table 5.3, last column).

**Table 5.3.** Data acquisition parameters at specific operation points.

Engine speed [rpm]	Engine cycle frequency [Hz]	Engine cycle duration [ms]	Oscillation frequency [Hz]	Acquisition time step [ms] (main parameters)	Acquisition rate [Hz] (main parameters)
1250	21	96	42	12	83
2500	42	48	84	6	166
3600	60	33	120	4	250

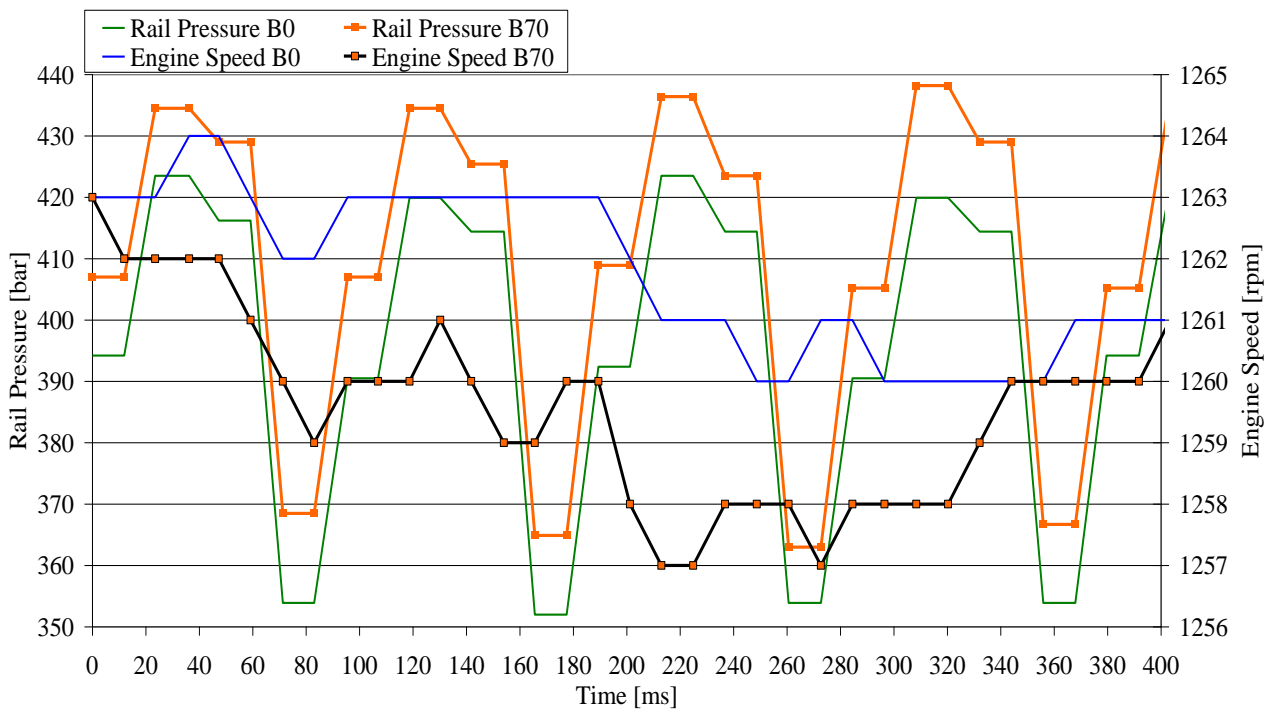


**Figure 5.2.** Comparison of rail pressure and engine speed for B0 and B70 at the steady state operation point, 1250 rpm-40 Nm, recorded for a period of 400 ms.

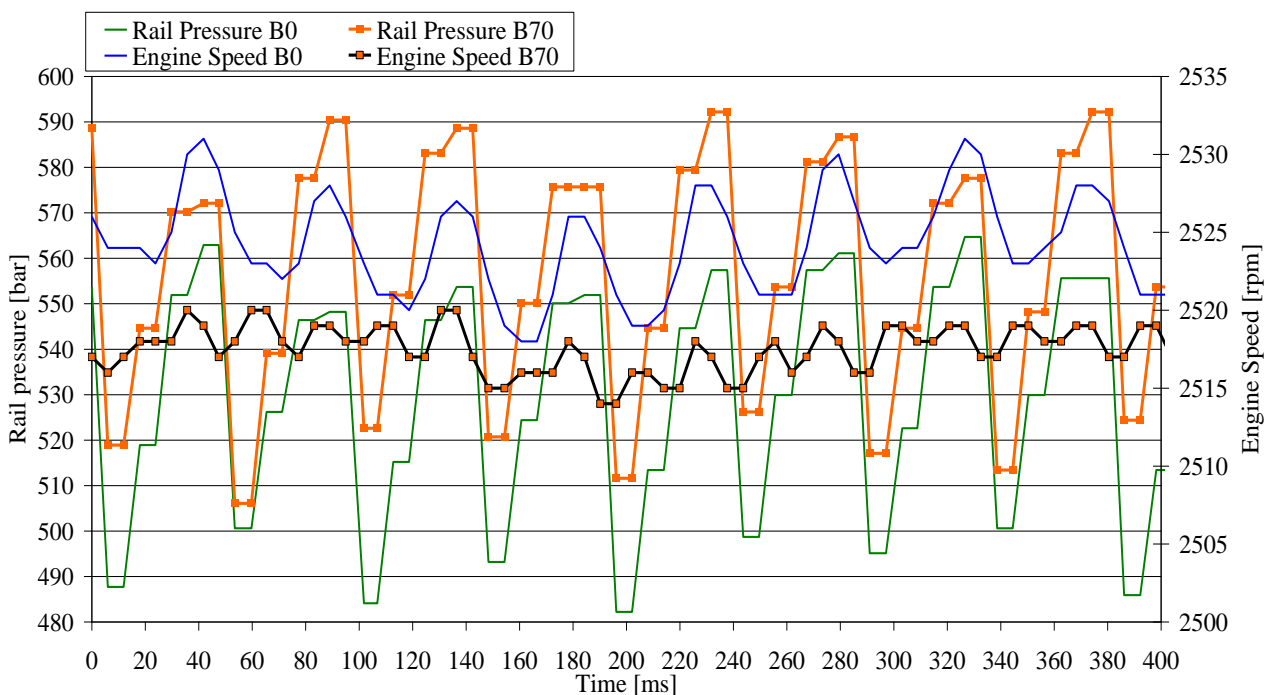


**Figure 5.3.** Comparison of rail pressure and engine speed for B0 and B70 at the steady state operation point, 2500 rpm-70 Nm, recorded for a period of 400 ms.

A first observation that can be made in these figures is a certain degree of aliasing in the acquisition of the rail pressure signal, which is oscillating with a frequency comparable to the engine cycling frequency. (A higher acquisition rate of the order of at least 1 kHz would be optimal here). The rail pressure increase with the B70 blend is apparent in all three figures. This is explained by the algorithm of calculation of this variable by the ECU; the rail pressure is mapped in the ECU as a function of the engine speed and fuel

delivery per stroke. Since biodiesel has a lower volume heating value than pure diesel, more fuel needs to be injected into the engine cylinder, which causes a higher fuel delivery and thus increased rail pressures for the B70 fuel blend.

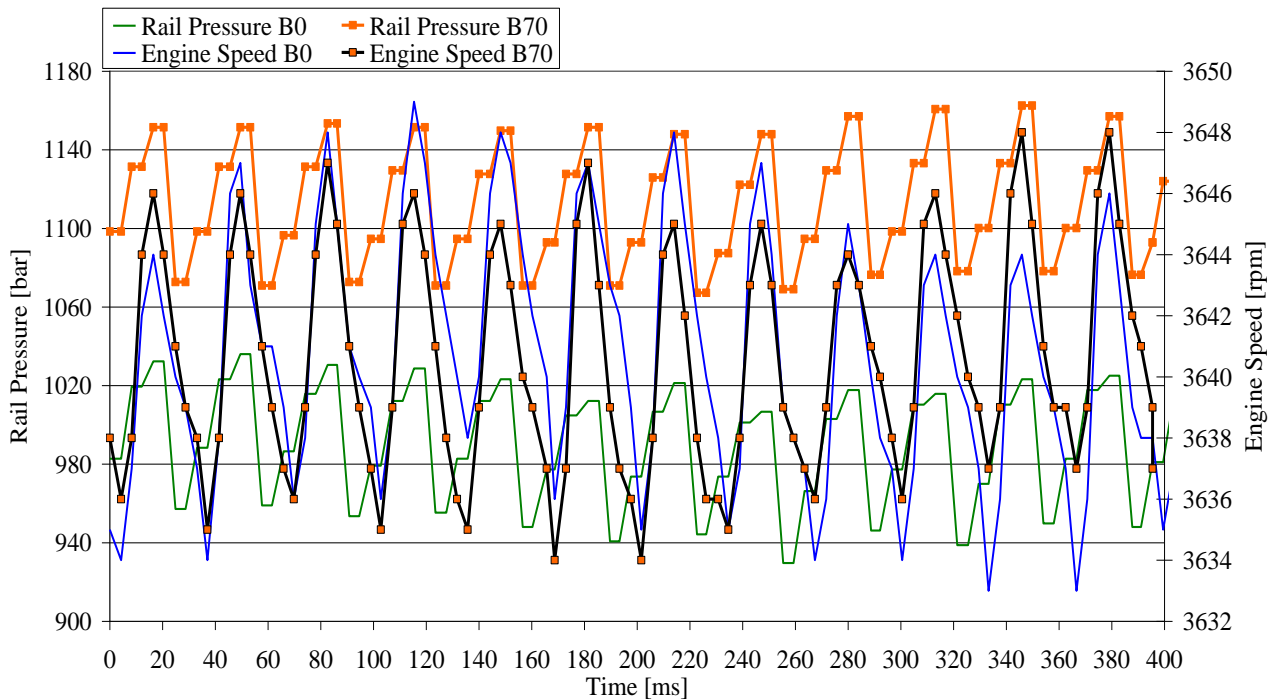


**Figure 5.4.** Comparison of rail pressure and engine speed for B0 and B70 at the steady state operation point, 3600 rpm-130 Nm, recorded for a period of 400 ms.

The rail pressure drop caused by injector opening and the rail pressure rise induced by its closure are observable in these figures, which also demonstrate that the rail pressure is not constant as predicted in simplified models [119], but may oscillate with significant amplitude that reaches sometimes 100 bar or even more, especially in 1<sup>st</sup> generation common rail systems like this one.

The oscillation period is slightly influenced by the rail pressure, and in particular, it is smaller for higher pressures. This is explained by the fact that the speed of sound increases with increasing pressure and is higher for biodiesel than for diesel fuel [49].

This is consistent with the observation that higher pressures imply higher wave propagation speed, according to the relation:

$$c = \sqrt{\frac{B}{\rho}} \quad [5.1]$$

The mean value of the amplitude of pressure oscillations at steady state is increased with the B70 blend, along with the increase in the rail pressure levels.

In order to better understand the dynamics of the injection process, the frequencies of the measured signals were analyzed. The results are presented below in the form of FFT graphs of the rail pressure signal for the B0 and B70 fuel at the specific steady state operation points (Figure 5.5 and Figure 5.6 respectively).

The horizontal axis contains always the frequency analysis results of the 3 operation points.

As already reported, the main frequency of the pump signal is given by the equation:



$$\text{Frequency [Hz]} = \frac{\text{Number of pump plungers} * \text{Engine Speed [rps]}}{2} \quad [5.2]$$

which calculates a frequency of 31.25 Hz at 1250 rpm, 62.5 Hz at 2500 rpm and 90 Hz at 3600 rpm.

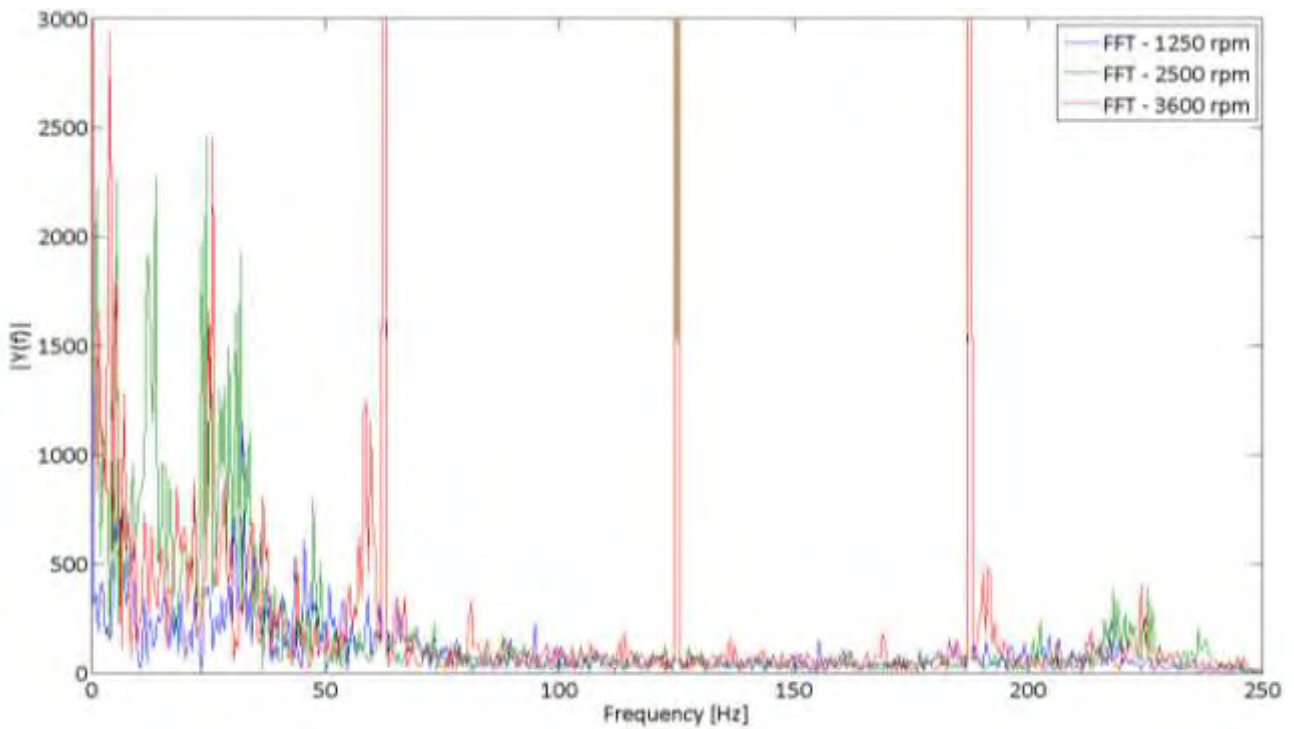


**Figure 5.5.** FFT of the rail pressure at steady state operations points at 1250, 2500 and 3600 rpm, with base fuel.

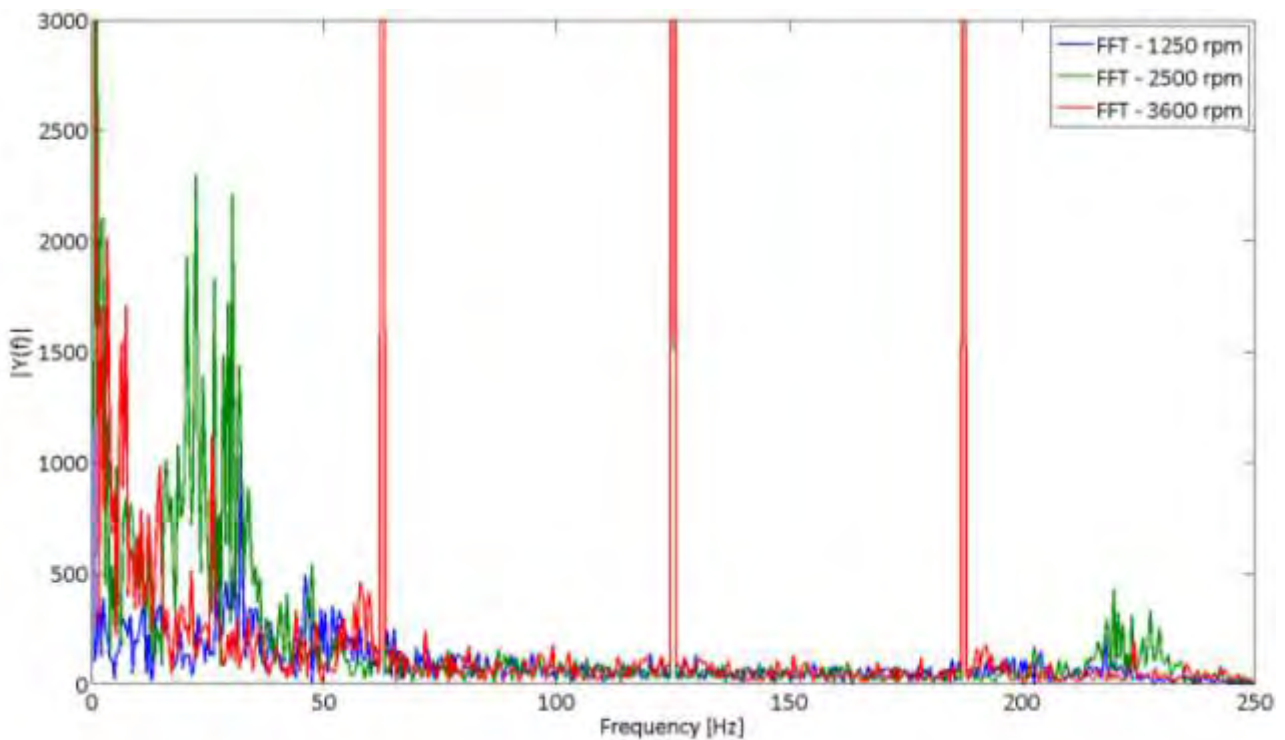


**Figure 5.6.** FFT of the rail pressure at steady state operations points at 1250, 2500 and 3600 rpm, with B70.

The first frequency with the highest amplitude is the one close to 125 Hz, which should be correlated with the injector dynamics. According to [49] the water hammer due to injector closure and the compression wave coming from the rail are in phase, producing large oscillations in the nozzle. The time required to a pressure wave to travel from the nozzle to the rail and back, is equal to half the free oscillation period. The above peaks are visible for all operation points. The peak at 83 Hz at 1250 rpm is the acquisition rate at 1250 rpm. Similarly, the frequency of 166 Hz and 250 Hz correspond to the respective acquisition rates at 2500 and 3600 rpm. By comparison of the overall behavior with B0 and B70 in the same operation points in Figure 5.5 and Figure 5.6 respectively, it may be noted that the dynamics with the B70 fuel are characterized by an increased degree of damping (presumably due to the higher viscosity of biodiesel).

### 5.4.2 Transient results

Figure 5.7 shows the variations of fuel injection parameters, fuel consumption, engine speed, turbocharger parameters (inlet manifold pressure, inlet air mass flow, turbo valve position) and EGR valve position for B0 during the full throttle step from idle to 3600 rpm–130 Nm.

In a turbocharged engine undergoing such a transient, the first thing that happens is that the quantity of fuel injected increases rapidly to its maximum allowed value, thus putting more energy into the exhaust gases which then accelerate the turbocharger. As the turbocharger accelerates, the flow and pressure to the inlet manifold increase which in turn permits more fuel to be injected. From this figure one can observe large overshoots in boost pressure and inlet air mass flow, due to turbocharger lag. The waste-gate valve is also activated as soon as the boost pressure exceeds 2 bars.

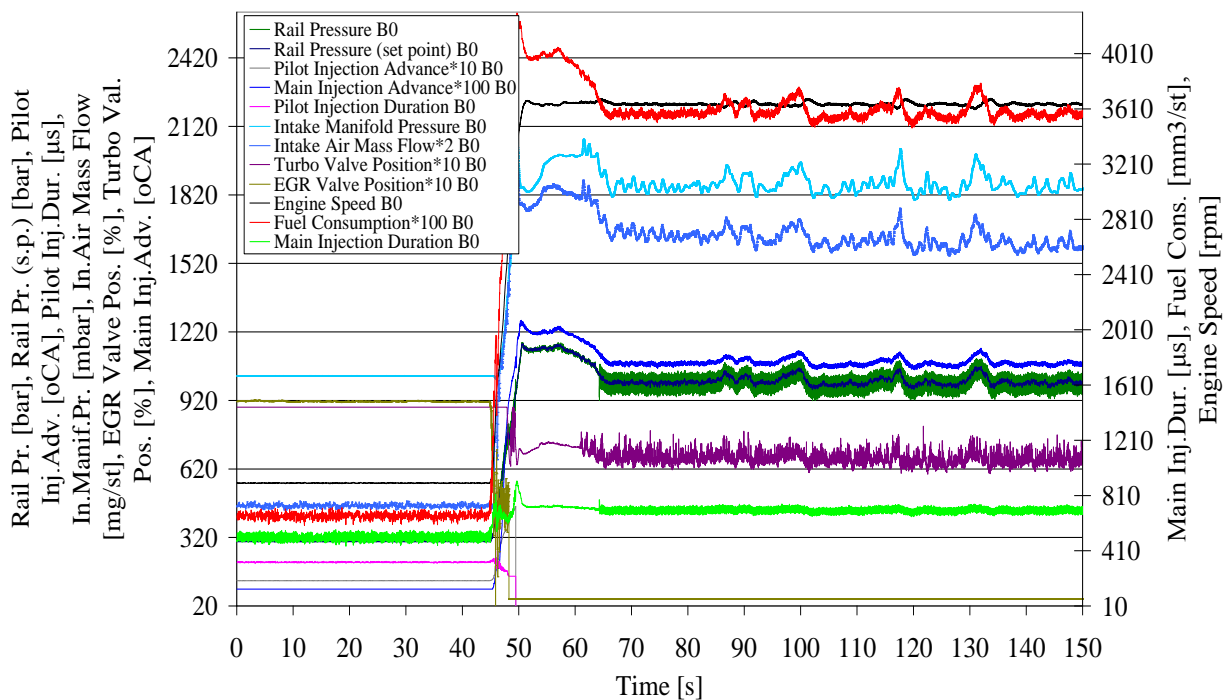


**Figure 5.7.** Differences in fuel injection parameters (common rail pressure and pressure set point, pilot and main injection advance and pilot and main injection duration), fuel consumption, turbocharger parameters, EGR valve position and engine speed for B0 during the ‘foot down’ acceleration step from idle to 3600 rpm–130 Nm.

The turbocharger response is non linear, which leads to a period of stagnation followed by a sudden flip open. The stagnation causes an overshoot in pressure and airflow. Then the rapid opening leads to undershoot, stabilizing after several seconds. The same behavior is presented by inlet air mass flow. The closure of the EGR valve allows the boost pressure to reach the turbo valve's operating range [120].

The actuation strategy of the smoke limiter is a key factor in explaining engine behavior at fast transients like this one. At the start of the transient process, the accelerator is pushed to its full- load position. At this moment, the pressure in the intake manifold and the air mass flow rate, which are usually the input signals for the smoke corrector device, have not changed from their values at idle. Consequently, the smoke corrector allows only a small increase in the injected fuel mass, while the intake air mass flow rate remains unchanged. This is one of the points where the minimum A/F ratio is attained. During a short time, when the engine is running with the increased injected fuel mass, the induced air flow is increasing slowly, due to the higher energy in the exhaust, and consequently higher boost pressure. The result is the increase in A/F ratio up to a point determined by the boost pressure threshold for the smoke corrector to start increasing the injected fuel mass. From this point on, the injected fuel mass is increased according to the rise in the boost pressure, reaching the point of maximum fuel delivery.

A strategy of constant A/F is usual for engines without EGR. The steeper constant A/F ratio line (lower A/F limit) results in the faster the engine transient, but also to the highest soot emissions. Thus, engines equipped with EGR like this one are employing an improved control strategy that takes into account the accelerator position derivative and other related variables [121].

The following table tabulates a number of characteristic transient operation modes recorded in the frame of our tests. All transient modes were programmed with a 5-second duration of the speed or load step.

**Table 5.4.** Table with the design of the transient tests.

Engine speed step [rpm] – Tested fuels B0, B70			
Start point	End point	Engine torque [Nm]	Transition time [s]
900	1250	20	5
1250	1750	40	5
1750	2500	70	5
2500	1500	100	5
1500	2000	130	5
2000	2400	160	5
2400	2800	180	5
2800	3000	200	5
3000	3300	180	5
3300	3600	130	5
Engine load step [Nm] – Tested fuels B0, B70			
Start point	End point	Engine speed [rpm]	Transition time [s]
130	160	2000	5

Most steps are relatively mild shifts in engine operation points. The aim is to understand the differences between the transient operation with the reference fuel and the B70 blend. A typical speed step from 900 to 1250 rpm at very low load is presented in Figure 5.8. The increased volume fuel consumption of the biodiesel blend (lower part of the diagram) is mainly due to the lower volume energy content of the biodiesel (Table 5.2) [117]. It should be noted here that the data acquisition rate is automatically increased following the engine speed, due to the triggering mode applied by the ECU.

Figure 5.9 presents the comparative results of a step to a higher speed of 2500 rpm, at a medium load level of 70 Nm. Now the acquisition rate is faster and the overshoot in rail pressure and main injection advance are more apparent.

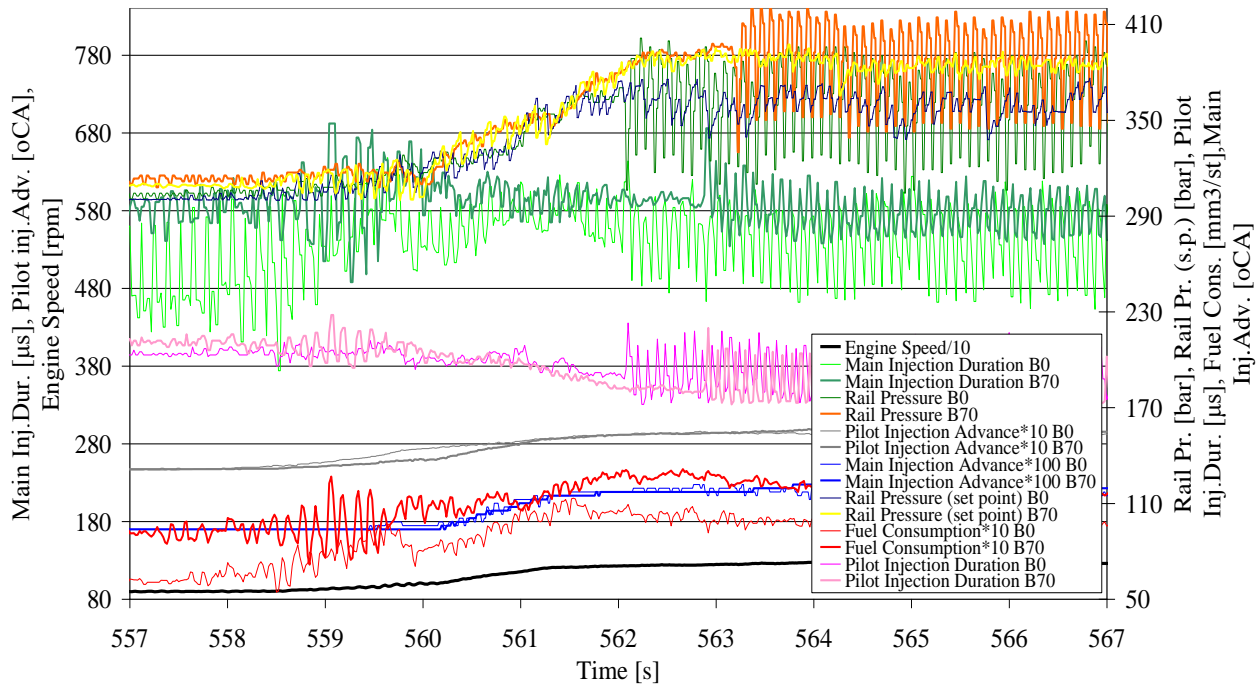


**Figure 5.8.** Differences in fuel injection parameters (common rail pressure and pressure set point, pilot and main injection advance and pilot and main injection duration) and fuel consumption for B0 and B70 during the 900-1250 rpm step at 20 Nm.

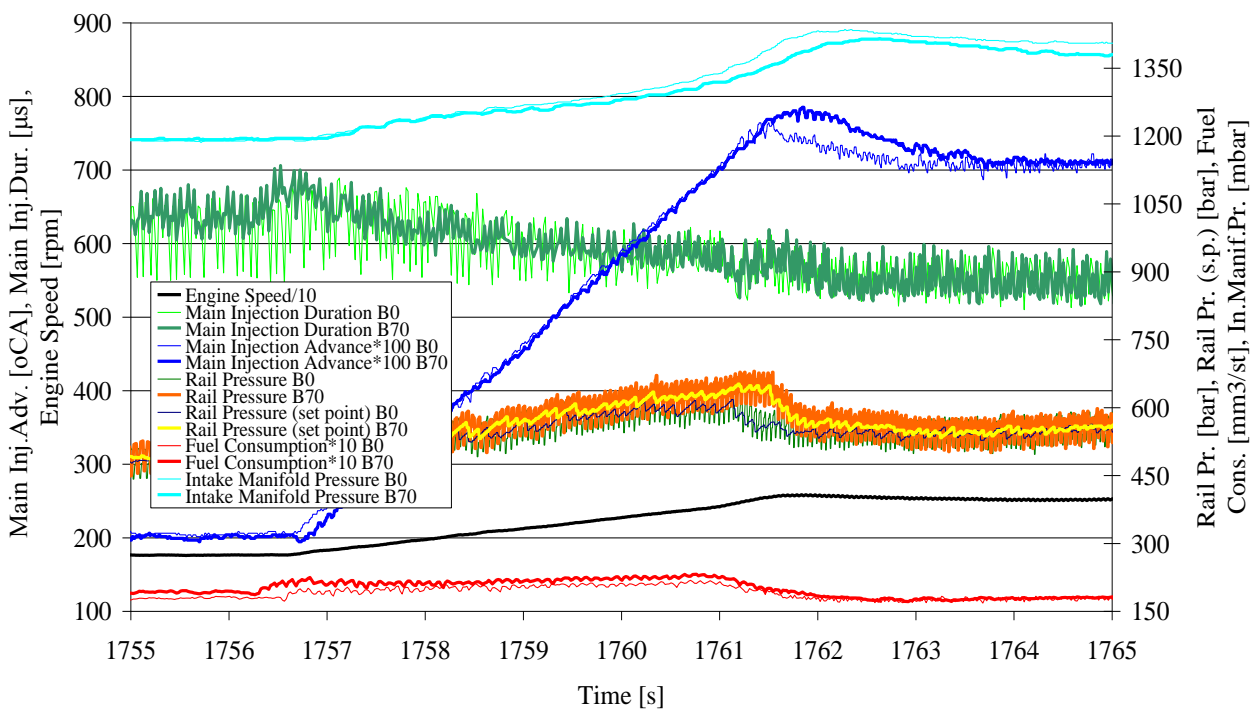


**Figure 5.9.** Differences in fuel injection parameters (common rail pressure and pressure set point, main injection advance and main injection duration), turbocharger parameter (intake manifold pressure), and fuel consumption for B0 and B70 during the 1750-2500 rpm step at 70 Nm.

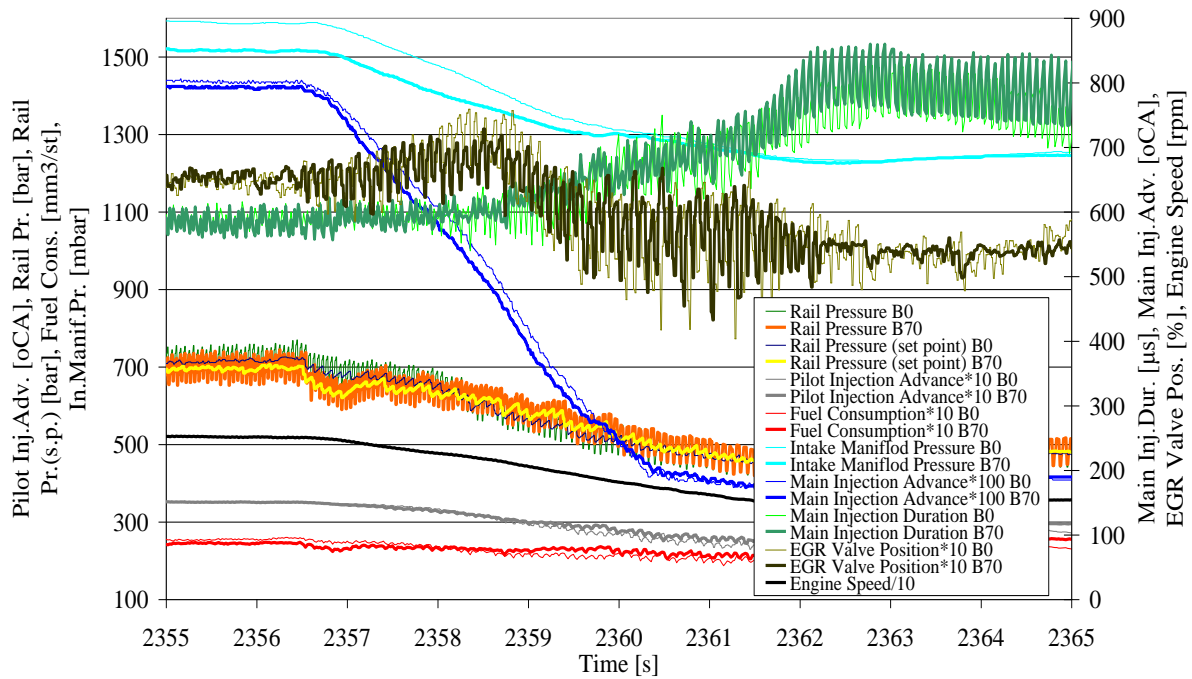


**Figure 5.10.** Differences in fuel injection parameters (common rail pressure and pressure set point, pilot and main injection advance and main injection duration), fuel consumption, intake manifold pressure and EGR valve position for B0 and B70 during the 2500-1500 rpm step at 100 Nm.

Rail pressure levels and overshoot are higher with the B70 blend. This should be resulting from the reduced volume energy content of the biodiesel blend. Higher rail pressure and fuelling levels lead also to higher injection advance crank angles. Fuelling rates per stroke are gradually reduced as we shift to operation points of higher engine efficiency. Reduced amplitude of rail pressure oscillations is observed with the B70 fuel.

Figure 5.10 shows the respective results of a step decrease from 2500 rpm to 1500 rpm, at a load level of 100 Nm. Increased amplitude in rail pressure oscillations with the B70 fuel is observed in this figure. On the other hand, the amplitude of rail pressure oscillations is increasing as we shift to the 1500 rpm regime. The same is true for the fuelling rates per stroke which are gradually increased as we shift to operation points of lower brake engine efficiency. EGR valve setting and intake manifold pressure are also recorded in this figure.

As already mentioned, this is a 1<sup>st</sup> generation system (CP1 pump). There exist significant pressure and injection duration oscillations at part load, that are reduced at high loads, where the return fuel rate is significantly reduced. As we shift to high- load points, the engine increasingly fails to perform the acceleration steps, presumably due to the reduced heating value of the biodiesel fuel. As the engine speed is increased, oscillations in rail pressure and main injection duration are less pronounced. The engine operation stabilizes at 2400 rpm with reduced fluctuations in the duration of main injection. This is true both for the reference and the B70 fuel. The engine can hardly fulfill the task of accelerating from 2800 to 3000 rpm at the high load level of 200 Nm only with the reference fuel.

In Figure 5.11 it is observed that the engine cannot sustain the 3000 rpm-200 Nm operation point. This results in large engine speed oscillations. The change in behavior of the engine in this regime can be explained by the structure of the specific fuel injection ECU maps (pilot injection is shut off beyond 3250 rpm).

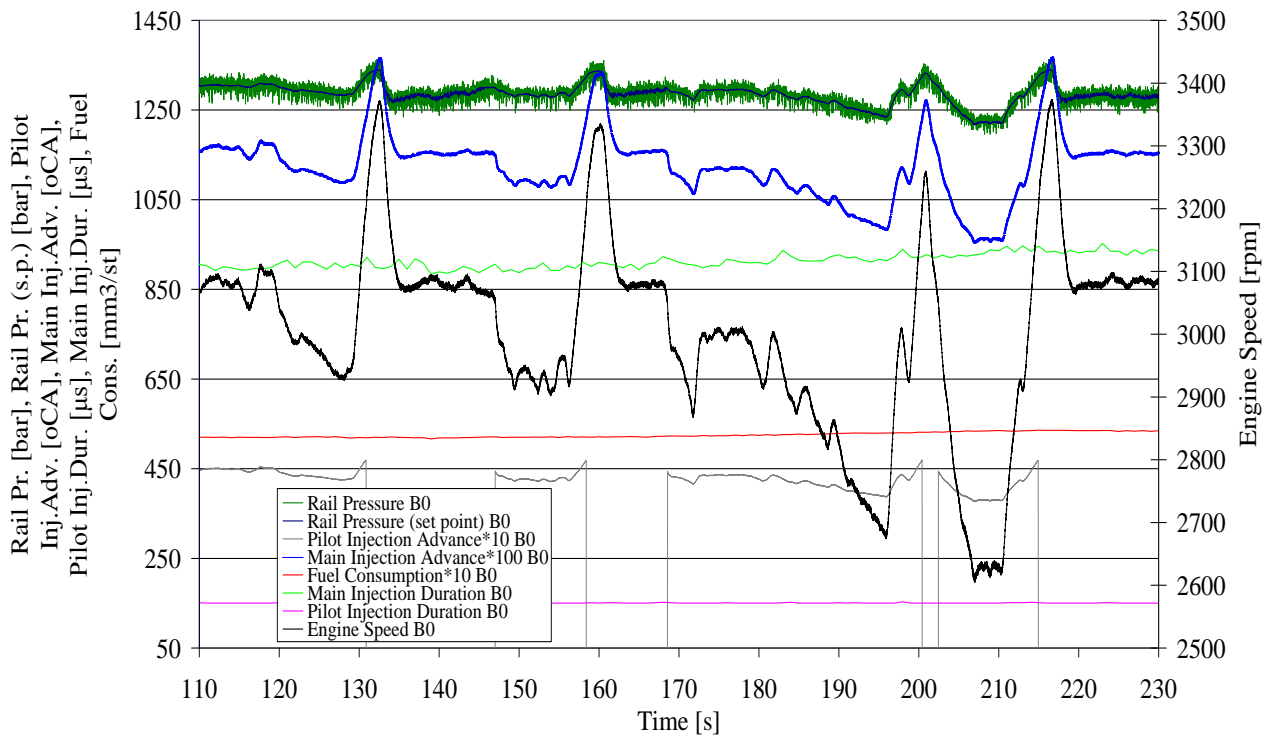


**Figure 5.11.** Fuel injection parameters, fuel consumption and engine speed for B0 at the failing operation point, 3000 rpm-200 Nm.

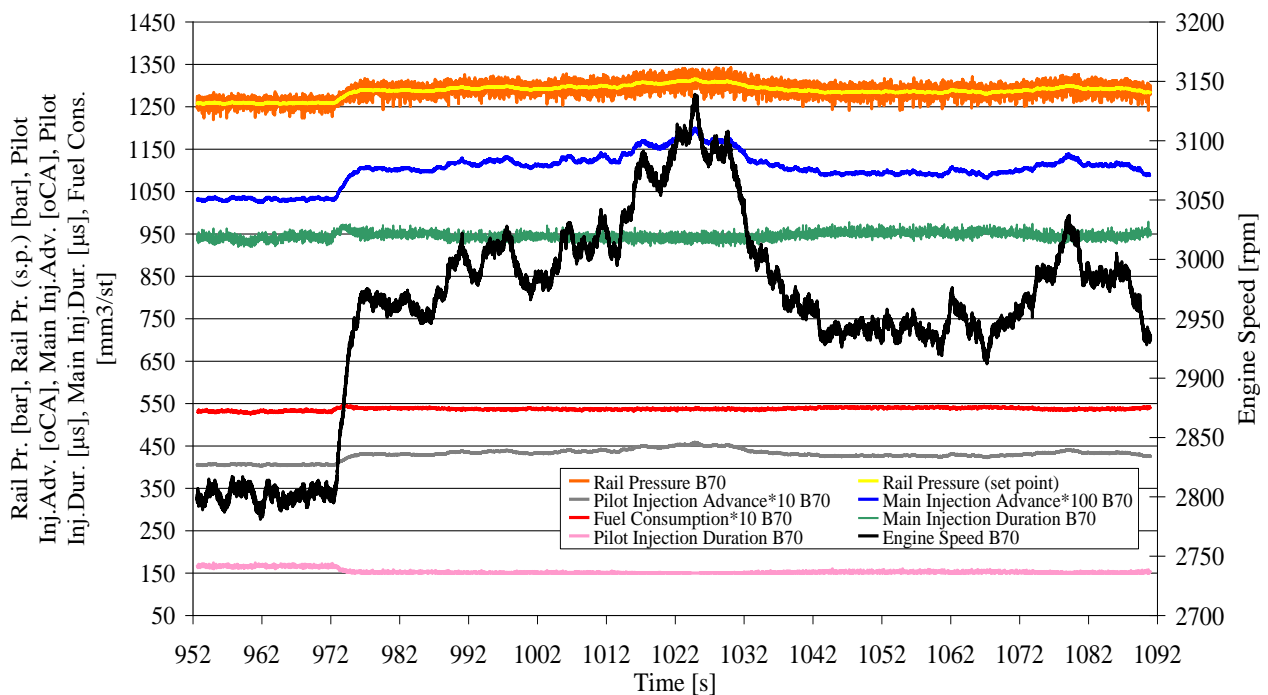


**Figure 5.12.** Fluctuations of fuel injection parameters (common rail pressure and pressure set point, pilot and main injection advance and pilot and main injection duration), fuel consumption and engine speed for B70 during the 2800-3000 rpm failing step at 200 Nm.

According to Figure 5.12, the 3000 rpm-200 Nm operation point is completely impossible to catch with the B70 fuel. The reason must be attributed to the smoke limit of  $52.8 \text{ mm}^3/\text{st}$  imposed by the smoke map

(Figure 5.1). The resulting, significant oscillations in fuel delivery are affecting also the main injection advance, thus leading to more complex speed and torque perturbations. Finally the engine behavior in load steps, 130 Nm to 160 Nm at 2000 rpm, is smoother because the speed which is the main influence parameter in the ECU maps is fixed.

As a general conclusion from the above comparisons, it can be stated that the reduced heating value of the biodiesel fuel is limiting the engine's ability to attain the highest-load points of the operation map. Clearly, it is necessary to expand the operating envelope of the following engine operating parameters: pilot and main injection advance, rail pressure and injection duration. Modern engine calibration techniques that typically employ Design of Experiments (DoE) based test programmes are useful in this process [122]. In addition to the expansion of the fuelling and injection advance maps employed by the engine ECU, the combined effect on the engine operation should be studied. That is, while each one of the above injection parameters will increase in its mapped maximum setting, the combination of several parameters could take the engine into unstable regions.

Modern DoE techniques should be applied to limit the additional experimentation tests that should cover the upper part of the limit space, exploiting prior knowledge with the specific engine. Clearly in such cases it is necessary to have an understanding of how the calculated response is perturbed by adjustments made within the engine controller. For example, increasing the air mass flow (typically by throttle angle or waste-gate control) at constant fuelling conditions to achieve a target lambda will have a different effect compared to reducing the fuel flow rate (typically by injection duration) while leaving air mass flow unchanged. A certain extent of remapping of the engine control unit could extend the maximum fuel per stroke by about 15%. This will affect a number of ECU maps that have fuel delivery per stroke as independent variable. Also, the maps affecting fuelling strategy during transients may need some improvement, based on a compromise between minimum NO<sub>x</sub> emissions, minimum smoke emissions and minimum specific fuel consumption [123]. The difference in air mass flow requirements of the biodiesel could also be taken into account to some extent for further fine tuning. However, the requirement that the same engine is able to use alternatively diesel fuel and biodiesel blends of varying percentage should be always covered by the ECU programming. The use of some type of fuel quality sensor would be essential in this direction. The development of engine models that are flexible in fuelling by high percentage biodiesel blends could be rewarded by an improved performance of the exhaust treatment system (especially the diesel particulate filter) [63, 64].

## 5.5 Suggested engine improvements

According to previous sections, it becomes obvious that the difference between pure diesel and biodiesel gross heating value affects the engine performance. As it was mentioned in [117] the most important control variables of Engine Control Unit are the fuel delivery per stroke and engine speed. In addition, fuel density is important since the rail pressure, main and pilot injection advance are determined from the desired fuel delivery per stroke. The proposed improvement approach lies in the introduction of the changeable fuel density in ECU's cartography in order to increase the volume of injected fuel but sustain stable the total input energy per stroke. Figure 5.13 (left) presents the maximum fuel delivery per stroke, which approaches the value of 55 mm<sup>3</sup>/ stroke. Based on the above, the maximum increase of the fuel injected volume for B100 is given by the equation:

$$E_{\text{strB0}} = E_{\text{strB100}} \Leftrightarrow \rho_{\text{B0}} b_{\text{spB0}} H_{\text{UB0}} = \rho_{\text{B100}} b_{\text{spB100}} H_{\text{UB100}} \quad [5.3]$$

$$b_{spB100} = \frac{\rho_{B0} b_{spB0} H_{UB0}}{\rho_{B100} H_{UB100}} = \frac{(825 \text{ kg/m}^3)(55 \text{ mm}^3/\text{st})(43.3 \text{ MJ/kg})}{(865 \text{ kg/m}^3)(37.7 \text{ MJ/kg})} \Leftrightarrow b_{spB100} = 60.25 \text{ mm}^3/\text{st}$$

In our case, the measurements were conducted by using B70 blend. The maximum fuel delivery per stroke is defined as:

$$b_{spB70} = b_{spB0} + BR(b_{spB100} - b_{spB0}) \quad [5.4]$$

$$b_{spB70} = (55 \text{ mm}^3/\text{st}) + 0.7[(60.25 \text{ mm}^3/\text{st}) - (55 \text{ mm}^3/\text{st})] \Leftrightarrow b_{spB70} = 58.68 \text{ mm}^3/\text{st}$$

Taking into account these calculations, rail pressure and pilot injection fuel delivery maps are modified, as Figure 5.13 and Figure 5.14 show. The orange-coloured rectangle area represents the maps proposed extension to the value of 60 mm<sup>3</sup>/st.

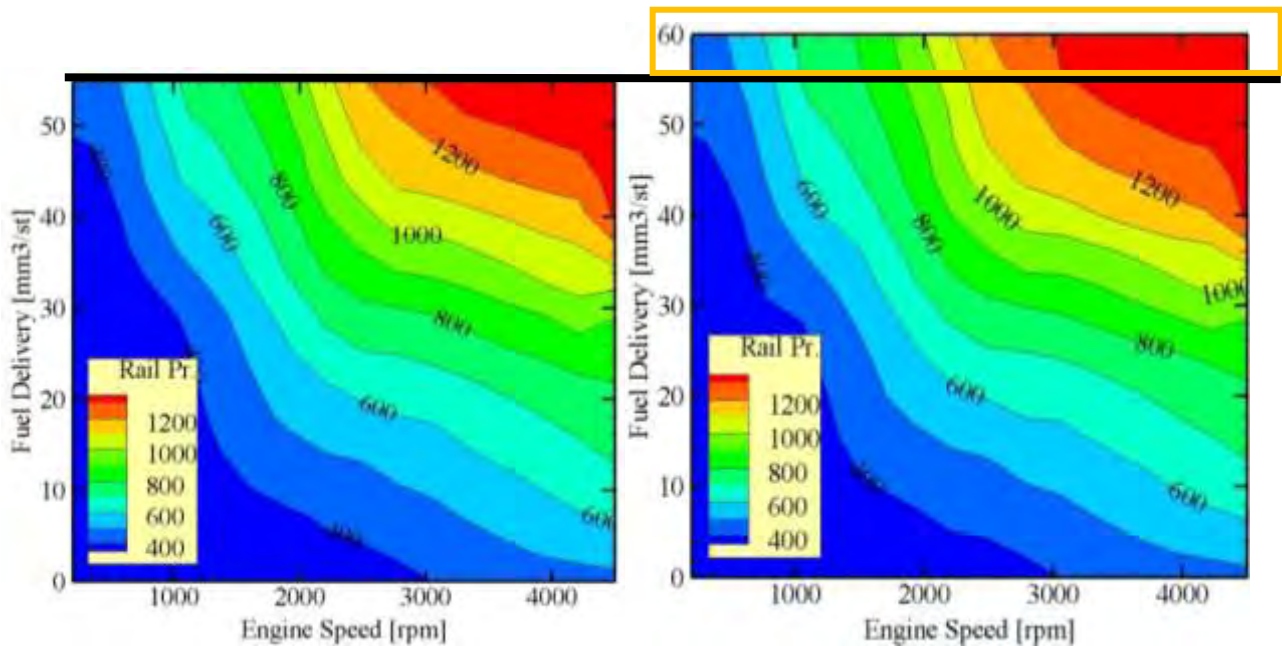


Figure 5.13. Differences between original rail pressure map (left) and proposed map (right).

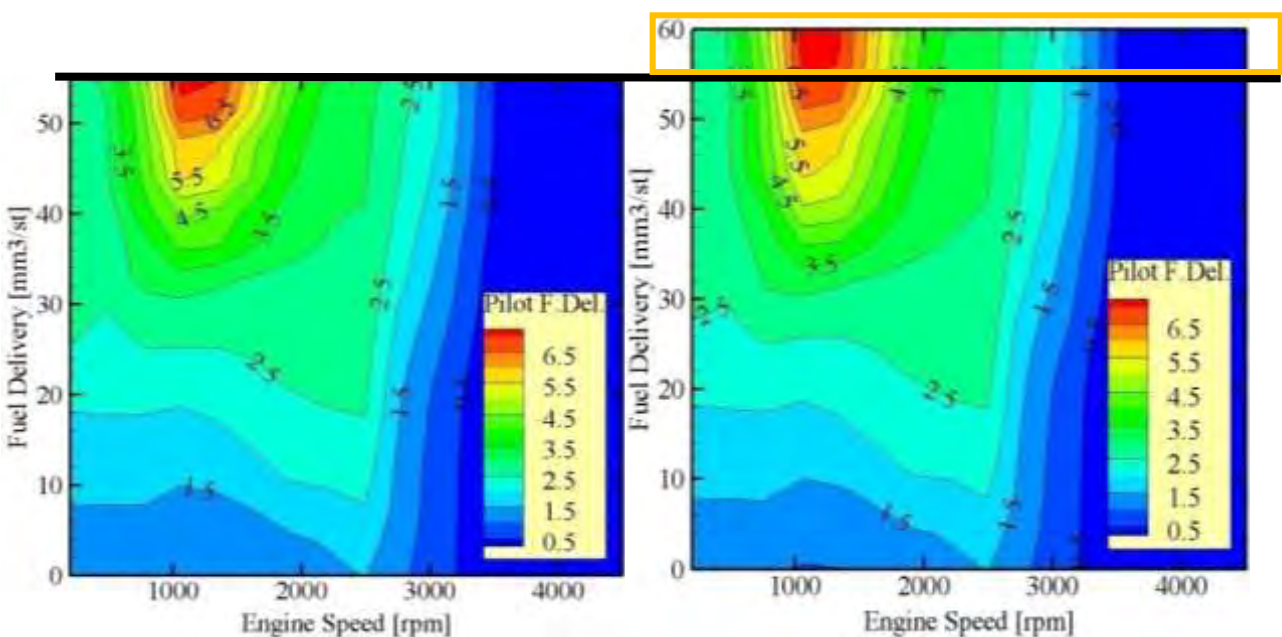


Figure 5.14. Differences between original pilot injection fuel delivery map (left) and proposed map (right).



However, it must be mentioned here that prolonged testing of the specific engine during the last two years resulted in the unpleasant experience of failure of the high pressure fuel pump. Based on this experience, which confirms experience from other researchers, it would not be wise to exploit the full range of biodiesel blending with this type of engines, until the required fuel system modifications are decided by the manufacturers. A maximum blending of 30% on the average would be a more conservative approach.

## 5.6 Conclusions

- Comparative test results in steady state and transient mode with a common rail, high pressure injection, passenger car diesel engine fuelled by B70 versus normal diesel fuel are presented.
- The biodiesel employed in the tests was a FAME based on 40% rapeseed oil, 30% soybean oil and 30% waste cooking oils as raw material, supplied by a local factory.
- The decreased volume heating value of the biodiesel explains the deterioration in engine performance during speed transients at high loads.
- As expected, decreased air to fuel ratio values were measured with the B70 blend. On the other hand, lambda was observed to increase at the medium-to-high load range.
- The effect of the B70 blend on the dynamics of the main fuel injection parameters (common rail pressure, pilot and main injection advance and duration) was measured and explained based on the ECU maps and control strategy.
- Certain improvements are suggested to the ECU maps that could allow engine operation at high biodiesel blends without significant loss in engine performance or deterioration in transient mode emissions. The maximum fuel delivery per stroke is proposed to extend by about 10%.
- Continued operation of the engine with the specific, high biodiesel fuel blend, resulted in the failure of the high pressure fuel pump. Based on this experience, it was decided to continue the tests with lower percentage of biodiesel blending.

## **PART 2**

# **EXPERIMENTS WITH A CONVENTIONAL DI DIESEL ENGINE FUELLED BY LOW PERCENTAGE BIODIESEL BLENDS**

In the second part of this thesis we focus on the effect of low percentage biodiesel blends on the combustion characteristics, energy balance and filter regeneration behavior of a single cylinder DI Diesel engine.

The results of engine bench tests of a 0.477 l single cylinder, direct injection diesel engine fuelled by B20 biodiesel blend are compared with the corresponding results of baseline tests with diesel fuel. The effects of biodiesel blend (B20) on the diesel engine smoke, fuel consumption, engine efficiency, cylinder pressure and mass fraction burned are analyzed and presented. A series of characteristic steady state operation points for engine testing is selected to serve this purpose. Also, additional analysis of indicator diagrams based on commercial simulation software (GT-Suite) was carried out, in order to better understand the effect of biodiesel on combustion. The combustion of biodiesel blend (B20) in an unmodified engine results in advanced combustion, reduced ignition delay, increased total burn duration and increased burn rate in the initial uncontrolled premixed combustion phase. The advanced combustion assists in the reduction of smoke compared to pure diesel combustion. The lower calorific value of the fuel blend results in increased fuel consumption; however, the engine thermal efficiency is not affected significantly. According to the engine energy balance there is a small reduction of brake power and a respective increase of exhaust losses.

The combustion of biodiesel fuel in compression ignition engines results in lower smoke, particulate matter, carbon monoxide and hydrocarbon emission compared to standard diesel fuel [124-126]. In general, the combustion of biodiesel in unmodified diesel engines equipped with pump-line-nozzle systems results in advancement of the combustion process compared to diesel fuel. This is due to differences in chemical and physical properties of the fuels [127-130]. On the other hand, for engines equipped with common rail injection systems this relationship is not so clear and it depends on the respective ECU maps [117] as presented in Chapter 5.

In this part, the combined effects of B20 blend on engine performance and smoke emissions are analyzed and compared with the results obtained from the engine operating on EN590 diesel fuel. The diesel engine used is equipped with pump line nozzle type fuel injection system.

## 6. Experimental layout and test procedure with the single cylinder Diesel engine

In this chapter, the effect of a biodiesel blend (B20) on diesel engine fuel consumption, engine efficiency, smoke emissions, injection and combustion characteristics are analyzed and presented. In order to better analyze and understand the effect of B20 on combustion characteristics, analysis of indicator diagrams was conducted by means of commercial engine simulation software, GT-Suite v.7.0. The combustion of our FAME (40% rapeseed oil, 30 % soybean oil, 30% recycling cooking oils) as blended with diesel fuel in an unmodified engine results in advanced combustion, reduced ignition delay and increased heat release rate in the initial premixed combustion phase as indicated by means of mass fraction burned versus crank angle graphs. The more advanced combustion along with the higher oxygen presence assists in the reduction of smoke compared to pure diesel combustion. The lower calorific value of FAME results in increased fuel consumption. Reduced in-cylinder pressure, in the case of B20, leads to lower indicated power, engine thermal efficiency and higher exhaust gas losses. Further combustion analysis indicates an increase in total combustion duration (0 %-100 %) due to slow combustion of B20. It should be mentioned that the combustion process is strongly related with the injection characteristics (velocity and diameter distributions) of the injected fuel. The effect of biodiesel on injection characteristics will be presented in Chapter 9.

### 6.1 The injection process in a PLN injection system

The Ruggerini RF91 engine injection system is a typical PLN arrangement consisting basically of a piston-type pump, a high pressure line and an injector. In the pump, a cam-driven plunger operates in a closely fitting barrel. The barrel communicates with the fuel supply line through a feed port and with the high pressure line through a delivery valve. When the plunger is at its bottom dead centre the feed port is open and fuel from the supply pump fills the barrel. An injection event begins when the pump cam pushes plunger up, covering the feed port. At this time the pressure of the fluid in the barrel starts to rise. The mounting pressure lifts the delivery valve cone from its seal and fuel passes through the valve into the high pressure delivery line towards the injector. Fuel pressure pushes against the lower side of the injector needle. When it reaches a value that can overcome its spring force, NOP, the needle lifts and injection starts. The injection process is completed when the helix of the pump plunger uncovers the feed port and the pressure in the plunger chamber drops.

In most injection pumps, part of the delivery valve stem has the form of a “retraction piston” that fits closely into the valve guide. This type of delivery valve is usually referred to as constant valve. In this case, when the valve spring pushes the valve stem back, the retraction piston slides into the valve guide and shuts off the high pressure delivery line from the plunger chamber. As a consequence of valve motion, the space available for the fuel in the high pressure line increases by the charge volume of the retraction piston, causing an abrupt pressure reduction and precise closure of the injection nozzle [131]. At the end of the valve stroke, the delivery valve cone is pressed back against the valve seat, isolating the space above the pump plunger from the high pressure portion of the system until the next delivery stroke. The fuel pressure in the injection pipe at the start of the delivery is referred to as residual pressure.

In constant volume valves, return flow restrictions may be used to dampen the pressure waves produced when the nozzle closes. Furthermore, constant pressure waves may be used in high pressure fuel injection systems to maintain a virtually constant static pressure in the high pressure delivery line between

fuel injection phases. Advantages of constant pressure wave valves include prevention of cavitation, improved hydraulic stability, and more precise fuel injection.

Fuel flow to injection valve

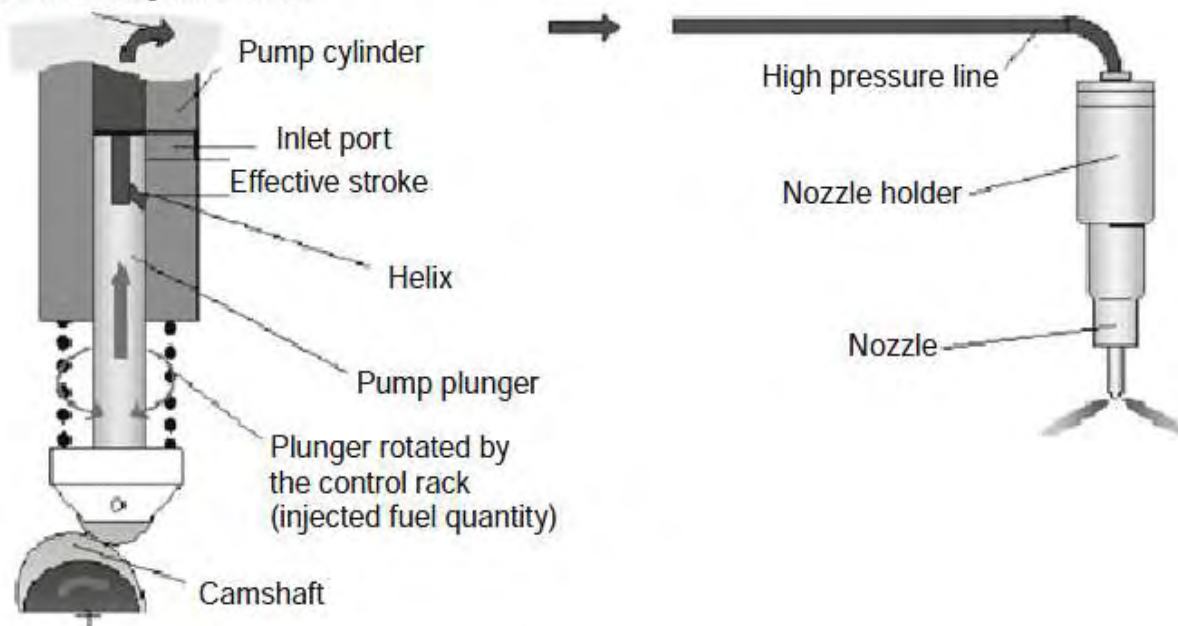


Figure 6.1. Design and functional principle of inline pump [101].

## 6.2 Experimental setup

### 6.2.1 Engine test equipment and injection system

The experiments were carried out on a Ruggerini RF91 engine. The engine is a 477 cm<sup>3</sup>, naturally aspirated, air cooled, single cylinder direct injection diesel engine equipped with a SiC diesel particulate filter. The fuel injection system, which is presented in Figure 6.2 and Figure 6.3, has a four hole nozzle with hole diameter of 0.24 mm located near the combustion chamber centre with an opening pressure of 210 bar. The engine piston is a bowl –in– piston design and is presented in Figure 6.5. The engine is coupled with a single phase generator (MS100LG by NSM generators) with a maximum power of 6 kVA loaded with a set of 4 resistances with a maximum capacity of 1.5 kW for each resistance. In order to better realize single phase generator behavior under different operating conditions, active output power measurements were conducted by means of Fluke 1735 Three phase power logger under several low, medium and high load engine operation points. The measurement setup is presented in Figure 6.4. The main engine and injection system specifications are summarized in Table 6.1 and Table 6.2 respectively.

Table 6.1. Ruggerini RF91 engine specifications.

Engine type	DI 4 stroke naturally aspirated diesel engine
Engine model	RF91
Number of cylinders	1
Bore	90 mm
Stroke	75 mm
Rated power	8.1 kW, 3600 rpm
Rated torque	25 Nm, 2500 rpm
Compression ratio	18.5:1
Diesel particulate filter	IBIDEN SiC filter

**Table 6.2.** RF91 conventional injection system specifications

Engine type	NEW DIESEL pump in line nozzle injection system
Needle diameter	4 mm
Number and diameter of nozzle holes	4 x 0.24 mm
Nozzle hole length	0.6 mm
Pin height	0.125 mm – 0.175 mm
Sump volume	0.36 mm <sup>3</sup>
Opening Pressure	210 bar
Pump plunger diameter	7 mm
Drive rod length	65.8 mm – 66 mm
High pressure line length	400 mm



**Figure 6.2.** High pressure line (left), injector location (centre) and diesel pump (right).

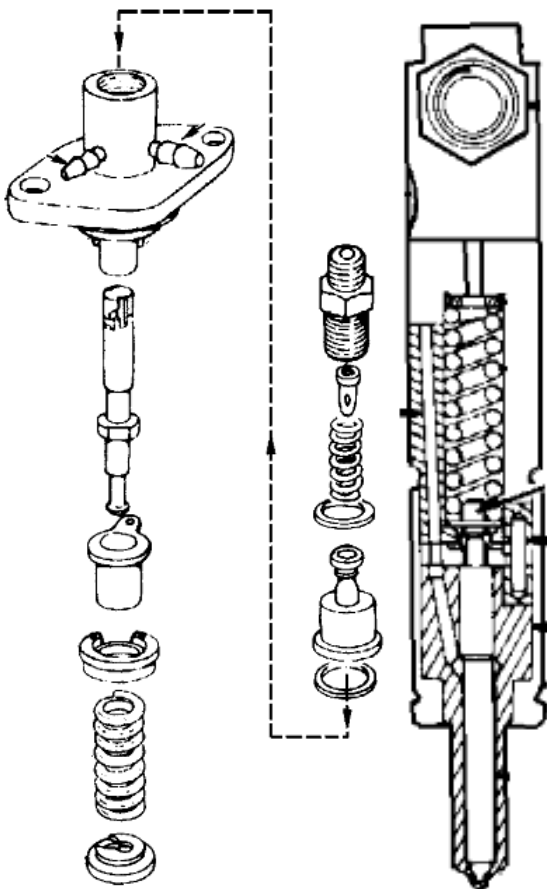


**Figure 6.3.** RF91 injection system. Injection pump components and disassembly view (left) and mechanical injector cutaway view (right).

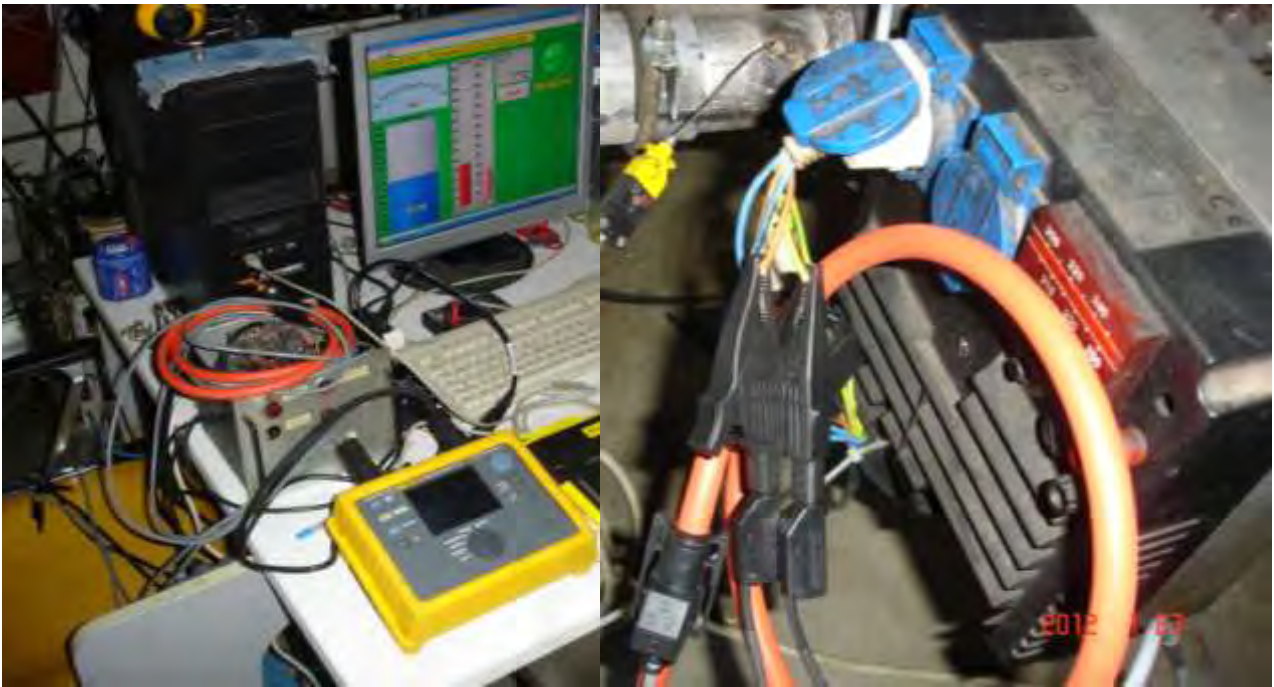


**Figure 6.4.** Experimental setup for single phase generator active output power measurements. Fluke 1735 data logging device (yellow one, left) and electrical connections at generator output cable (right).



**Figure 6.5.** Cylinder head disassembly.

For the measurement of cylinder pressure, (indicator diagram), a Kistler 6052B1 piezoelectric transducer is used flush mounted to the cylinder head, close to the injector, and connected to a Kistler AG5044A charge amplifier (main characteristics in Table). The crankshaft position was measured using a digital shaft encoder. The engine test rig included other standard engine instrumentation such as K-type thermocouples, pressure transducer and an electronic balance for fuel consumption measurement.

The temperatures were measured at the cylinder outlet, at the inlet of the diesel particulate filter and at 2 positions inside the filter, centre and periphery. The loading level of the diesel particulate filter was measured using a JUMO 0-500 mbar differential pressure transducer. A Kern electronic balance with a weighting range of 0.1 to 4000 g was used for the monitoring of engine fuel consumption. The exhaust gas A/F ratio was measured by means of an UEGO sensor (type 6110A). Figure 6.8 shows a full schematic arrangement of the exhaust line instrumentation and data logging system. The output signals from the above sensors were collected by 3 National Instruments data acquisition cards using different acquisition rate for each card.

Particulate samples were collected for B0 and B20 at a medium load steady state operation, 3250 rpm with 16.2 Nm. To ensure repeatability and comparability of the measurements, samples were collected after the engine has reached the steady state as indicating by exhaust gas temperature when they reached steady values. Moreover, upon switching the test fuel, the engine was allowed to operate with the new fuel for fifteen minutes (15 min) to clean the fuel system.

The recorded particulate sampling was not carried out from diluted exhaust gas, the samples taken from undiluted gas before and after the diesel particulate filter in 47 mm filters, 3 for each fuel. After that, the samples were measured in order to determine the collected soot mass and the efficiency of the filter. Pallflex filter device was mounted in two positions, as shown in Figure 6.6.

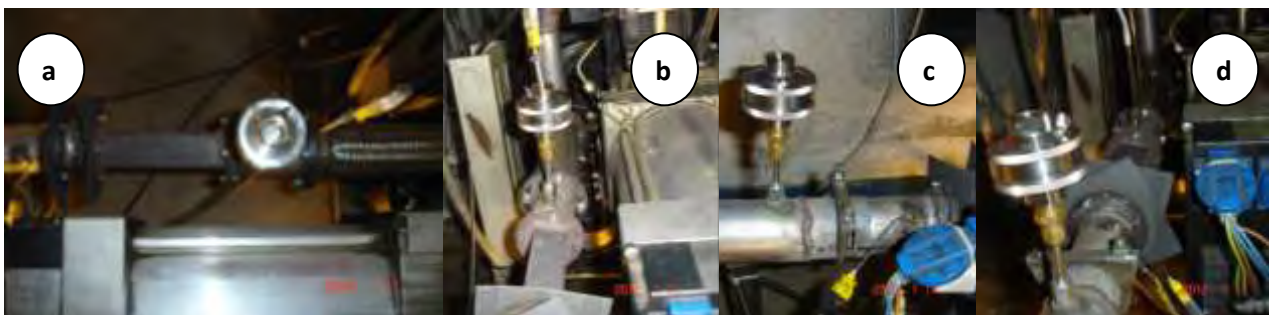


**Figure 6.6.** Pallflex filter device mounted in two positions at the exhaust line, before diesel particulate filter (a and b images) and after diesel particulate filter (c and d images).

Single phase generator active output power measurements are presented in Figure 6.7. As it can be seen, there are 4 equations one for each resistance. Another important observation is related with the maximum output power from each resistance which is increased in accordance with the engine speed and reaches the values of 1.8 kW, 3.1 kW, 3.7 kW and 4.4 kW for 1R, 2R, 3R and 4R respectively.

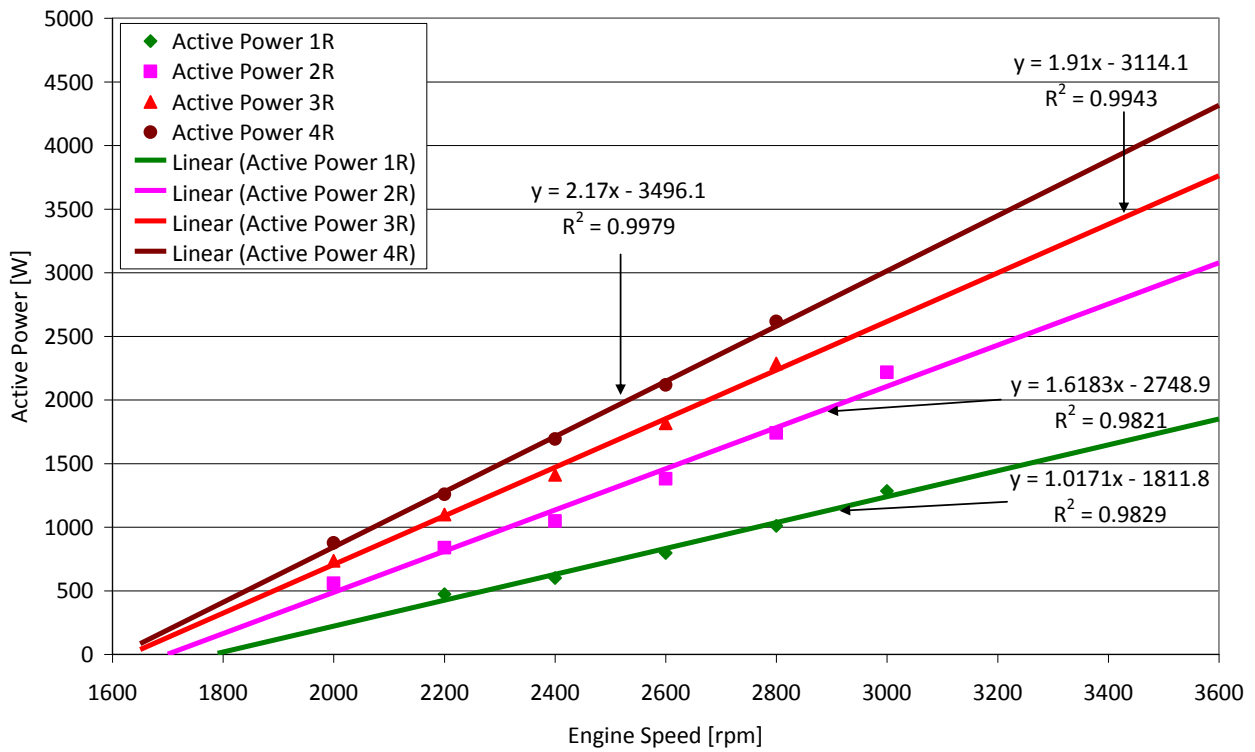


Figure 6.7. Single phase generator characteristic curves.

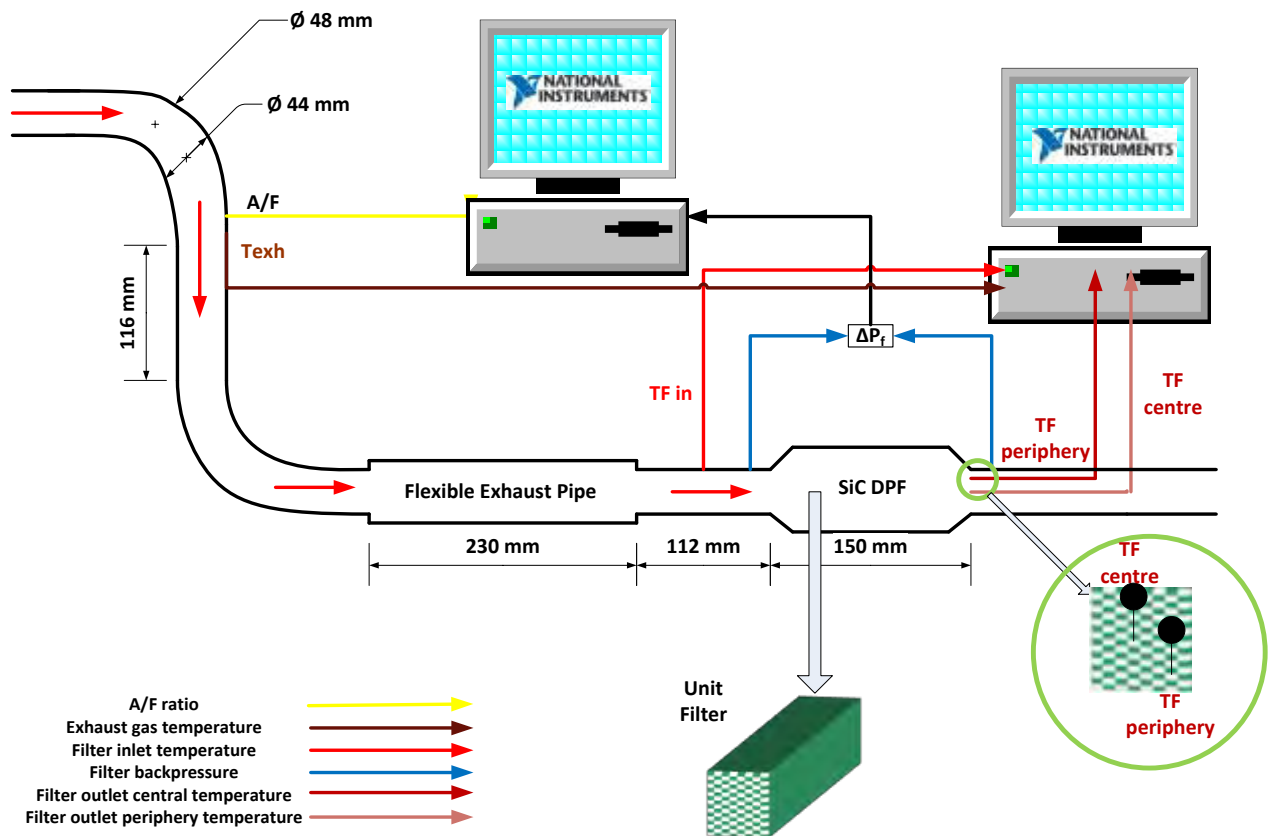


Figure 6.8. RF91 exhaust line instrumentation included six sensors and data logging system.



## 6.2.2 Equipment for indicator diagrams

In this paragraph, a detailed presentation of the equipment for indicator diagrams is given. In order to create an indicator diagram a pair of measurements is necessary, in-cylinder pressure and crank angle. In this case, the first was measured with a KISTLER 6052B1 piezoelectric pressure transducer and the second with a digital shaft encoder. Piezoelectric sensor's signal was transferred via a high insulated cable to the 2-channel charge amplifier, KISLTER AG5044A.

The charge amplifier is used to convert charge signals, pC, from the piezoelectric sensor into proportional voltages, which represents amplifier's sensitivity. The sensitivity can be set to three significant figures with coding switches. This makes is very easy to put the amplifier into operation, in which only the sensitivity of the sensor used needs to be entered. There is another scale in bar/V, in order to be converted the signal from bar to volt and send it to the data acquisition card. In our case, the acquisition was conducted by means of high-speed National Instruments PCI-6259, with maximum sample 1.25 MSamples/s, as shown in Figure 6.11 and Table 6.5. Piezoelectric pressure transducer position along with the high insulated transfer cable and the charge amplifier are presented in Figure 6.9.

As already mentioned, the sensor was carefully mounted to engine's cylinder head. The mounting sleeve and the sensor are presented in Figure 6.10. As it can be seen, there is significant dimensional difference between the sleeve and the sensor. KISTLER 6052B1 has a length 9 mm and diameter of 4.4 mm. Detailed technical data of piezoelectric sensor and charge amplifier ,included the coding for the switches, are presented in Table 6.3 and Table 6.4 respectively.

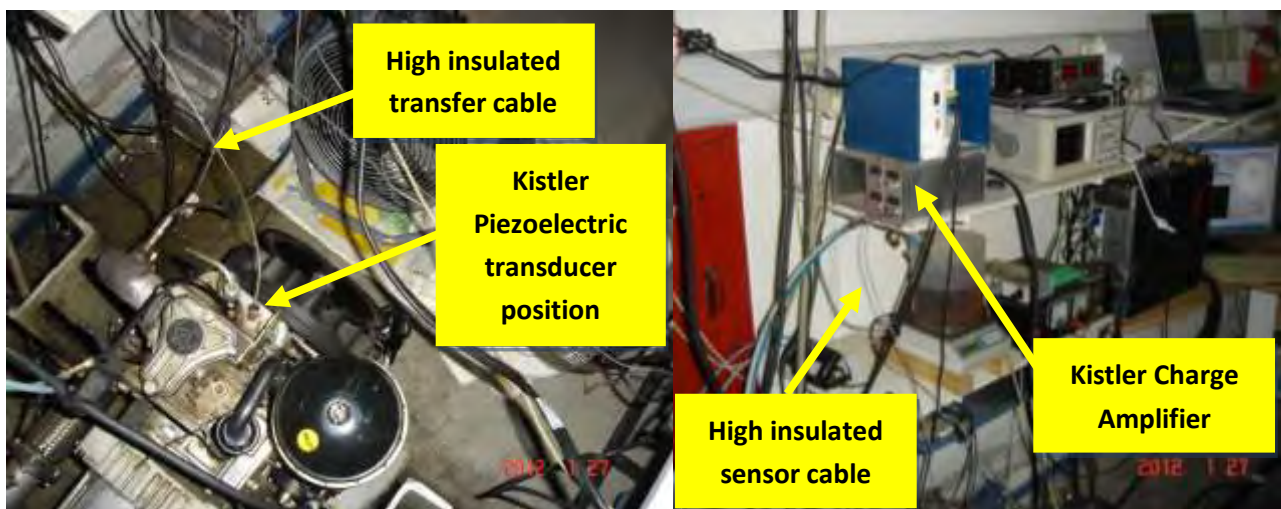


**Figure 6.9.** Experimental equipment for indicator diagrams. KISTLER piezoelectric transducer (6052B1) position on engine's cylinder head and high insulated transfer cable (1929A1) (left) along with KISTLER charge amplifier (AG5044A) position (right) are presented.



**Figure 6.10.** Mounting sleeve 6525Asp (left) and piezoelectric sensor 6052B1 (right).

**Table 6.3.** Piezoelectric sensor technical data.

Manufacturer	Kistler
Type	6052B1
Measuring range [bar]	0...250
Sensitivity [pC/bar]	-20
Natural frequency [kHz]	≈130
Linearity [%FSO]	≤ ± 0.4
Temperature range [°C]	-50...400
Sensitivity change 200 °C ± 50 °C [%] 23...350 °C [%]	<± 0.5 < ± 2
Thermal shock at 9 bar p <sub>mi</sub> [1500 1/ min] Δp (short term) [bar] Δp <sub>mi</sub> [%] Δp <sub>max</sub> [%]	≤ ± 0.5 ≤ ± 2 ≤ ± 1.5
Dimensions D [mm] L [mm]	4.4 9

**Table 6.4.** Charge amplifier technical data

Manufacturer	Kistler
Type	5044A
Number of channels	2
Measuring range (Offset jumper to NC) [pC] (Offset jumper to -8 V) [pC]	± 100...±49950 (-20...+180)...(-10,000...+90,000)
Accuracy [%]	<± 1
Sensor sensitivity [pC/M.U.]	1...99.9
Scale (in 1,2,5 stages) [M.U./V]	1...500
Drift (0...60 °C) [pC/s] (25 °C) [pC/s]	<± 0.2 <± 0.05
Reset-Long transition [pC]	<± 1
Time constant: Long [s]	>1000,000
Output voltage [V]	0...± 10
Output current [mA]	0...± 2
Output resistance [Ω]	10
Zero point error (Reset) [mV]	± 15
Frequency range (20 V <sub>pp</sub> ) [Hz]	≈ 0...>45,000
Low-pass filter [Hz]	10...20,000
“Overload” threshold [V]	≈± 10.5
Offset adjustable with jumper [V]	-8.0 ± 1 %
Max voltage between sensor GND and output/supply GND [V]	<± 50



**Figure 6.11.** PCI-6259 high speed data acquisition card.

**Table 6.5.** Main specifications of high speed multifunction M Series data acquisition card.

General	
Product name	PCI-6259
Product family	Multifunction data acquisition
DAQ product family	M Series
Measurement type	Quadrature encoder, digital, voltage, frequency
Analog Input	
Channels	32, 16
Single-ended channels	32
Differential channels	16
Resolution	16 bits
Sample Rate	1.25 MS/s
Max Voltage	10 V
Analog Output	
Channels	4
Resolution	16 bits
Max Voltage	10 V
Digital I/O	
Bidirectional channels	48
Max clock rate	10 MHz
Physical specifications	
Length	15.5 cm
Width	9.7 cm
I/O Connector	68-pin VHDCI female

### 6.2.3 Properties of fuels and blending

The fuels under investigation are pure Diesel (0% biodiesel), and two blends of 20 vol.% biodiesel in pure diesel. B0 conforms to European standard EN 590. The biodiesel employed in the measurements is a fatty acid methyl ester produced by 40% rapeseed oil, 30% soybean oil and 30% recycled cooking oils. It was supplied by ELIN biofuels SA (Volos factory) and conforms to EN-14214:2008 specifications [118]. The main specifications of the used fuels, along with the properties of B40 and pure biodiesel are shown in Table 6.6.

**Table 6.6.** Fuel properties.

Specifications / ranges	B0	B20	B40	B100
Cetane number	50	-	-	55
(A/F) <sub>st</sub>	14.5	14.10	13.69	12.48
Lower heating value [MJ/kg] (calculated)	43.3	42.18	41.06	37.7

### 6.2.4 Experimental procedure

Data acquisition and combustion analysis were carried out using in-house developed LabVIEW-based code and commercial engine simulation software respectively. Output from the analysis of consecutive engine cycles included peak engine cylinder pressure, values of indicated mean effective pressure (imep), percentage coefficient of variation of imep (% COV<sub>imep</sub>), average crank angle for ignition delay and burn duration. The COV of imep was used as criteria for combustion stability (cyclic stability).

The combustion of the examined fuels was examined at 3 engine operating points as shown in Table 6.7. The total number of recorded engine cycles for each fuel and operation point is also presented in this table.

**Table 6.7.** RF91 engine steady state operation points and total number of captured engine cycles.

Engine Speed [rpm]/Pel [kW]	Engine cycles-A		Engine cycles-B		Engine cycles-C		Engine cycles-D	
	B0	B20	B0	B20	B0	B20, B40	B0	B20,B40
2000/0.22	922	300	453	419	525	314	153	171
2600/0.83	1302	833	367	641	476	589	661	571
3250/2.51	2100	277	1568	794	2797	1005	1717	1400

## 6.3 Results and Discussion

### 6.3.1 Calculation of injection timing advance in a PLN injection system

Tat and Van Gerpen [132] proposed a model calculate injection delay in a PLN system by evaluating differences in injection timing between conventional diesel and soy methyl ester in a John Deere 4276T engine running at 2100 rpm. The model is summarized below.

Assessment of the injection timing advance related to biodiesel took into account two factors: the faster pressure wave propagation due to higher speed of sound and the faster pressure rise produced by the pump due to lower compressibility of biodiesel (high bulk modulus).

The rate of fuel pressure rise was related to the volume change produced by the injection pump plunger, the volume of compressed fluid and the fluid bulk modulus, as follows:

$$\frac{dp}{d\theta} = -BM \frac{dV}{d\theta} \frac{1}{V_f} \quad [6.1]$$

where p: fuel pressure in the injection line,  $V_f$ : volume of compressed fuel, BM: isentropic bulk modulus and  $\theta$ : crankshaft angle.

The rate of volume change produced by the injection pump plunger is given by the following equation:

$$-\frac{dV}{d\theta} = \frac{dx}{d\theta} A_p = u_\theta A_p \quad [6.2]$$

where u: plunger velocity,  $A_p$ : plunger area and the Eq.(1) takes the following form,

$$\frac{dp}{d\theta} = \frac{BM}{V_f} u_\theta A_p \quad [6.3]$$

Taking all the variables in Eq.(3) as constants the equation can be integrated to describe fuel pressure as a function of crankshaft angle:

$$p(\theta) = \frac{BM u_\theta A_p}{V_f} (\theta - \theta_0) + p_0 \quad [6.4]$$

According to Eq.(4) the crankshaft rotation required to reach the nozzle opening pressure (NOP) was:

$$\Delta\theta = \theta - \theta_0 = \frac{(NOP - p_0)}{BM u_\theta A_p} V_f \quad [6.5]$$

The results of the calculated crankshaft rotations until the nozzle opening pressure for 4 fuels, B0, B20, B40 and B100 are summarized in Table 6.8. Based on these results, it is obvious that the higher bulk modulus of biodiesel fuel leads to an injection timing advance of 0.22°, 0.42° and 1.1° for B20, B40 and B100 respectively.

**Table 6.8.** Calculated crankshaft rotation until NOP (impact of bulk modulus).

Crankshaft rotation required to reach the NOP - B0 [CA]	10.22
Crankshaft rotation required to reach the NOP - B20 [CA]	10.0
Crankshaft rotation required to reach the NOP - B40 [CA]	9.8
Crankshaft rotation required to reach the NOP - B100 [CA]	9.12

In addition, the impact of the speed of sound should be taking into account for the total calculation of the injection timing advance.

The Ruggerini RF91 engine has injection line of 0.4 m long, as shown in Figure 6.2. If the fuel supplied to the engine is at 40 °C, the speed of sound for conventional diesel and rapeseed methyl ester are 1302 m/s and 1345 m/s respectively (at atmospheric pressure). A pressure wave moving through diesel fuel in the injection line will take 0.307 ms to propagate from the pump to nozzle. This corresponds to 2.95 CA of crankshaft rotation at 1600 rpm. Detailed results for B0, B20, B40 and B100 fuels under several engine speeds from 1600 rpm to 3600 rpm are summarized in Table 6.9.

**Table 6.9.** Calculated injection timing advances (impact of speed of sound).

Engine Speed [rpm]	ms/CA	Total CA for B0 case - PtN time	Total CA for B20 case - PtN time	Total CA for B40 case - PtN time	Total CA for B100 case - PtN time
1600	0.1042	2.95	2.93	2.91	2.86
1700	0.0980	3.13	3.11	3.09	3.03
1800	0.0926	3.32	3.30	3.28	3.21
1900	0.0877	3.50	3.48	3.46	3.39
2000	0.0833	3.69	3.66	3.64	3.57
2100	0.0794	3.87	3.85	3.82	3.75
2200	0.0758	4.06	4.03	4.00	3.93
2300	0.0725	4.24	4.21	4.19	4.10
2400	0.0694	4.42	4.40	4.37	4.28
2500	0.0667	4.61	4.58	4.55	4.46
2600	0.0641	4.79	4.76	4.73	4.64
2700	0.0617	4.98	4.95	4.91	4.82
2800	0.0595	5.16	5.13	5.10	5.00
2900	0.0575	5.35	5.31	5.28	5.17
3000	0.0556	5.53	5.49	5.46	5.35
3100	0.0538	5.71	5.68	5.64	5.53
3200	0.0521	5.90	5.86	5.82	5.71
3250	0.0513	5.99	5.95	5.91	5.80
3300	0.0505	6.08	6.04	6.01	5.89
3400	0.0490	6.27	6.23	6.19	6.07
3500	0.0476	6.45	6.41	6.37	6.25
3600	0.0463	6.64	6.59	6.55	6.42

Combining the above results, we observe that the injection timing advance in the case of our 3 measured operation points is:

**B20**

$$ITA_{2000} = ITA_{\text{bulkmodulus}} + ITA_{\text{speedofsound}} = 0.22^\circ + (3.69^\circ - 3.66^\circ) = 0.25^\circ$$

$$ITA_{2600} = ITA_{\text{bulkmodulus}} + ITA_{\text{speedofsound}} = 0.22^\circ + (4.79^\circ - 4.76^\circ) = 0.25^\circ$$

$$ITA_{3250} = ITA_{\text{bulkmodulus}} + ITA_{\text{speedofsound}} = 0.22^\circ + (5.99^\circ - 5.95^\circ) = 0.26^\circ$$

**B40**

$$ITA_{2000} = ITA_{\text{bulkmodulus}} + ITA_{\text{speedofsound}} = 0.42^\circ + (3.69^\circ - 3.64^\circ) = 0.47^\circ$$

$$ITA_{2600} = ITA_{\text{bulkmodulus}} + ITA_{\text{speedofsound}} = 0.42^\circ + (4.79^\circ - 4.73^\circ) = 0.48^\circ$$

$$ITA_{3250} = ITA_{\text{bulkmodulus}} + ITA_{\text{speedofsound}} = 0.42^\circ + (5.99^\circ - 5.91^\circ) = 0.5^\circ$$

As it can be seen, the highest injection timing advance is calculated using B40 fuel under high engine speed operation point, 3250 rpm. Start of injection was earlier for 0.26° and 0.5° with B20 and B40 respectively. These observations are in accordance with the literature [4, 29]. Nevertheless, it becomes obvious that there is not significant effect of the blending ratio on the injection timing advance.

### 6.3.2 Cycle-to-cycle variation

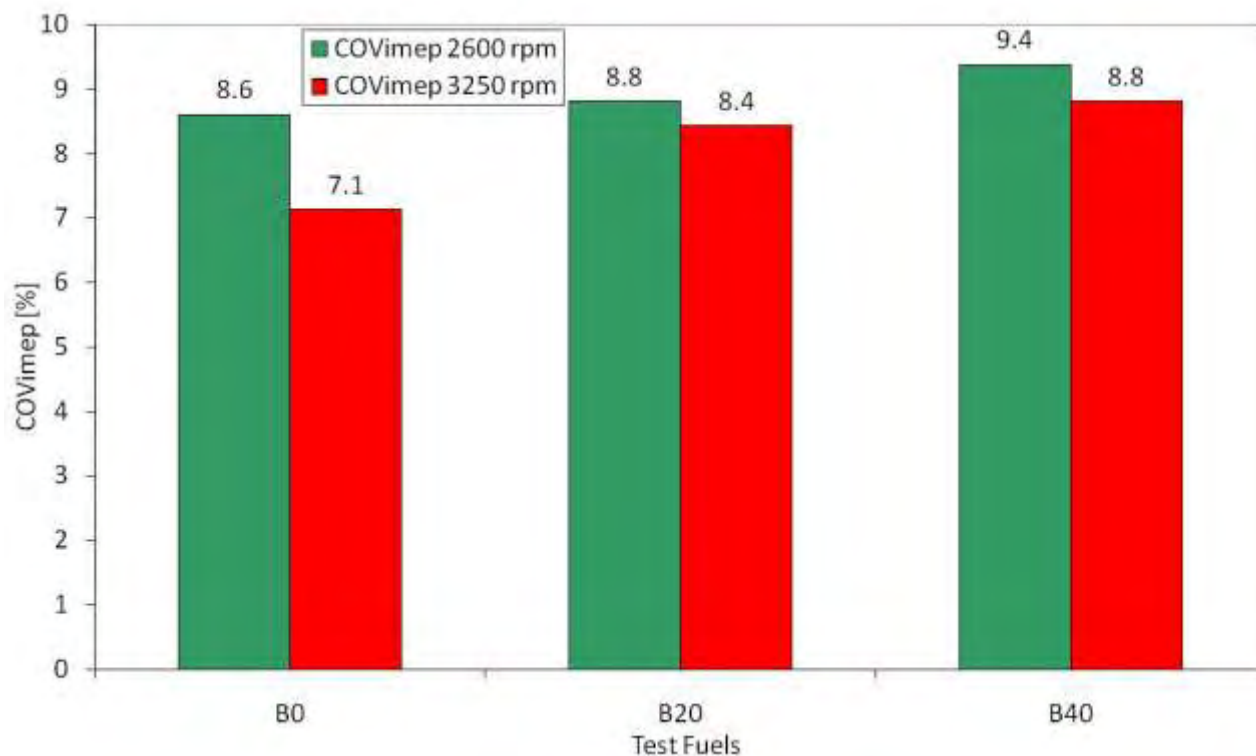


**Figure 6.12.** Differences in percentage coefficient of variation of imep for B0, B20 and B40 during two steady state operation points, 2600 rpm/12.7 Nm and 3250 rpm/16.2 Nm.

Figure 6.12 presents the measured effects of the biodiesel blending ratio on the coefficient of variance of the indicated mean effective pressure at 2600 rpm-12.7 Nm and 3250 rpm-16.2 Nm. In all the tests, the COVs were below the engine normal operation limit of 10 % [131]. The increase of the biodiesel blending ratio appears to increase the  $COV_{imep}$  from 8.6 % (B0) to 8.8 % (B20) and 9.4 % (B40). As a result, the combustion of blended fuels is less stable compared to B0, modifying the soot formation procedure and enhancing biodiesel combustion stochastic behavior. On the other hand, a reduction of COV during the transition from 2600 rpm/12.7 Nm to 3250 rpm/16.2 Nm is observed for all the fuels.

### 6.3.3 Combustion characteristics

The effect of injection timing and blending ratio of biodiesel on the combustion pressure, normalized cumulative burning rate and combustion duration in the single cylinder direct injection diesel engine was investigated. Figure 6.13 illustrates the influence of the blending ratio on various typical combustion intervals (0-90%, 10-90%, 0-10%, 0-50%, 10-75%, 0-100%). The duration of these characteristic intervals was calculated based on the processing of the indicator diagrams by means of the GT-Power software, using the provided Engine Heat Release Utility [133].

As it can be seen, there is an increase of the overall combustion duration from 45° for B0 to 46.7° for B20 blend due to higher droplet diameters which lead to slower combustion. The higher the Sauter Mean

Diameter the less easily it is for a droplet to evaporate [134]. Biodiesel atomization characteristics are clearly presented in Chapter 7. On the other hand, burn duration 0-10 % and 0-50 % are lower using B20, leading to faster combustion during combustion premixed phase until crank angle of 50 % burn point.

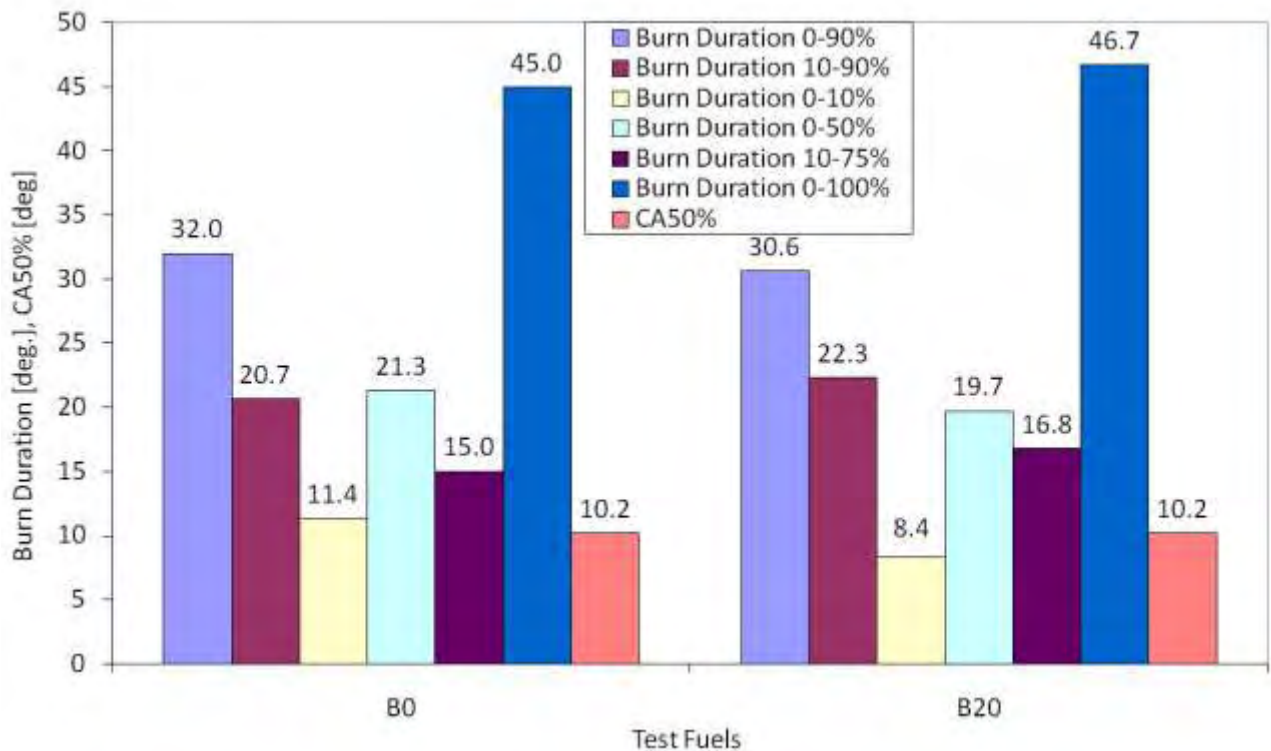


**Figure 6.13.** Differences in combustion characteristics (burn duration and crank angle of 50% burn point) for B0 and B20 during the steady state operation point, 3250 rpm/16.2 Nm.

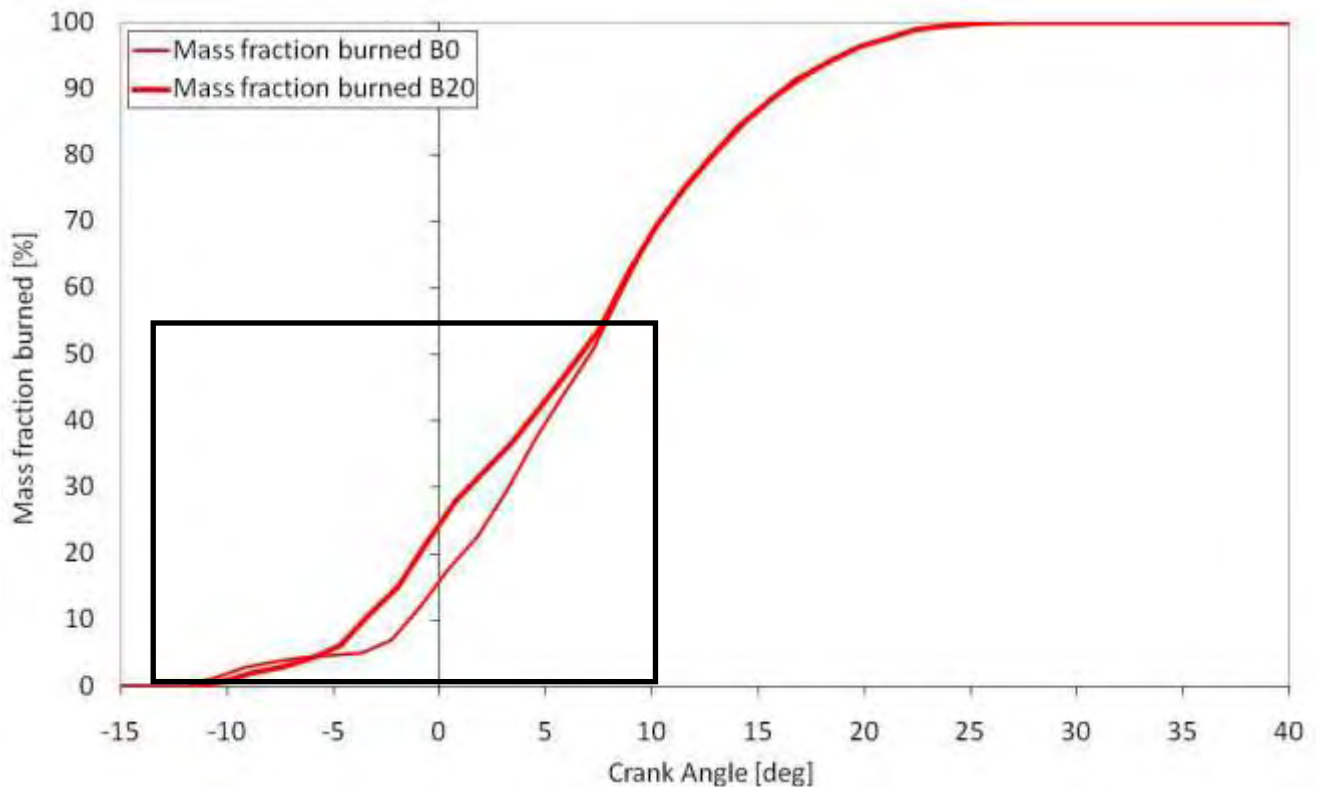


**Figure 6.14.** Comparison of mass fraction burned versus crank angle curve for B0 and B20 blend during the operation point, 2600 rpm/12.7 Nm.



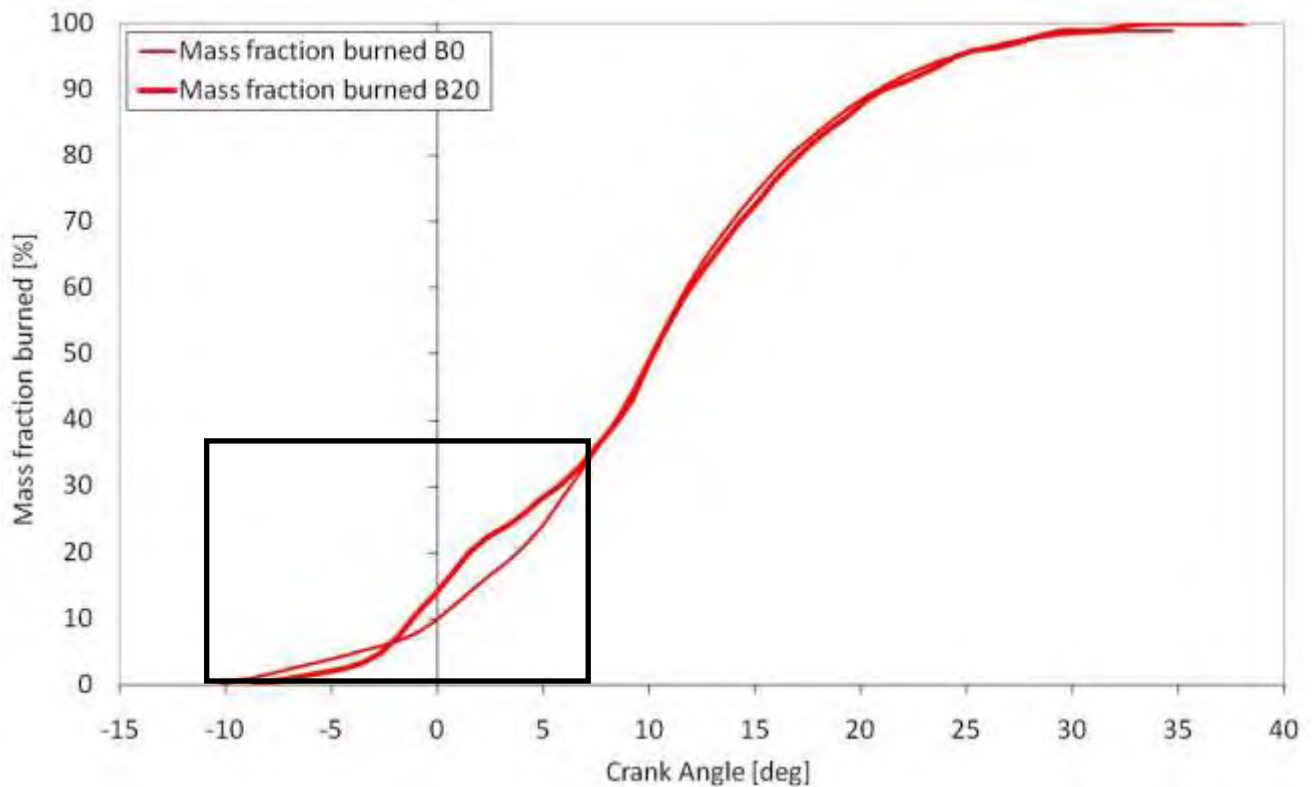


**Figure 6.15.** Comparison of mass fraction burned versus crank angle curve for B0 and B20 blend during the filter loading operation point 3250 rpm/16.2 Nm.

More details on the calculated evolution of combustion are presented in the form of cumulative fuel burning for 2600 rpm/12.7 Nm and 3250 rpm/ 16.2 Nm in Figure 6.14 and Figure 6.15 respectively. The increase of the FAME percentage in the fuel blend appears to reduce the ignition delay and shift the start of combustion to an earlier stage from  $10.3^\circ$  (B0) to  $8.7^\circ$  (B20). According to these figures, premixed combustion burn rate is higher for B20 due to the contribution and the amount of oxygen atoms, enhancing the exothermic reactions.

### 6.3.4 Soot emissions

The collected particulate samples for B0 and B20 are presented in Figure 6.16. The oxygen content of the biodiesel may contribute to improved fuel oxidation even in locally rich fuel combustion zones, thus resulting in the reduction of smoke. The increased oxygen concentration in the soot-forming region at the centre line of the fuel jet and the reduced residence time of fuel element in the soot-forming jet may enhance the soot reduction. The increased availability of oxygen from the combustion of biodiesel in the rich premixed reaction zones results in lower production of soot precursor species and hence in reduced rates of the soot producing reactions. The amount of soot precursor species available to produce soot strongly depends on the amount of oxygen available in the mixture. When sufficient oxygen is available, soot precursors species react with molecular oxygen or oxygen-containing radicals and eventually rather than aromatics and soot [135]. Differences in the engine soot emissions level for B20 and B20 comparing the collected mass of 3 Pallflex filters after 15 min operation on diesel particulate filter's loading point, 3250 rpm/16.2 Nm, are summarized in Table 6.10.

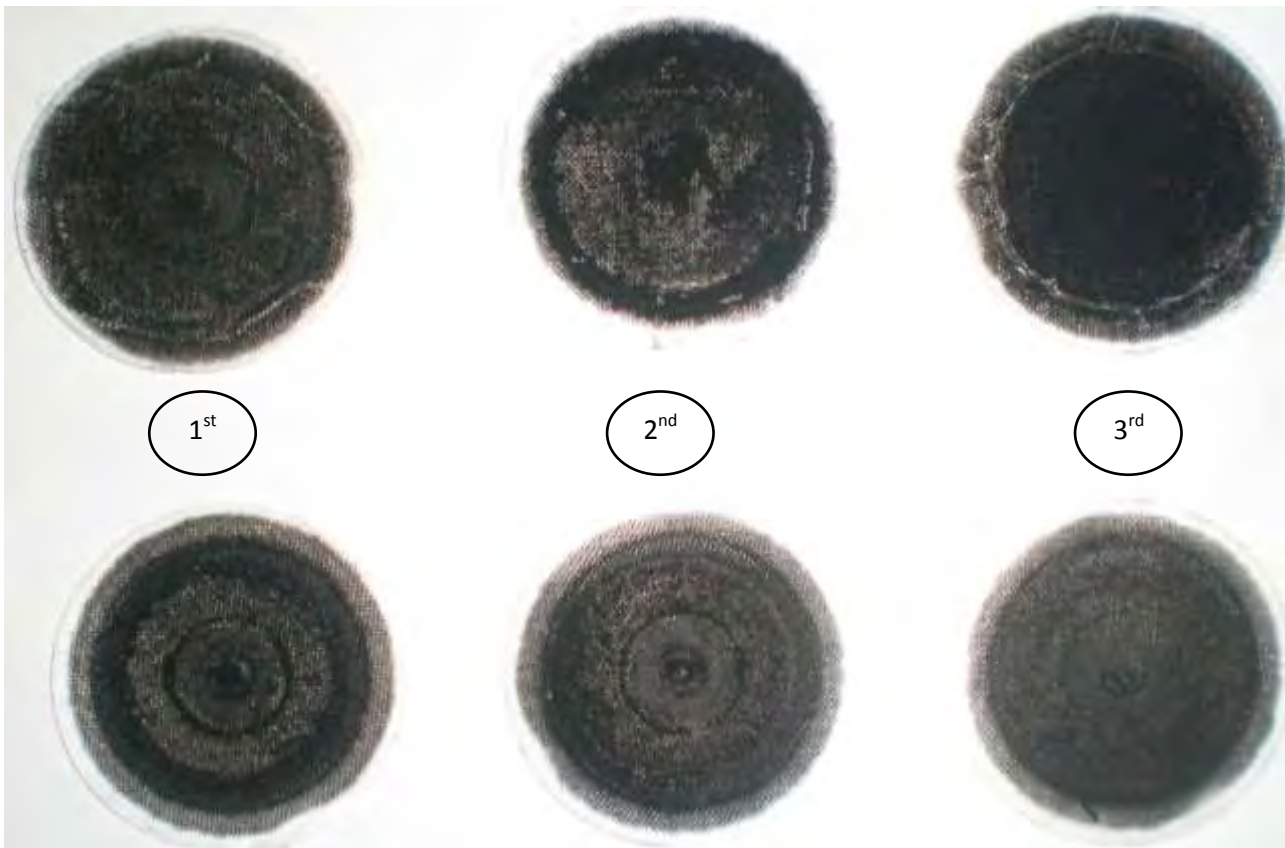


**Figure 6.16.** Comparison of particulate samples, 3 for each fuel, undiluted exhaust gas upstream filter passing through a Pallflex 47mm filter, collected during the filter loading point, 3250rpm/16.2 Nm. Up: conventional diesel (B0), Down: B20 biodiesel blend.

**Table 6.10.** Differences in the engine soot emissions level for B20 and B20 comparing the collected mass of 3 Pallflex filters after 15 min operation on diesel particulate filter's loading point, 3250 rpm/16.2 Nm.

Fuel	B0			B20		
Filter number	1st	2nd	3rd	1st	2nd	3rd
A/F	33.98	31.96	31.50	32.62	30.6	30.14
Clean filter mass [g]	0.090	0.092	0.091	0.092	0.093	0.092
Loaded filter [g]	0.101	0.103	0.103	0.098	0.099	0.100
Soot Loading mass [g]	0.011	0.011	0.012	0.006	0.006	0.008

Although the engine particulate emissions were not measured based on a legislated procedure with diluted exhaust gas, it is interesting to see the results of simple tests with undiluted exhaust gas, and subsequent weighing of the samples after conditioning at 48h at 25 °C, 50% RH. The lower blackening of the filters in the case of B20 is apparent together. These observations, which are in accordance with the literature [136-140] can be mainly explained by the oxygen content of biodiesel molecule, which enables more complete combustion and promotes the oxidation of the already-formed soot. In addition, the lower stoichiometric need for air in the case of biodiesel blend combustion reduces the probability of fuel-rich regions in the non-uniform fuel-air blend. Moreover, the advanced combustion in the case of B20, already discussed in Section 6.3.3, enlarges the residence time of soot particles in a high-temperature atmosphere, which in the presence of oxygen promotes further oxidation.

### 6.3.5 Energy balance

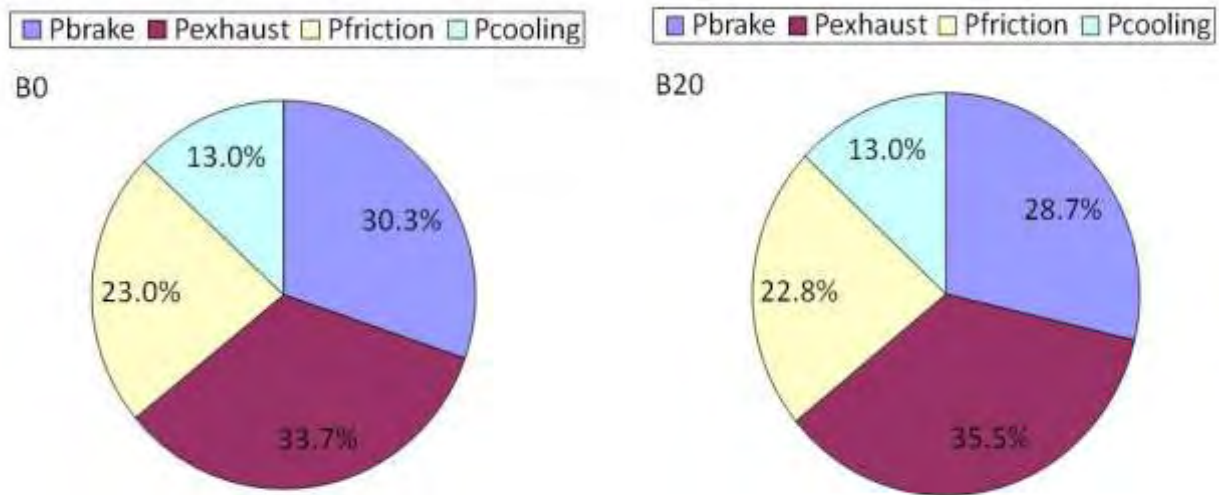


**Figure 6.17.** Differences in energy balance for B0 and B20 during the steady state operation point, 3250 rpm/16.2 Nm. Decreased engine brake power along with increased exhaust gas losses are presented in the case of B20 blended fuel.

Energy balance at a typical engine operation point was calculated, based on the measurement of engine torque and speed, friction losses, indicated mean effective pressure, exhaust enthalpy and check with estimation of heat losses to cooling air (by means of infrared thermography). The increased fuel consumption with the increase of the biodiesel content of the fuel blend is mainly due to the lower calorific value of the biodiesel and results in an increase of bsfc, from 274.3 g/kWh (B0) to 297.7 g/kWh (B20). In addition, there is a decrease of 1.6 % of engine thermal efficiency in the case of B20, from 30.3 % (B0) to 28.7 % (B20) along with an increase of exhaust gas losses from 33.7 % (B0) to 35.5 % (B20). Friction and cooling losses were not affected from the combustion of the B20 blend.

Figure 6.18, Figure 6.19 and Figure 6.20 present infrared images of engine external surfaces under steady state operation conditions, 2600 rpm/ 12.7 Nm, using pure diesel as fuel.

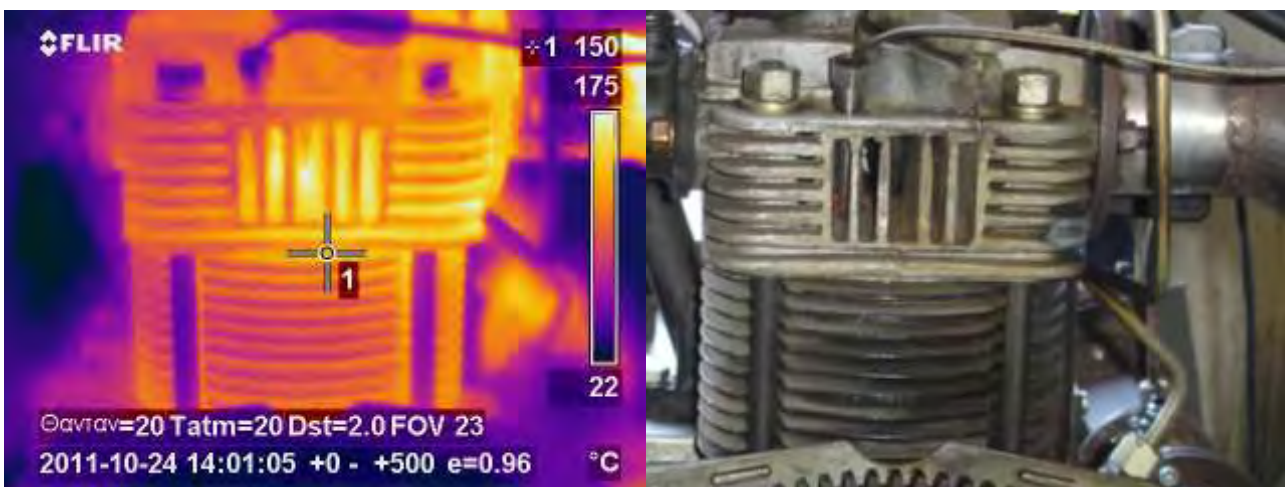


**Figure 6.18.** Infrared (left) and digital (right) image of engine's cylinder head and block under steady state operation conditions, 2600 rpm/12.7 Nm, using B0 fuel.

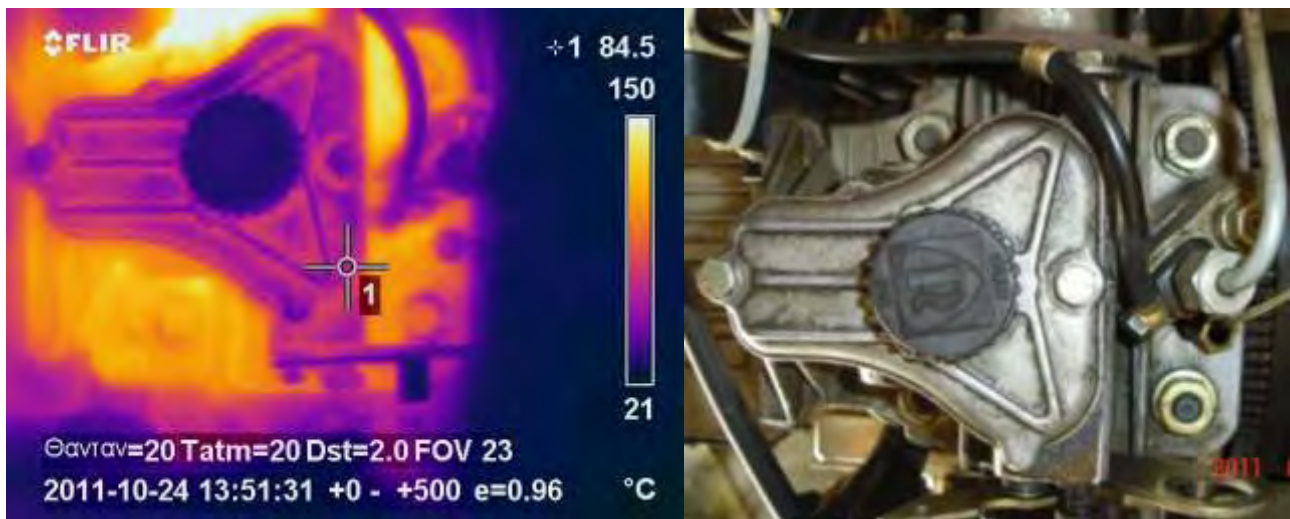


**Figure 6.19.** Infrared (left) and digital (right) image of engine's cylinder head under steady state operation conditions, 2600 rpm/12.7 Nm, using B0 fuel.

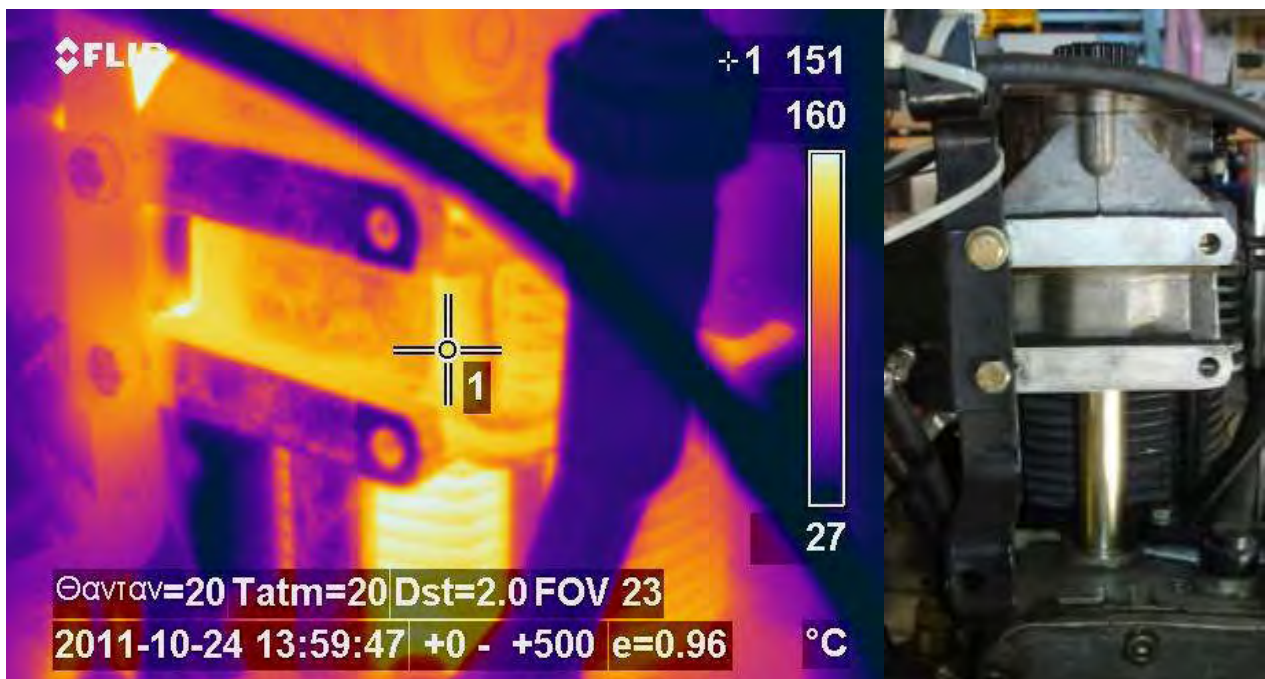


**Figure 6.20.** Infrared (left) and digital (right) back side view of engine's cylinder head and block under steady state operation conditions, 2600 rpm/12.7 Nm, using B0 fuel.

As already reported the engine cooling was not calculated using appropriate infrared images but estimated due to the complex calculation procedure.

## 6.4 Conclusions

The combustion of two biodiesel blends, B20 and B40, was investigated and the main findings are summarized below.

- The combustion of B20 and B40 in the unmodified engine with pump-line-nozzle injection system resulted in advance combustion compared to B0, as indicated by the presented mass fraction burned curves. The ignition delay was reduced while the initial uncontrolled premixed combustion phase was higher.

- The advanced combustion resulted in the reduction of smoke. The increased amount of oxygen in the biodiesel molecule and hence in the locally fuel-rich combustion zones is believed to be an additional reason for the reduced smoke.
- The increase of the fuel consumption is mainly due to the lower calorific value of biodiesel compared to diesel.
- Significant decrease of engine thermal efficiency along with an increase of the exhaust gas losses was reported in the case of B20 fuel.
- Total combustion duration of B20 blend was longer due to higher injected fuel droplet diameters which lead to slower combustion.
- The increase of the biodiesel blending ratio appears to increase the  $COV_{imep}$  from 8.6 % (B0) to 8.8 % (B20) and 9.4 % (B40).

## 7. Investigation of the effect of biodiesel blends on the performance of a fuel additive-assisted diesel filter regenerations system<sup>§</sup>

In this chapter, the results of characteristic full-scale regeneration tests are presented with a unit SiC filter. Two sets of transient regeneration experiments, one for each fuel blend used, with high level of exhaust gas flow rate (normalized per filter volume) and markedly different levels of soot loading were performed. The test fuels were conventional diesel (denoted as B0) and B20 biodiesel blend. The effect of the biodiesel on the filter regeneration was further investigated by means of infrared thermography. The main objective is to investigate the complex ignition and propagation phenomena involved in the process of catalytic regeneration in the case of biodiesel blend and their effects on the temperature distribution across the filter channels and the evolution of the regeneration at the central and peripheral parts of the filter.

### 7.1 Experimental

The regeneration tests were performed on a SiC, 200 cpsi filter fitted to the exhaust system of the 0.477 liter – displacement, naturally aspirated DI diesel engine. The filter is fitted about 600 mm downstream the exhaust manifold. The engine is tested on one small test bench (see previous chapter). DPX-9 fuel additive was available from previous experiments and was employed also in this case. A dosimetry of 25 ppm Ce in fuel was first tested. However, due to the relatively low exhaust temperatures at filter inlet, and the lack of active regeneration means (e.g. post-injection etc), it was considered necessary to increase to 50 ppm, which was kept constant in all the experiments, both with B0 and B20. The engine and diesel filter specifications are presented in Table 7.1.

Figure 7.4 presents the experimental layout for the filter loading and regeneration experiments. A novel setup and layout was developed to study the evolution of regeneration with the use of infrared thermography. Figure 7.5 shows the infrared regeneration acquisition setup, which consists of filter's lateral face (Figure 7.1 left) and IR camera. The distance between the lateral face of the filter and camera's lens was set at 500 mm. Infrared regeneration video acquisition and frame by frame analysis were conducted by means of ThermaCAM Researcher Pro 2.8 software [141]. The main specifications of the infrared camera are summarized in Table 7.2.

**Table 7.1.** Engine technical data and diesel filter specifications.

Engine manufacturer	Ruggerini
Engine model	RF91
Engine type	DI 4 stroke naturally aspirated diesel engine
Number of cylinders	1
Bore	90 mm
Stroke	75 mm
Rated power	8.1 kW, 3600 rpm
Rated torque	25 Nm, 2500 rpm
Compression ratio	18.5:1

<sup>§</sup> Part of this chapter was submitted for publication to the International Journal of Engine Research: Investigation of the effect of biodiesel blends on the performance of a fuel additive-assisted diesel filter regenerations system.

Diesel filter manufacturer	Ibiden
Filter type	SiC (19/200) cpsi (cells per square inch)
Filter side width x side length x length	34 mm x 34 mm x 150 mm
Cell pitch	1.89 mm
Filter wall thickness	0.4 mm

Infrared video acquisition process was initiated at the start of regeneration. Start and end points of regeneration were set according to the engine load step from 16.2 Nm to 22.2 Nm respectively. Video duration varies from 3 to 6 min and is in accordance with regeneration duration.

Temperatures were measured simultaneously at the exhaust pipe 80 mm downstream the exhaust manifold exit, at the inlet of the filter and inside the filter at 2 positions inserted at 35 mm deep from the back of the filter (Figure 7.2). Characteristic photos of the SiC filter and the positions of the inside thermocouples are presented in Figure 7.1. The O<sub>2</sub> concentration was calculated by the A/F ratio obtained from the UEGO sensor installed after cylinder outlet. The loading level of the filter was measured using a JUMO 0-500 mbar differential pressure transducer. A Kern electronic balance with a weighting range of 0.1 to 4000 g was used for the monitoring of engine fuel consumption. The previous signals were collected and recorded by means of National Instruments hardware and software.

Inserted thermocouples were used to measure the local temperature rise during the PM combustion [142, 143]. They revealed that in some cases a rapid local temperature rise of several hundreds °C occurred. Unfortunately, these local measurements did not provide information on the dynamic features of the combustion and the spatial temperature distribution in the channel.

The main advantage of such measurements is that they determine the temperature within an actual DPF. However, these experiments cannot determine the mode of the combustion or the evolution and motion of a temperature peak. Moreover, they may not be able to distinguish between a moving high temperature emanating from a single ignition point or that emanating from one of several ignition points [144, 145].

The main advantage of IR temperature measurements is that provide direct information on the combustion mode on the dynamic features of the high temperature zones generated at various ignition sites. A disadvantage of the IR measurements is that the need to view the surface by the camera leads to heat losses that are higher than those encountered in an actual insulated DPF. Visual observations enable temperatures of the spatio-temporal temperature in the DPF. Thus, while IR measurements provide useful information about all the possible dynamic features of the combustion they cannot accurately bound the conditions under which they occur.

Visual measurements were conducted by Herz and Sinkevitch [146], McCabe and Sinkevitch [147], Hanamura et al. [148], An et al. [149] and infrared measurements by Gallant [150]. Detailed infrared analysis of the spatiotemporal temperature on a planar DPF, not full scale filter analysis like our case, under sudden changes in soot feed conditions are presented by Martirosyan [144].

Their experimental setup enabled measurements of the spatiotemporal temperature during the combustion of PM on one layer planar DPF (cut from commercial Cordierite DPF). They found that the soot combustion may occur in three different modes, depending on the number of ignition points (hot spots) and the number of ignition points increases as the PM loading is decreased.



**Figure 7.1.** SiC filter view, monitored filter's lateral surface.



**Figure 7.2.** Thermocouples positions at the selected filter exit channels.

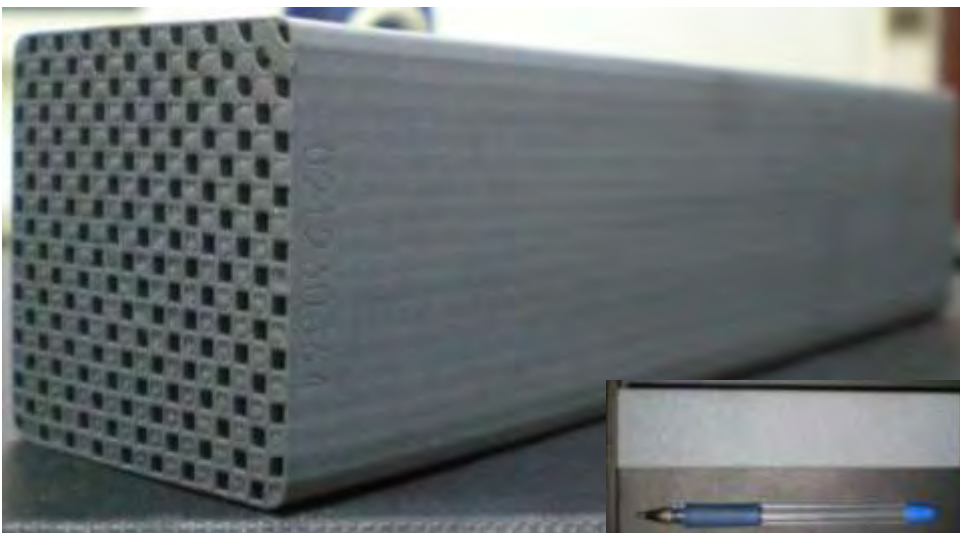


**Figure 7.3.** SiC 200 cpsi filter single module. Length: 150 mm, Side width: 34 mm and Side length: 34 mm.

Closer view of the filter in order to better understand its dimensions is presented in Figure 7.3. Our unit filter consists of 324 (18 x 18) channels. The main specifications of the filter are shown in Table 7.1.



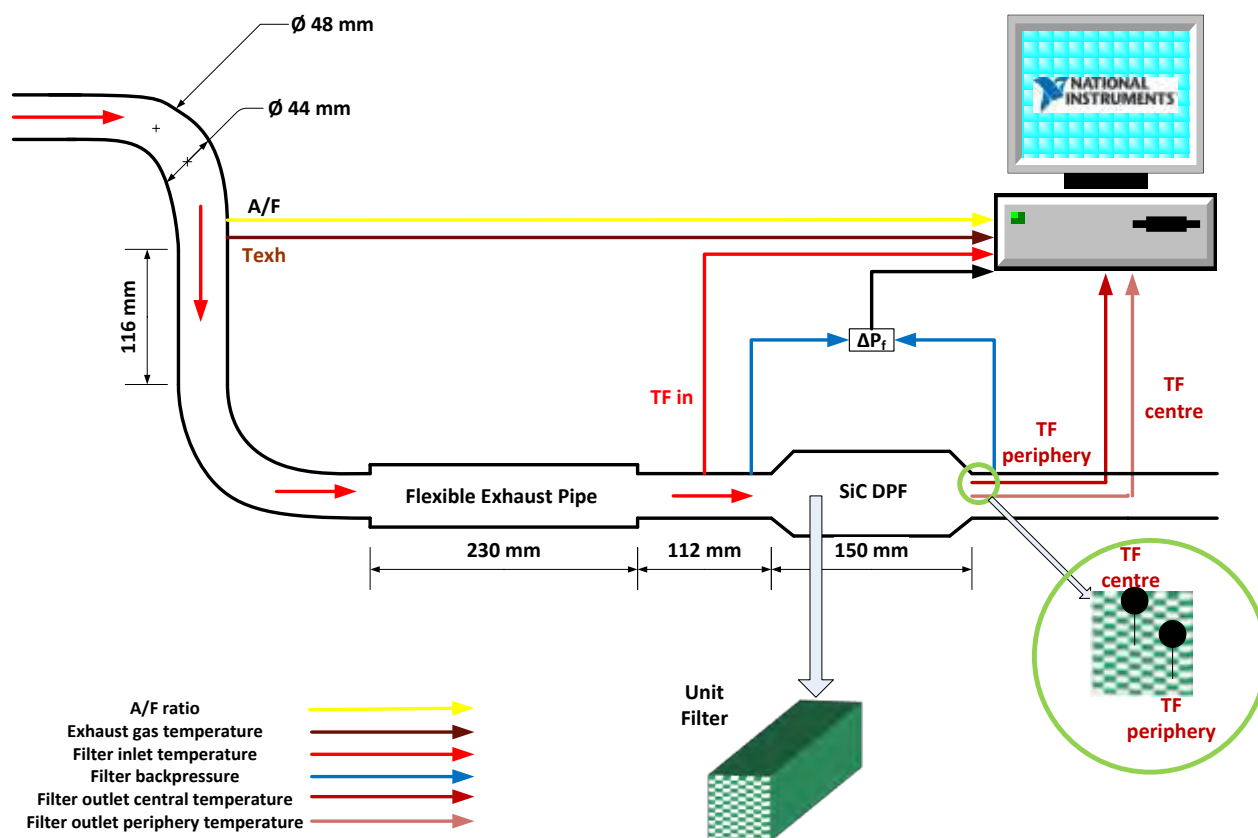


**Figure 7.4.** Experimental layout. Exhaust line instrumentation is shown along with the main diesel filter measurements and data acquisition system.

**Table 7.2.** ThermoCAM S45 main specifications.

Field of view/min focus distance	24°x18°/0.3 m (with 35 mm lens)
Thermal sensitivity	0.08 °C at 30 °C
Image frequency	50/60 Hz non-interlaced
Detector type	Focal Plane Array (FPA), uncooled microbolometer 320x240 pixels
Spectral range	7.5 to 13 μm
Temperature range	-40 °C to + 1500 °C
Accuracy	+/-2 °C, +/-2% of reading
Emissivity correction	Variable from 0.1 to 1.0 or select from listings in pre-defined materials list
Reflected ambient temperature correction	Automatic, based on input of optics/windows transmission and temperature
Voice annotation of images	30 s of digital voice "clip" stored together with the image
Image file formats	Standard JPEG
Operating temperature range	-15 °C to +50 °C
Shock	Operational, 25 G
Vibration	Operational, 2 G

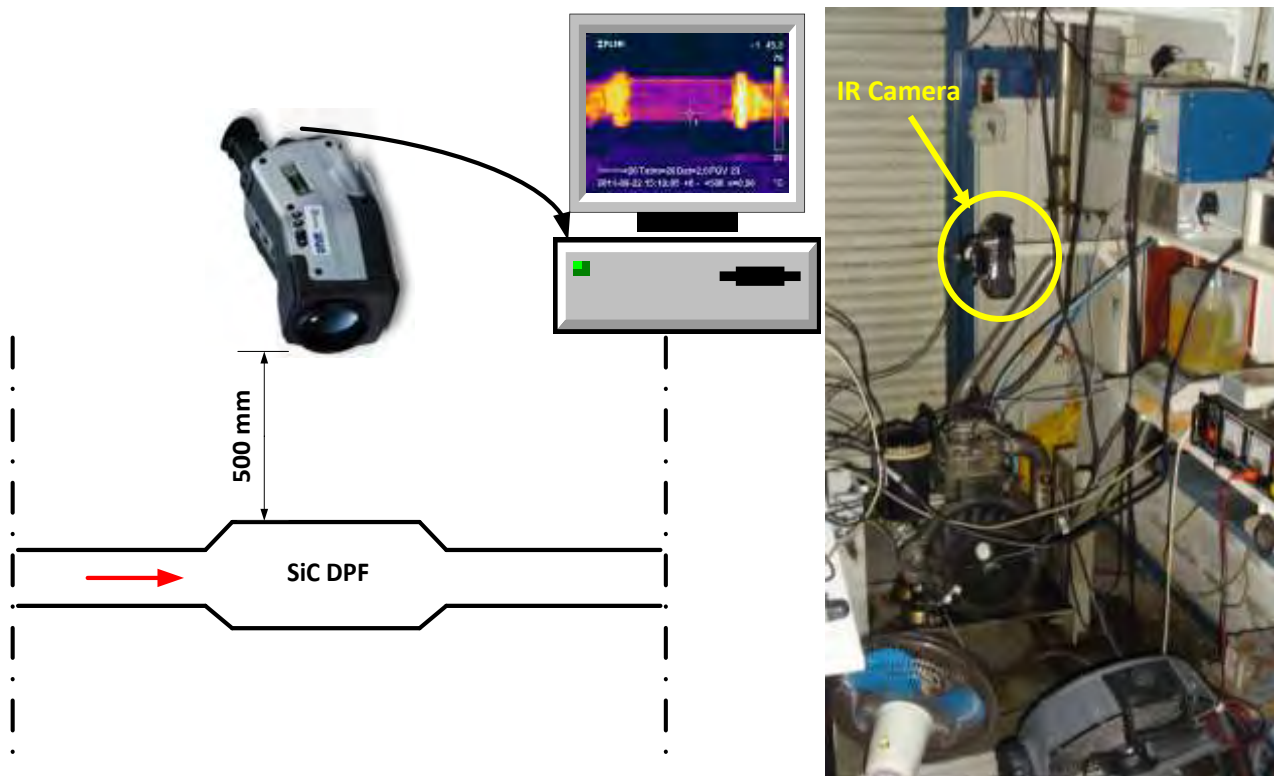


**Figure 7.5.** Experimental layout of infrared regeneration video acquisition. IR camera (ThermaCAM S45) was set at 500 mm above filter's lateral face (left). Experimental setup and ThermaCAM S45 position during the experiments (right).

### 7.1.1 Filter loading test protocol

First a mapping process was performed to assess the engine exhaust gas temperature, central channel filter temperature and A/F ratio in the low, medium and high load engine operating range. This investigation was necessary in order to find the most appropriate operation point for the filter loading tests. The final choice was made by taking into account wall filter temperature and filter backpressure increase rate. The last part of the assessment cycle is presented in Figure 7.6 and contains 7 operation points which are summarized in Table 7.3.

**Table 7.3.** Main characteristics of assessment cycle operation points.

Operation point	Engine Speed [rpm]	Engine Torque [Nm]	TF centre [°C]	Air to Fuel ratio [A/F]	Backpressure increase rate [mbar/min]
1	1900	11.9	110	60	-
2	1900	12.2	125	59	-
3	2400	10.7	165	56	-
4	2400	14.1	193	52	-
5	2700	22.7	310	39	1.4
6	3000	19.7	296	42	1.5
7	3250	16.2	375	35	2.8

It is obvious that the last operation point, 3250 rpm/16.2 Nm was selected to be the filter loading operation point. It should be mentioned that this point was also used in the case of B20 blend.

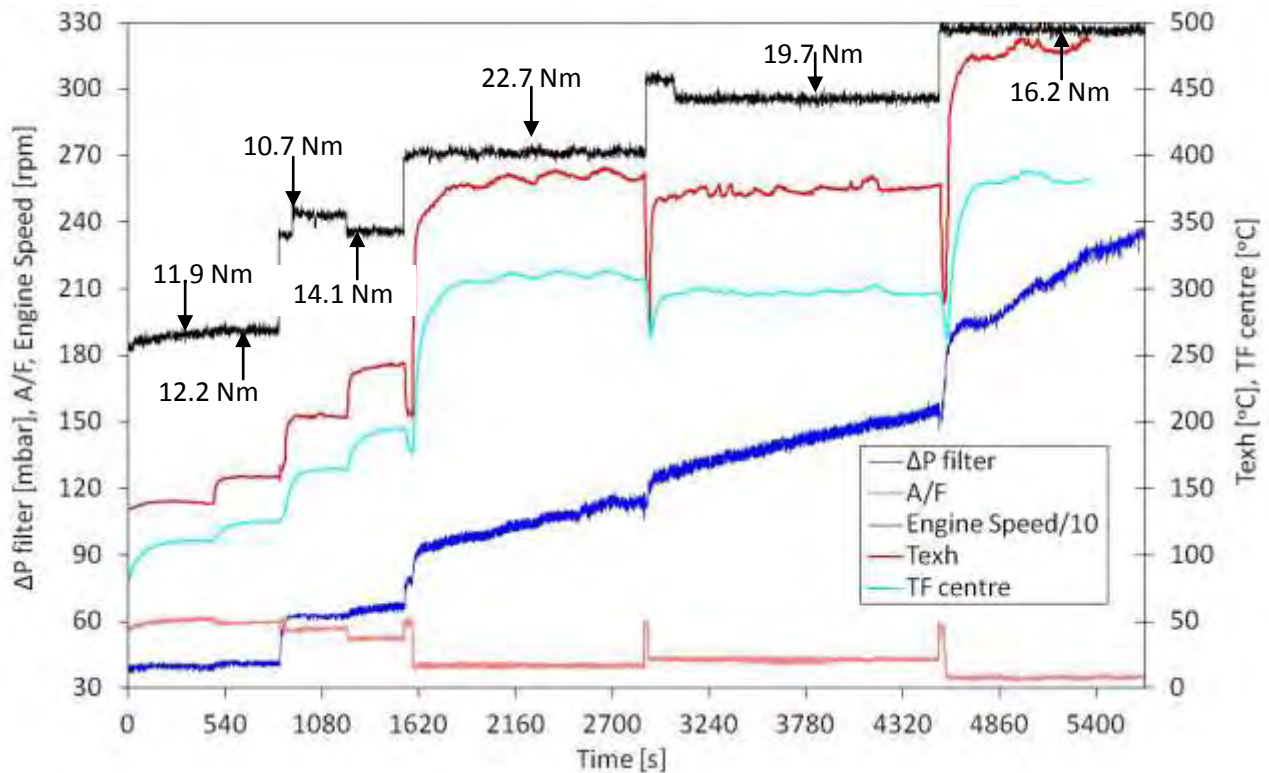


**Figure 7.6.** Last part of the assessment cycle using B0 without fuel additive as fuel. Engine speed, engine torque, A/F, exhaust gas temperature at cylinder's outlet, filter central channel wall temperature and filter backpressure are presented. The test consists of 7 operation points ranging from 1900 rpm/11.9 Nm to 3250 rpm/16.2 Nm. Filter backpressure increase rate varies from 1.36 mbar/min (30 mbar in 22 min) at the 2700 rpm/22.7 Nm operation point (A/F=45), to 2.78 mbar/min (50 mbar in 18 min) during the last operation point, 3250 rpm/16.2 Nm, with A/F = 35.

The filter loading test protocol is shown in Figure 7.7 and consists of 3 operation points. The engine operates for 450 s at 2000 rpm/11.9 Nm in order to complete the engine warm up procedure and then for another 200 s at 2600 rpm/ 12.7 Nm. After that, the engine accelerates to 3250 rpm/16.2 Nm and remains there until inside wall filter temperatures reach the value of 370 °C. During the loading period, the central wall filter temperature was increased from 120 °C to 370 °C and the maximum reported filter backpressure was 235 mbar.

Comparison of the two monitored filter wall temperatures (center and periphery) shows that the periphery was systematically colder than the center by about 5 °C. The same difference was also reported in the case of B20 biodiesel blend. Of course, the observed temperature differences could be suppressed somewhat by an improved insulation of the filter. Because of this temperature gradient, one would expect the VOF content to be a little higher at the periphery.

It should be noted that the filter wall temperature is the critical parameter for the initiation of a stochastic regeneration since it is the main factor affecting the adsorption-desorption phenomena that determine the filter soot VOF content. If the filter wall temperature exceeds 380 °C - 420 °C, most VOF is vaporized and only dry soot remains accumulated on the filter wall. On the other hand, prolonged operation of a heavily loaded filter with dry soot under low load and speed conditions can lead to re-adsorption of heavy hydrocarbons emitted in the particulate layer, thus increasing its VOF content [151].

Based on previous results [75], one could estimate that under these conditions the filter is loaded with soot at a low – to- medium VOF content, gradually enhancing its stochastic behavior during regeneration.

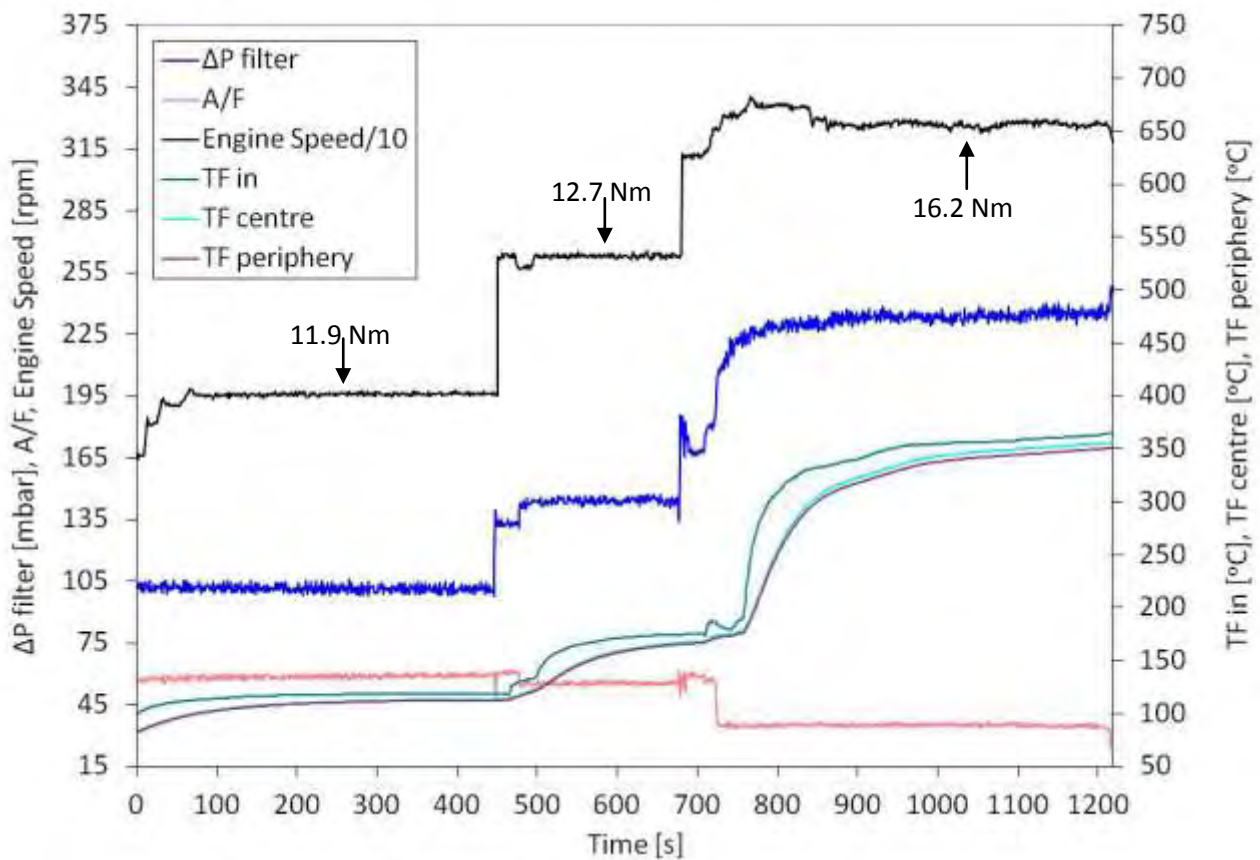


**Figure 7.7.** The loading cycle applied consists of 3 consecutive operation points with decreasing VOF contents, from medium to low. Measured temperatures near filter channels' exit, filter inlet, A/F, engine speed and engine torque and filter backpressure during loading period using B0-50 ppm fuel are presented.

### 7.1.2 Transient regeneration experiments

In this section, we present and discuss typical regeneration experiments that were carried out in order to better understand the engine and filter behavior with the use of the B20 blend. Experiments were extended also to B40 blend however the results were not so clear because of the fact that the filter was quickly attaining equilibrium temperature with even small increases of filter loading.

Typical regeneration using B40-50 ppm Ce doped blend is presented in Figure 7.8. The most marked observation is the slow soot oxidation rate with slow temperature increase inside filter exit channels. This behavior can be explained by the higher soot VOF content than that of B0 and B20.

Four regeneration experiments are selected for presentation with B0 fuel, along with 7 regeneration experiments at comparable conditions with the B20 fuel. The experiments and their main characteristics, like fuel mass consumed during loading and temperatures at filter inlet and inside filter exit (central and peripheral channel) are summarized in Table 7.4. As it can be seen, filter wall temperatures during loading period was kept under the VOF oxidation temperature range of 380 °C – 420 °C.

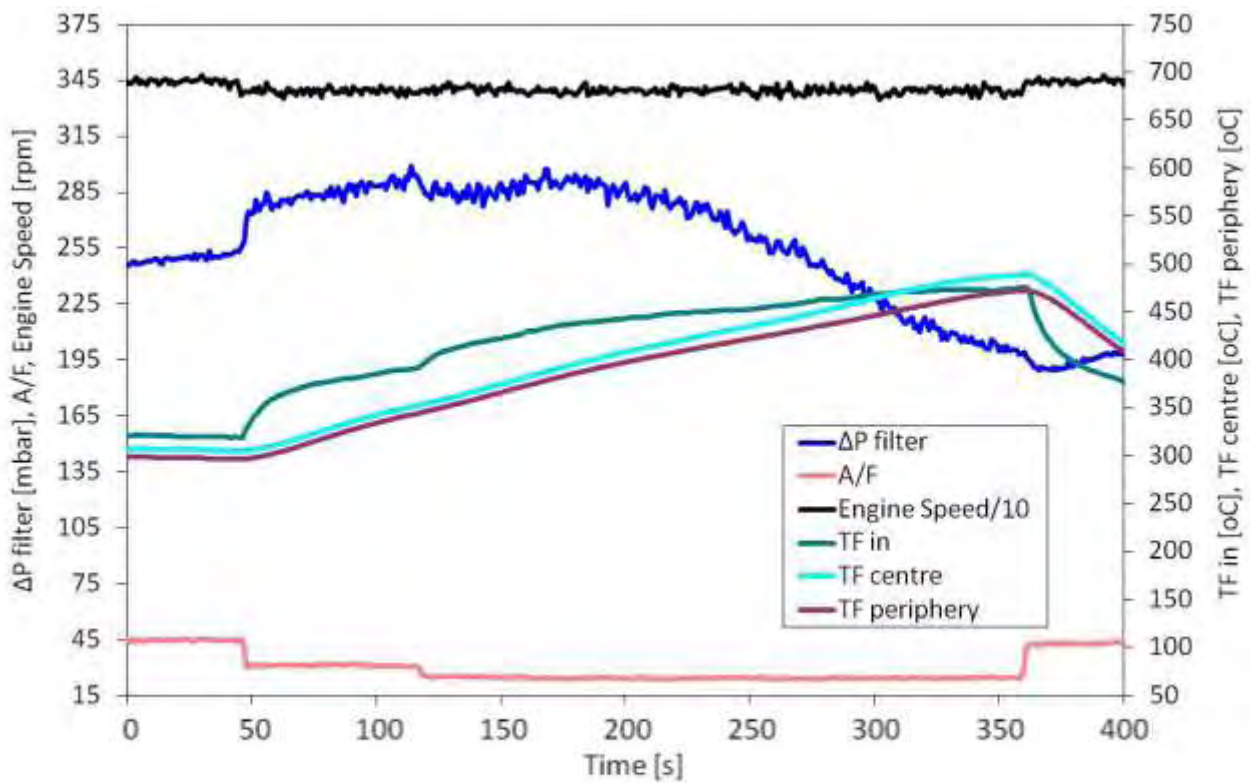


**Figure 7.8.** High flow rate regeneration scenario (exhaust mfr = 16 g/s). Measured temperatures at filter inlet, at filter channels' exit and filter backpressure are presented during a high exhaust mass flow rate regeneration performed at 3450 rpm/21.2 Nm for a highly loaded filter (1.87 kg consumed fuel mass at 3450 rpm/15.2 Nm loading operation point) with B40-50 ppm Ce doped fuel.

**Table 7.4.** Experimental protocol of the catalytic regeneration experiments.

a/a	Fuel mass consumed during loading [kg]	TF in [°C]	TF centre [°C]	TF periphery [°C]
B0-01	1.43	367	345	341
B0-02	1.38	369	360	355
B0-03	1.3	382	368	362
B0-04	1.94	366	353	348
B20-01	1.57	360	330	326
B20-02	1.42	355	332	329
B20-03	1.26	370	351	347
B20-04	1.08	372	359	355
B20-05	0.99	358	331	326
B20-06	0.76	355	331	325
B20-07	0.67	416	406	398

According to this scenario, the engine is stabilized at 3250 rpm, medium load, 16.2 Nm for the first loading phase, and remains there for about 20 minutes. This period is sufficient to load the filter to about 3 times the backpressure of the clean filter. The filter temperature levels prevailing during this period are shown at the left side of Figure 7.10 along with the exhaust temperatures at filter inlet.

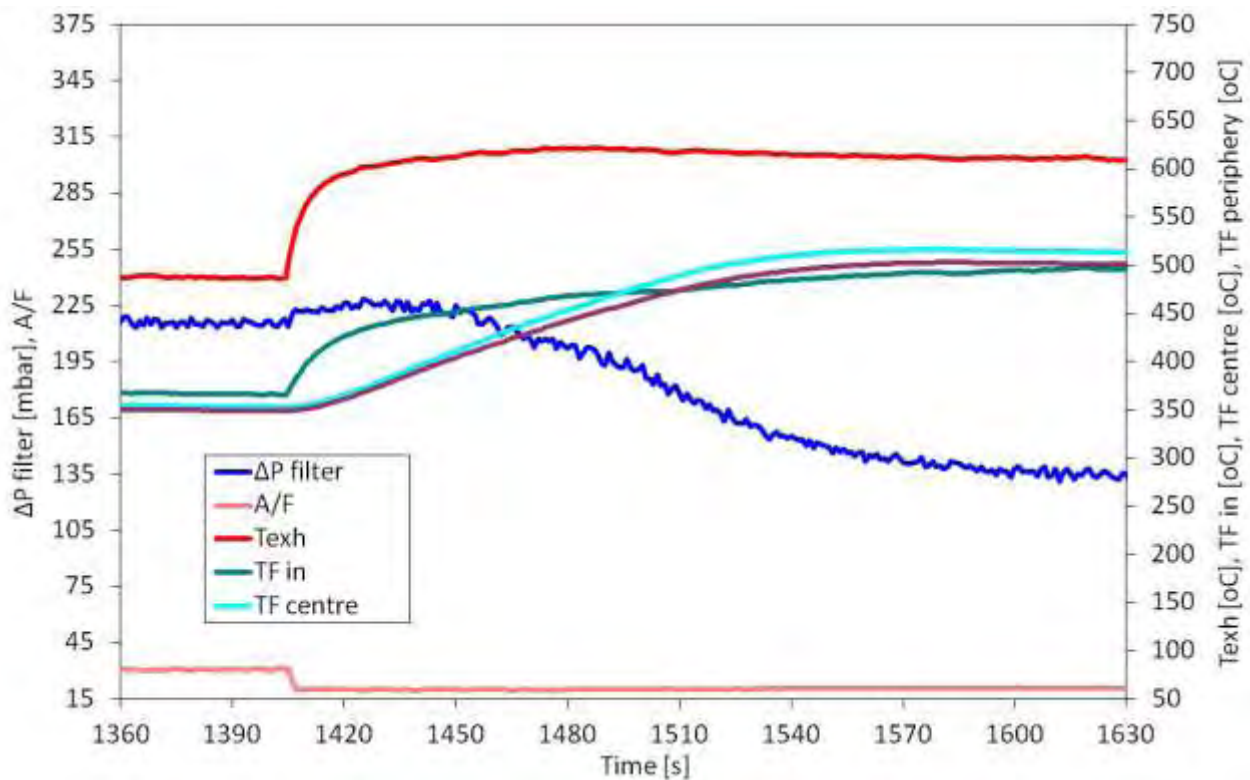


**Figure 7.9.** Typical first loading phase (B0-04 regeneration high flow rate regeneration scenario (exhaust mfr = 15 g/s). Engine operating conditions, filter backpressure, A/F ratio, exhaust gas temperature at exhaust manifold and temperatures at filter inlet and exit are presented during the transition from 3250 rpm/16.2 Nm to 3250 rpm/22.2 Nm using B0-50ppm Ce doped fuel.

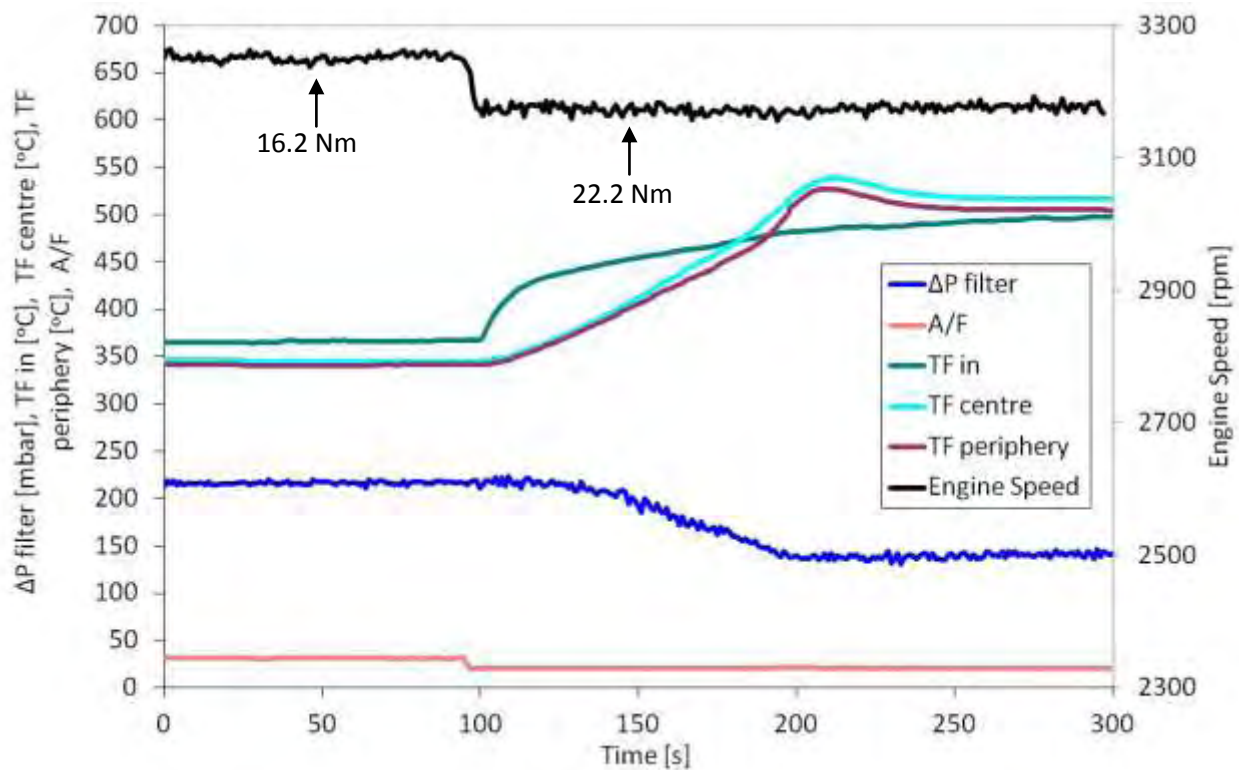


**Figure 7.10.** End of second loading phase followed by regeneration (B0-01 regeneration, high flowrate scenario (exhaust mfr = 15 g/s)). Engine operating conditions, filter backpressure, A/F ratio and temperatures at inlet and exit of the filter are presented during the load step from 3250 rpm/16.2 Nm to 3250 rpm/22.2 Nm using B0-50ppm Ce doped fuel.

A regeneration scenario follows this second loading phase. The onset of regeneration is induced by increasing the load to 22.2 Nm. This results in an increase of exhaust temperature at filter inlet to about 500 °C or even higher (right side of Figure 7.10) and the subsequent soot ignition and regeneration that is clearly visible at the middle-to-right side of Figure 7.10. There exist some remarks that pertain to all loading and regeneration experiments. The regeneration scenario typically consisted of a first, long-duration (three minutes) regeneration with an almost invisible filter temperature peak and a less pronounced filter backpressure drop. Typical first phase regeneration scenario is shown in Figure 7.9. As it can be seen, filter wall temperatures did not exceed the value of 520 °C.

After the completion of this regeneration, which was judged by the stabilization of filter backpressure, a second loading phase was applied on the filter by shifting to the loading engine operation point. This second loading phase was of shorter duration, typically 15 minutes, and resulted in a faster increase of filter backpressure. After the completion of this second loading phase, the onset of regeneration was induced by shifting to the higher load operation point. This second regeneration is the one shown in all figures with the regeneration experiments, except of Figure 7.17, B0-04 experiment, which is the first phase regeneration of B0-01 experiment presented in Figure 7.11. Further analysis has shown that, during the first phase regeneration filter backpressure decreased from 227 mbar to 129 mbar in a period of 193 s achieving the lowest reported filter backpressure decrease rate of 0.5 mbar/ s. On the other hand, analysis of the regeneration following the second loading phase, shown the same level of filter backpressure decrease but with significantly different rate, 0.9 mbar/s. A possible explanation of this effect would be the following: The initial filter loading at this medium load operation point is expected to consist of particulate with high VOF content [75, 151]. During the first regeneration attempt, we observe desorption and possibly some oxidation at low temperatures, of the majority of this VOF part. This results in a fast degradation of filter backpressure. However, a significant level of backpressure is essential to the onset of regeneration at this critical temperature range. Thus, the regeneration is feeble and stops after about one minute.

During the second loading phase, the filter is loaded again with a second layer of particulate, which increases the backpressure, however, this time we expect that the average VOF content of the total soot layer is reduced compared to the previous phase. Thus, when the onset of the second regeneration is induced, the initial, fast drop in filter backpressure is less enhanced and enough backpressure levels remain to sustain an active and clearly observable regeneration.

An inclusive set of results from regeneration experiments will be presented below by means of comparative graphs that include, along with the experimental, also computational results, as well as a sequence of 18 characteristic infrared images captured by ThermoCAM S45 [152]. Frame-by-frame analysis of the videos captured by the camera was completed using ThermoCAM Researcher software [141]. The first and the last of the 18 frames of each figure, correspond to the start and the end of the respective regeneration. Start and end of regeneration were judged by the start of soot oxidization and the stabilization of the filter backpressure drop respectively. As a first step, the case of conventional diesel soot oxidation is studied. The experimental and computational results of a regeneration of a filter loaded by 1.43 kg fuel mass, at 3250 rpm/16.2 Nm with the engine operating on B0-50 ppm Ce doped fuel are presented in Figure 7.11. A simultaneous elevation to the temperatures measured by the thermocouples located at the center and periphery near the filter exit peaking at about 210 s is observed. This indicates a uniform evolution of regeneration across the different filter channels. The convective heating seems to be the dominant phenomenon responsible for the initiation and the uniform propagation of the soot oxidation. Due to the high flowrate, the filter is heated quickly, which results, in this case, to the shortest-duration regeneration of the group of experiments with B0. The soot starts to oxidize when a temperature

level of 380 °C is achieved, resulting to a filter backpressure drop of 92 mbar in a period of 102 s, which is expressed as a 0.9 mbar/s filter pressure drop reduction rate. The temperatures in the periphery are about 13 °C lower, because of the heat losses of the uninsulated filter to the ambient air. Furthermore, maximum filter central and peripheral wall temperatures of 540 °C and 527 °C respectively are reported 110 s after the onset of regeneration, at 210 s. It is obvious that there is no significant delay between the onset of regeneration at the central and peripheral channels.

The values of E determined from previous TGA experiments [153] produce a satisfactory prediction of the full-scale process in the filter by use of the CATWALL model. However, a certain discrepancy between the measured and the predicted filter backpressure is observed. As it can be seen, the model predicts a slower reduction to the pressure drop as the regeneration initiates. One reason for this discrepancy could lie in the fact that this initial phase of regeneration is associated with a VOF desorption process that is responsible for the rapid backpressure decrease. This situation is not predictable by the 1D pressure drop model, which considers an average soot permeability value during the whole regeneration process.

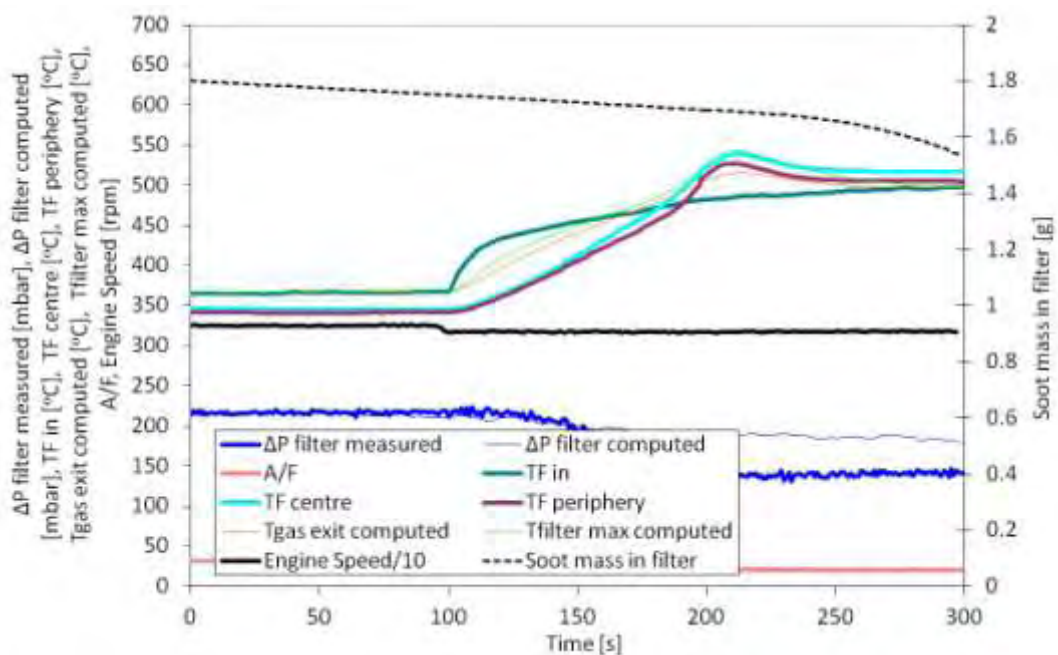
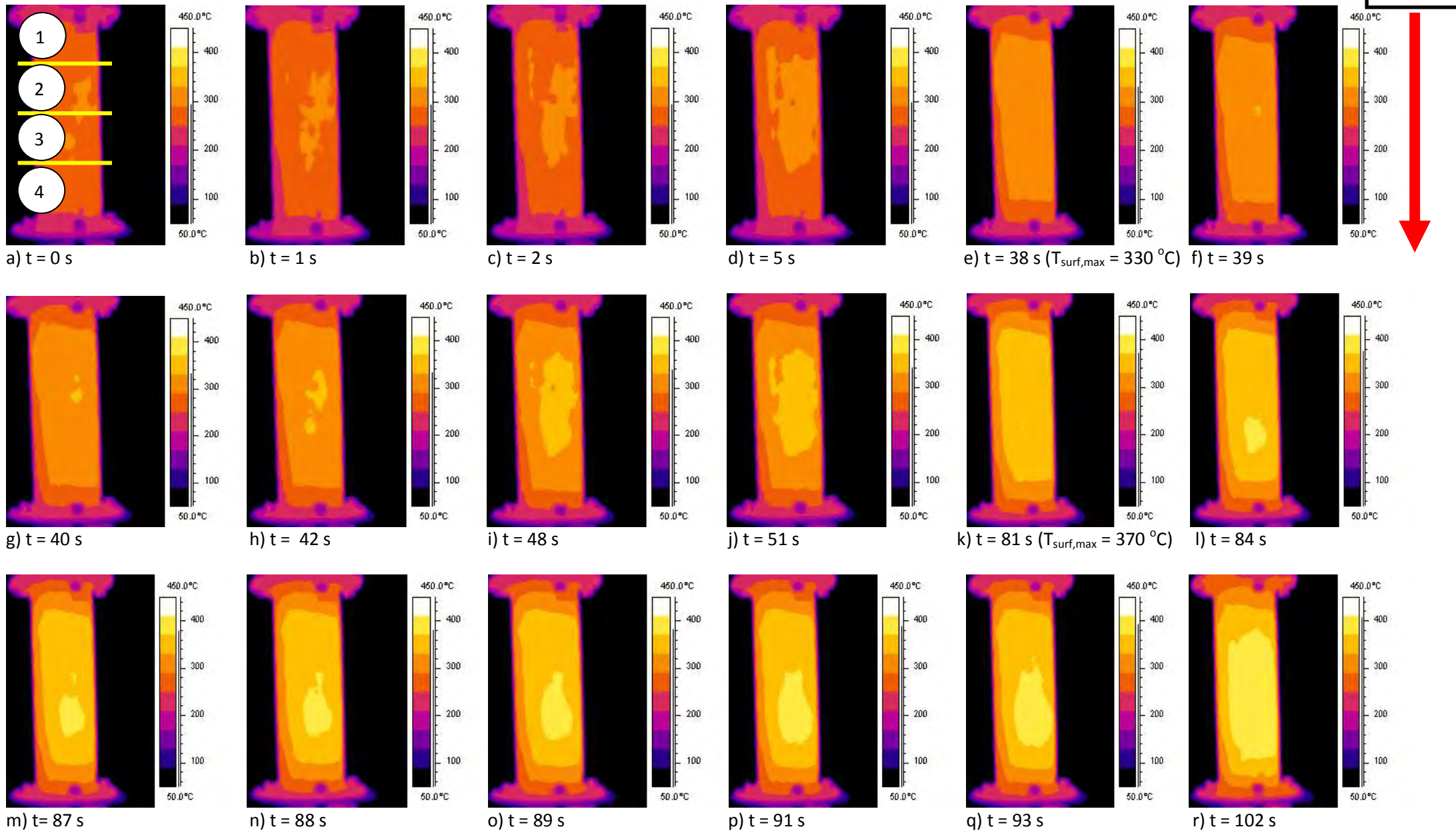


**Figure 7.11 BO-01.** Simulation of regeneration of a filter loaded (1.43 kg consumed fuel mass) with diesel soot emitted by the engine operating with 50 ppm Cerium doped fuel. Measured and predicted filter measurements near at the exit of a central and peripheral channel with the engine running on 3250 rpm/22.2 Nm. Also A/F ratio, engine speed, filter inlet temperature and measurement–vs–prediction of filter backpressure together with soot mass prediction are presented. Computation was made with activation energy values:  $E_1 = 1.9E+5$ ,  $E_2 = 1.5E+05$ ,  $E_3 = 1.1E+05$ ,  $E_4 = 0.8E+05$ ,  $E_5 = 0.8E+05$  J/mole and frequency factor values:  $A_1 = 8E+16$ ,  $A_2 = 8.5E+11$ ,  $A_3 = 3E+11$ ,  $A_4 = 9E+08$ ,  $A_5 = 8E+08$  mole/m<sup>3</sup>s.

In order to better understand the effect of different loading levels and biodiesel blending ratio (B20) on the evolution of regeneration, each scenario was captured and analyzed by means of the infrared camera and the manufacturer’s software respectively. A typical sequence of 18 infrared images is presented in Figure 7.12. There exist 4 frames which will be important for the comparative analysis of infrared thermograms. The first and the last frame, at  $t = 0$  s and  $t = 102$  s, respectively, indicate the start and the end of the regeneration. As it can be seen, B0-01 regeneration had a total duration of 102 s. There are 2 more frames, (e) and (k), which show the temperature transition of filter’s lateral surface monitored by the camera, from the selected characteristic temperature thresholds of 330 °C to 370 °C.



Start of Regeneration



Exhaust gas



End of Regeneration

**Figure 7.12 B0-01.** Sequence of 18 infrared thermograms showing the evolution of regeneration with B0-50 ppm fuel (loaded fuel mass, 1.43 kg). Also total duration (102 s) and interval temperature transition (from  $T_{surf,max} = 330\text{ }^{\circ}\text{C}$  to  $370\text{ }^{\circ}\text{C}$  in 43 s) duration are presented.

It is obvious that in this case the transition was completed in 43 s. The monitored lateral surface of the filter is separated in 4 sections, oriented by 3 yellow lines, in order to better localize the regeneration onset. According to Figure 7.12, the regeneration process may be seen to propagate by means of 2 wave fronts. These wave fronts are presented by 7 frames each, from (e) to (k) and from (l) to (r) respectively. During the propagation of the first wave front, the regeneration starts in the middle section of the filter, creating 2 hot spots of 340 °C, as shown in frame (h), which are moving and growing downstream, frame (i), and finally cover the largest part of the monitored filter's surface as presented in frame (k). The second wave front starts from the 3<sup>rd</sup> section of the filter, further downstream than the 1<sup>st</sup> wave front, and moves upstream, namely, opposite to the exhaust gas flow. The same observation was also reported by Chen K., Martirosyan, K.S. and Luss D. [144, 154, 155].

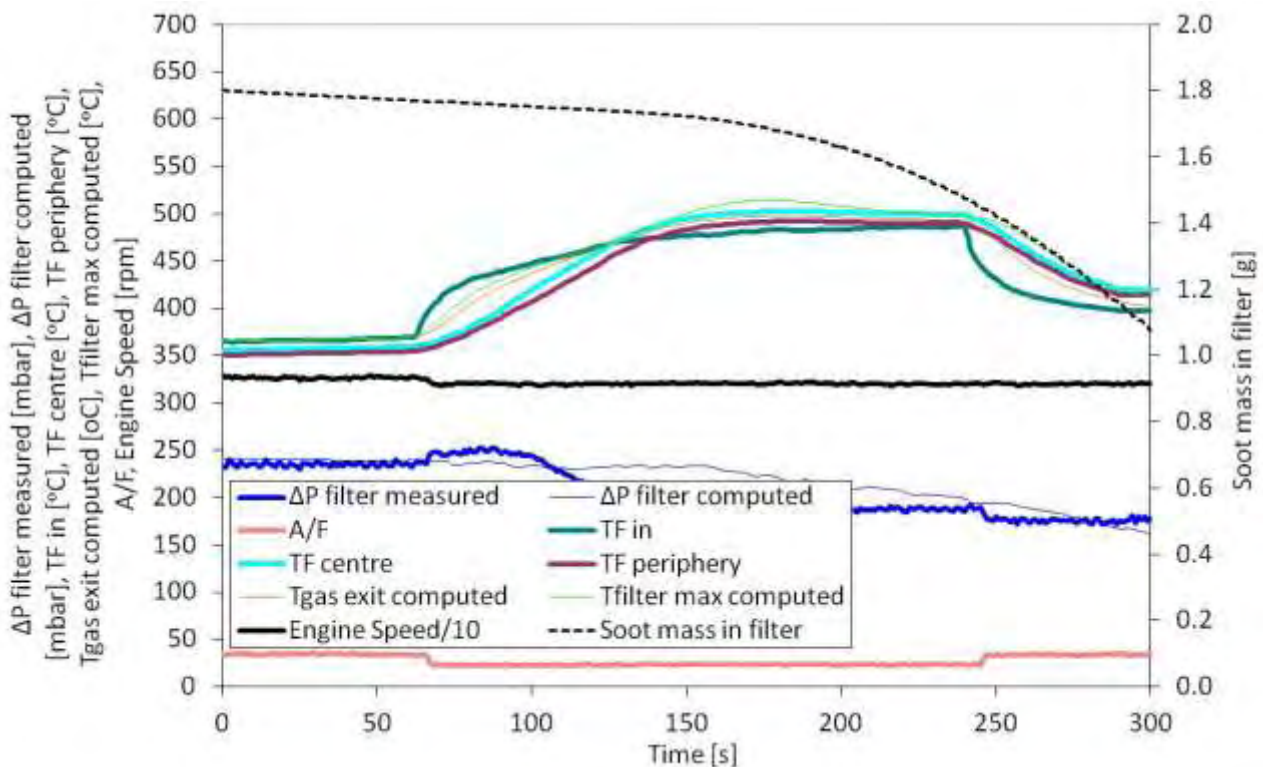
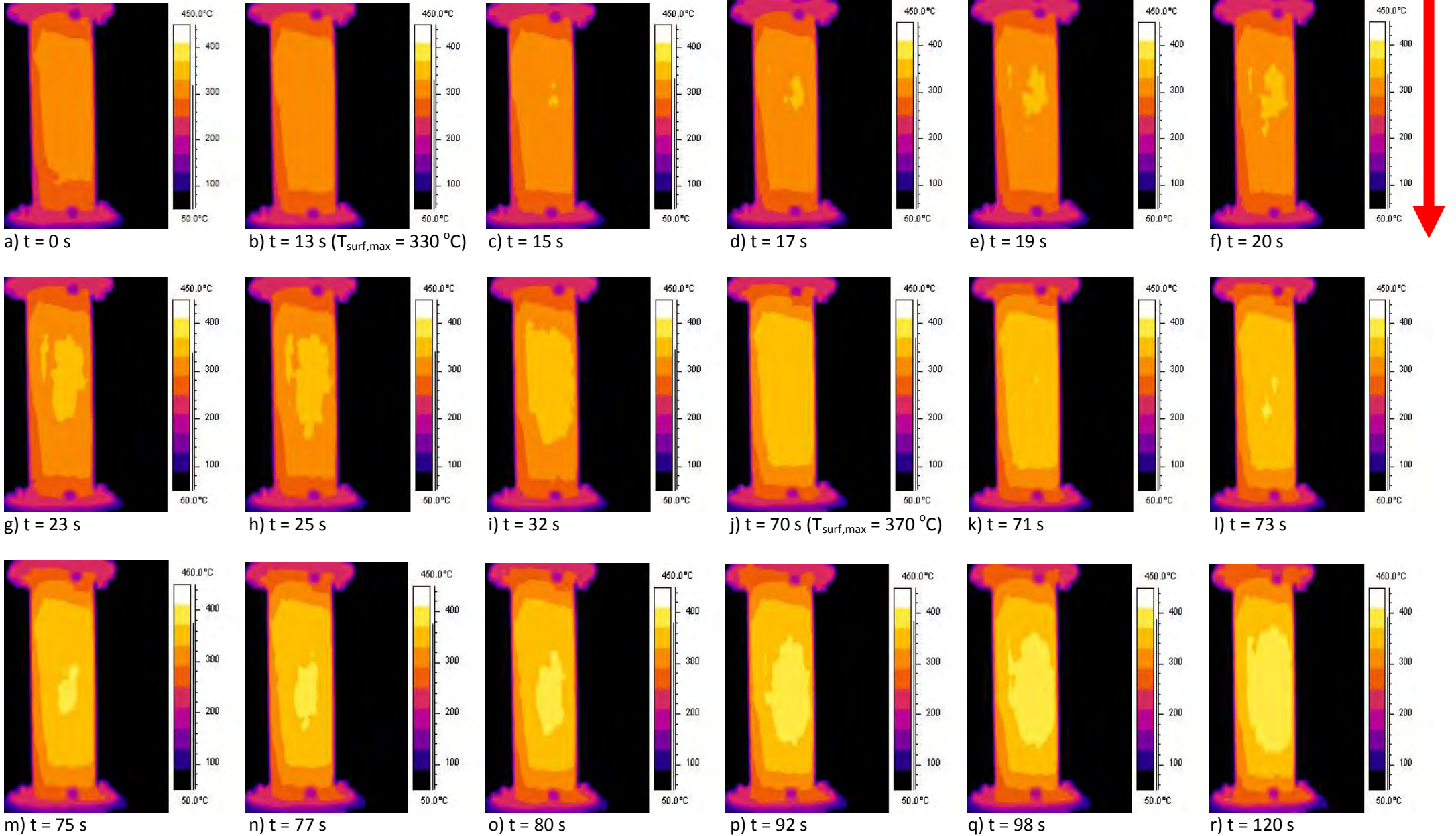


**Figure 7.13 B0-02.** Simulation of regeneration of a filter loaded (1.38 kg consumed fuel mass) with diesel soot emitted by the engine operating with 50 ppm Cerium doped fuel. Measured and predicted filter measurements near at the exit of a central and peripheral channel with the engine running on 3250 rpm/22.2 Nm. Also A/F ratio, engine speed, filter inlet temperature and measurement–vs–prediction of filter backpressure together with soot mass prediction are presented. Computation was made with activation energy values:  $E1 = 1.9E+5$ ,  $E2 = 1.5E+05$ ,  $E3 = 1.1E+05$ ,  $E4 = 0.8E+05$ ,  $E5 = 0.8E+05$  J/mole and frequency factor values:  $A1 = 1E+16$ ,  $A2 = 8.5E+11$ ,  $A3 = 3E+11$ ,  $A4 = 9E+08$ ,  $A5 = 8E+08$  mole/m<sup>3</sup>s.

As a next step, two regeneration experiments with B0-50 ppm Cerium doped fuel with different loading levels and filter inlet temperatures were performed and presented in Figure 7.13 and Figure 7.15 respectively. Figure 7.13 shows the regeneration of a filter loaded with 1.38 kg B0-50 ppm fuel and filter inlet temperature of 369 °C. The soot starts to oxidize when a temperature level of 380 °C is achieved, resulting to a filter backpressure drop of 70 mbar in a period of 120 s which is expressed as a 0.6 mbar/s filter pressure drop reduction rate. The temperatures in the periphery are about 10 °C lower, because of the heat losses of the uninsulated filter to the ambient air.

Start of Regeneration



Exhaust  
gas



End of  
Regeneration

**Figure 7.14 B0-02.** Sequence of 18 infrared thermograms showing the evolution of regeneration with B0-50 ppm fuel (loaded fuel mass, 1.38 kg). Also total duration (120 s) and interval temperature transition (from  $T_{\text{surf,max}} = 330$  °C to 370 °C in 57 s) duration are presented.

Furthermore, maximum filter central and peripheral wall temperatures of 502 °C and 492 °C respectively are reported at 160 s. It is obvious that there is no significant delay between the onset of regeneration at the central and peripheral channels. Starting with the simulation results, there is satisfactory prediction of the filter wall temperatures and good agreement between the measured and the predicted filter backpressure drop. As already mentioned, 1D pressure drop model cannot predict VOF desorption phenomena which are responsible for the rapid backpressure decrease. Frame by frame analysis, Figure 7.14, indicates that B0-02 regeneration had a total duration of 120 s and the temperature transition of filter's lateral surface, from the selected thresholds of 330 °C to 370 °C, frame (b) and frame (j), was completed in 57 s. There are also 2 regeneration wave fronts which are started from the 2<sup>nd</sup> and 3<sup>rd</sup> section of the filter respectively. Another observation relates to the appearance of hot spots at different positions on filter's surface. This situation is clearly presented in the frames (f) and (g). There are 2 regeneration areas, at the axial line and left side of the filter.

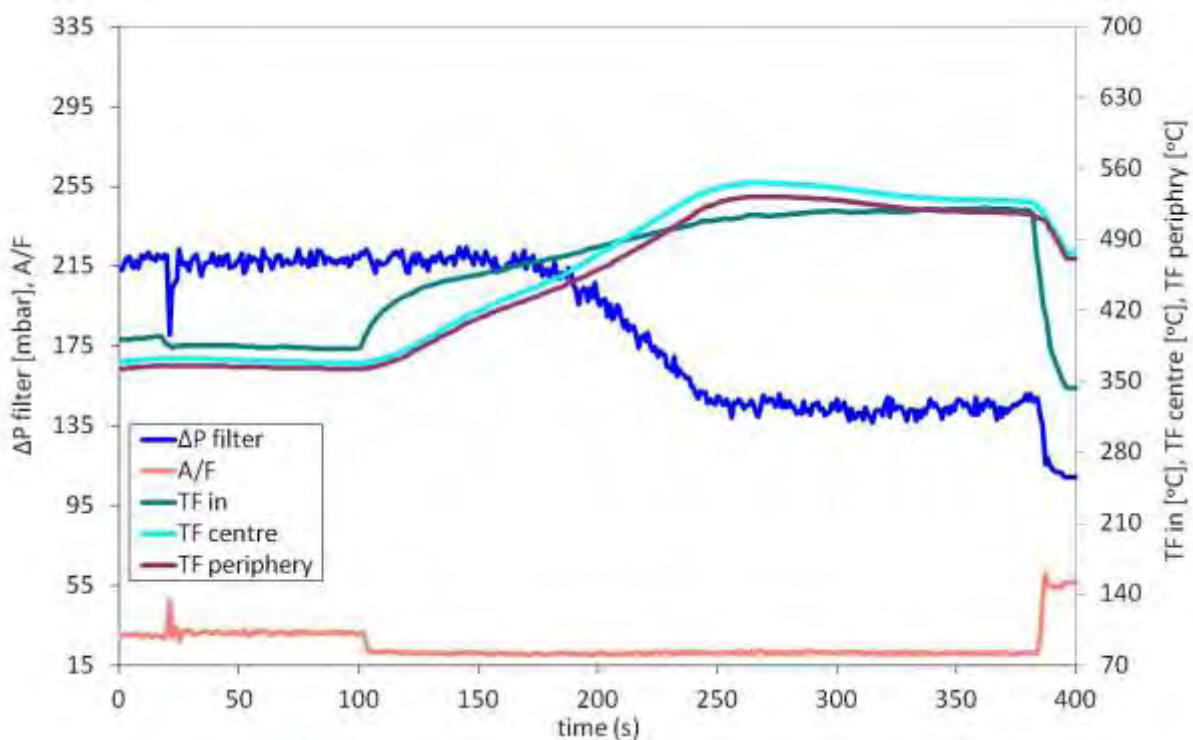
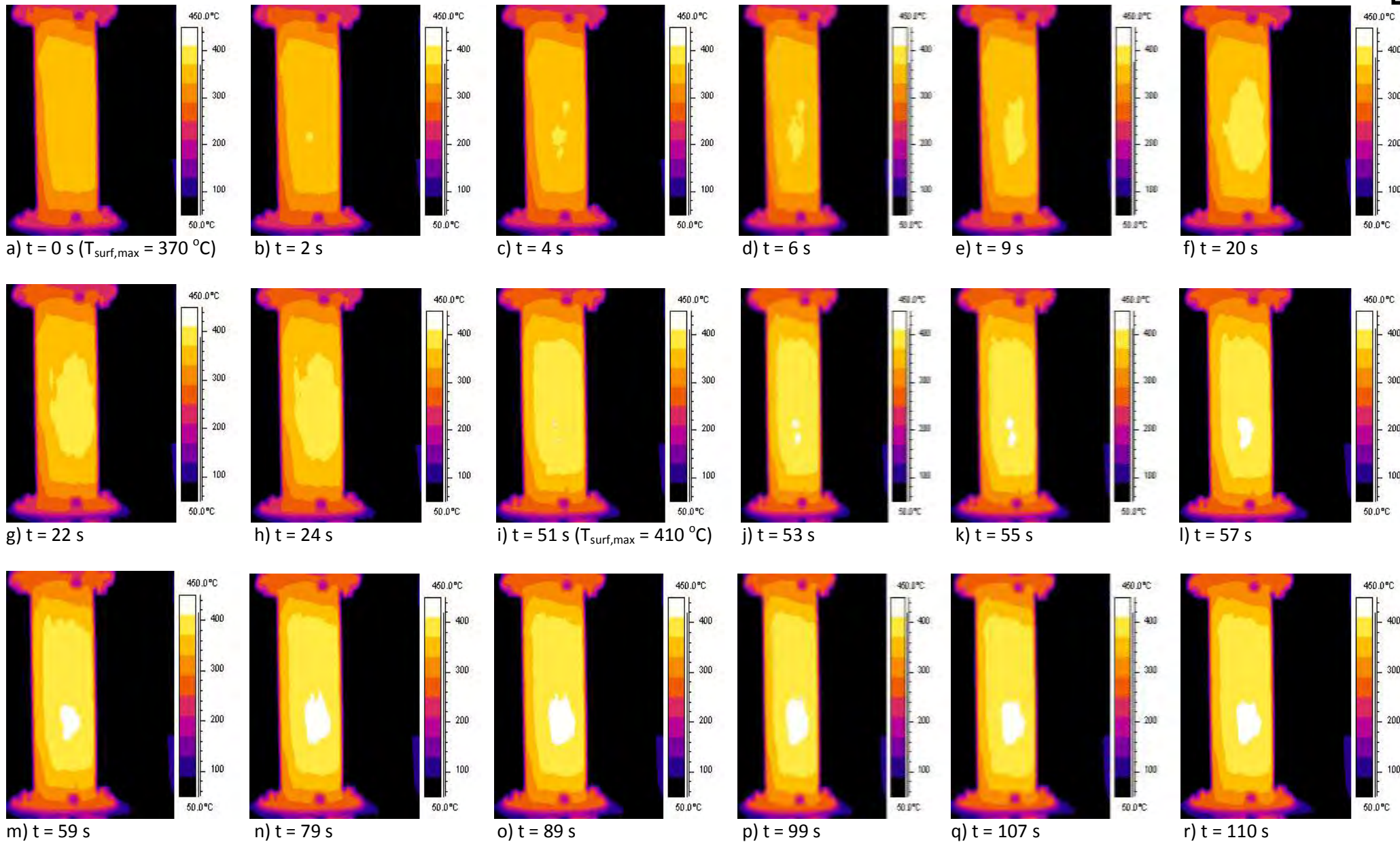


**Figure 7.15 B0-03.** Measured temperatures along filter's diameter near channels exit together with filter inlet temperature, filter backpressure and A/F ratio are presented during a high mass flow rate regeneration (exhaust mfr = 15g/s) performed at 3250 rpm/22.2 Nm for a filter loaded (1.3 kg consumed fuel mass) with B0 fuel including 50 ppm Ce dose.

Figure 7.15 presents the regeneration of a filter loaded with 1.3 kg B0-50 ppm fuel and filter inlet temperature of 382 °C. The soot starts to oxidize when a temperature level of 410 °C is achieved resulting to a filter backpressure drop of 86 mbar in a period of 110 s which is expressed as a 0.8 mbar/s filter pressure drop reduction rate. The temperatures in the periphery are about 15 °C lower, because of the heat of the uninsulated filter to the ambient air. It should be mentioned, that the B0-03 regeneration reported the highest measured temperatures compared to other 3 experiments. Maximum filter central and peripheral wall temperatures of 546 °C and 536 °C respectively are reported at 260 s. According to Figure 7.16, total regeneration duration was 110 s and the temperature transition of filter's lateral surface, from the selected thresholds of 370 °C to 410 °C, frame (a) and frame (i), was completed in 51 s. We can observe the propagation of 2 regeneration wave fronts which are started from the 3<sup>rd</sup> section of the filter.

Start of Regeneration



Exhaust  
gas



End of  
Regeneration

**Figure 7.16 B0-03.** Sequence of 18 infrared thermograms showing the evolution of regeneration with B0-50 ppm fuel (loaded fuel mass, 1.3 kg). Also total duration (110 s) and interval temperature transition (from  $T_{surf,max} = 370$  °C to 410 °C in 51 s) duration are presented.

As it can be seen, 2<sup>nd</sup> regeneration wave front starts from the 3<sup>rd</sup> section of the filter, frame (i), creating a hot core of about 410 °C which is moved upstream, namely, opposite to the exhaust gas flow. Hot spots are clearly presented in frame (c).

Finishing with the B0-50 ppm set of experiments, the results of Figure 7.17 and Figure 7.18 indicate that the regeneration behavior was significantly affected by the particulate VOF content. As already mentioned, the regeneration scenario typically consisted of a first, long-duration (three minutes) regeneration with an almost invisible filter temperature peak and a less pronounced filter backpressure drop. This type of regeneration scenario is presented in Figure 7.17. As it can be seen, filter wall temperatures did not exceed the value of 520 °C. The soot starts to oxidize when a temperature level of 380 °C is achieved.

Further analysis showed that, during B0-04 regeneration filter backpressure decreased from 227 mbar to 129 mbar in a period of 193 s achieving the lowest reported filter backpressure drop reduction rate of 0.5 mbar/ s with the highest filter loading level, 1.94 kg of consumed fuel mass. Maximum filter central and peripheral wall temperatures of 510 °C and 502 °C respectively are reported at 1530 s. According to Figure 7.18, total regeneration duration was 190 s and the temperature transition of filter's lateral surface, from the selected thresholds of 330 °C to 370 °C, frame (a) and frame (h) respectively, was completed in 54 s. There are also 2 regeneration wave fronts which are started from the 2<sup>nd</sup> and 3<sup>rd</sup> section of the filter respectively. During the first regeneration attempt, we observe desorption and possibly oxidation at low temperatures of the majority of this VOF part which results in a fast degradation of filter backpressure. In addition, during the first phase regeneration we meet lower filter's surface temperatures than in the second loading phase regeneration. Overall frame by frame regeneration analysis results are summarized in Table 7.5.

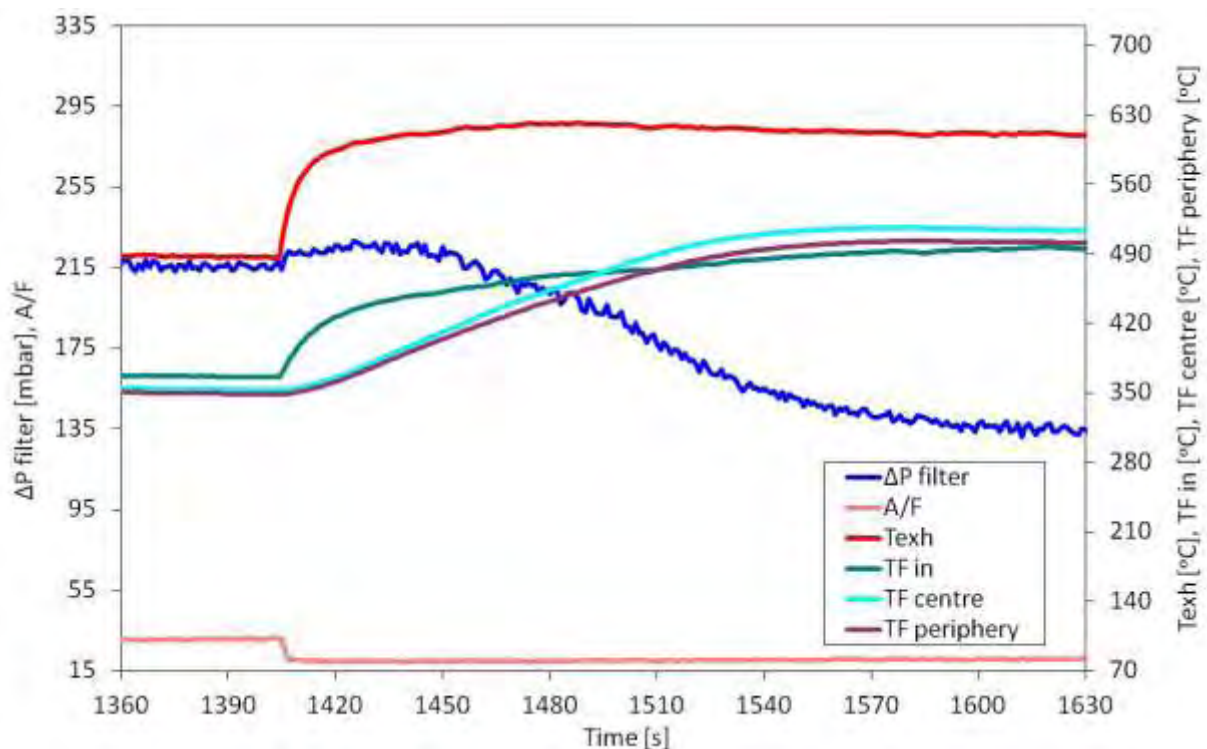


**Figure 7.17 B0-04.** Measured temperatures along filter's diameter near channels exit together with filter backpressure, filter inlet temperature and A/F ratio are presented during a high mass flow rate regeneration (exhaust mfr = 15 g/s) performed at 3250 rpm/22.2 Nm for a filter loaded (1.94 kg consumed fuel mass) with B0 fuel including 50 ppm Ce dose.

Start of Regeneration

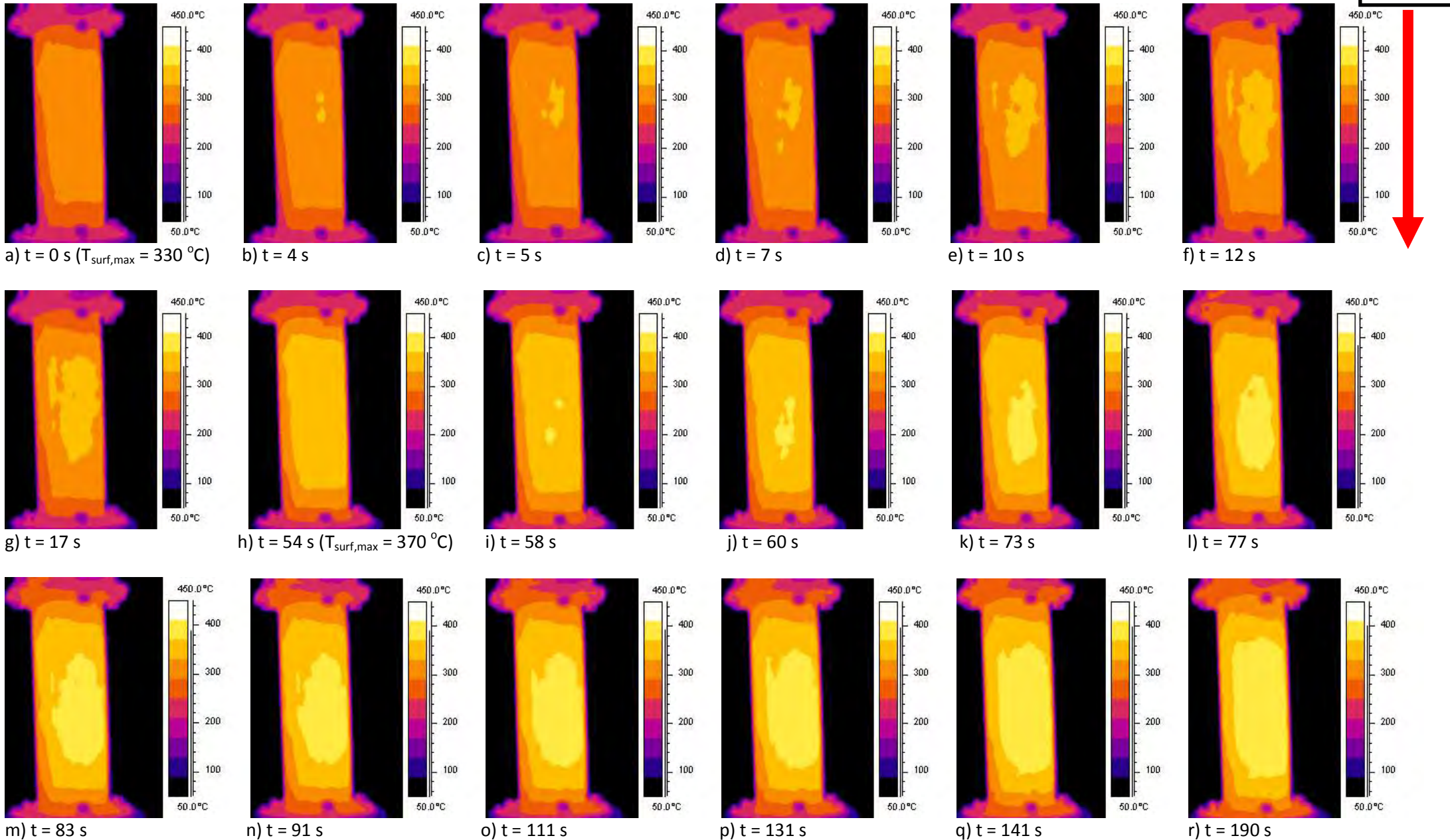


**Figure 7.18 B0-04.** Sequence of 18 infrared thermograms showing the evolution of regeneration with B0-50 ppm fuel (loaded fuel mass, 1.94 kg). Also total duration (190 s) and interval temperature transition (from  $T_{\text{surf,max}} = 330$  °C to 370 °C in 54 s) duration are presented.

End of  
Regeneration

**Table 7.5.** Results from the processing of infrared images in the case of B0-50 ppm Cerium doped fuel.

Fuel	Fuel mass consumed during loading [kg]	Regeneration duration [s]	Regeneration rate [mbar/s]	Transition time from $T_{\text{surf,max}} = 330\text{ °C}$ to $370\text{ °C}$	Transition time from $T_{\text{surf,max}} = 370\text{ °C}$ to $410\text{ °C}$
B0-03	1.3	110	0.8	-	51
B0-02	1.38	120	0.6	57	-
B0-01	1.43	102	0.9	43	-
B0-04	1.94	190	0.5	54	-

Based on these results, the increase of filter loading level, between B0-02 and B0-01 experiments, induced a decrease of the total regeneration duration and of the transition time between the characteristic temperature thresholds of 330 °C and 370 °C. Moreover, it induced a significant increase in the filter backpressure reduction rate. On the other hand, the results of experiment B0-04 indicated the effect of the higher VOF content during the regeneration following the first loading phase. The effect of a higher filter inlet temperature was clearly observable in the B0-03 experiment, where a lower loading level combined with a higher filter inlet temperature than those of B0-02 experiment, led to a faster regeneration with higher peak temperatures.

Summarizing the results of the B0 experiments, we can state the following basic findings:

- Four transient regeneration tests with high exhaust mass flow rate were performed at one engine operation point, 3250 rpm/ 22.2 Nm, with markedly different levels of filter inlet temperature and filter loading.
- The regeneration scenario consisted of a first, long-duration (three minutes) regeneration with an almost invisible filter temperature peak and a less pronounced filter backpressure drop. After the completion of this regeneration, which was determined by the stabilization of filter backpressure, a second loading phase was applied on the filter. This second loading phase was of shorter duration and resulted in a faster increase of filter backpressure and after that in a faster decrease of filter backpressure. A possible explanation to this effect would be the initial filter loading with high VOF content soot.
- In all experiments, it was observed that the catalytic soot oxidation initiates at about 380 °C - 420 °C, and the temperatures at the periphery were about 13 °C lower, because of the heat losses of the uninsulated filter to the ambient air, and there were 2 regeneration wave fronts, starting from the 2<sup>nd</sup> and 3<sup>rd</sup> section of the filter, respectively. A possible explanation to this effect would be the level of the filtration velocity. Usually for low filtration velocity most of the incoming oxygen was consumed in the upstream of the DPF. The heat generated by the reaction in that region was not efficiently removed by the low filtration velocity, leading to ignition in the upstream section. The temperature front moved in the same direction as the gas flow. On the other hand, at high filtration velocities, like our experiments, the high rate of heat removal prevented ignition of the upstream soot. The heat generated by the reaction heated the downstream flowing gas, causing ignition at the downstream. The corresponding reaction front moved in a direction opposite to that of the gas flow. This observation is in accordance with the concluding remarks of Chen et al.[156]. X-ray analysis has been applied by Blanchard et al. [157] in order to depict the ash loading field. The results indicated that the



greater amount of ash is collected downstream of the middle of the filter enhancing, with this way, the generation of the upstream propagated wave front.

- As expected, the increase in filter loading levels leads to faster regenerations with higher peak temperatures.
- The model is capable to predict temperatures inside the filter with high accuracy. As expected, the 1D model does not successfully predict the evolution of the filter backpressure during regeneration [158]. The model predicts a slower reduction to the pressure drop as the regeneration initiates. The reason could lie in the fact that this initial phase of regeneration is associated with a VOF desorption process that is responsible for the rapid backpressure decrease. This situation is not predictable by the 1D pressure drop model, which considers an average soot permeability value during the whole regeneration process.
- As a general remark, the specific engine-filter combination faces a certain degree of difficulty to perform regeneration at the specific temperature levels, with the B0 fuel. The situation is improved very much with the B20 blends, as will be discussed in the respective experiments.

## 7.2 Effect of B20 blend on regeneration behavior

In this section seven regeneration experiments are selected for presentation with B20-50 ppm Cerium doped fuel. The experiments and their main characteristics, like fuel consumed mass in loading phase and temperatures at filter inlet and inside filter exit (central and peripheral channel) are summarized in Table 7.4. As it can be seen, filter wall temperatures during loading period was kept under the VOF oxidation temperature range of 380 °C – 420 °C.

The experimental and computational results of a regeneration of a filter loaded by 1.57 kg fuel mass, at 3250 rpm/16.2 Nm with the engine operating on B20-50 ppm Cerium doped fuel is presented in Figure 7.19. As it can be seen, a simultaneously elevation to the temperatures measured by the thermocouples located at the center and periphery near the filter exit peaking at about 205 s is observed.

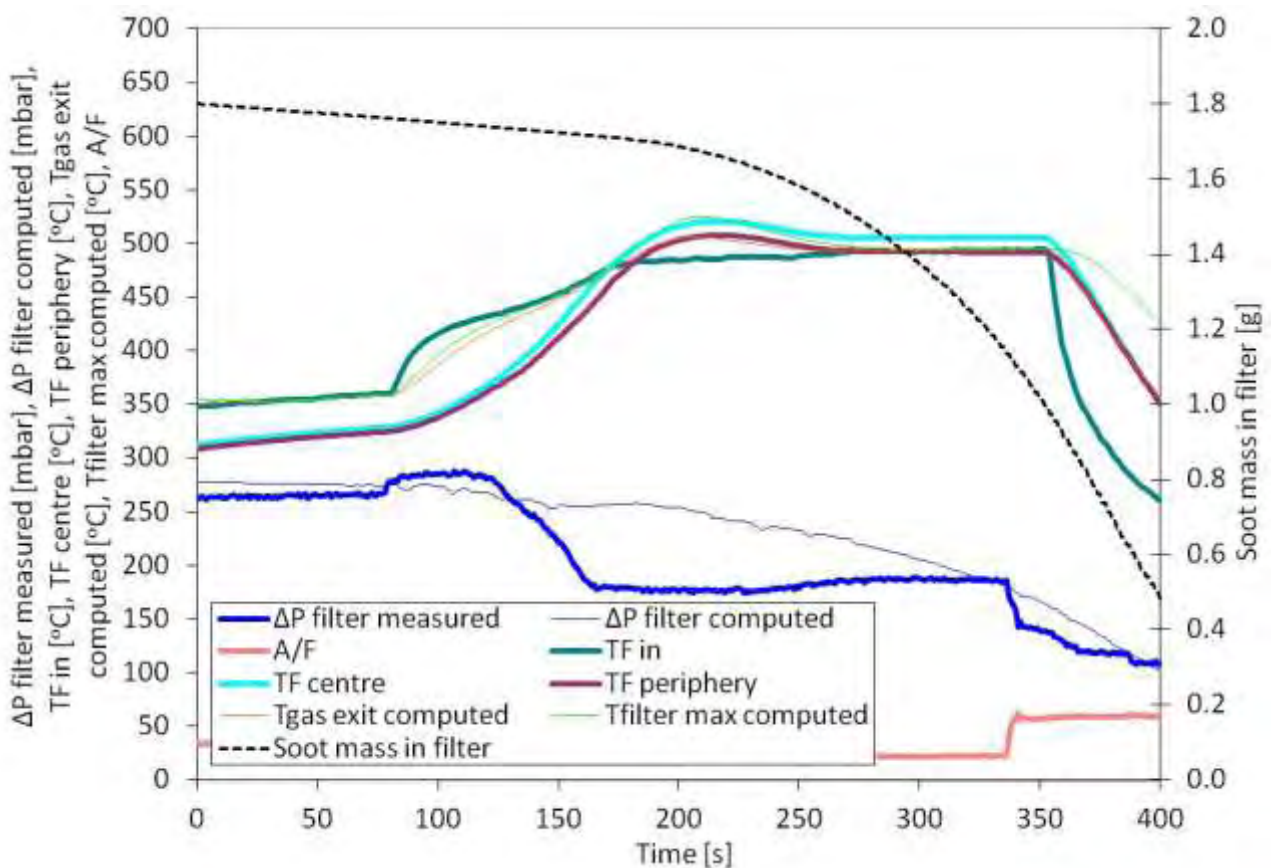
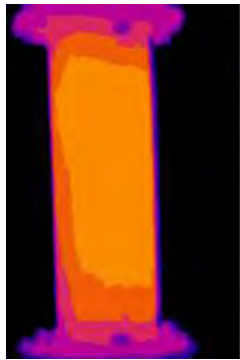


**Figure 7.19 B20-01.** Simulation of regeneration of a filter loaded (1.57 kg consumed fuel mass) with B20 biodiesel blend soot emitted by the engine operating with 50 ppm Cerium doped fuel. Measured and predicted filter measurements near at the exit of a central and peripheral channel with the engine running on 3250 rpm/22.2 Nm. Also A/F ratio, filter inlet temperature and measurement–vs–prediction of filter backpressure together with soot mass prediction are presented. Computation was made with activation energy values:  $E1 = 1.9E+5$ ,  $E2 = 1.5E+05$ ,  $E3 = 1.1E+05$ ,  $E4 = 0.8E+05$ ,  $E5 = 0.8E+05$  J/mole and frequency factor values:  $A1 = 8E+15$ ,  $A2 = 8.5E+11$ ,  $A3 = 3E+11$ ,  $A4 = 9E+08$ ,  $A5 = 8E+08$  mole/m<sup>3</sup>s.

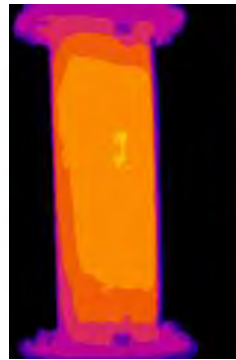
Start of Regeneration



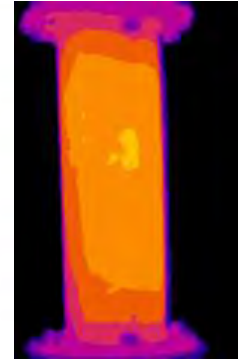
a)  $t = 0$  s ( $T_{\text{surf,max}} = 330$  °C)



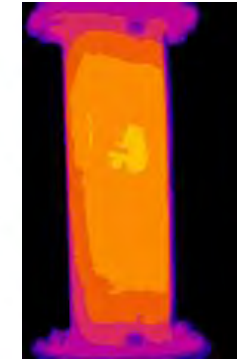
b)  $t = 1$  s



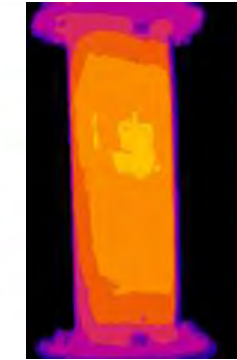
c)  $t = 2$  s



d)  $t = 3$  s

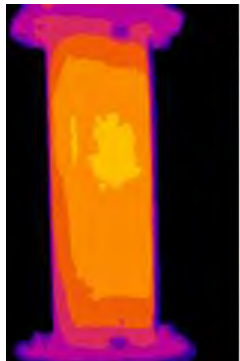


e)  $t = 4$  s

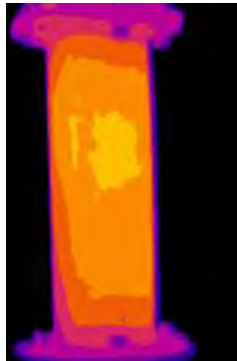


f)  $t = 5$  s

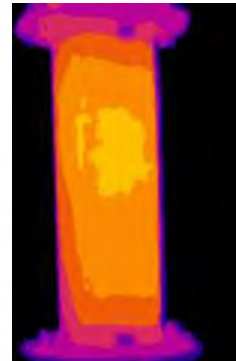
Exhaust  
gas



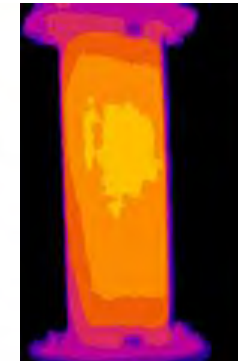
g)  $t = 6$  s



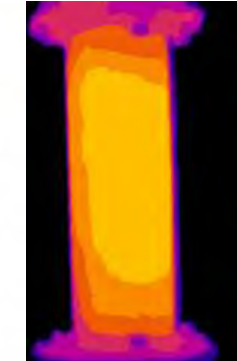
h)  $t = 7$  s



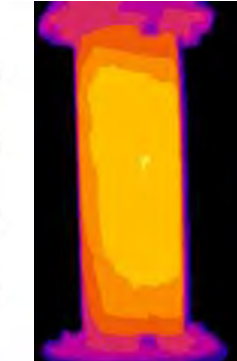
i)  $t = 8$  s



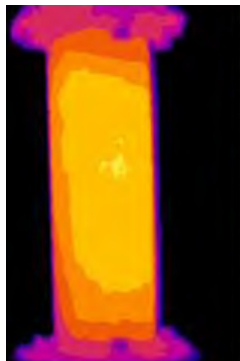
j)  $t = 9$  s



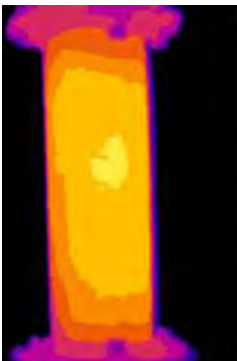
k)  $t = 30$  s ( $T_{\text{surf,max}} = 370$  °C)



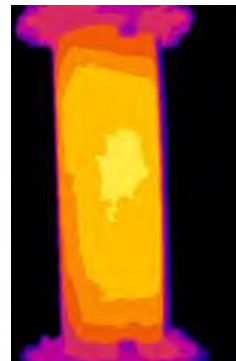
l)  $t = 32$  s



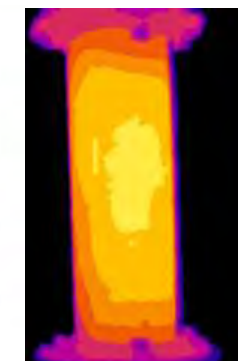
m)  $t = 33$  s



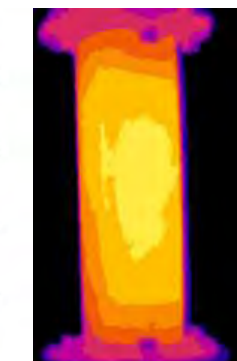
n)  $t = 36$  s



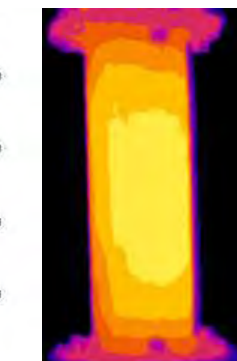
o)  $t = 39$  s



p)  $t = 44$  s



q)  $t = 47$  s



r)  $t = 94$  s

**Figure 7.20 B20-01.** Sequence of 18 infrared thermograms showing the evolution of regeneration with B20-50 ppm fuel (loaded fuel mass, 1.57 kg). Also total duration (94 s) and interval temperature transition (from  $T_{\text{surf,max}} = 330$  °C to 370 °C in 30 s) duration are presented.

End of  
Regeneration

The soot starts to oxidize when a temperature level of 335 °C is achieved resulting in a filter backpressure drop of 114 mbar in a period of 94 s which is expressed as a 1.2 mbar/s filter pressure drop reduction rate. The temperatures in the periphery are about 13 °C lower, because of the heat losses of the uninsulated filter to the ambient air. Furthermore, maximum filter central and peripheral wall temperatures of 520 °C and 507 °C respectively are reported 136 s after the onset of regeneration, at 216 s. It is obvious that there is no significant delay between the onset of regeneration at the central and peripheral channels. The known, from the previous simulations, values of E produce a satisfactory prediction of the full-scale process in the filter by use of the CATWALL model. The same discrepancy between the measured and the predicted filter backpressure is also observed in this set of experiments. As it can be seen the model predicts a significantly slower reduction to the pressure drop as the regeneration initiates. VOF content is higher in the case of B20-50 ppm fuel enhancing with this way the rapid decrease of the filter backpressure during the initial phase of regeneration and making more difficult its prediction from the 1D pressure model. It should be mentioned that the frequency factors, A, were tuned to represent the experimentally determined regeneration behavior of the filter. There are also 4 frames which will be important for the comparative analysis of the infrared thermograms. The first and the last frame, at  $t = 0$  s and  $t = 94$  s, respectively, indicate the start and the end of the regeneration. As it can be seen, B20-01 regeneration had a total duration of 94 s. There are 2 more frames, (a) and (k), which show the temperature transition of filter's lateral surface monitored by the camera, from the selected thresholds of 330 °C to 370 °C. It is obvious that in this case the transition was completed in 30 s. According to Figure 7.20, the regeneration process maybe seen to propagate by means of 2 wave fronts. These wave fronts are presented by 7 frames each, from (e) to (k) and from (l) to (r) respectively. Another observation is related with the appearance of hot spots at different positions on filter's monitored surface. There are 2 regeneration zones at the axial line and left side of the filter. As it can be seen, 1<sup>st</sup> regeneration wave front starts from the 2<sup>nd</sup> section of the filter, frame (d), creating a hot core of 330 °C and moves downstream in accordance with the exhaust gas flow. The same behavior is also reported for the 2<sup>nd</sup> regeneration wave front but with a different core temperature, 370 °C. Hot spots are clearly observable using B20-50 ppm fuel and presented in frames (c), (m) and (p). After that regeneration, we continue with the loading process consuming 1.42 kg B20-50 ppm Cerium doped fuel. Figure 7.21 presents the regeneration of a filter loaded with 1.42 kg B20-50 ppm fuel and filter inlet temperature of 355 °C. The soot starts to oxidize when a temperature level of 350 °C is achieved leading to a filter backpressure drop of 115 mbar in a period of 120 s which is expressed as a 0.96 mbar/s filter pressure drop reduction rate. The temperatures in the periphery are about 12 °C lower, because of the heat losses of the uninsulated filter to the ambient air. Maximum filter central and peripheral wall temperatures of 503 °C and 491 °C respectively are reported at 240 s. According to Figure 7.22, total regeneration duration was 120 s and the temperature transition from 330 °C to 370 °C, frame (a) and frame (f) respectively, was completed in 55 s. There are also 2 regeneration wave fronts start, both of them, from the 2<sup>nd</sup> section of the filter and move downstream. Hot zones of 330 °C are also reported in this regeneration experiment, during the 1<sup>st</sup> regeneration wave. The simulation reacts with the known reported behavior leading, this time, to faster filter backpressure reduction in the initial regeneration phase. As a next step, two regeneration experiments with B20-50 ppm Cerium doped fuel with different loading levels but the same filter inlet temperature of 370 °C were performed and presented in Figure 7.23 and Figure 7.25 respectively. Figure 7.23 presents the regeneration of a filter loaded with 1.26 kg B20-50 ppm fuel and filter inlet temperature of 370 °C. The soot starts to oxidize when a temperature level of 345 °C is achieved resulting to filter backpressure drop of 87 mbar in a period of 65 s which is expressed as a 1.34 mbar/s filter pressure drop reduction rate. The temperatures in the periphery

are about 14 °C lower, because of the heat losses of the uninsulated filter to the ambient air. Maximum filter central and peripheral wall temperatures of 538 °C and 246 °C respectively are reported at 125 s.

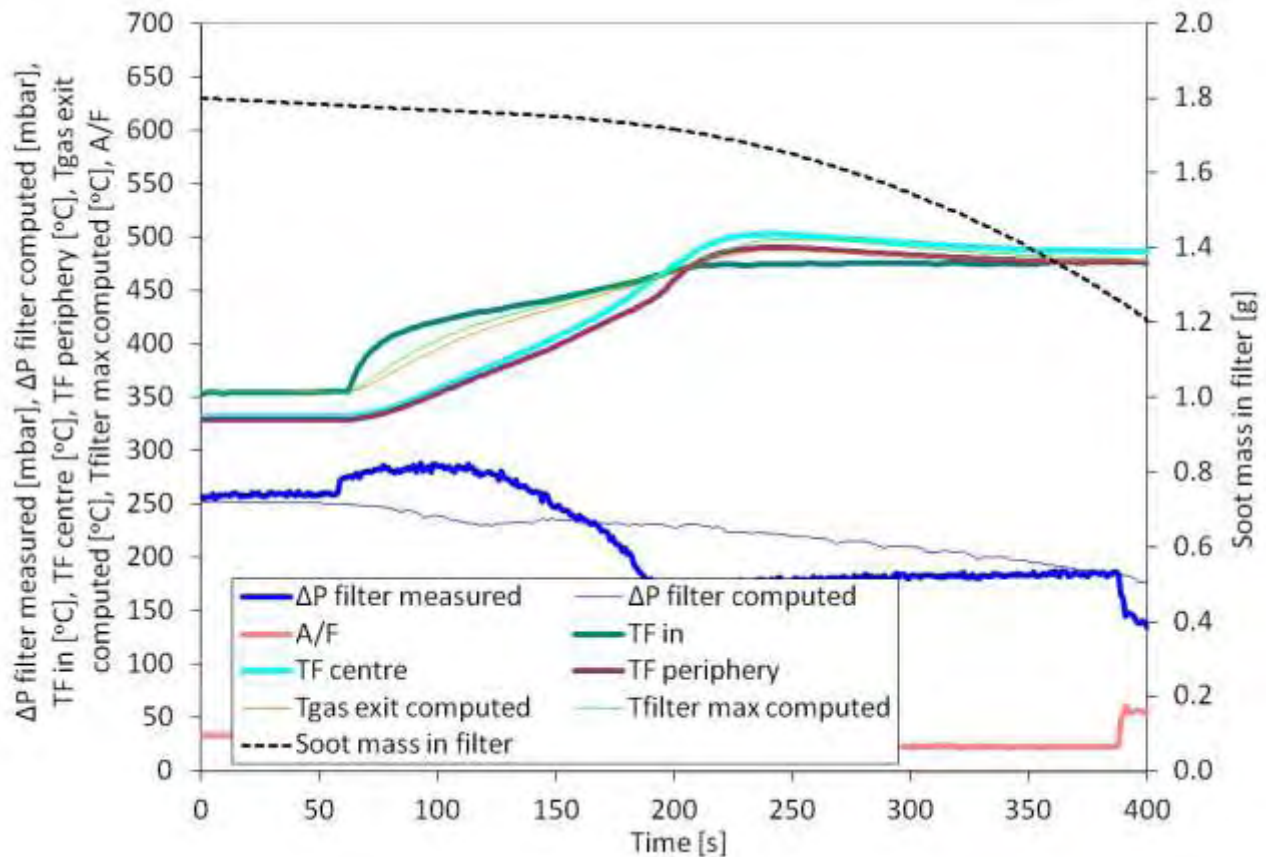
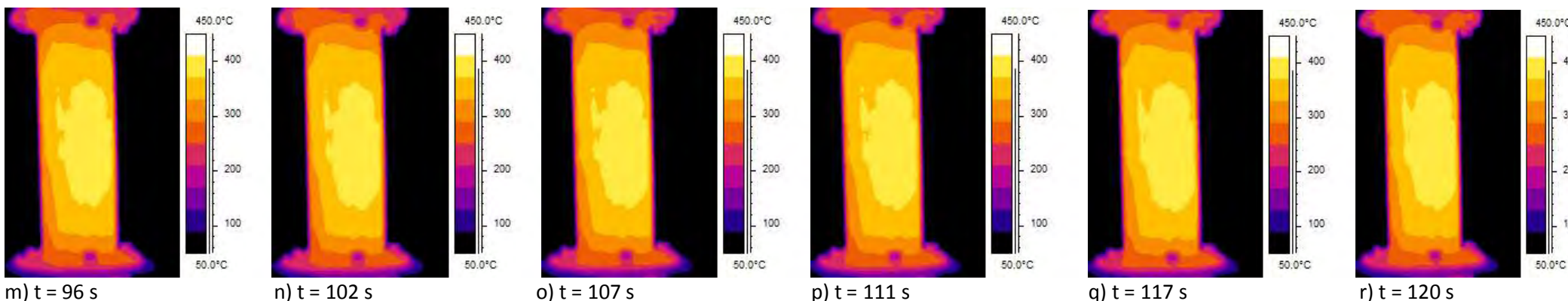
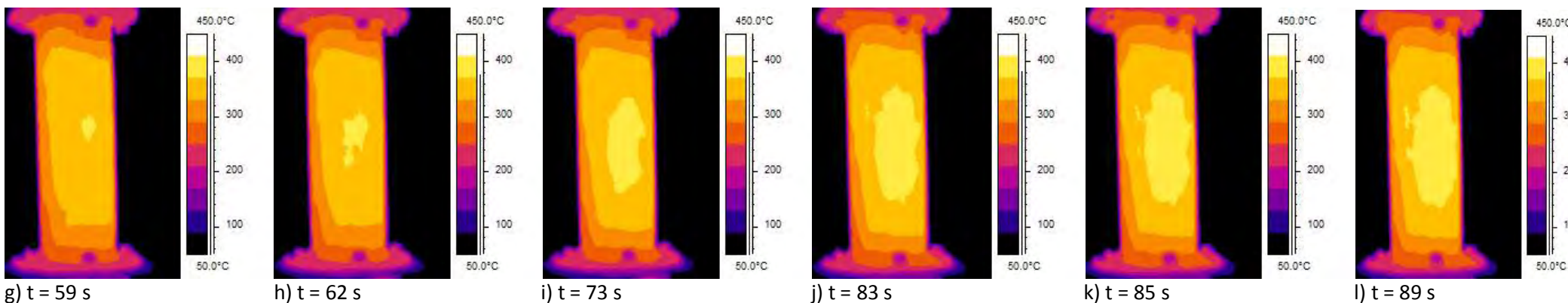
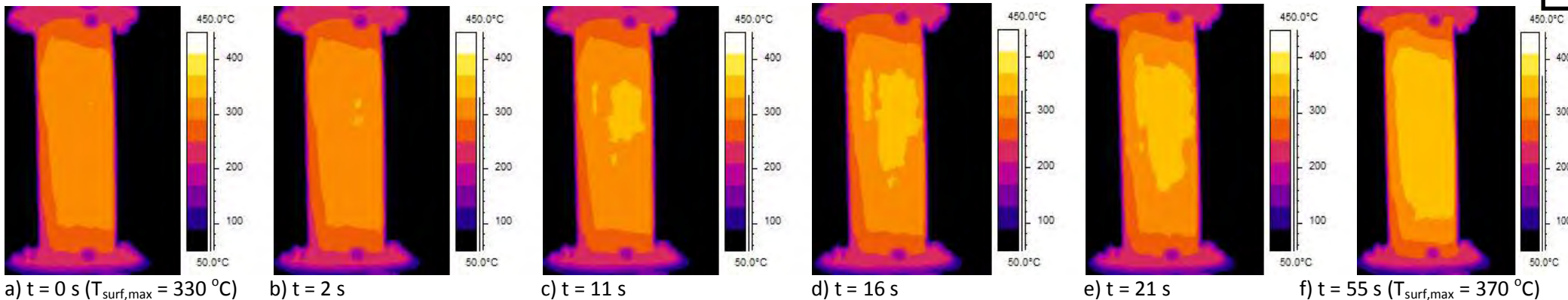


**Figure 7.21 B20-02.** Simulation of regeneration of a filter loaded (1.42 kg consumed fuel mass) with B20 biodiesel blend soot emitted by the engine operating with 50 ppm Cerium doped fuel. Measured and predicted filter measurements near at the exit of a central and peripheral channel with the engine running on 3250 rpm/22.2 Nm. Also A/F ratio, filter inlet temperature and measurement–vs–prediction of filter backpressure together with soot mass prediction are presented. Computation was made with activation energy values:  $E1 = 1.9E+5$ ,  $E2 = 1.5E+05$ ,  $E3 = 1.1E+05$ ,  $E4 = 0.8E+05$ ,  $E5 = 0.8E+05$  J/mole and frequency factor values:  $A1 = 8E+15$ ,  $A2 = 8.5E+11$ ,  $A3 = 3E+11$ ,  $A4 = 9E+08$ ,  $A5 = 8E+08$  mole/m<sup>3</sup>s.

Figure 7.25 shows the regeneration of a filter loaded with 1.08 kg B20-50 ppm fuel and filter inlet temperature of 372 °C. The soot starts to oxidize when a temperature level of 365 °C is achieved resulting to a filter backpressure drop of 72 mbar in a period of 129 s which is expressed as a 0.56 mbar/s filter pressure drop reduction rate. The temperatures in the periphery are lower about 12 °C, because of the heat losses through the periphery to the ambient air. Furthermore, maximum filter central and peripheral wall temperatures of 505 °C and 493 °C respectively are reported at 220 s. It is obvious that there is no significant delay between the onset of regeneration of the central and peripheral channels. Starting with the simulation results, there is satisfactory predictions of the inside filter developed temperatures and filter backpressure levels. Frame by frame analysis, Figure 7.26, indicates that B20-04 regeneration had a total duration of 129 s and the face temperature increase from 330 °C to 370 °C, frame (b) and frame (l), respectively, was completed in 57 s. There are also 2 regeneration waves, which start from the 2<sup>nd</sup> section of the filter and move downstream to filter exit. Another observation is related with the appearance of hot spots at different positions on filter’s surface.

Start of Regeneration



Exhaust  
gas



End of  
Regeneration

**Figure 7.22 B20-02.** Sequence of 18 infrared thermograms showing the evolution of regeneration with B20-50 ppm fuel (loaded fuel mass, 1.42 kg). Also total duration (120 s) and interval temperature transition (from  $T_{\text{surf,max}} = 330$  °C to 370 °C in 55 s) duration are presented.

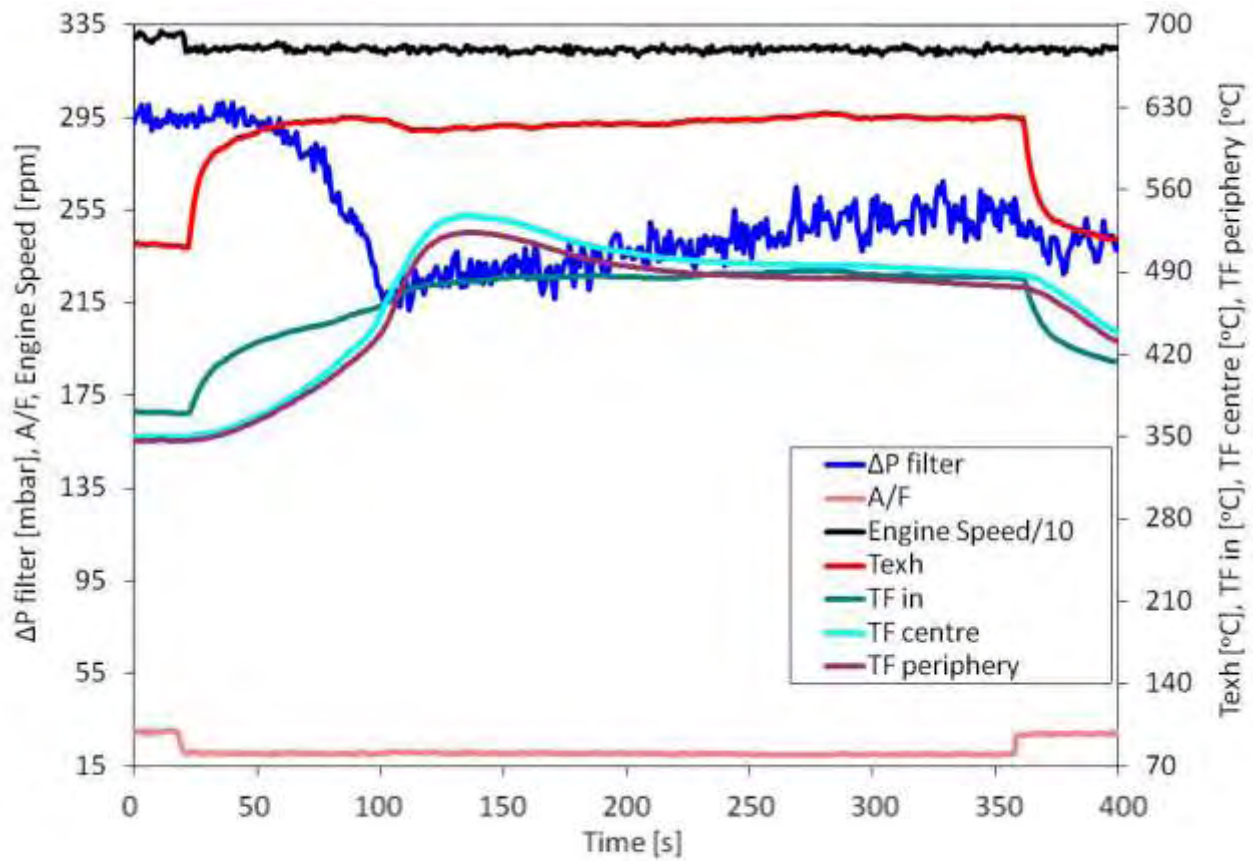


**Figure 7.23 B20-03.** Measured temperatures along filter’s diameter near channels exit together with filter backpressure, engine speed, engine outlet temperature, filter inlet temperature and A/F ratio are presented during a high mass flowrate regeneration (14g/s) performed at 3250 rpm/22.2 Nm for a filter loaded (1.26 kg consumed fuel mass) with B20 fuel including 50 ppm Ce dose.

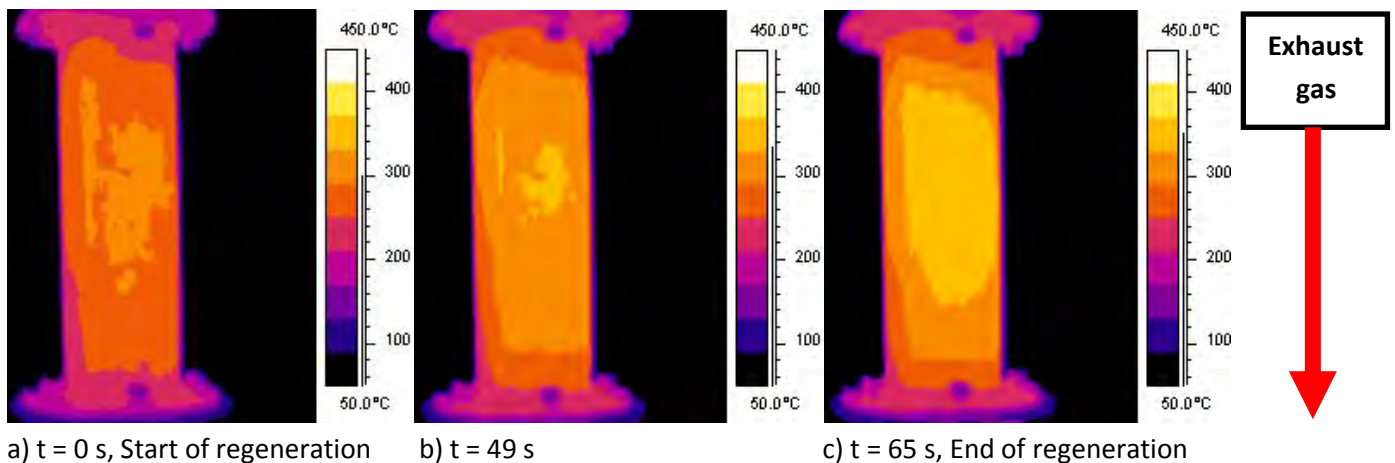


**Figure 7.24 B20-03.** Three infrared images showing the evolution of regeneration with B20-50 ppm fuel (loaded fuel mass, 1.26 kg).

This is a high loading experiment. At about 100 s (Figure 7.23) we observe a sharp decrease in filter backpressure, although the temperature levels are relatively low (about 345 °C). This is a low temperature regeneration that unfortunately was not recorded well in the thermograms, due to its very fast character, Figure 7.24. It is of the erratic (stochastic) type mentioned in the literature [75].

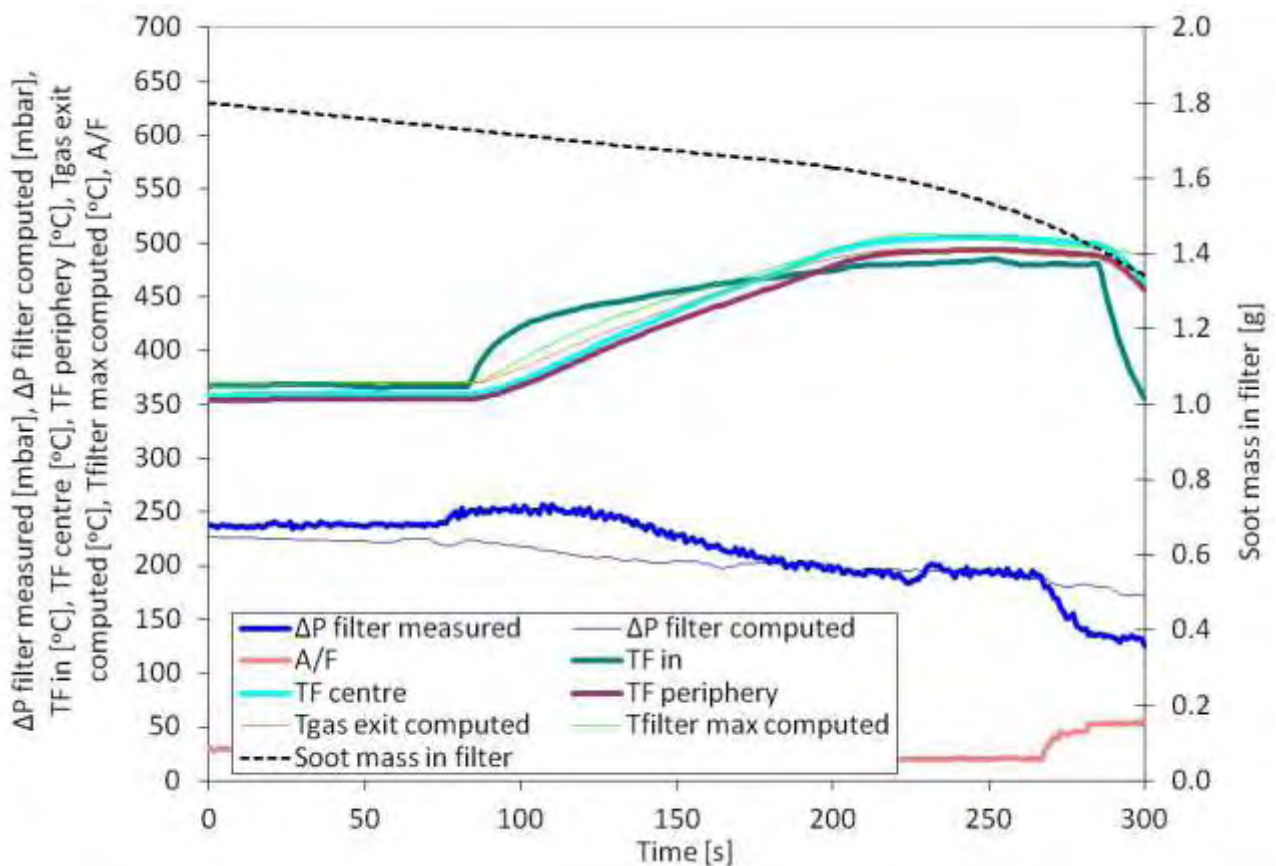


**Figure 7.25 B20-04.** Simulation of regeneration of a filter loaded (1.08 kg consumed fuel mass) with B20 biodiesel blend soot emitted by the engine operating with 50 ppm Cerium doped fuel. Measured and predicted filter measurements near at the exit of a central and peripheral channel with the engine running on 3250 rpm/22.2 Nm. Also A/F ratio, filter inlet temperature and measurement–vs–prediction of filter backpressure together with soot mass prediction are presented. Computation was made with activation energy values:  $E1 = 1.9E+5$ ,  $E2 = 1.5E+05$ ,  $E3 = 1.1E+05$ ,  $E4 = 0.8E+05$ ,  $E5 = 0.8E+05$  J/mole and frequency factor values:  $A1 = 6E+16$ ,  $A2 = 8.5E+11$ ,  $A3 = 3E+11$ ,  $A4 = 9E+08$ ,  $A5 = 8E+08$  mole/m<sup>3</sup>s.

Continuing with the analysis of the B20-04 experiment the described situation is clearly observable in frames (h) and (i). There are 3 areas, at the axial line and the left side of the filter. The last area is visible in all B20-50 ppm regeneration experiments.

Continuing with the presentation of the regeneration experiments, computational and experimental results of B20-05 regeneration experiment are presented in Figure 7.27. During this regeneration, the soot starts to oxidize when a temperature level of 368 °C is achieved resulting to a filter backpressure drop of 121 mbar in a period of 177 s which is expressed as a 0.68 mbar/s filter pressure drop reduction rate.

The temperatures in the periphery are about 14 °C lower, because of the heat losses of the uninsulated filter to the ambient air. Furthermore, maximum filter central and peripheral wall temperatures of 513 °C and 499 °C respectively are reported at 220 s. In this case, 1D model predicts slower reduction of filter backpressure drop and on the other hand, predicts with high accuracy filter wall temperatures. According to Figure 7.28 B20-05 regeneration had a total duration of 177 s and the face temperature increase from the selected temperature thresholds of 330 °C to 370 °C, frame (a) and frame (n), was completed in 45 s.

There are also, in this experiment, 2 regeneration wave fronts, which start from the 2<sup>nd</sup> section of the filter and move downstream to filter exit. Hot zones are appeared in 1<sup>st</sup> regeneration wave front and presented in frame (i).



Start of Regeneration

Exhaust gas

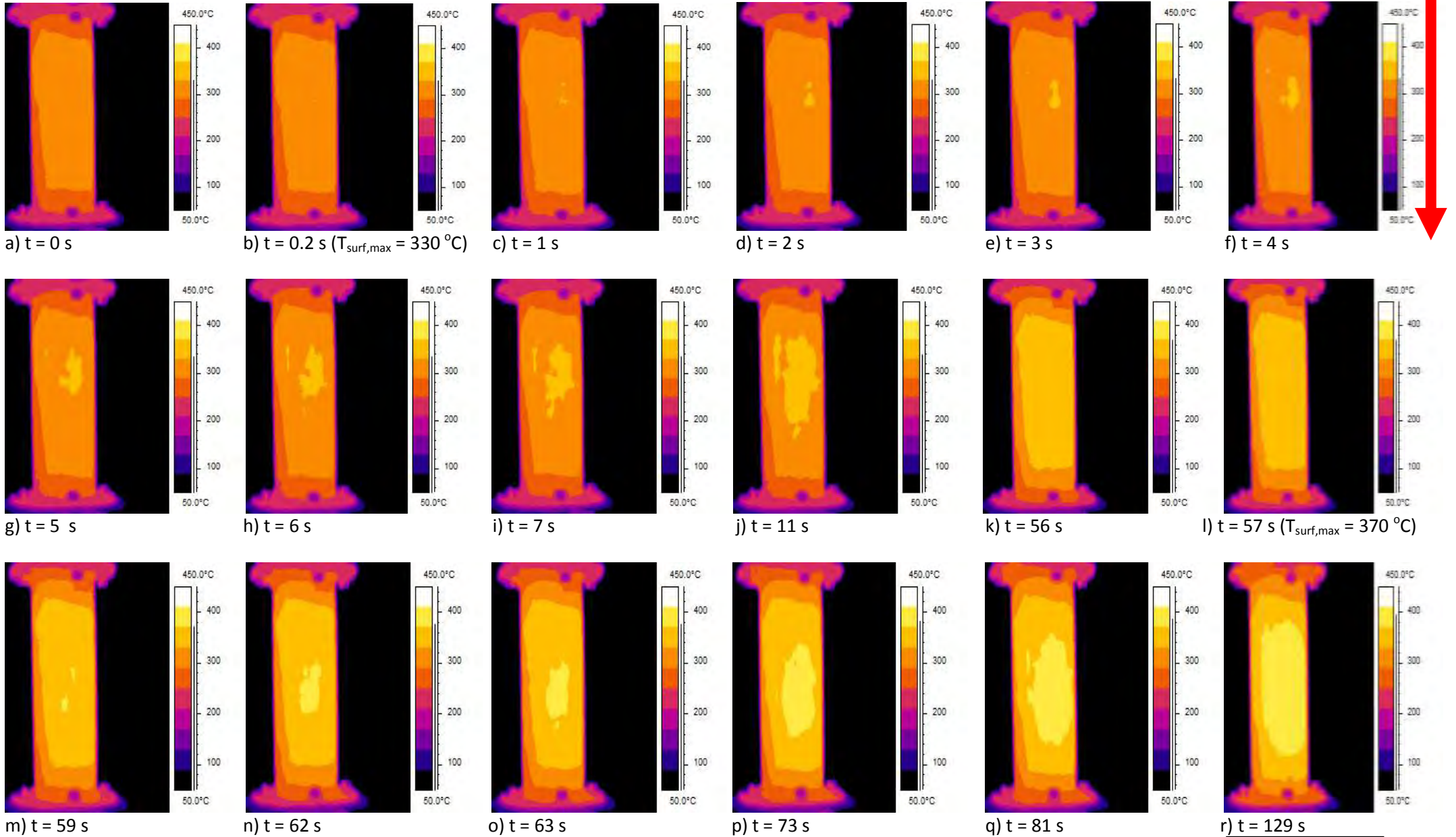


**Figure 7.26 B20-04.** Sequence of 18 infrared thermograms showing the evolution of regeneration with B20-50 ppm fuel (loaded fuel mass, 1.08 kg). Also total duration (129 s) and interval temperature transition (from  $T_{\text{surf,max}} = 330\text{ }^{\circ}\text{C}$  to  $370\text{ }^{\circ}\text{C}$  in 57 s) duration are presented.

End of Regeneration

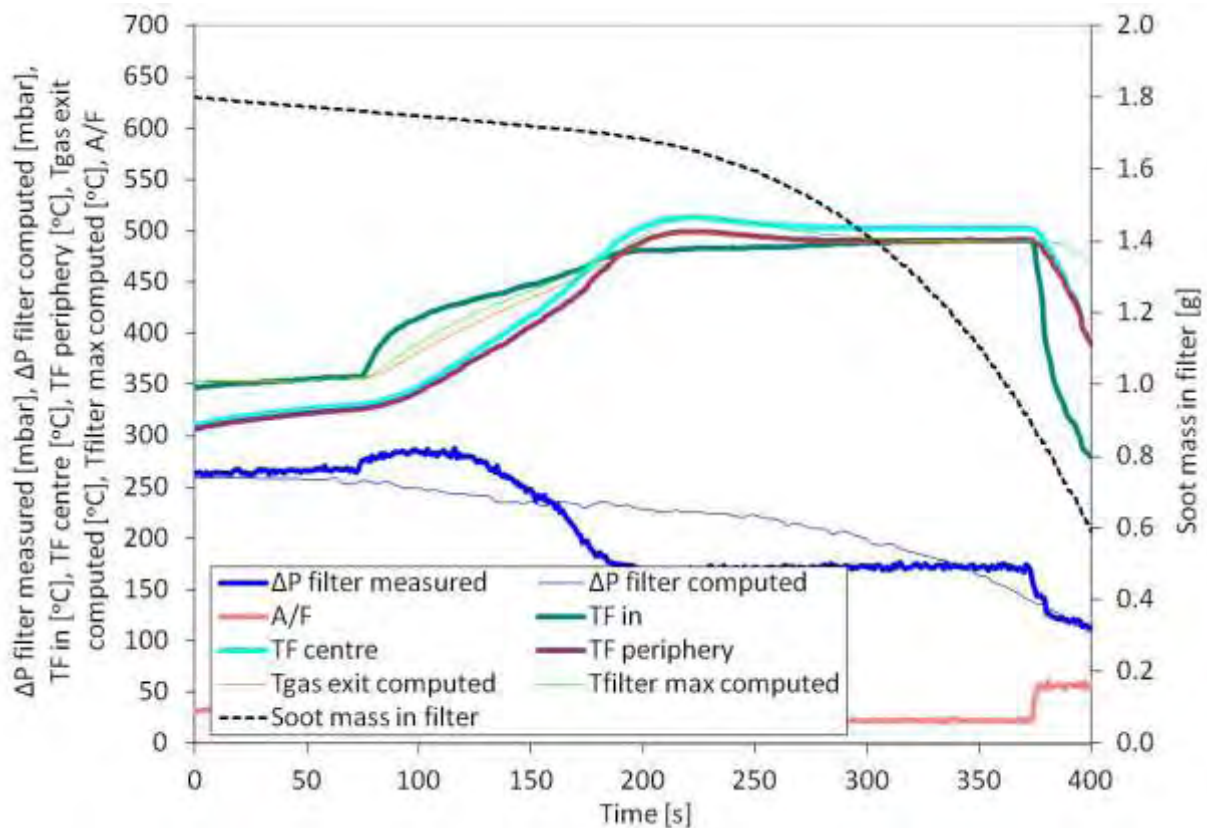
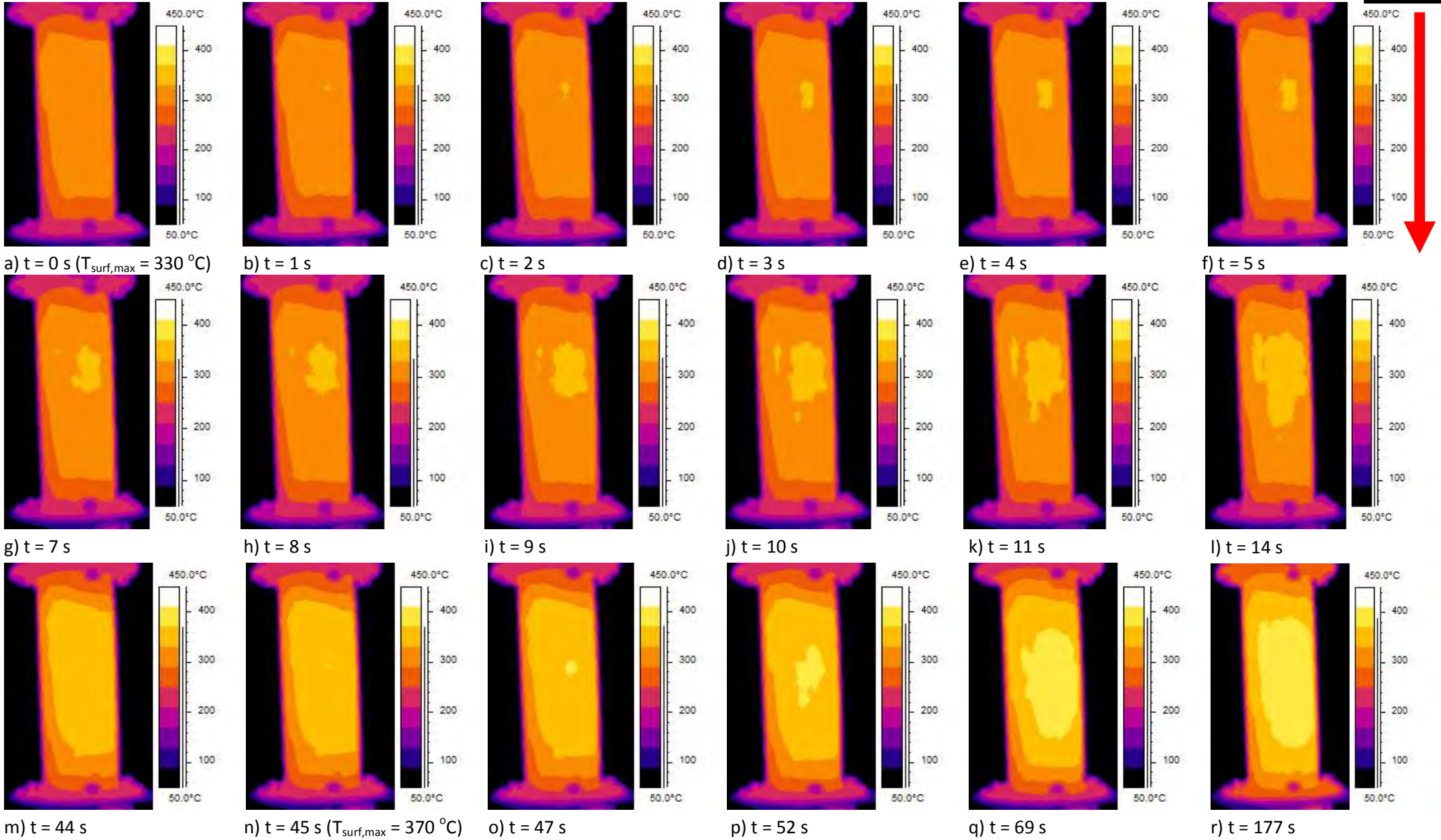


**Figure 7.27 B20-05.** Simulation of regeneration of a filter loaded (0.99 kg consumed fuel mass) with B20 biodiesel blend soot emitted by the engine operating with 50 ppm Cerium doped fuel. Measured and predicted filter measurements near at the exit of a central and peripheral channel with the engine running on 3250 rpm/22.2 Nm. Also A/F ratio, filter inlet temperature and measurement–vs–prediction of filter backpressure together with soot mass prediction are presented. Computation was made with activation energy values:  $E_1 = 1.9E+5$ ,  $E_2 = 1.5E+05$ ,  $E_3 = 1.1E+05$ ,  $E_4 = 0.8E+05$ ,  $E_5 = 0.8E+05$  J/mole and frequency factor values:  $A_1 = 8E+15$ ,  $A_2 = 8.5E+11$ ,  $A_3 = 3E+11$ ,  $A_4 = 9E+08$ ,  $A_5 = 8E+08$  mole/m<sup>3</sup>s.

Figure 7.29 presents the regeneration of a filter loaded with 0.76 kg B20-50 ppm fuel and filter inlet temperature of 355 °C. The soot starts to oxidize when a temperature level of 330 °C is achieved resulting to a filter backpressure drop of 92 mbar in a period of 181 s which is expressed as a 0.51 mbar/s filter pressure drop reduction rate. The temperatures in the periphery are lower about 10 °C, because of the heat losses through the periphery to the ambient air. Furthermore, maximum filter central and peripheral wall temperatures of 490 °C and 480 °C respectively are reported at 150 s. It is obvious that there is no significant delay between the onset of regeneration at the central and peripheral channels. It should be mentioned that, during B20-06 regeneration experiment the lowest temperatures, of all the B20-50 ppm experiments, were reported. Frame by frame analysis, as shown in Figure 7.30, indicates that B20-06 regeneration had a total duration of 181 s and the filter’s monitored surface temperature transition from the selected characteristic thresholds of 330 °C to 370 °C, frame (a) and frame (g), respectively, was completed in 130 s. There are also 2 regeneration wave fronts, start from the 2<sup>nd</sup> section of the filter and move downstream to filter exit. Comparing these wave fronts, it becomes obvious that the 2<sup>nd</sup> wave front, frames (h) to (r), is significantly weaker than the 1<sup>st</sup> wave front. Another important observation is related with the minimum number of hot spots. A possible explanation is the lower filter wall temperatures. This regeneration unexpectedly evolved as a less enhanced one, in spite of the fact that the initial conditions seemed favorable for an enhanced regeneration with observable peaks.

Start of Regeneration

Exhaust gas



End of Regeneration

**Figure 7.28 B20-05.** Sequence of 18 infrared thermograms showing the evolution of regeneration with B20-50 ppm fuel (loaded fuel mass, 0.99 kg). Also total duration (177 s) and interval temperature transition (from  $T_{\text{surf,max}} = 330 \text{ }^\circ\text{C}$  to  $370 \text{ }^\circ\text{C}$  in 45 s) duration are presented.

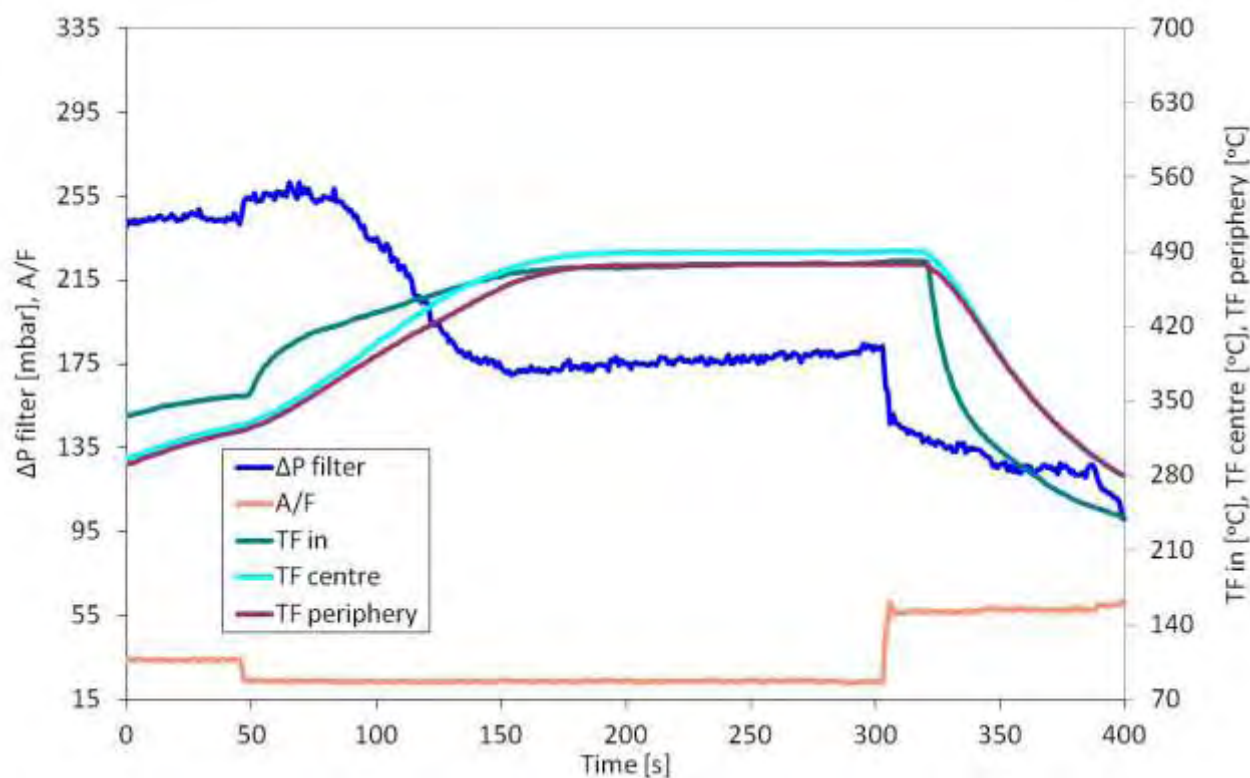


**Figure 7.29 B20-06.** Measured temperatures along filter's diameter near channels exit together with filter backpressure, filter inlet temperature and A/F ratio are presented during a high mass flow rate regeneration (14g/s) performed at 3250 rpm/22.2 Nm for a filter loaded (0.76 kg consumed fuel mass) with B20 fuel including 50 ppm Ce dose.

The last regeneration of B20-50 ppm set of experiments with the lowest loading level but with the highest inlet and filter wall temperatures is presented in Figure 7.31. During this experiment the filter was loaded with 0.67 kg B20-50 ppm fuel with filter inlet temperature of 416 °C. The soot starts to oxidize when a temperature level of 420 °C is achieved resulting to a filter backpressure drop of 100 mbar in a period of 189 s which is expressed as a 0.53 mbar/s filter pressure drop reduction rate.

The temperatures in the periphery are about 14 °C lower, because of the heat losses of the uninsulated filter to ambient air. Furthermore, maximum filter central and peripheral wall temperatures of 543 °C and 529 °C respectively are reported at 5990 s.

Frame by frame analysis, as shown in Figure 7.32, indicates that B20-07 regeneration had a total duration of 189 s and the face temperature increase from 330 °C to 370 °C, frame (a) and frame (k) and from 370 °C to 410 °C, was completed in 101 s and 70 s respectively. There are also 2 not so visible regeneration wave fronts, which start from the 2<sup>nd</sup> and 3<sup>rd</sup> section of the filter, respectively, and move downstream to filter exit. As it can be seen, there are a lot of hot spots on filter's surface which leads to an uncontrolled regeneration. The most representative frames are frames (f) and (h).

Start of Regeneration

Exhaust gas

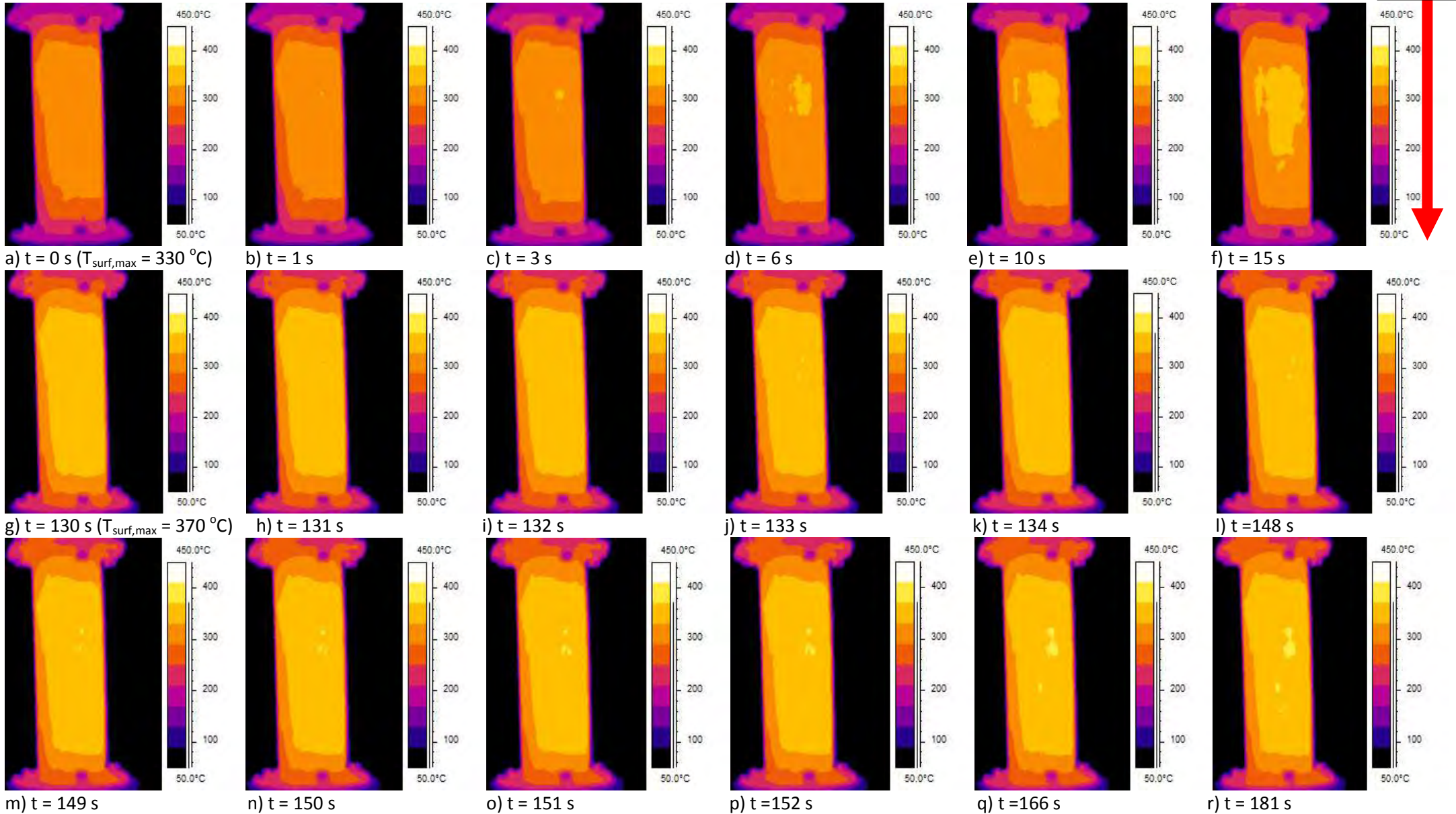


**Figure 7.30 B20-06.** Sequence of 18 infrared thermograms showing the evolution of regeneration with B20-50 ppm fuel (loaded fuel mass, 0.76 kg). Also total duration (181 s) and interval temperature transition (from  $T_{\text{surf,max}} = 330$  °C to 370 °C in 130 s) duration are presented.

End of  
Regeneration

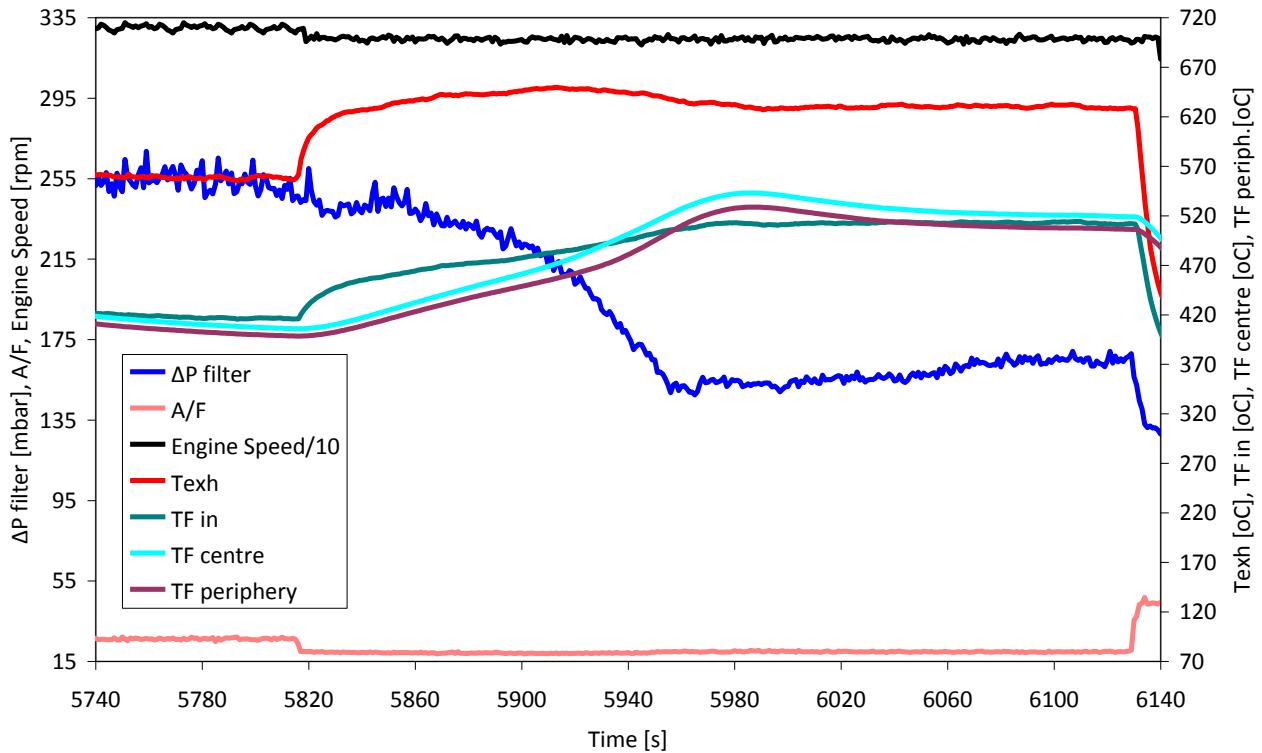


**Figure 7.31 B20-07.** Measured temperatures along filter’s diameter near channels exit together with filter backpressure, engine speed, engine outlet temperature, filter inlet temperature and A/F ratio are presented during a high mass flow rate regeneration (14g/s) performed at 3250 rpm/22.2 Nm for a filter loaded (0.67 kg consumed fuel mass) with B20 fuel including 50 ppm Ce dose.

Frame by frame regeneration analysis results are summarized in Table 7.6.

**Table 7.6.** Results from the processing of infrared images in the case of B20-50 ppm Cerium doped fuel.

Fuel	Fuel mass consumed during loading [kg]	Regeneration duration [s]	Regeneration rate [mbar/s]	Transition time from $T_{surf,max} = 330\text{ }^{\circ}\text{C}$ to $370\text{ }^{\circ}\text{C}$	Transition time from $T_{surf,max} = 370\text{ }^{\circ}\text{C}$ to $410\text{ }^{\circ}\text{C}$
B20-07	0.67	189	0.53	101	70
B20-06	0.76	181	0.51	130	-
B20-05	0.99	177	0.68	45	-
B20-04	1.08	129	0.56	57	-
B20-03	1.26	65	1.34	-	-
B20-02	1.42	120	0.96	55	-
B20-01	1.57	94	1.2	30	-

Based on these results, the increase of filter loading level, between B20-06 and B20-01 experiments, induced a decrease of the total regeneration duration and of the transition time between the characteristic temperature thresholds of  $330\text{ }^{\circ}\text{C}$  to  $370\text{ }^{\circ}\text{C}$ . Moreover, it induced a significant increase in the filter backpressure reduction rate. B20-04 results indicated an erratic regeneration. The effect of a higher filter inlet temperature was clearly observable in the B20-07 experiment, led to the highest measured temperatures on filter’s surface.

Start of Regeneration

Exhaust gas

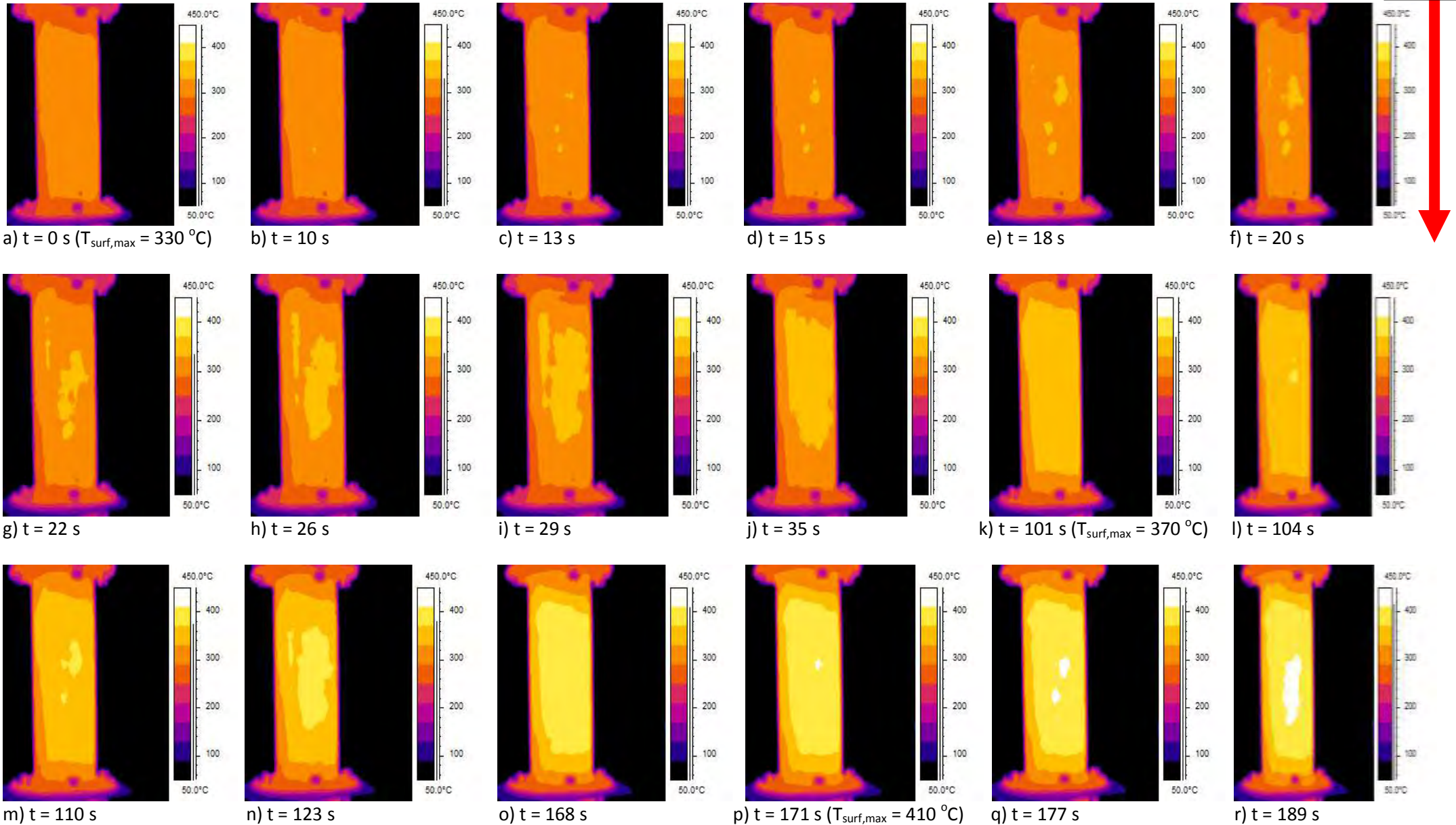


**Figure 7.32 B20-07.** Sequence of 18 infrared thermograms showing the evolution of regeneration with B20-50 ppm fuel (loaded fuel mass, 0.67 kg). Also total duration (189 s) and interval temperature transition (from  $T_{\text{surf,max}} = 330$  °C to 370 °C and 410 °C in 101 s and 70 s respectively) duration are presented.

End of  
Regeneration

Summarizing the results of the B20 experiments, we can state the following basic findings:

- Seven transient regeneration tests were performed at one high exhaust mass flow rate engine operation point, 3250 rpm/22.2 Nm, with markedly different levels of filter inlet temperature and filter loading.
- In all experiments, it was observed that the catalytic soot oxidation initiates at about 330 °C - 420 °C, and the temperatures at the periphery were about 13 °C lower, because of the heat losses of the uninsulated filter to the ambient air, and there were 2 regeneration wave fronts started from the 2<sup>nd</sup> section of the filter.
- As expected the increase in filter loading levels leads to faster regenerations with higher peak temperatures.
- The model is capable to predict temperatures inside the filter with high accuracy. As expected the 1D model does not successfully predict the evolution of filter during regeneration. The model predicts a slower reduction to the pressure drop as the regeneration initiates. The reason could lie in the fact that this initial phase of regeneration is associated with a VOF desorption process that is responsible for the rapid backpressure decrease. VOF content is higher in the case of B20-50 ppm enhancing this process.
- Hot spots are clearly observable, using B20-50 ppm Cerium doped fuel, and increase in accordance with the increase in the filter inlet temperature.

Comparative basic findings for B0 and B20 fuel:

- Soot oxidation temperature was 387 °C and 367 °C in the case of B0-50 ppm and B20-50 ppm fuel respectively. It is obvious that there is a decrease 20 °C using B20 blend, leading to lower temperatures inside filter walls and on filter's surface during regeneration process. This observation, which is in accordance with other researchers [64, 159], can be mainly explained by the higher reactivity of biodiesel soot.
- Comparing B0-02 with B20-02, it is obvious that at the same regeneration duration higher filter backpressure decrease is achieved with lower filter wall temperatures, about 28 °C, using B20-50 ppm Cerium doped fuel due to the higher reactivity and the higher Cerium quantity in the accumulated B20 soot layer.
- Another difference is related with the evolution of the regeneration wave front. B20 wave fronts start from the second section of the filter (middle zone) and move downstream in accordance with the exhaust gas flow. On the other hand, B0 wave fronts start from the 2<sup>nd</sup> and 3<sup>rd</sup> section respectively and move downstream (1<sup>st</sup> wave front) and then upstream (2<sup>nd</sup> wave front), namely, opposite to the exhaust gas flow.
- Infrared regeneration analysis shown that B20 blend enhances the appearance of erratic regenerations creating significant number of hot spots at different positions of the filter's surface due to the higher VOF content and the soot reactivity.
- Soot mass reduction prediction is more accurate using B20 blend, which is expressed as a cleaner filter with lower filter wall temperatures.



### 7.3 Model and reaction scheme employed

The in-house model CATWALL v4r3b [160] was employed in the computational investigations. This is an 1-D model with the following reaction scheme:

**Table 7.7.** Reaction and rate expressions of the regeneration model

	Reaction	Rate expression
1	$C + O_2 \longrightarrow CO_2$	$r_1 = k_1 \gamma$
2	$C + 0.5O_2 \longrightarrow CO$	$r_2 = k_2 \gamma$
3	$C + 4CeO_2 \longrightarrow 2Ce_2O_3 + CO_2$	$r_3 = k_3 \psi$
4	$C + 2CeO_2 \longrightarrow Ce_2O_3 + CO$	$r_4 = k_4 \psi$
5	$Ce_2O_3 + 0.5O_2 \longrightarrow 2CeO_2$	$r_5 = k_5 (1 - \psi)$
	Where: $k_i = A_i e^{-E/R_g T}$ $i=1...5$	

More details on the model's characteristics and capabilities are contained in [71, 72, 158, 161, 162]

### 7.4 Filter geometry and model input data

The main filter geometry and input data of the simulation model are summarized in the following table:

**Table 7.8.** Model main input data (DPF parameters).

# DPF PARAMETERS	
'monolith length [m]'	0.15
'monolith diameter [m]'	0.034
'cpi'	177
'plug length [m]'	0.005
'substrate thickness [m]'	0.0006
'cp deposit [J/kgK]'	1.51E+03
'deposit density [kg/m <sup>3</sup> ]'	240
'deposit conductivity [W/mK]'	2.10E+00
'wall density [kg/m <sup>3</sup> ]'	1800
'wall permeability [m <sup>2</sup> ]'	1.7E-13
'soot permeability [m <sup>2</sup> ]'	2.02E-10
'initial filter loading [kg]'	0.0025
'initial filter temperature [°C]'	346

### 7.5 Tuning of kinetics parameters

The kinetics parameters of the model were adapted using those of Stratakis et al [158] as a starting point. The final values after manual tuning to match the experimental results of the previous section are presented in the following Table:

**Table 7.9.** Final kinetic parameters after manual tuning to the experimental results (B0-50ppm and B20-50 ppm experiments respectively).

# REACTION SCHEME	B0		B20	
	A [mole/m <sup>3</sup> s]	E [kJ/mole]	A [mole/m <sup>3</sup> s]	E [kJ/mole]
'C + O2 --> CO2'	8.00E+16	190000	8.00E+15	190000
'C + (1/2)O2 --> CO'	8.50E+12	150000	8.50E+11	150000
'C + 4CeO2 --> 2Ce2O3 + CO2'	6.00E+11	110000	3.00E+11	110000
'C + 2CeO2 --> Ce2O3 + CO'	7.00E+09	95000	9.00E+08	80000
'Ce2O3 + (1/2)O2 --> 2CeO2'	8.00E+08	80000	8.00E+08	80000

For comparison, we present a graph with kinetic parameters estimated on the TGA by other researchers [74, 76]. These data are not directly comparable, since the data of Stratakis refer to soot samples taken directly from the filter, whereas the data of Lu et al. to samples collected in 47 mm quartz filters from diluted exhaust.

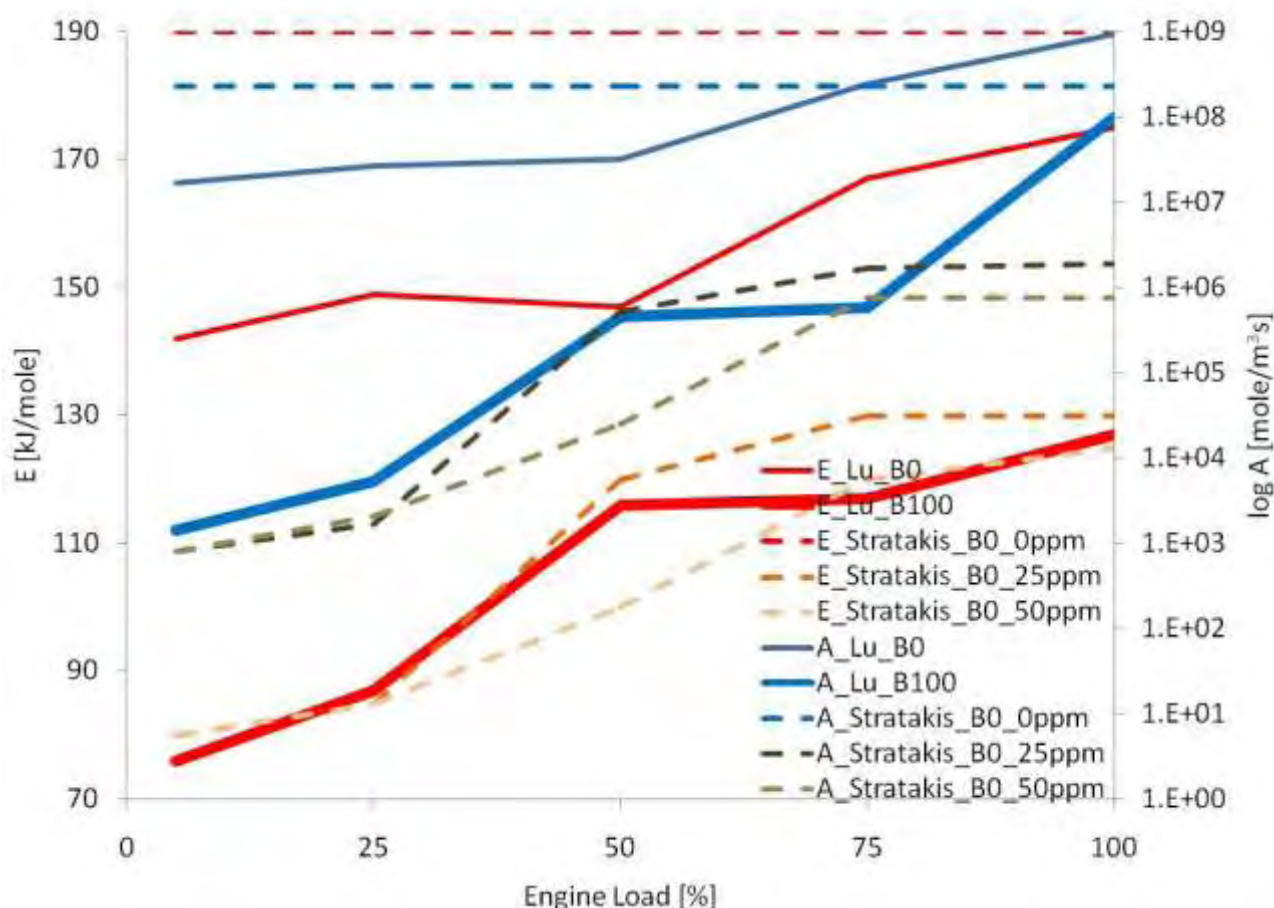


**Figure 7.33.** Comparison of kinetic parameters estimated in the TGA by other researchers [74, 76]. The data of Stratakis refer to soot samples taken directly from the filter, whereas the data of Lu et al. to samples collected in quartz filters from diluted exhaust.

The following remarks can be made on the comparison of computed and measured evolution of the regenerations of the previous section:

- The values of E determined from previous TGA experiments produced a satisfactory prediction of the full-scale regeneration process in the filter for both of the used fuels.
- During all the experiments, a discrepancy between the measured and the predicted filter backpressure was observed. The model predicts a slower reduction to the pressure drop.
- The reason would be lie in the fact that the initial phase of the regeneration is associated with a VOF desorption process that is responsible for the rapid backpressure decrease. This situation is not predictable by the 1D pressure drop model which considers an average soot permeability value during the whole regeneration process.
- As a general rule of thumb, the catalytic regeneration kinetics (frequency factors) were tuned to represent the experimentally determined, low temperature (catalytic) regeneration behavior of the filter.

## 8. Impact of biodiesel on fuel system components durability

In this chapter, the impact of high and low percentage biodiesel blends on fuel system components durability of modern and conventional diesel engines is presented. In this thesis, high percentage biodiesel blend, B70, and low percentage biodiesel blends, B20 and B40, was used in a PSA DW10ATED HDi and a Ruggerini RF91 DI diesel engine, respectively. In the case of DW10, the engine was subjected to steady state and transient testing with the B70 fuel for a total of 30 h in the period 2008–2010. This prolonged use led to the failure of the high pressure pump and pressure regulator and the wear of injector's moving parts. On the other hand, RF91 was subjected to steady state testing with B20 and B40 fuels for a total of 13 h and 2 h respectively in the period December 2011-January 2012 without any operation problems.

### 8.1 Introduction

Biodiesel is defined as the mono alkyl esters of long chain fatty acids derived from vegetable oils or animal fats. The term Fatty Acid Methyl Ester (FAME) [163] is often used as a generic expression for the trans-esters of these naturally occurring triglycerides which find application as either a replacement for or a blending component for use with fossil derived diesel. There is a great potential for significant variation in product quality and specification for products generally described as biodiesel. Research has shown that there are fuel quality, handling, storage and vehicle operability requirements which need to be addressed where biodiesel is used in the automotive diesel vehicle fleet. This has led to numerous initiatives by fuel producers, Original Equipment Manufacturers (OEMs) and their Industry Associations to publicize their issues and to lobby fuel legislators to include a number of parameters in regional biodiesel specifications.

In the United States, this has led to the development of a specification for biodiesel, ASTM D6751-03 [164]. This standard is intended to address the quality of pure biodiesel (B100) when used a blend stock of 20% lower. Recently, ASTM D7467-10 specification [165] was developed in order to cover fuel blend grades of 6 to 20 volume percent (%) biodiesel with the remainder being a light middle or middle distillate diesel fuel. Biodiesel blends are generally referred to as BX, where X is a number which denotes the volume percent of biodiesel incorporated in the finished fuel. The ASTM D6571 standard specifies biodiesel as long chain fatty acid methyl esters from vegetable or animal fats containing only the alcohol molecule on one ester linkage. This effectively excludes raw or unrefined vegetable oils which contain three ester linkages. Within the United States and the European Union soybean oil [166] and rapeseed oil [27] respectively are the leading source biodiesel feedstock. The European Committee for Standardization developed a uniform standard, EN14214 [118], to replace the respective national standards.

The compatibility of seal and hose materials commonly encountered in automotive fuels, using conventional hydrocarbons fuels, has long been established and elastomer manufacturers are able to make recommendations for their use. Studies [140, 167] and in use experience has shown that certain seals, gaskets and hoses may degrade under certain operating conditions in contact with B50 or high percentage blends. Most elastomer materials will undergo a physical or chemical change when in contact with fuel. The degree of change depends upon the tendency of the material to absorb a fuel or on compounds being dissolved or extracted by the fuel. This can lead to a number of changes in the physical characteristic of the material including swelling, shrinkage, embrittlement and changes in tensile properties. The limit of a permissible physical change varies with the application and some degree of change can usually be tolerated. For example, a material that swells in a fuel or suffers a decrease in hardness may well continue

to be fit for purpose for a long time as a static seal. However, in dynamic applications, swelling may result in increased friction and wear and so a lower degree of volume change can be tolerated.

Effects to produce low and ultra low sulfur fuels by hydro-treatment have resulted in the removal of polar nitrogen and oxygen compounds and hence reduced the good lubricating properties of diesel fuel. Several investigations have reported that biodiesel can significantly improve lubricity of low sulfur diesel fuel at relatively low concentrations. In addition, it has been reported that the use of biodiesel can reduce the concentration of metal wear particles and increase engine life span [168]. However, it has also been reported that the formulation of corrosive materials (such as organic acids, water and methanol), polymers, gum formation, thermal and oxidative instability and water separation may give rise to engine operability problems. The following engine operability problems have been identified during extensive field trials as being caused by these fuel characteristics:

- corrosion of fuel Injection components
- elastomeric seal failures
- low pressure fuel system blockage, including in tank pipe and fuel filter
- fuel injector spray hole blockage
- increased dilution and polymerization of engine sump oil
- pump seizures due to high fuel viscosity at low temperatures

Besides of the fuel system durability problems, use of biodiesel can lead to serious engine problems, including piston ring sticking and piston and cylinder head deposits.

As a consequence, OEM's and their Industry Associations have been cautious in their acceptance of biodiesel and biodiesel blends [28, 169].

The effect of fuel on engine components wear is very important as it affects the engine durability, fuel economy, and emissions. The main causes of wear are metal to metal contact, the presence of abrasive particles, and attack by formed corrosive acids during the combustion process. The lubricant transports protective chemicals to the sites where they are needed and transports waste products away from the sites where they generated [170]. Several researchers reported that soot is one of the main factors that increases engine wear as it interacts with oil additives and reduces the effectiveness of antiwear additives [171-174]. This results in breakdown of the oil permitting contact between soot particles and the engine surfaces. Under these conditions the lubricant boundary layer is about 0.001-0.05  $\mu\text{m}$  thick. However, soot particles have diameters ranging from 0.01  $\mu\text{m}$  to 0.8  $\mu\text{m}$  and could therefore cause abrasive wear. Boundary lubrication occurs at top dead center (TDC) and bottom dead center (BDC) positions of the cycle and hence, maximum wear occurs at these positions [172, 175].

Cylinder liner wear mainly corresponds to wear of the surface topography in the peak and core zones. The valley zone is less affected. Surface wear at TDC and BDC locations is more severe than the middle [176]. Atomic absorption spectroscopy is one of the most commonly used techniques for qualitative and quantitative analysis of wear debris in techniques oil [168, 177-180].

Peterson et al. [64] reported 1000 h EMA engine test with three engines fueled with B25, B50 and B100 blends of hydrogenated soy ethyl ester (HySEE) and observed lower wear and cleaner internal engine parts with B100 HySEE. Ziejewski [181] conducted 200 h EMA durability test with sunflower methyl ester as a fuel on turbocharged intercooled DI engine and compared it with base line mineral diesel data. Initial and final measurements on engine did not indicate any significant wear, less carbon buildup in the intake ports, intake valve tulips, and comparable carbon buildup in the exhaust port with methyl ester. Slightly more

carbon deposits were observed on the valve stems and on the cylinder sleeves above the ring travel area and piston top land in the case of methyl ester fuel. Agarwal et al. [168, 178] found less carbon deposits and lower wear of engine parts in the case of B20 linseed oil methyl ester fueled engine during endurance test on a constant speed DI diesel engine. Kalam and Masjuki [180] performed 100 h test with half throttle setting at constant speed (2000 rpm) for different blends of palm oil methyl ester containing anti-corrosion additive and observed lower wear with B15 blend. Similar results have also been reported by Kenneth et al. [182] and Kearney et al. [183] after different conducted field trails by using B20 blend. In addition, Chase et al. [184] did not find significant engine wear after long test of 322,000 km using B50 HySEE blend.

On the other hand, Clark et al. [185] reported comparable deposits on engine wear, however slightly different in color and texture, with the methyl ester engine experiencing greater carbon and varnish deposits on the pistons. The physical measurements and inspection showed no noticeable difference. No wear was measurable on the cylinder walls (liners) and pistons, and no rings were found stuck in the grooves. In all cases, the original honing marks in the liners were clearly visible. Slightly higher levels of aluminum and lead in lubricating oil were reported with methyl ester. Fraer et al. [186] reported higher sludge formation on the valve deck around the rocker assemblies and more injector replacement for B20 fueled engine particularly for Mack tractor engines. Higelin and Charlet [187] reported heavy deposits in the combustion chamber and injector nozzle tip after a 20 h test with sunflower oil as fuel. Their test was performed at idle speed and low load. In the same way, National Biodiesel Board [188] has reported that in 1000 h durability test on engine with B20 soyester blend caused serious technical problems like failure of engine pump, softening of fuel system seals, deposits on air box covers, piston components and injectors.

Furthermore, some truckers have complained that fuel filter plugging is increasing as animal fat and soybean-based fuels are being introduced nationwide [189]. Based on the previous paragraphs, it is obvious that fuel system problems, including filter plugging by use of B100 fuel have been mainly documented in the United States. According to a survey conducted by the Minnesota Trucking Association [190], 62% of 900 fleets said they had experienced fuel filter plugging. In most of the studies, the most common problems were fuel filter plugging and injector coking.

Biodiesel can also affect the condition of the lubrication oil. An engine equipped with an active regenerated DPF can lead to fuel dilution of the engine oil. The dilution of fuel in engine oil is a function of the engine operating strategy and properties of the fuel used. Biodiesel is made of fatty acid methyl esters which have different physical attributes compared to conventional diesel: higher surface tension, higher viscosity and lubricity and lower volatility. The mechanism for oil dilution, regardless of fuel used, is driven by the low volatility components in the fuel [20]. These low volatile components require longer vaporizing after post-injection, which may lead to deposition on the cylinder walls during combustion. As the piston moves down during the power stroke, these deposits can be pushed down into the crankcase. Fuel dilution of motor oil can be detrimental to an engine and its components. Viscosity is an important factor in the quality of engine oil. As the viscosity decreases metal to metal contact can occur causing catastrophic failure of bearings and the wearing of the pistons and rings. Nowadays, the engine oil viscosity can be measured using specific sensor provided by global manufacturers like Delphi Corporation. There are also commercial sensors in order to monitor engine oil condition [191].

These sensors electrically stimulate the oil at a particular low voltage and frequency that is designed to obtain the greatest response from both additives and oxidation by products in the oil. The oil itself does not react electrically. The reading is obtained by measuring the overall conductivity of the oil and compensating for changes due to variations on the oil temperature.

In this thesis, we investigated the impact of high (B70) and low percentage biodiesel blends (B20 and B40) on 1<sup>st</sup> generation common rail injection system and pump in line nozzle injection system respectively. It should be mentioned that the experiments were conducted on unmodified diesel engines. The most serious failure was that of the common rail high pressure fuel pump. The results of the biodiesel impact are presented by means of photos, with and without magnification, of injection system components.

## 8.2 Fuel filter plugging

Following the fuel line, the first component of the injection system is the fuel filter, which consists of the box and the filter. Figure 8.1 and Figure 8.2 illustrate fuel filter's condition after 30 h operation with B70 blend. It is obvious that the filter totally plugged by sticky slurry causing problems in the fuel flow from the filter to the high pressure pump. This finding is in accordance with the reported results of other researchers and associations [189, 190, 192]. After that, the box was carefully cleaned and the filter was replaced.



**Figure 8.1.** Fuel filter box. Significant quantity of brown dense slurry was found at the bottom of the box.



**Figure 8.2.** Fuel filter condition after 30 h operation with B70 fuel.

### 8.3 Common Rail injector wear

The second easily affected component of the injection system is the injectors. The effect of biodiesel fuel on the long-term durability of fuel pumps or injectors is an important subject for all biodiesel fleet users since fuel injectors and especially high pressure pump are costly parts. A brand new set of DW10 common rail injectors is shown in Figure 8.3.



**Figure 8.3.** Brand new set of Common Rail injector (left) and closer view of injector nozzle (right).

On the other hand, Figure 8.4 presents injectors condition after the prolonged testing with B70 fuel. It is obvious that the nozzle body and the holes were totally covered by dense slurry.



**Figure 8.4.** Used Common Rail injectors (left) and closer view of the deposits (right).

In order to better understand the impact of biodiesel, each injector was analyzed by means of electric microscope. Several photos, magnification 10X, of the nozzle body, tip of the nozzle and nozzle holes area were taken. Figure 8.5 to Figure 8.8 indicate heavy oily deposits on injector nozzle disturbing the flow pattern of the injected fuel. Nozzle holes were totally covered except of the 1<sup>st</sup> injector, where the holes remained open. Based on these figures, 3<sup>rd</sup> and 4<sup>th</sup> injector seems to have serious operation problems.

Next step was the disassembling of the injectors according to official repair manual, as shown in Figure 8.9, Figure 8.10 and Figure 8.11.

The main components of a common rail injector are presented in Figure 8.11 and Figure 8.12. According to these figures, this type of injector consists of 2 parts, injector body and nozzle body. The most easily affected parts, besides the nozzle holes, are injector's moving components like needle, plunger and spring.



Following move was the cleaning of the injectors using laboratory's ultrasonic tank, Figure 8.12. The cleaning procedure included several ultrasonic baths of each component using commercial cleaning fluid.



**Figure 8.5.** 1<sup>st</sup> cylinder Common Rail injector magnified view after 30 h operation with B70 fuel.

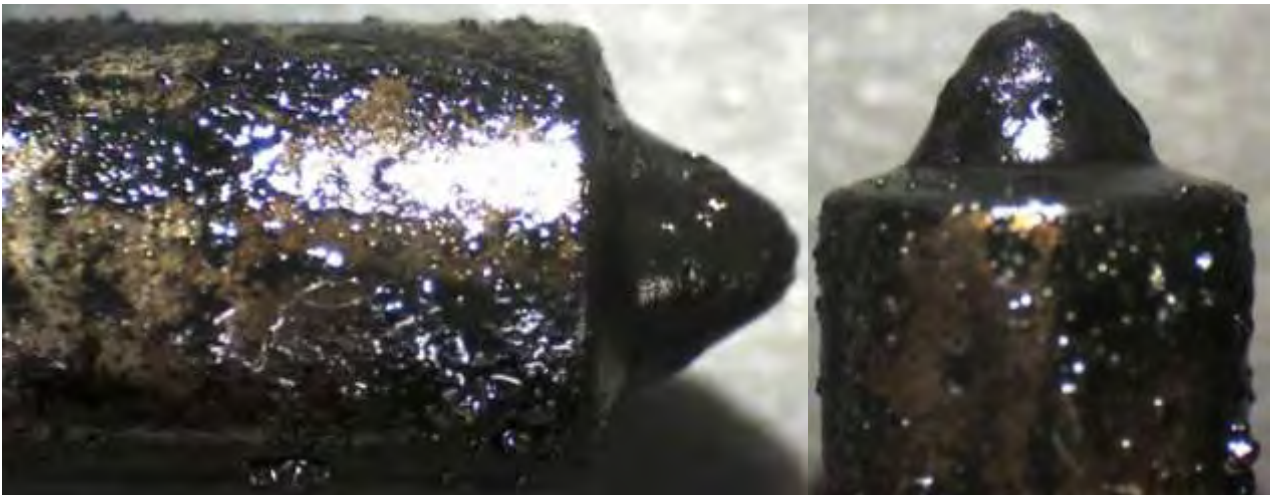


**Figure 8.6.** 2<sup>nd</sup> cylinder Common Rail injector magnified view after 30 h operation with B70 fuel.

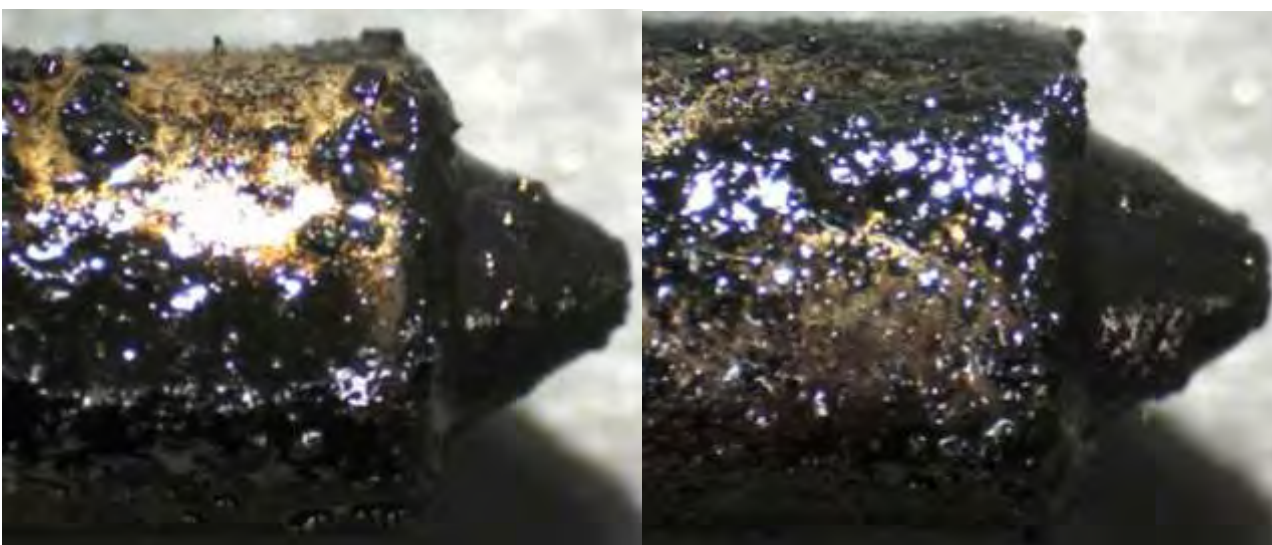


**Figure 8.7.** 3<sup>rd</sup> cylinder Common Rail injector magnified view after 30 h operation with B70 fuel.

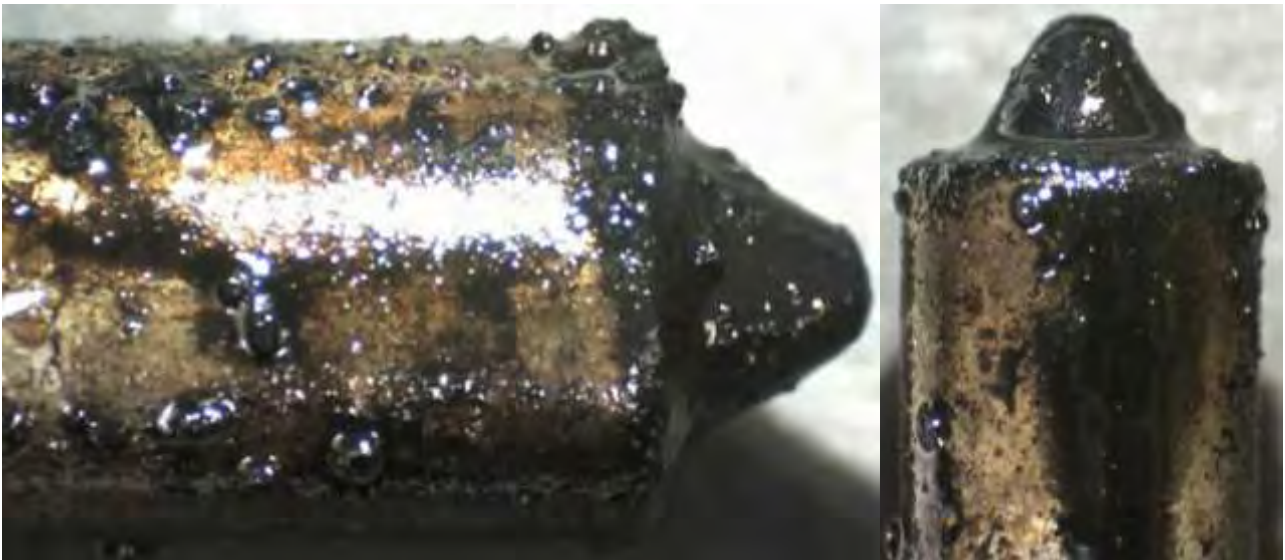


**Figure 8.8.** 4<sup>th</sup> cylinder Common Rail injector magnified view after 30 h operation with B70 fuel.



**Figure 8.9.** Disassembly view of the injectors (left) and closer view of the nozzle (right).

After the cleaning procedure, it was necessary to search carefully the surfaces of each part for extensive wear by means of electric microscope. Figure 8.13 to Figure 8.16 present several photos of clean nozzle holes areas and plungers. It becomes obvious that, the prolonged testing led to extensive corrosion of the plungers, as indicated by the red circles.

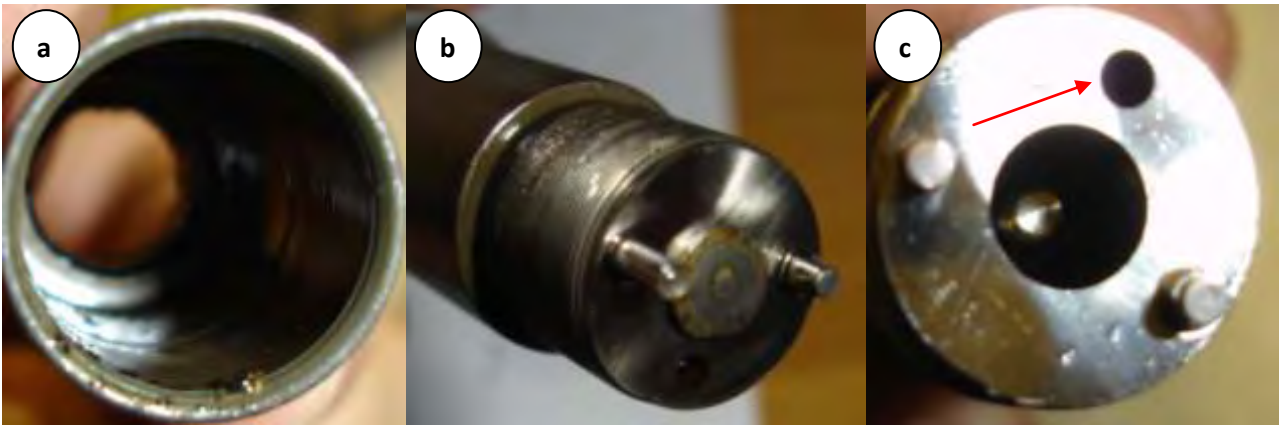


**Figure 8.10.** Nozzle house (a), plunger and alignment pins (b) and moving piston and fuel return hole (c).



**Figure 8.11.** Common rail injector components. From right to left we have, injector body including supply and return fuel line, spring, plunger, nozzle body including needle, nozzle house and washer.



**Figure 8.12.** Cleaning procedure using ultrasonic bath (left) and disassembly view of the clean injectors (right).

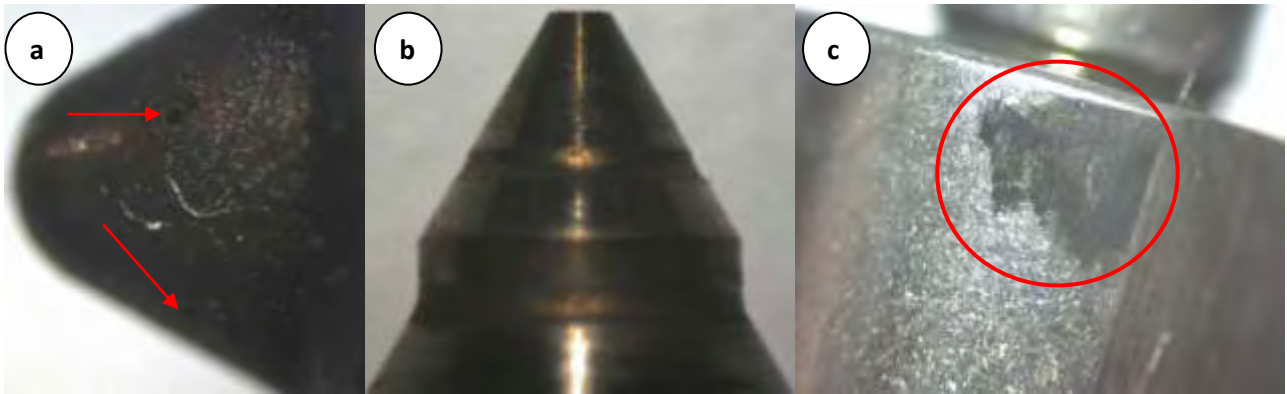


**Figure 8.13.** After cleaning magnified view of the 1<sup>st</sup> injector nozzle holes (a), needle tip (b) and plunger (c).



**Figure 8.14.** After cleaning magnified view of the 2<sup>nd</sup> injector nozzle holes (a), and plunger (b) and (c).



**Figure 8.15.** After cleaning magnified view of the 3<sup>rd</sup> injector nozzle holes (a), and plunger (b) and (c).

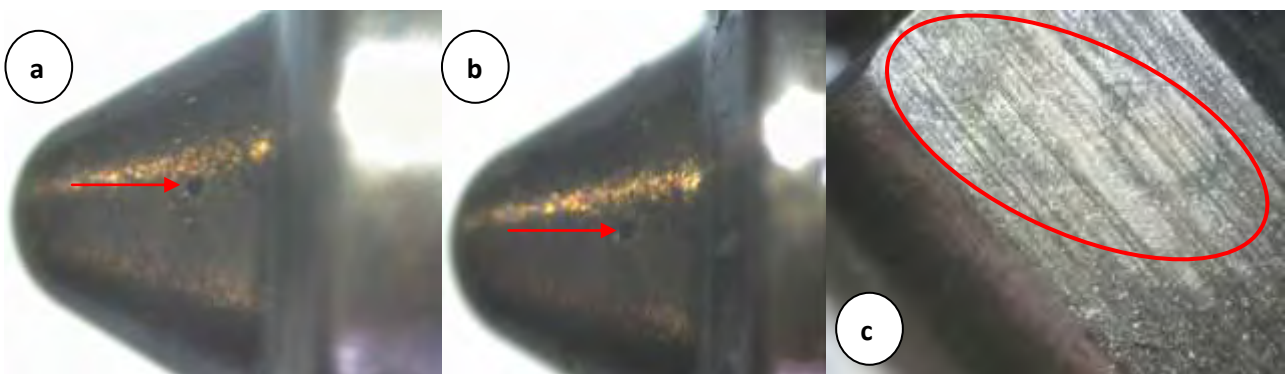


**Figure 8.16.** After cleaning magnified view of the 4<sup>th</sup> injector nozzle holes (a) and (b), and plunger (c).

## 8.4 Pressure regulator replacement

After the cleaning, inspection and replacement of the injectors, we inspected and finally replaced the high pressure regulator which is found at the discharge side of this 1<sup>st</sup> generation high pressure pump, Figure 8.17.

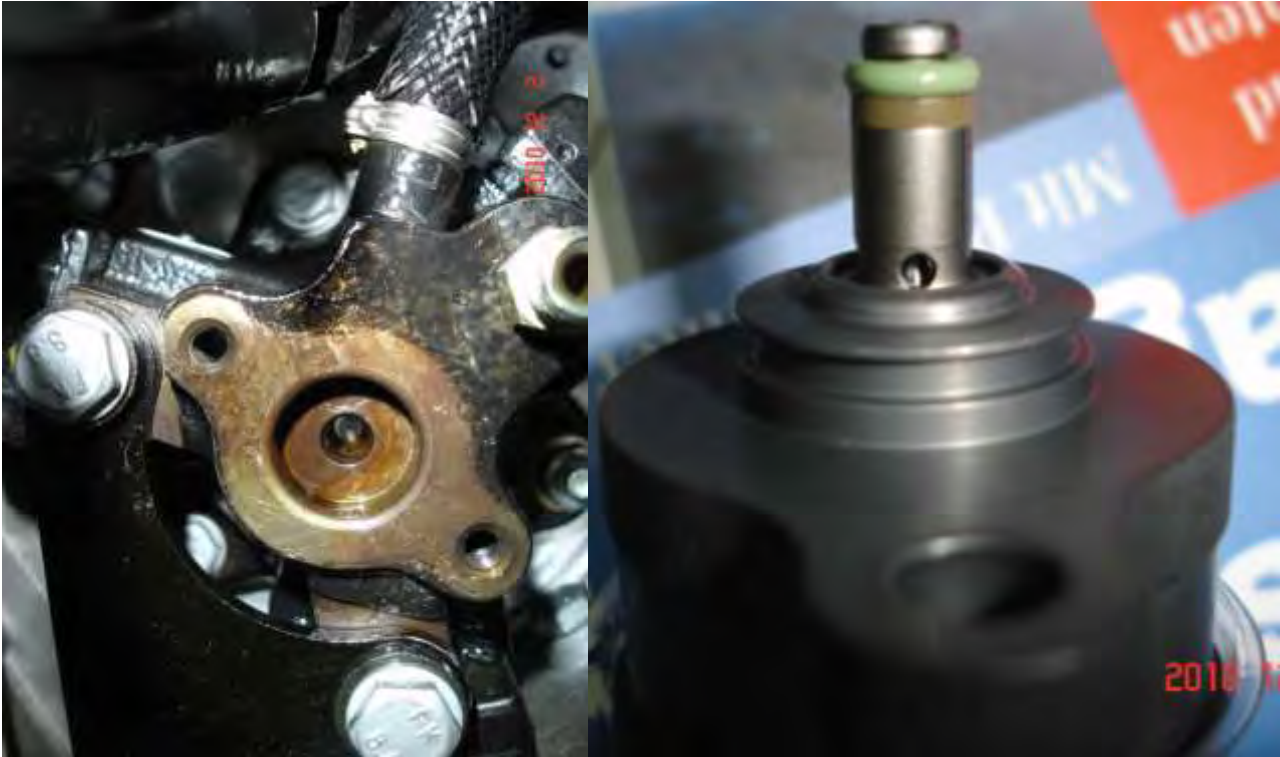


Figure 8.17. Pressure regulator place (left) and brand new one (right).

## 8.5 Common Rail high pressure pump replacement



Figure 8.18. Brand new Bosch high pressure pump (left) and model characteristics (right).

As it was mentioned above, the most serious failure was that of the high pressure pump. A summary of the diagnosis procedure is presented below. In October 2010, the engine refused to start and we made a thorough inspection of the fuel lines and injection system. Our findings were presented above. The most serious failure was that of the high pressure fuel pump, Figure 8.18. Starting from the fuel filter, Figure 8.1

and Figure 8.2, we observed the existence of a significant quantity of dense slurry rich in fatty esters. After cleaning the fuel filter we proceeded with removing the fuel injectors. The injector's nozzle and holes covered by heavy oily carbon deposits. We proceeded with disassembling the set of injectors. A certain degree of the same oily deposit was found in the needle tip. After installing a new set of fuel injectors the engine still could not start. Moreover, the indication from the INCA interface was zero rail pressure. Thus, we continued with inspection of the high pressure fuel lines and the common rail without any important findings. We continued upstream to the high pressure fuel pump and found out that all fuel was diverted to the return line.

Next, we removed and inspected the pressure regulator which is found at the discharge side of this 1st generation fuel pump (Figure 8.17 left, with the regulator removed from the pump). We mounted a new pressure regulator (Figure 8.17 right) however the engine again failed to start and all fuel diverted to the return line. Finally, we were obliged to install a new fuel pump (Figure 8.18) and the engine now runs smoothly. We did not yet proceed to disassembly of the failed high pressure fuel pump to find the exact cause of the pump failure.

Based on the above findings, which agree experience from other researchers [140, 167], it would not be wise to exploit the full range of biodiesel blending with this type of engines, until the required fuel system modifications are decided by the manufacturers. A maximum blending of 30% on the average would be a more conservative approach.

Taking into account our previous findings, we employed the same procedure on RF91 mechanical injector. Figure 8.19 presents a closer view of the injector after 40 h operation with diesel fuel. The nozzle body and the holes were not covered by carbon deposits, as reported in the case of B70 blend. On the other hand, Figure 8.20 and Figure 8.21 indicate the impact of biodiesel on injector durability. As shown in these figures injector had the same view with that presented in paragraph 8.3. Nozzle holes area and nozzle body were totally covered by oily deposits and white additive ash.

Next, we cleaned and inspected again the injector using ultrasonic tank and electric microscope respectively. The final view of the nozzle body is presented in Figure 8.22. RF91 engine continues to run smoothly using different biodiesel blends, B10, B20 and B40 including 50 ppm cerium doped fuel additive.



**Figure 8.19.** RF91 injector closer view after 40 h operation with conventional diesel fuel (B0 and 0 ppm fuel additive).

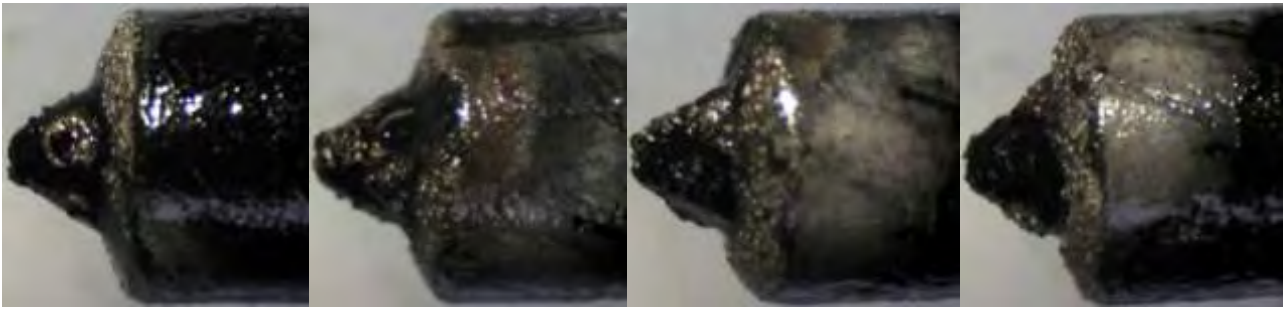


**Figure 8.20.** RF91 nozzle tip, magnified view, after 15 h operation with B20 and B40 including 50 ppm cerium doped fuel additive.

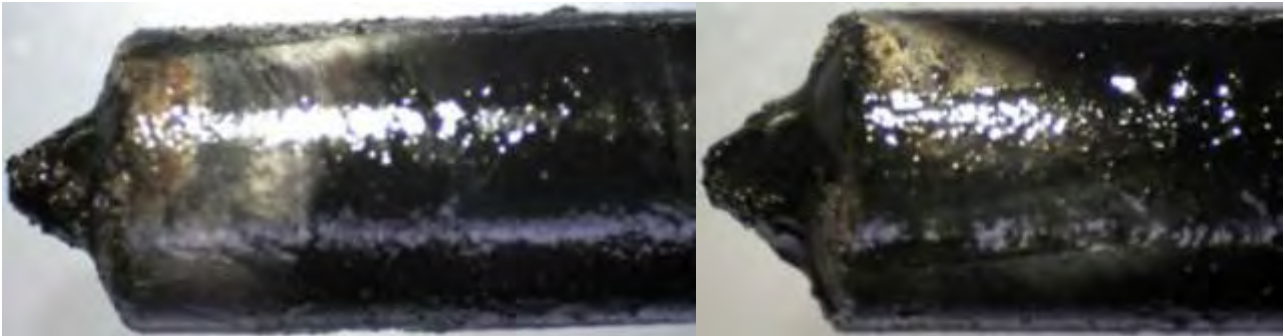


**Figure 8.21.** RF91 nozzle body, magnified view, after 15 h operation with B20 and B40 including 50 ppm cerium doped fuel additive

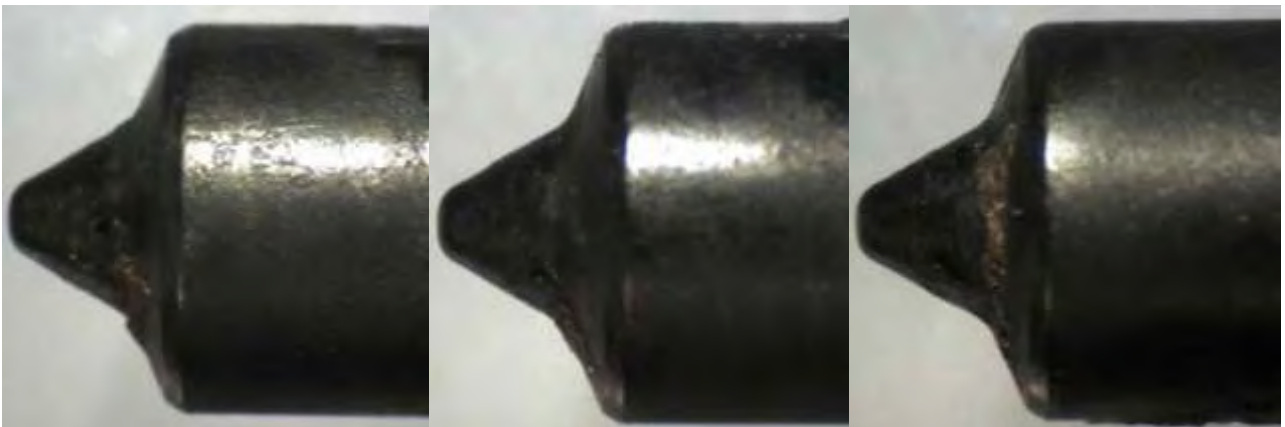


**Figure 8.22.** After cleaning magnified view of the injector nozzle holes and body.

## 9. Experimental investigation of the effect of biodiesel blends on the characteristics of fuel sprays

In this chapter, the injection characteristics of biodiesel fuel in low injection pressure conditions (Diesel burner) are presented. Experiments were conducted at various blending ratios, B0, B20, B40, B60, B80 and B100. The atomization characteristics of biodiesel blended fuels were investigated in terms of injection velocity, Sauter Mean Diameter, velocity and diameter distributions by using spray visualization system and 1D Laser Doppler Velocimetry device. The break-up characteristics are mainly influenced by the Weber number which is lower for biodiesel blends than with conventional diesel. The results indicate an increase in the Sauter mean diameter of droplets and a respective decrease in mean droplet velocity with increasing blending ratio. This is due to the viscosity and surface tension of the biodiesel being higher than those of conventional diesel fuel.

### 9.1 Introduction

The effects of biodiesel blends on the injection characteristics have been studied by other researchers. The atomization characteristics of biodiesel fuel such as spray tip penetration and mean droplet size play an important role in engine performance and emission characteristics. Moreover, biodiesel blends have different physical properties and their atomization characteristics [193, 194] need to be further investigated. Ramadhas et al. [195] studied correlations between the physical properties of biodiesel blends and their combustion characteristics in conventional engines. To study the effect of the high viscosity of biodiesels on the spray characteristics, Lee and Park [196] compared the process of spray development between the conventional diesel and biodiesel blends using a common rail injection system. Their results indicated that the spray tip penetration increase with the increase in mixing ratio of the biodiesel because the biodiesel blends are more difficult to atomize in comparison to conventional diesel due to their higher surface tension.

The purpose of this chapter is to investigate the effect of biodiesel blends on the spray characteristics in a conventional diesel burner injector by means of calculations and several set of LDV experiments.

### 9.2 Influence of fuel properties on droplet diameter

Droplet size distribution for high pressure nozzles is hard to obtain and thus considered to be not very accurate. A major problem is that the spray is very thick so that the optical techniques are difficult to use. The various physical phenomena involved in pressure swirl atomization are highly complex, and many empirical correlations have been developed to formulate mean droplet size as a function of fuel properties. Correlations for Sauter Mean Diameter (SMD) are presented in the following equations:

$$SMD=1.605 \times 10^6 (\Delta p)^{-0.458} (\dot{m})^{0.209} (v)^{0.215} \left( \frac{A_{orf}}{A(t)_{eff}} \right)^{0.916}, \text{ Knight [197]}$$

$$SMD=2.33 \times 10^3 (\Delta p)^{-0.135} (\rho_a)^{0.121} (v)^{0.131}, \text{ Hiroyasu and Kabota [198]}$$

$$SMD=3.08 \times 10^6 (v)^{0.385} (\sigma)^{0.737} (\rho_l)^{0.737} (\rho_a)^{0.06} (\Delta p)^{-0.54}, \text{ El-Kotb [199]}$$

$$SMD=2.25 (\sigma)^{0.25} (\mu)^{0.25} (\dot{m})^{0.25} (\Delta p)^{-0.5} (\rho_a)^{-0.5}, \text{ Lefebvre [90]}$$



where,  $V$  is the injection fuel volume [ $\text{m}^3/\text{stroke}$ ],  $\dot{m}$  is the injection rate [ $\text{kg/s}$ ],  $A_{\text{orf}}$  is the area of nozzle holes [ $\text{m}^2$ ] and  $A(t)_{\text{eff}}$  [ $\text{m}^2$ ] is the effective area of nozzle holes at  $\Delta p$ . These correlations are not applicable to our experiments, which are steady-state ones at atmospheric pressure and with a burner instead of an engine injector.

### 9.3 Diesel spray dynamics

The fuel sprays used in direct injection reciprocating engines are unsteady, so that their characteristics vary with time [200]. Although, some of these sprays, such as those used in direct injected spark ignited engines, are of much lower pressure and momentum than the typical high momentum diesel spray. In this section, diesel spray development will be presented. As break up takes place for the first liquid out of the nozzle, the droplets encounter the undistributed flow field. The first droplets then quickly give up their momentum to the air and suddenly slow down. The next droplets formed at the nozzle now see air set in motion by the preceding droplets and thus do not show slow down as quickly. Due to that fact, it is possible to build up the entrained airflow and to allow the following droplets to penetrate farther downstream. Droplets formed later pass droplets formed earlier. The unsteady air motion induced by the exchange of momentum with the droplets sweeps fresh into the spray and transports vapor toward the tip of the spray.

### 9.4 Laser Doppler Velocimetry overview

Laser Doppler Velocimetry measures the velocity of small particles that are moving in the fluid of interest [201]. Assuming the particles are small, the velocity of these particles can be assumed to be the velocity of the fluid itself. The physical principle used to measure the particle velocities is the scattering of light by the particles. The intersection of the two laser beams (for each component of velocity) results in a fringe pattern-series of light and dark fringes. As a particle moves through the measuring volume, it scatters light when it crosses a bright fringe and scatters no light as it passes a dark fringe. This results in a fluctuating pattern of scattered light intensity with a frequency proportional to the particle velocity. Since the distance between fringes and the time for particle to go-from one fringe to the next are known, the measured signal frequency can be converted to velocity. The scattered light is collected by optics and converted to electrical signals by photomultiplier tubes. The frequency of the signal, known as Doppler frequency  $f_D$ , is measured and then velocity,  $u$ , is calculated by multiplying the frequency by the fringe spacing,  $\delta_f$ .

### 9.5 Test equipment and procedure

Fuel properties such as viscosity, density and surface tension affect on the spray evolution. Fuel injection characteristics are some of the most important factors because they may be used to design injection systems and combustion chamber shapes. Table 9.1 summarizes LDV device main characteristics. The velocity measurement system was composed of an Ar-Ion laser. The Ar-Ion laser emits a laser beam with 514.5 nm wavelength. The continuous output beam was divided into two beams of equal intensity by a beam splitter, and a frequency shift of up to 40 MHz was created by a Bragg cell. The two beams were collimated and focused inside the injected fuel jet, to form an interesting fringe pattern. It should be mentioned that, seeding particles were not used during the experiments. The signal from the scattered light was collecting using a photomultiplier and a frequency processor interfaced to a PC.

**Table 9.1.** Characteristics of the Laser Doppler Velocimeter.

Laser Head (Melles Griot, LA300)	300 mW
Photo Detector Module (PDM 1000)	
Frequency range	0 Hz to 175 MHz
Maximum Power	3 mW
Wavelength	635 nm
Signal Processor (FSA 3500)	
Frequency range	300 Hz to 1000 MHz
Maximum Sampling Rate	400 MHz
Maximum Data Rate	100 kHz
Maximum Samples/Burst	256
Downmix Frequencies	0.1 to 40 MHz
TR 60 Series Probe (Model TLN06-135)	
Wavelength	514.5 nm
Probe Beam Diameter	2.65 mm
Probe Beam Spacing	50.0 mm
Lens Focal Distance	122.2 mm
Lens Diameter	61.5 mm
Numerical Aperture	0.228
Beam-Crossing Half Angle (Kappa)	10.7
Measurement Vol. Diameter	34 $\mu$ m
Measurement Vol. Length	0.18 mm
Fringe Spacing	1.39 $\mu$ m
Number of Fringes	24
Probe Length	464.3 mm
Probe Diameter	82.3 mm

The spray analyzed in this work was generated by a manually controlled low pressure injection system, which consists of a modified diesel burner mounted inside a water tunnel. The experimental setup is presented in Figure 9.2. The test nozzle used in the experiments has a hole of 0.2 mm diameter and an 80 deg spray angle. The fuel pump was powered by an electric motor running at rpm and the fuel was pressurized up to 10 bar. Figure 9.1 shows a schematic diagram of the injection velocity measuring system.

To investigate the atomization characteristics of biodiesel fuel 26 measuring points were selected at 5 mm intervals from 10 mm to 223 mm according to the axial direction and at 2 mm interval to radial direction. At each point, 60,000 droplets were captured and analyzed.

The spray visualization system was composed of a La Vision laser. The laser with a rotating mirror is employed to produce a level light sheet. The characteristics of the Laser are  $P_o=1.277$  W,  $F=10000$  Hz and  $\lambda=532$  nm, as presented in Figure 9.5. The laser sheet crosses perpendicularly the lateral plexiglass surface of the water tunnel and lights up a vertical section of the fuel spray. For the visualization analysis were selected 5 points at 1 cm, 2 cm, 3cm, 5.5 cm, 10.5 cm, and 15.5 cm from the tip of the nozzle for 3 fuels, B0, B40 and B100. Figure 9.4 shows a schematic of the flow visualization technique employed.

It should be mentioned that the experiments were conducted at room conditions, ambient temperature and pressure 25 °C and 1 atm respectively.

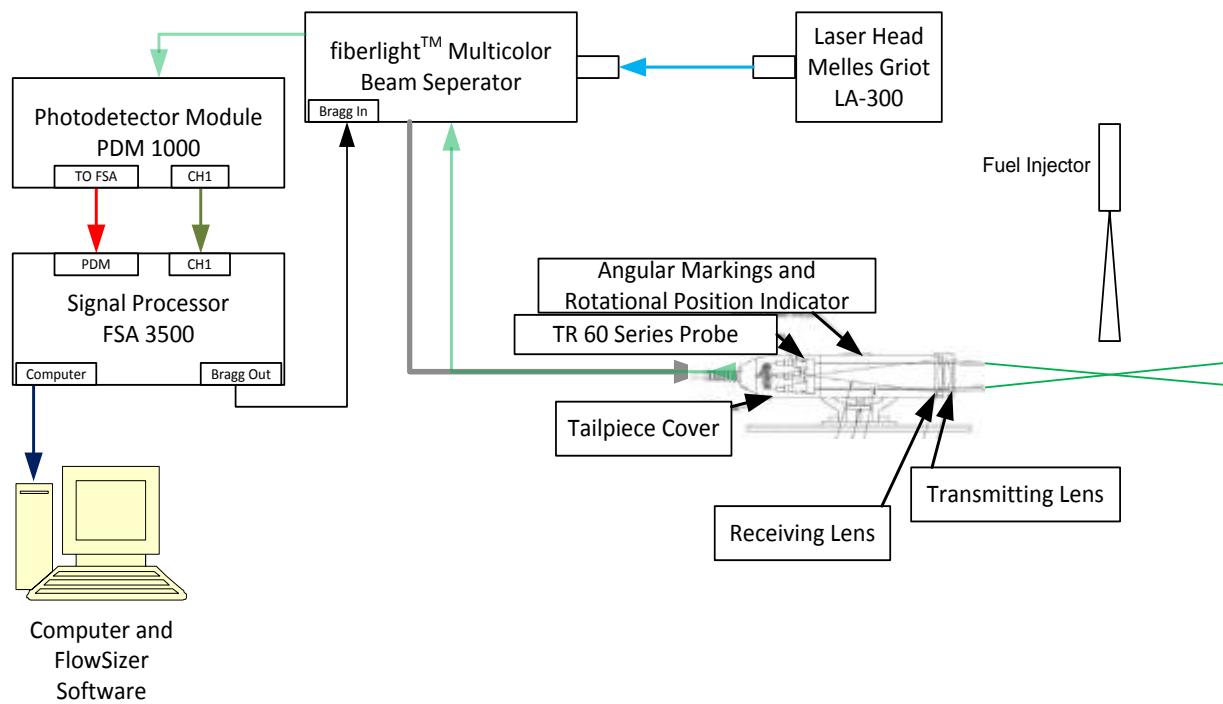


**Figure 9.1.** Experimental setup schematic diagram – LDV 1D components, injector nozzle and computer equipped with FlowSizer software.

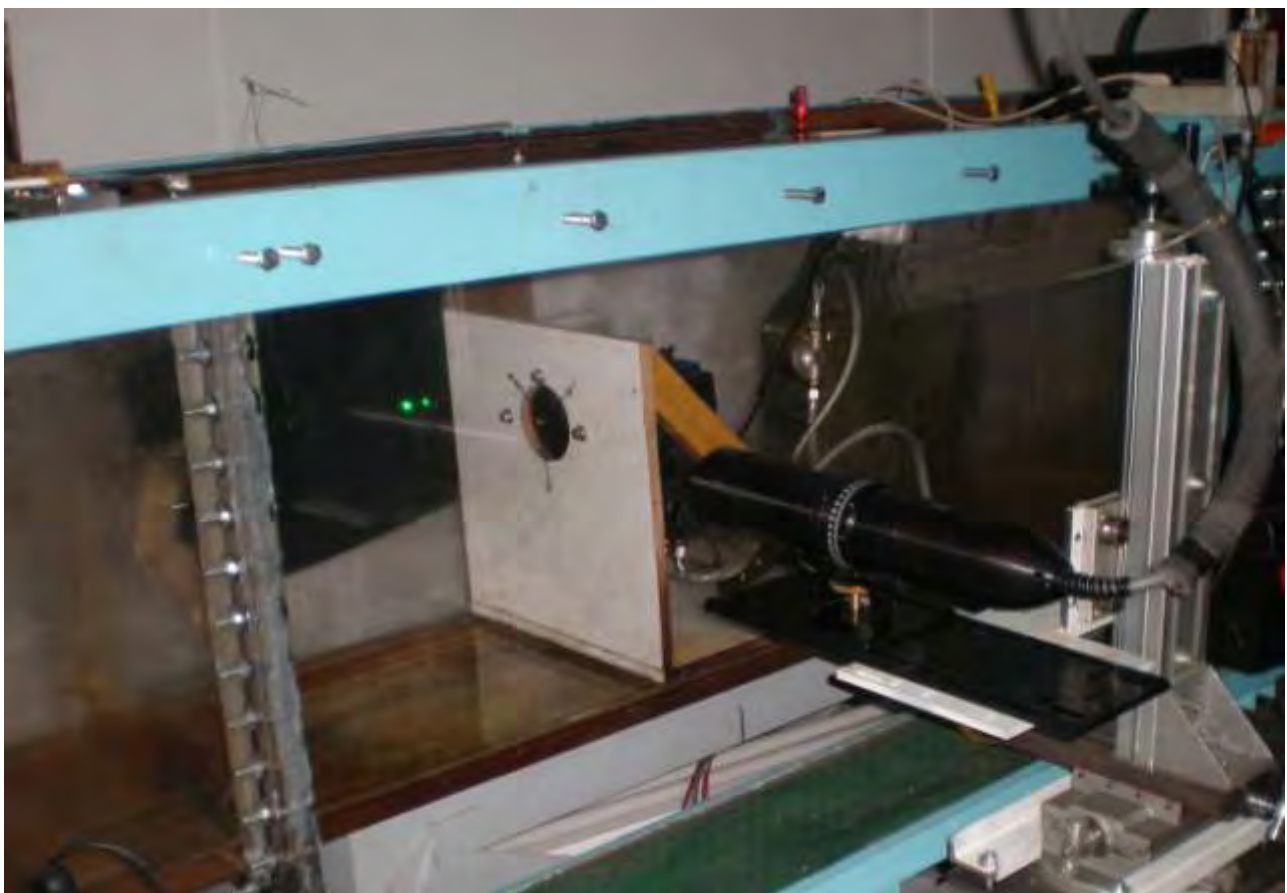


**Figure 9.2.** Low injection pressure (10 bar) experimental setup, including water tunnel, fuel tank, fuel pump, injection nozzle and TSI probe.



**Figure 9.3.** Low pressure diesel spray. Green laser beams and cross-section area (measurement volume) are clearly observable.

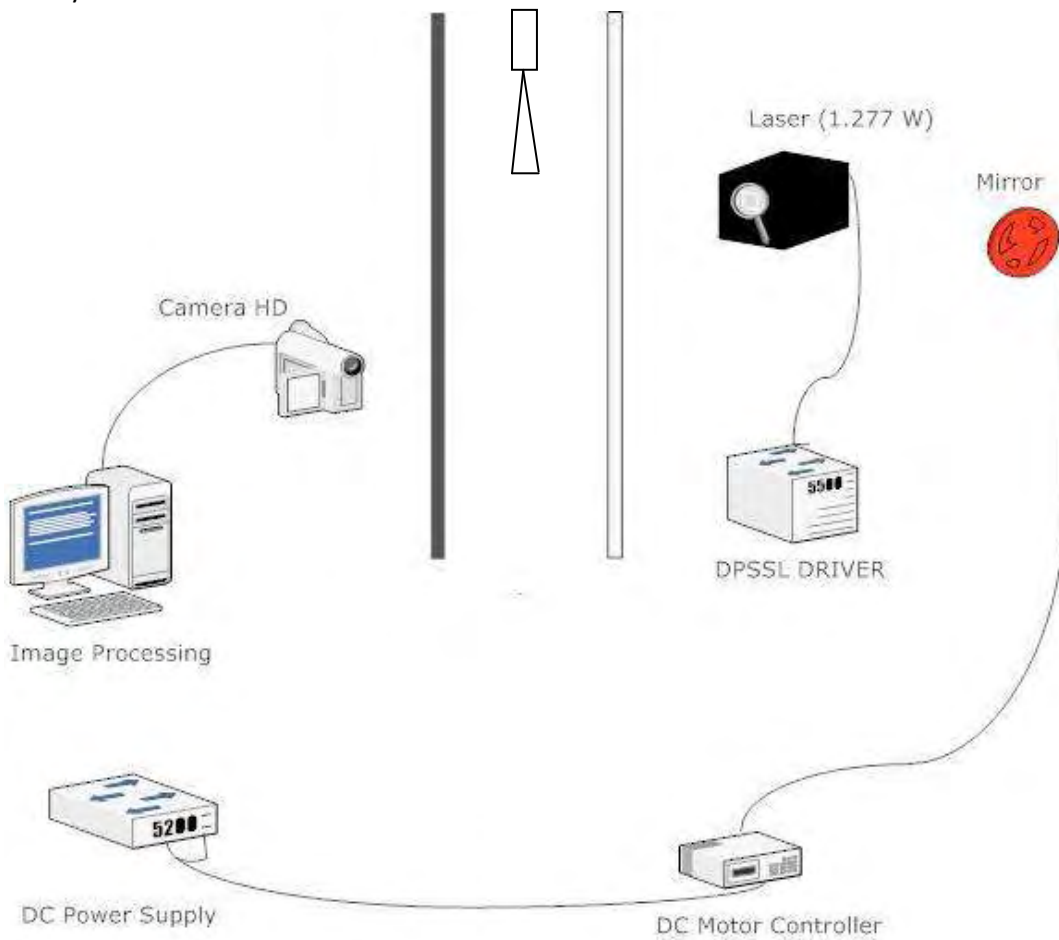


**Figure 9.4.** Schematic representation of the flow visualization layout.

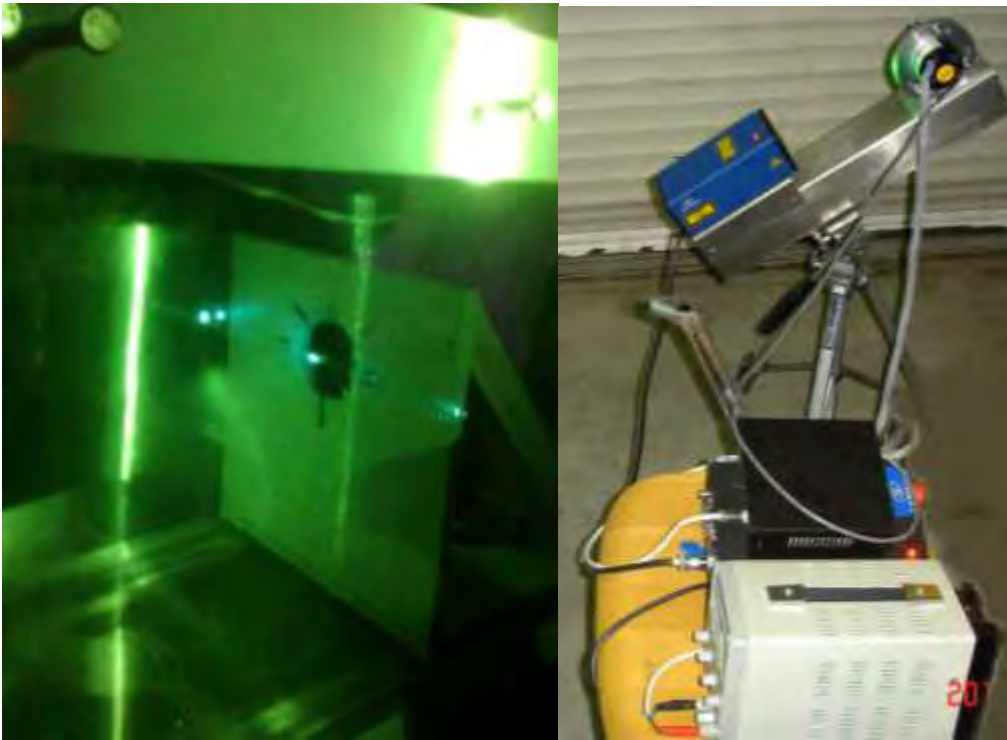


**Figure 9.5.** The green 1.277 W laser with the rotating mirror, power supply -control unit.

## 9.6 Test fuels

The fuels under investigation are pure Diesel (0% biodiesel) and two blends of Biodiesel in pure Diesel. The volume based blending ratios of biodiesel with conventional diesel fuel were set at 20%, 40%, 60%, 80% and 100% (pure Biodiesel). Throughout this work the tested fuels were denoted as B0, B20, B40, B60 B80 and B100 respectively. B0 conforms to European standard EN 590. The biodiesel employed in the measurements is a fatty acid methyl ester produced by 40% rapeseed oil, 30% soybean oil and 30% recycled cooking oils. It was supplied by ELIN biofuels SA (Volos factory) and conforms to EN 14214:2008 specifications. Tested fuels properties are listed in Table 9.2.

**Table 9.2.** Test fuel properties

Specifications / ranges	B0	B20	B40	B60	B80	B100
Density (15 °C) (kg/m <sup>3</sup> )	825	840	852	864	876	885
Viscosity (40 °C) (cSt)	2.493	3.039	3.384	3.730	4.075	4.720
Surface tension (N/m)	0.02600	0.02637	0.02674	0.02711	0.02748	0.02800

## 9.7 Results and discussion

In the present Thesis, experiments were conducted to investigate the effect of biodiesel properties on the spray evolution characteristics.

The most marked difference in the injection characteristics is the decrease in the injection velocity as presented in . Based on these results, the increase of the blending ratio induced an increase of the injection velocity because the injection pressure increases. The distributions of SMD are key parameters in analyzing spray characteristics because they are closely related to the combustion and emission characteristics in the engine. To study the atomization characteristics of biodiesel fuels, it is necessary to analyze the SMD distributions of biodiesel fuels because the physical properties such as the surface tension and viscosity of

the biodiesel are different from those of conventional diesel. It is obvious that the SMD of biodiesel blended-fuel is higher than that of the conventional diesel. The break up characteristics of a droplet are mainly influenced by the Weber number [202] and the surface tension which in the case of biodiesel is higher than that of commercial diesel. Therefore, it can be seen that the lower Weber number of biodiesel blended fuels caused by higher surface tension is the reason for higher SMD distributions.

#### Fuel atomization characteristics

The fuel droplet size is an important parameter in analyzing spray characteristics because it is closely related to the combustion and exhaust emission characteristics in the engine.

In order to compare the effect of the physical properties of biodiesel and diesel fuels on the atomization characteristics, the droplet diameter, axial mean velocity and fuel burn rate are analyzed at specific fuel injection conditions. The influence of blending ratio on droplet size distributions according to the axial distance from the nozzle tip is shown in Figure 9.8.

The SMD, VMD and arithmetic mean diameter (AMD) of diesel and biodiesel blending fuel decreased with an increase in the axial distance due to the fuel atomization process. As can be seen in these figure, the injection of diesel and biodiesel blends had a smaller droplet diameter than the injections in near area of nozzle tip. The comparisons of the SMD values show that biodiesel blended fuel is higher than that of conventional diesel fuel and the VMD and AMD values have similar trends.

It is generally known that the surface tension is a dominant factor of the droplet breakup mechanism. Therefore, the higher viscosity and surface tension of the biodiesel, due to the increased blending ratio as indicated in Table 9.2, induced the higher SMD distributions. The above results may influence the fuel injection velocity. The axial mean velocities of diesel and blending fuels are illustrated in Figure 9.6. The higher viscosity of biodiesel can become a factor in a lower axial mean velocity because it increases the friction between the nozzle surface and fuel.

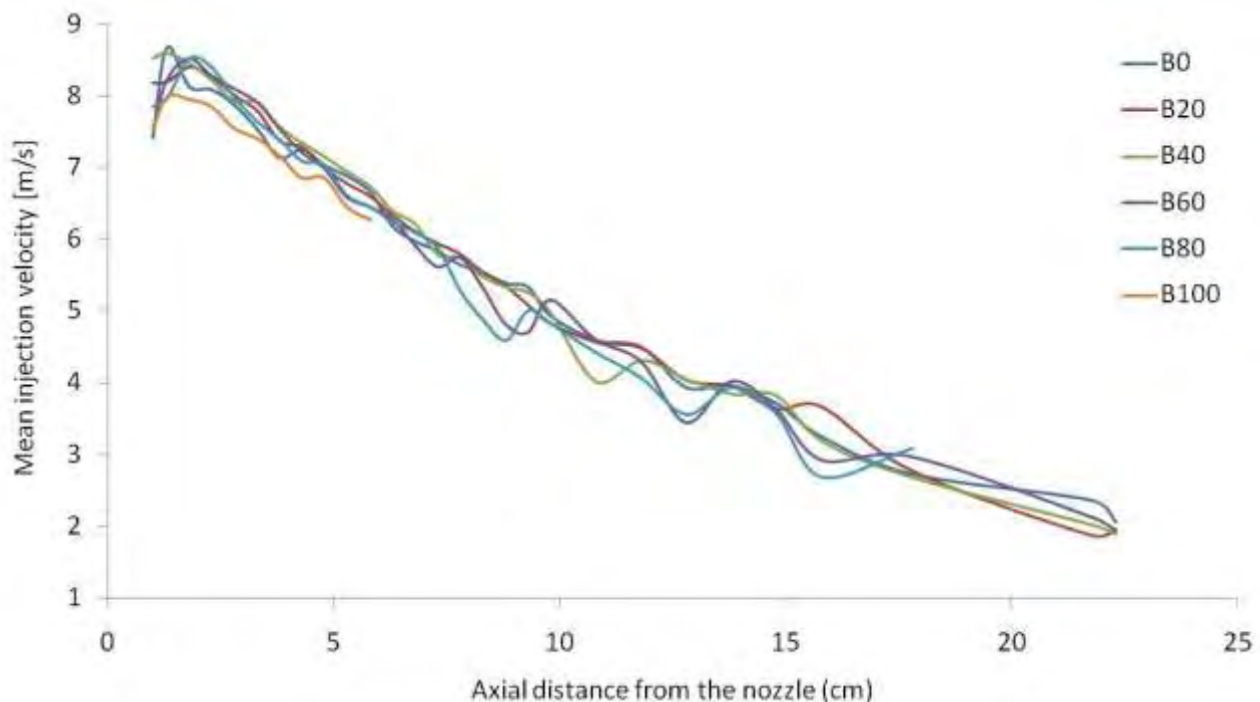


**Figure 9.6.** Axial mean velocity distribution for B0, B20, B40, B60, B80 and B100 fuels under low pressure injection conditions.  $P_{inj} = 10$  bar,  $P_{amb} = 1.01$  bar.

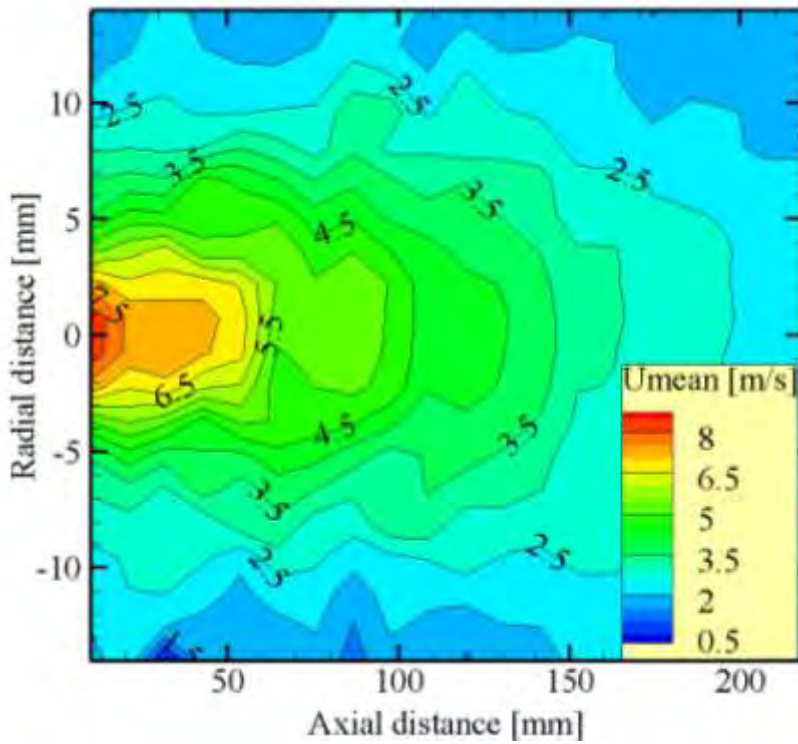


Figure 9.7. Mean droplet velocity distribution for B0.

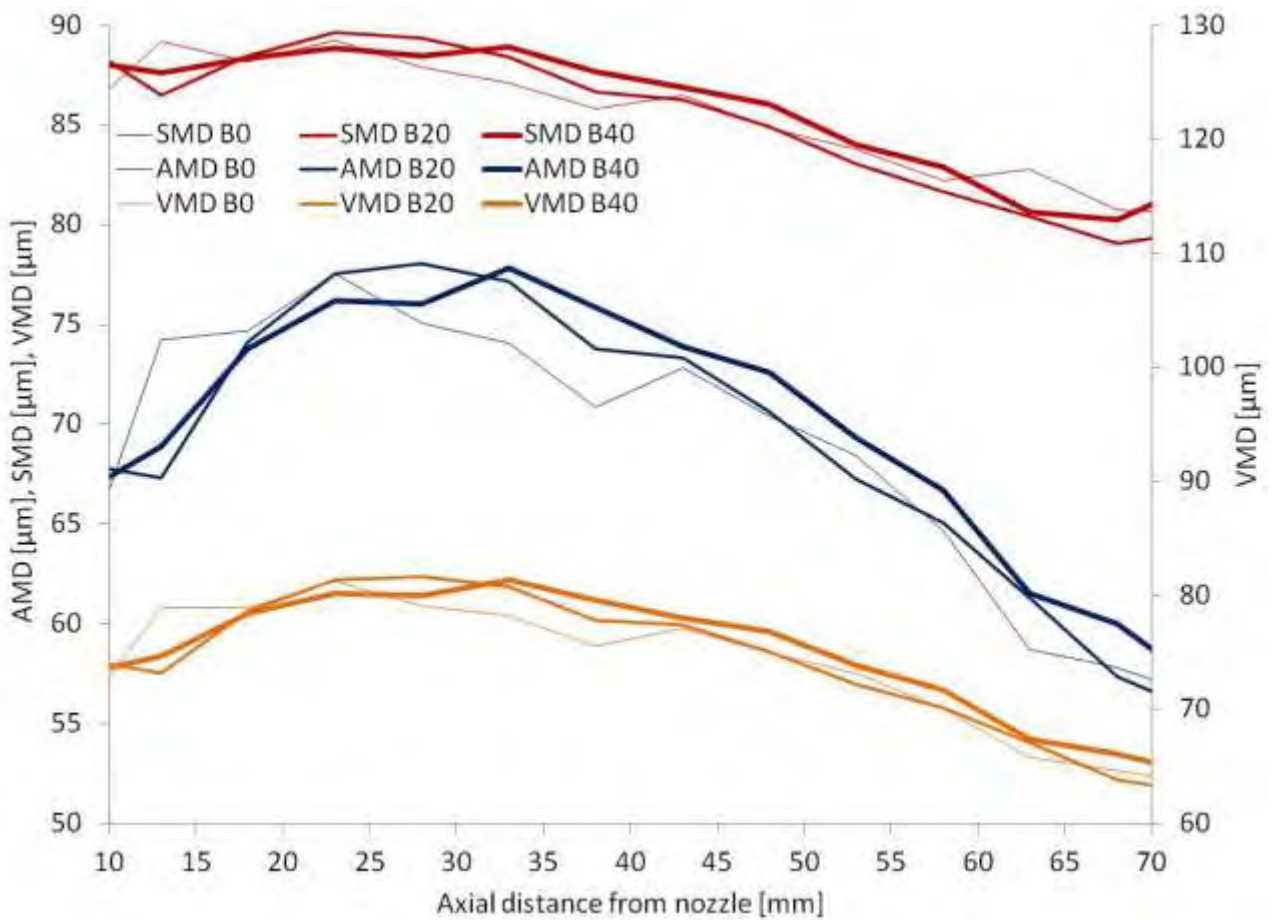
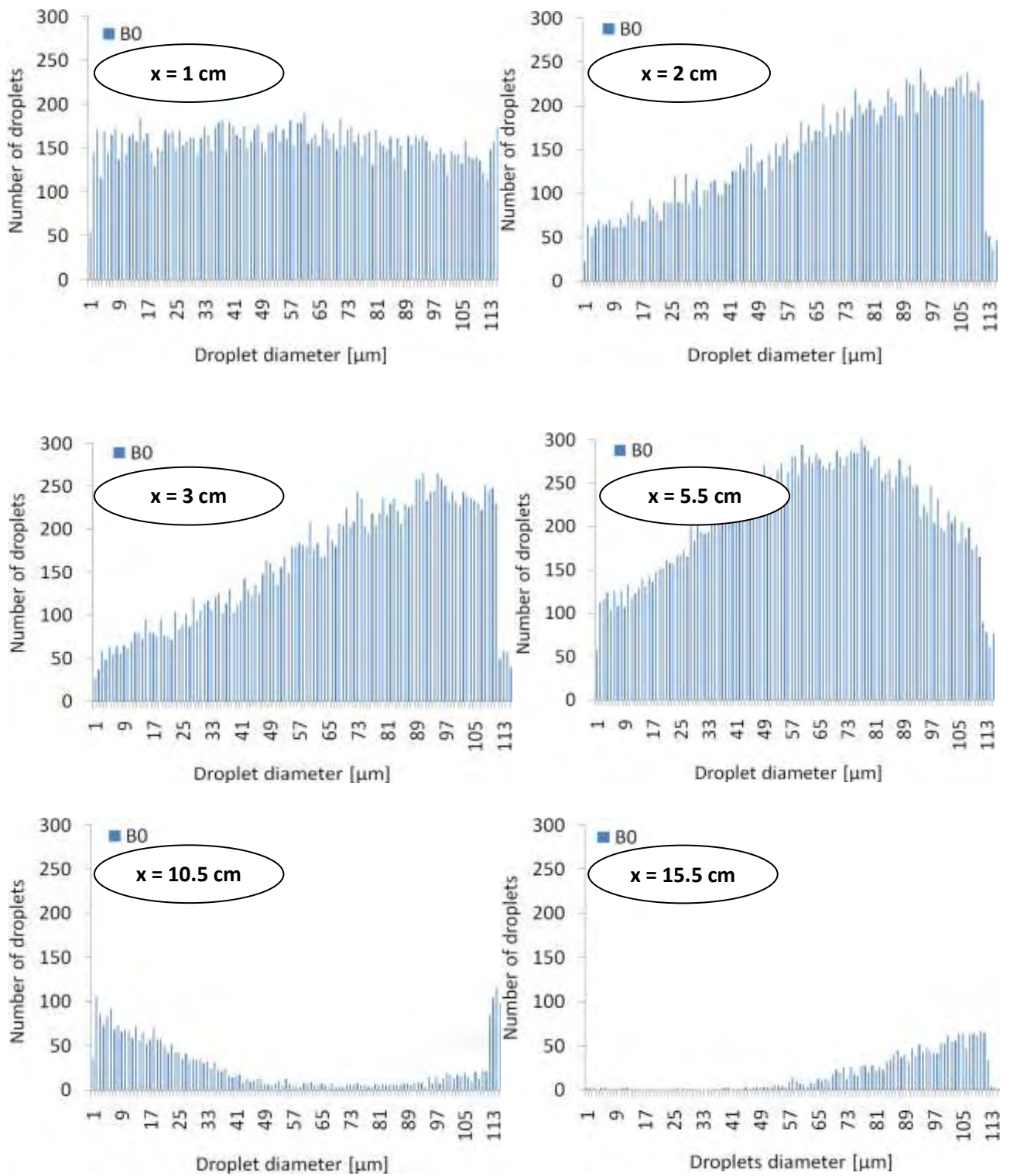
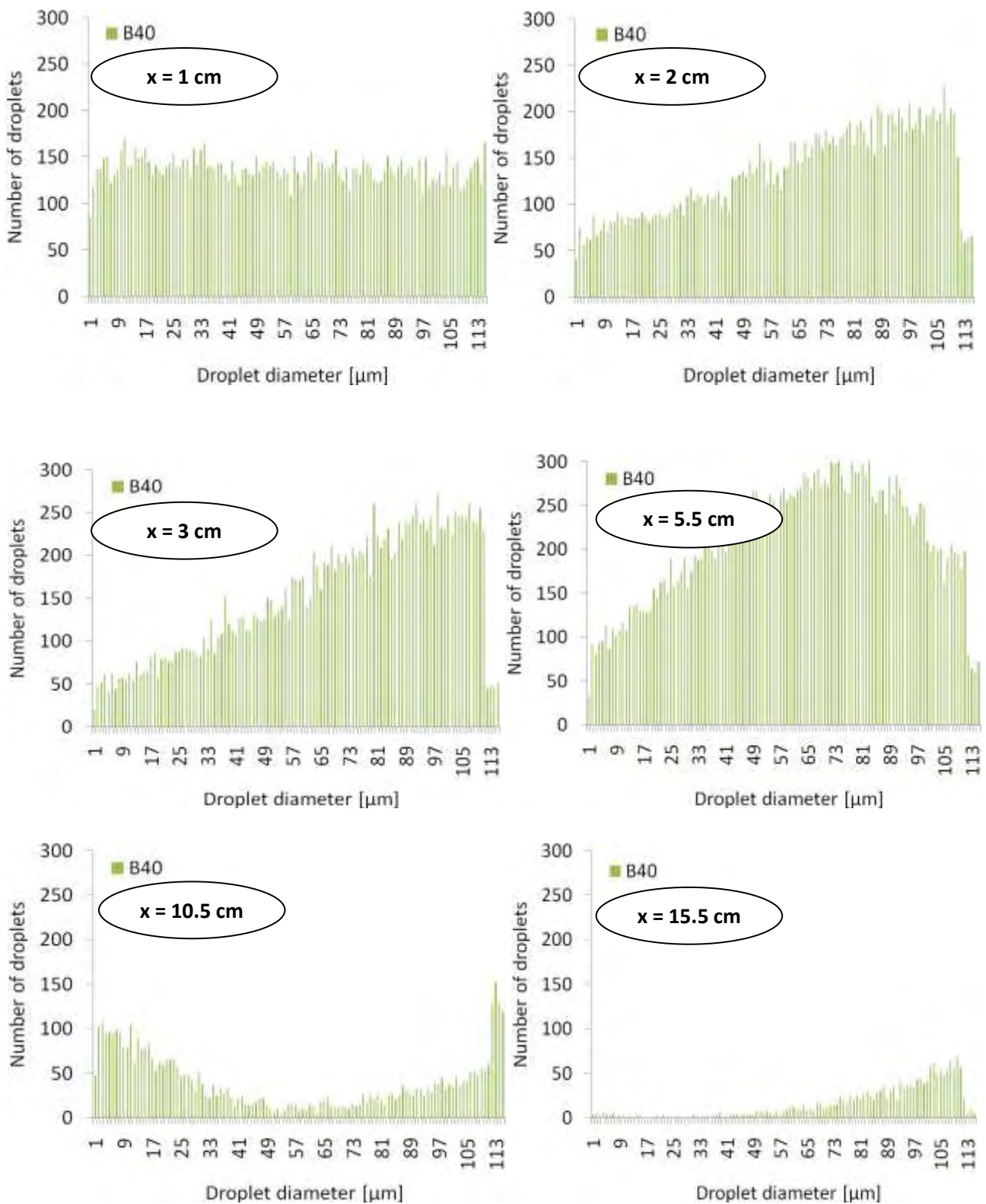


Figure 9.8. Differences in SMD, AMD, VMD distributions at several positions after the start of the injection for B0, B20 and B40 fuels.



**Figure 9.9.** Droplet diameters distribution for B0 fuel at several positions after the start of the injection.





**Figure 9.10.** Droplet diameters distribution for B40 fuel at several positions after the start of the injection

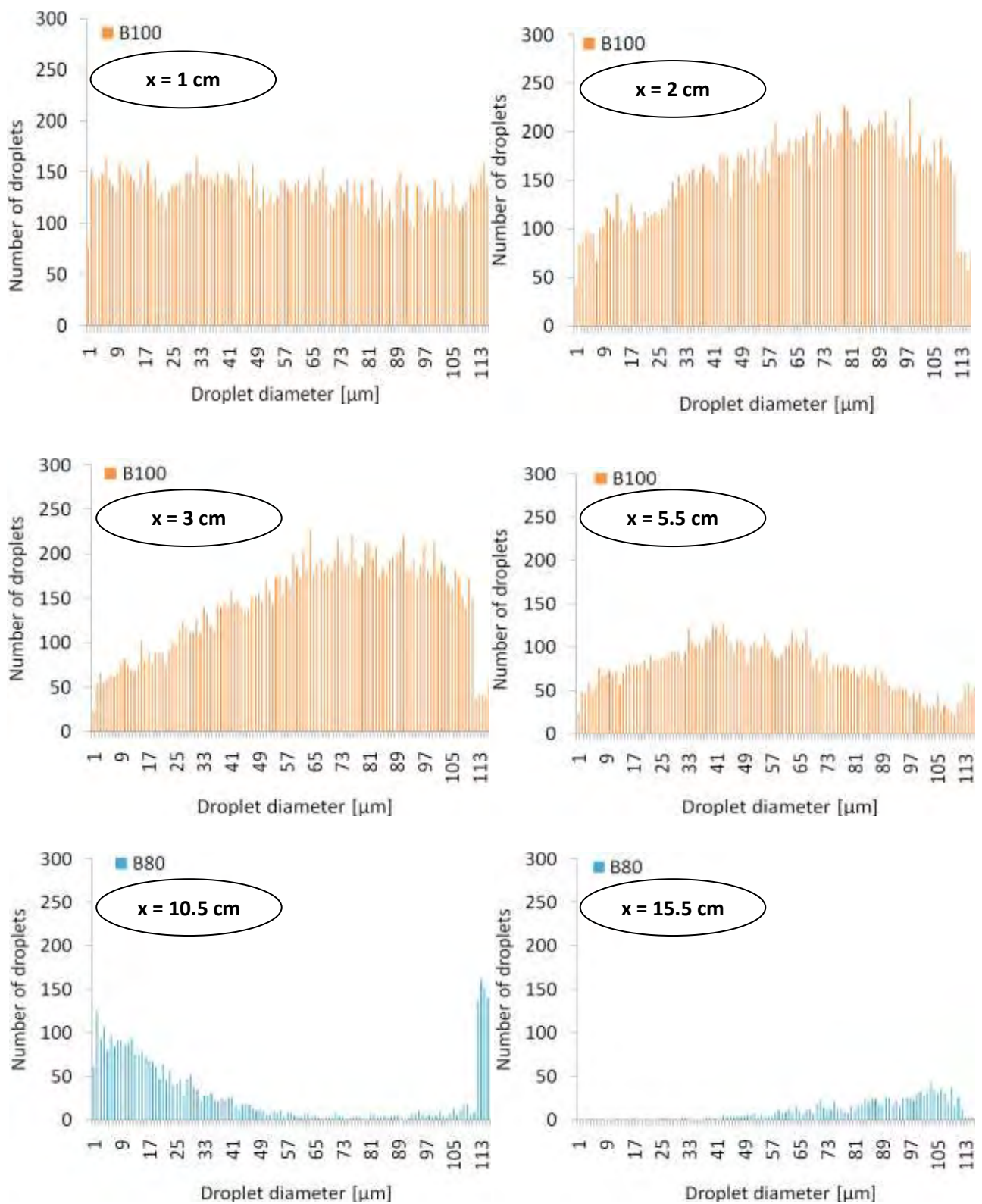


**Figure 9.11.** Droplet diameters distribution for B100 and B80 fuel at several positions after the start of the injection.

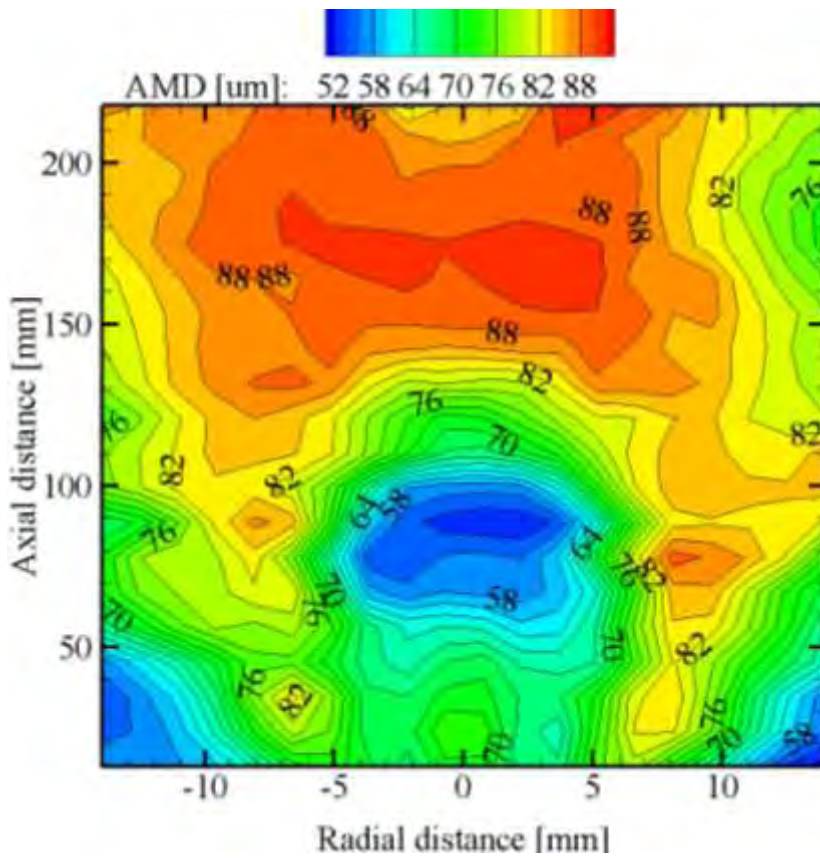


Figure 9.12. AMD distribution for B0.

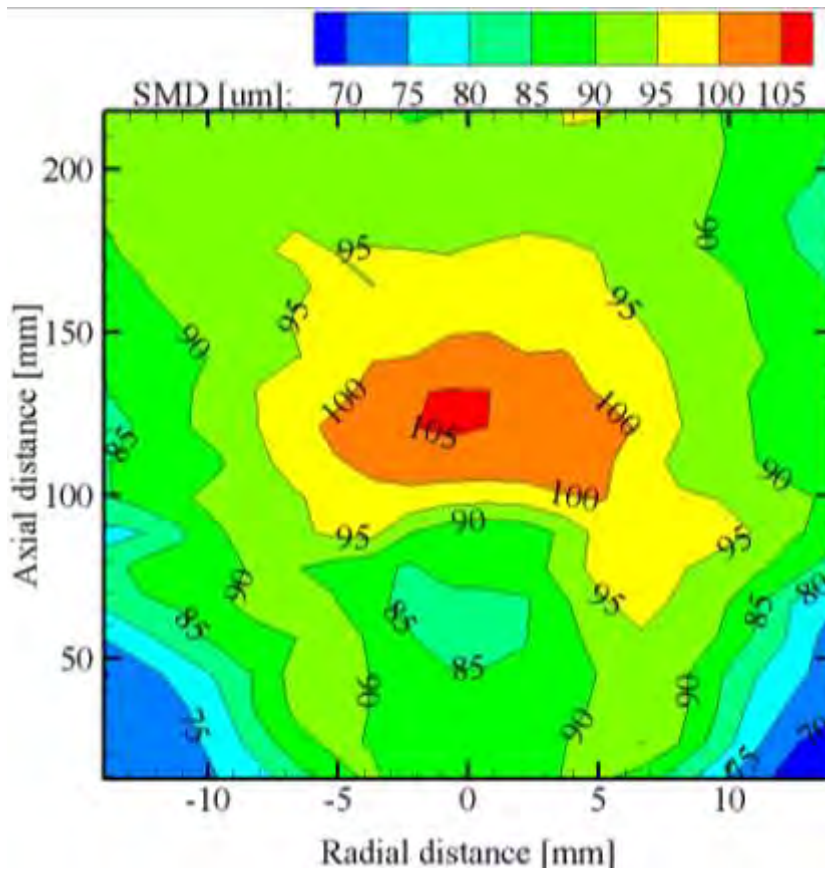
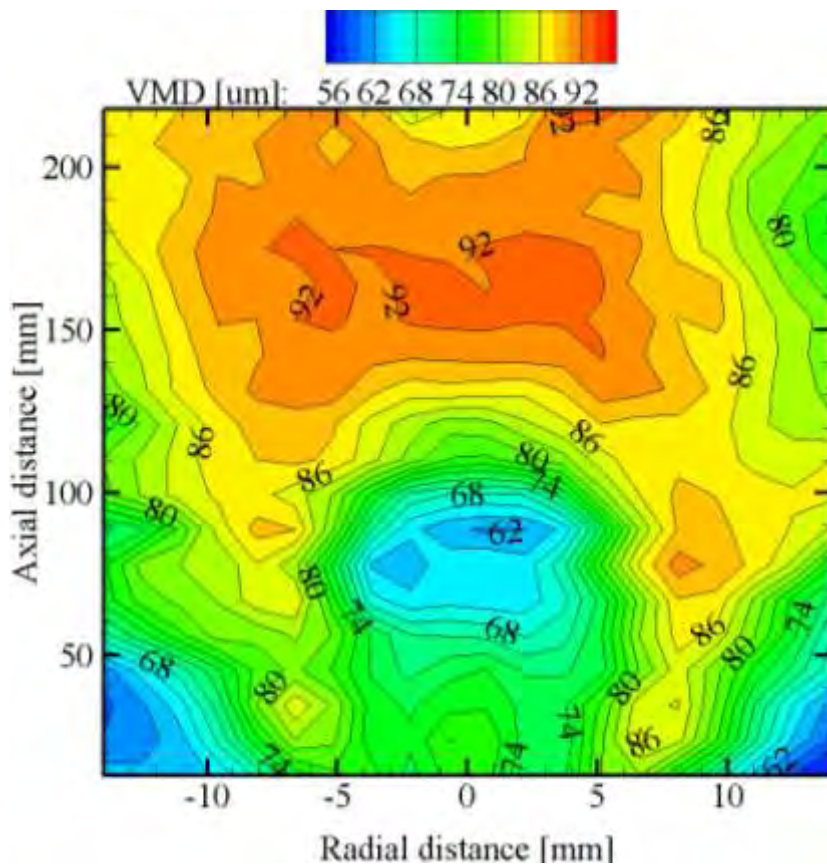


Figure 9.13. SMD distribution for B0.



**Figure 9.14.** VMD distribution for B0.

**Table 9.3.** Mean droplet velocity, Jet We, Jet Re and Jet Oh for all the blends.

Test Fuel	B0	B20	B40	B60	B80	B100
Mean droplet velocity [m/s]	25.31	24.95	24.60	24.25	23.92	23.81
Wej	5.91	5.66	5.43	5.21	4.50	4.86
Rej	1879	1642	1453	1300	1174	1078
Oh	0.034	0.038	0.043	0.047	0.051	0.055

### Spray evolution characteristics

The spray characteristics of diesel and biodiesel blends were investigated to study the influence of the viscosity and surface tension on spray development and atomization performance.



**Figure 9.15.** Differences in spray evolution of RF91 injector for B0, B60 and B100 fuels under specific injection conditions.  $P_{inj} = 210$  bar,  $P_{amb} = 1.01$  bar.



**Figure 9.16.** Closer view of spray evolution of RF91 injector for B0, B60 and B100 fuels under specific injection conditions.  $P_{inj} = 210$  bar,  $P_{amb} = 1.01$  bar.



**Figure 9.17.** Comparison of spray evolution (closer view) using low pressure nozzle for B40 and B100 fuels (1 cm from the tip of the nozzle) under specific injection conditions.  $P_{inj} = 10$  bar,  $P_{amb} = 1.01$  bar.

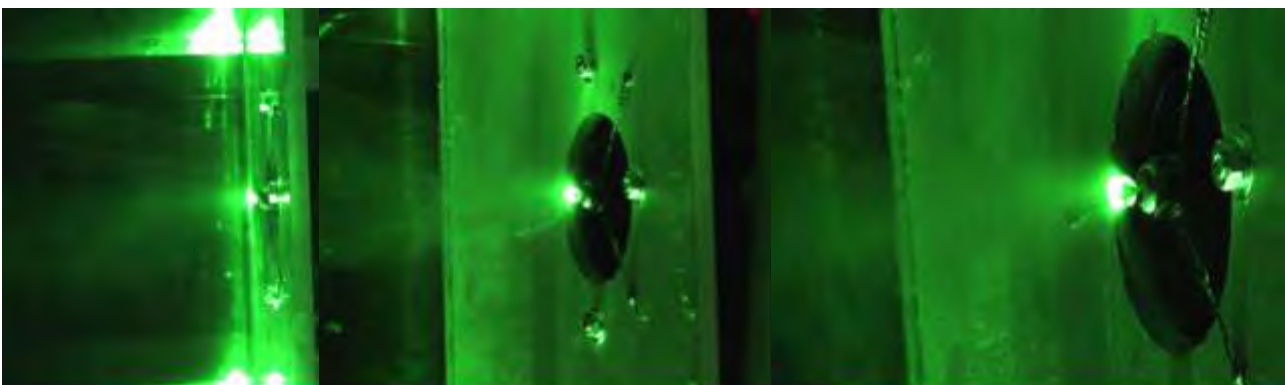


**Figure 9.18.** Comparison of spray evolution using low pressure nozzle for B0, B40 and B100 fuels (1 cm from the tip of the nozzle) under specific injection conditions.  $P_{inj} = 10$  bar,  $P_{amb} = 1.01$  bar.

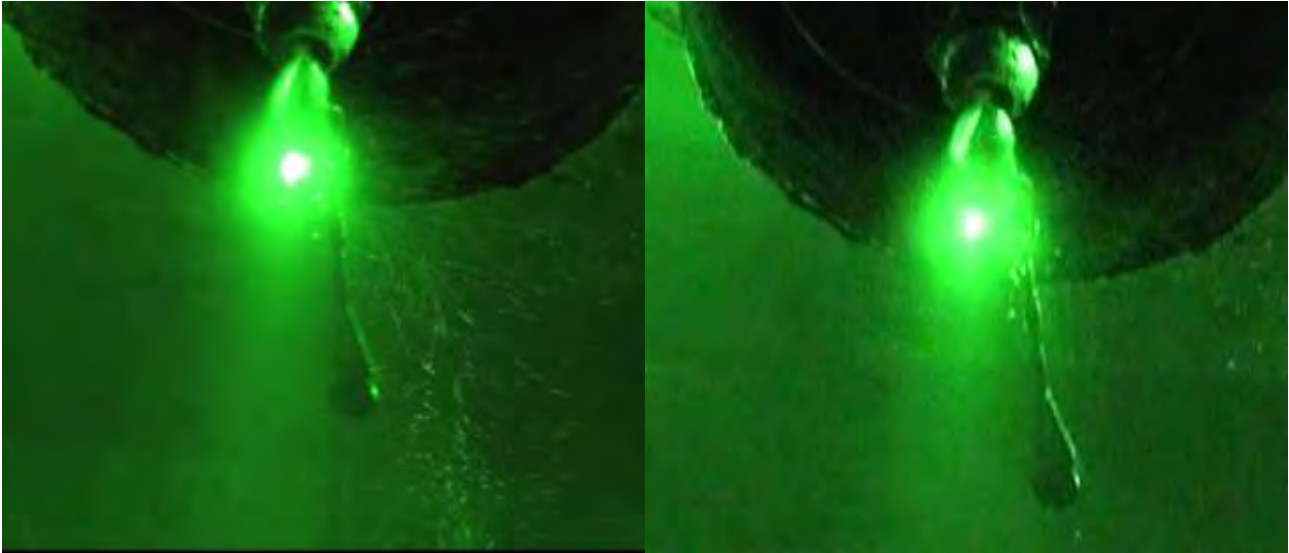


**Figure 9.19.** Comparison of spray evolution using low pressure nozzle for B40 and B100 fuels (2 cm from the tip of the nozzle) under specific injection conditions.  $P_{inj} = 10$  bar,  $P_{amb} = 1.01$  bar.

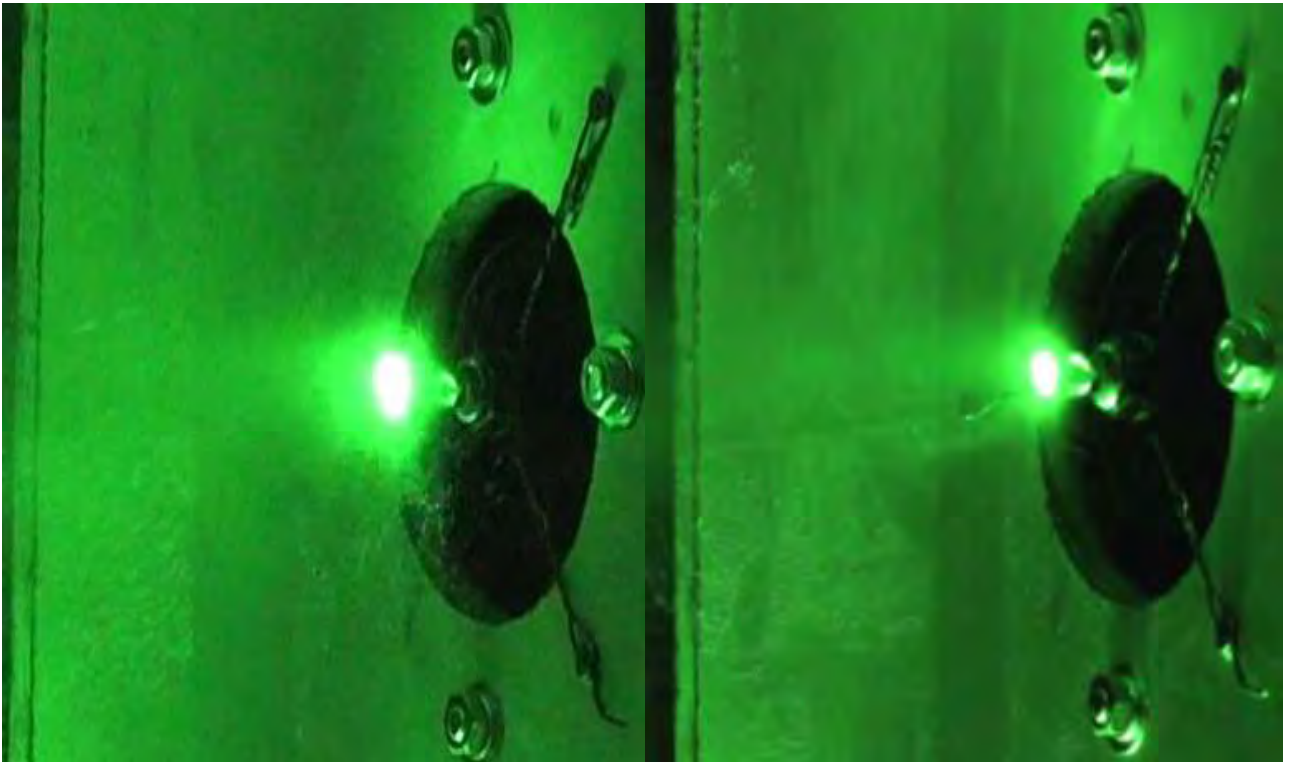


**Figure 9.20.** Comparison of spray evolution using low pressure nozzle for B0 and B100 fuel (2 cm from the tip of the nozzle) under specific injection conditions.  $P_{inj} = 10$  bar,  $P_{amb} = 1.01$  bar.

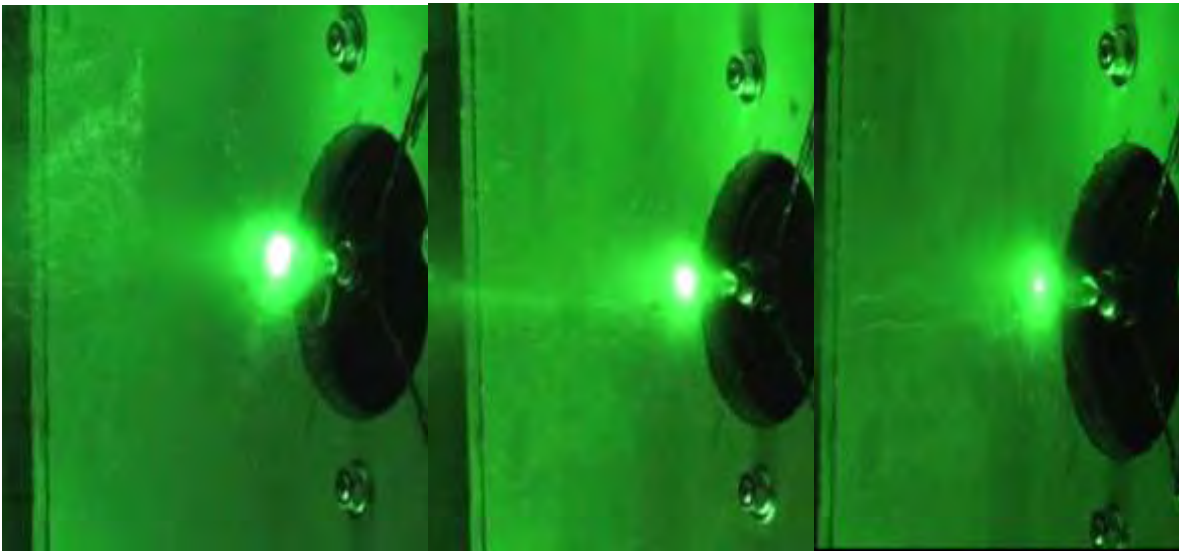


**Figure 9.21.** Comparison of spray evolution using low pressure nozzle for B0, B40 and B100 fuels (3 cm from the tip of the nozzle) under specific injection conditions.  $P_{inj} = 10$  bar,  $P_{amb} = 1.01$  bar.

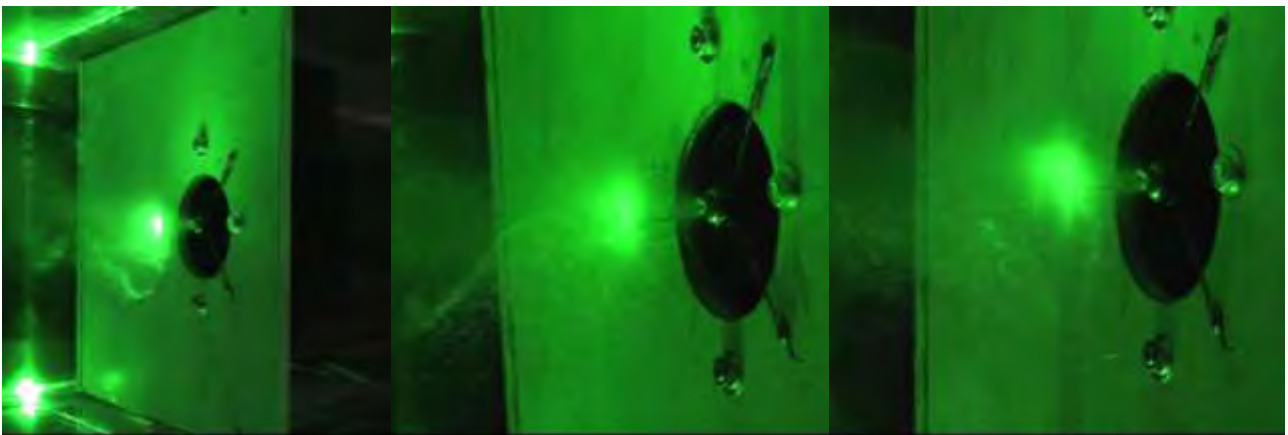


**Figure 9.22.** Comparison of spray evolution injections using low pressure nozzle for B0, B40 and B100 fuels (5.5 cm from the tip of the nozzle) under specific injection conditions.  $P_{inj} = 10$  bar,  $P_{amb} = 1.01$  bar.

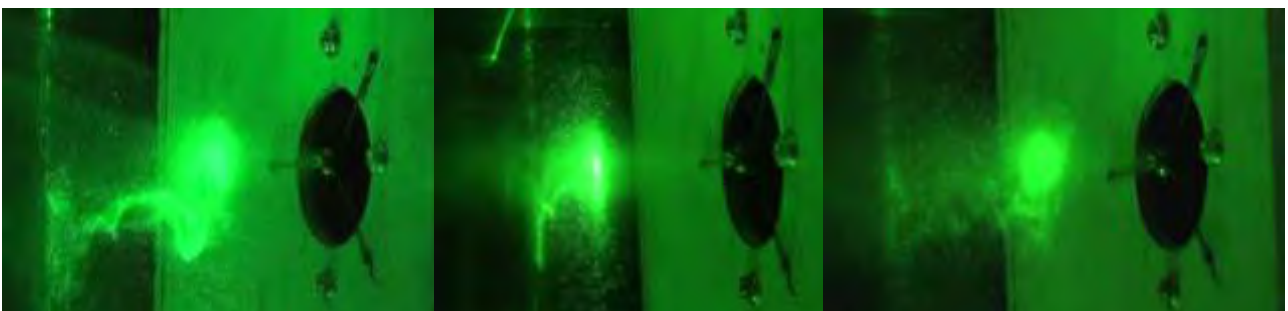


**Figure 9.23.** Comparison of spray evolution injections using low pressure nozzle for B0, B40 and B100 fuels (10.5 cm from the tip of the nozzle) under specific injection conditions.  $P_{inj} = 10$  bar,  $P_{amb} = 1.01$  bar.

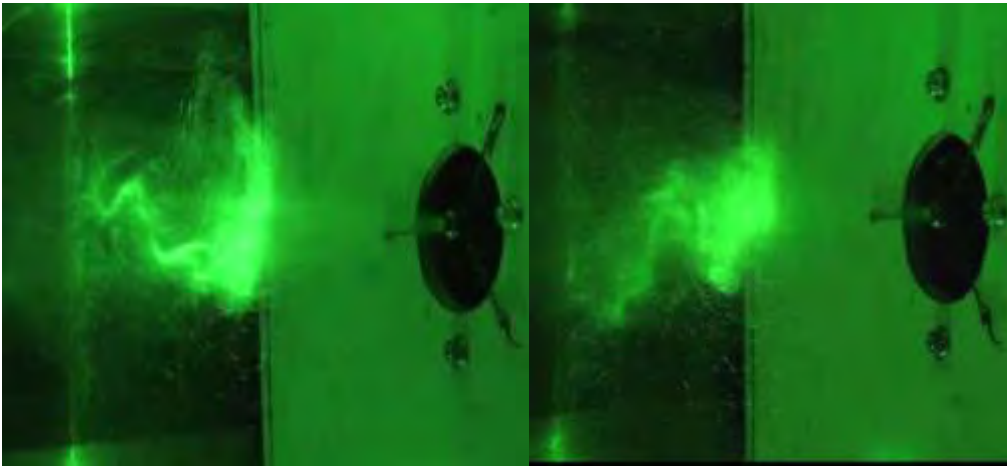


**Figure 9.24.** Comparison of spray evolution using low pressure nozzle for B0 and B100 fuels (15.5 cm from the tip of the nozzle) under specific injection conditions.  $P_{inj} = 10$  bar,  $P_{amb} = 1.01$  bar.



**Figure 9.25.** Spray evolution using low pressure nozzle for B40 fuel at several positions from the tip of the nozzle and under specific injection conditions.  $P_{inj} = 10$  bar,  $P_{amb} = 1.01$ .



**Figure 9.26.** Spray evolution injections using low pressure nozzle for B100 fuel at several positions from the tip of the nozzle and under specific injection conditions.  $P_{inj} = 10$  bar,  $P_{amb} = 1.01$ .



In order to have a comparison of approximate fuel burning rates, one can assume the the fuel burning rate of a spherical droplet is proportional to its external surface:

For example, a spherical droplet of 1 mm diameter may be atomized in 1 million droplets of 10 μm. Based on the above assumption for the fuel burning rate being proportional to the square of its diameter:

The burning rate for all 1 million droplets becomes:  $fbr_2 = 10^6 \cdot C \cdot (1 \cdot 10^{-5})^2$

Instead of the much lower burning rate of the 1 mm droplet:  $fbr_1 = C \cdot (1 \cdot 10^{-3})^2$

Thus, the droplet atomization results in 10,000 times faster fuel burning rate:  $\frac{fbr_2}{fbr_1} = 10000$

By applying this simplified approximate calculation for the total fuel burning rates for all 60,000 droplets of each sample measured by the LDV, we get the result of of Figure 9.27 which compares fuel buring rates of the sprays investigated in the above series of experiments.

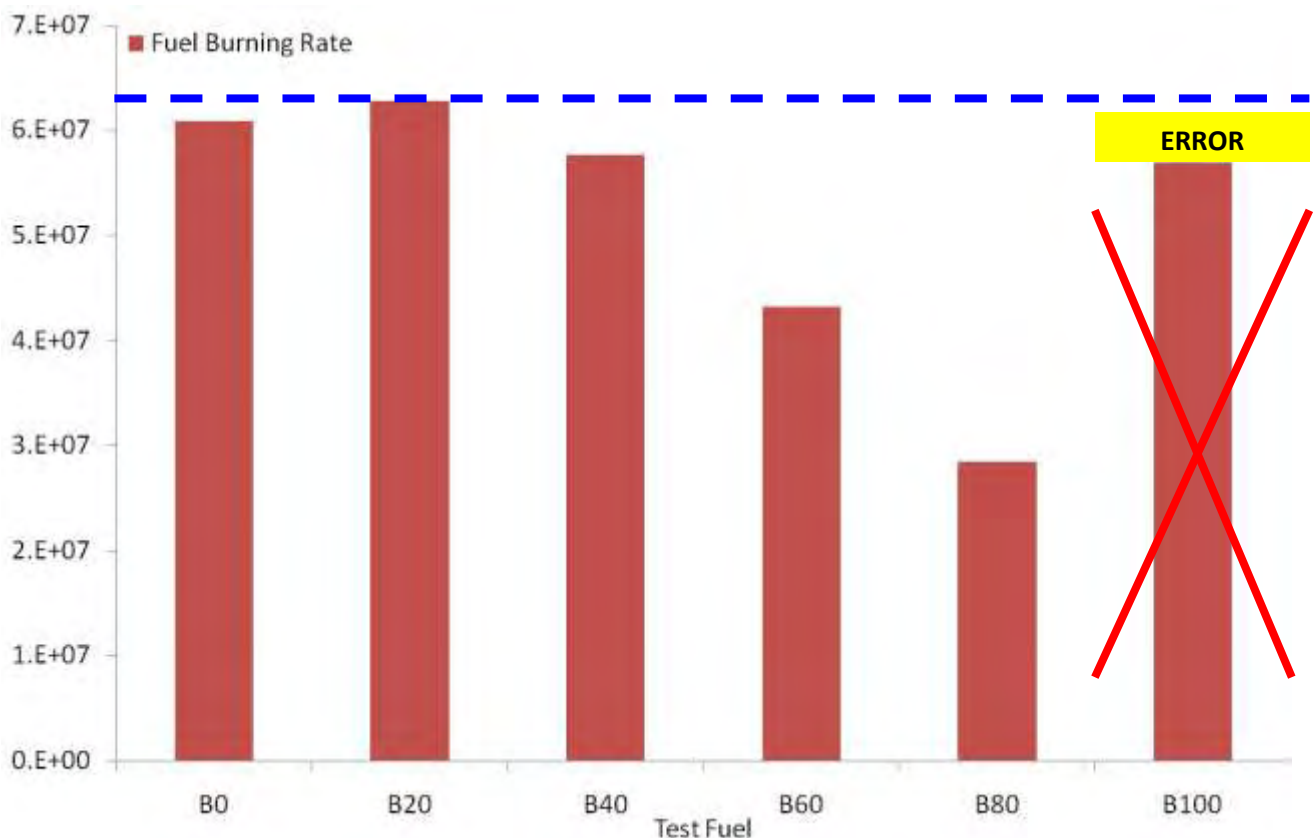


**Figure 9.27.** Differences in total fuel burnig rates for all 60,000 droplets of each fuel.

## 9.8 Conclusions

The effect of different mixing ratios of biodiesel-blended fuels on the atomization characteristics were investigated using convenstional low (10 bar) and medium (210 bar) pressure injection nozzles (the second, only for flow visualization purposes). The following findings are listed:

- The kinematic viscosity and surface tension become higher as the mixing ratio of the biodiesel increases. Because of the different physical properties of biodiesels, the atomization characteristics of blended fuels are different from those of commercial diesel fuel.

- The surface tension of the biodiesel is higher than that of commercial diesel, which gives a lower Weber number (less strong breakup tendency).
- The SMD, VMD and arithmetic mean diameter (AMD) of diesel and biodiesel blended fuels decreased with an increase in the axial distance due to the fuel atomization process.
- The comparisons of the SMD values show that the biodiesel blends present increasingly higher SMD than the conventional diesel fuel. The VMD and AMD values have similar trends.
- Comparisons of approximate fuel burning rates for different samples of 60,000 droplets each clearly indicate a decrease in fuel burning rate for B20 and higher blends.
- The higher viscosity of biodiesel can become a factor in a lower axial mean velocity because it increases the friction between the nozzle surface and fuel.

## 10. Conclusions

- The specialized literature is relatively sparse regarding the effect of fuelling modern, common rail diesel engines by high biodiesel content fuel blends. This study contributes to this area, by presenting comparative test results with a common rail, high pressure injection, passenger car diesel engine fuelled by B70 versus normal diesel fuel.
- A sequence of representative steady state engine operation points was selected on the engine operation map. This test sequence was programmed in the dyno controller and engine performance and emissions characteristics were recorded, with the engine fuelled by B70 and B0 fuel.
- The biodiesel employed in the tests was a FAME based on 40% rapeseed oil, 30% soybean oil and 30% waste cooking oils as raw material, supplied by a local factory.
- As expected, decreased air to fuel ratio values were measured with the B70 blend. On the other hand, lambda was observed to increase at the medium-to-high load range.
- Engine tests performed under low, medium and high load conditions have shown a sharp reduction in CO and HC emissions upstream catalyst, with the use of the B70 blend.
- The effect of the decreased volume heating value of the biodiesel on the brake specific fuel consumption was confirmed. Engine efficiency was not observed to change significantly with biodiesel, presumably due to the high injection pressures (500-1350 bar) and very small droplet sizes.
- The effect of the B70 blend on the main fuel injection parameters (common rail pressure, pilot and main injection advance and time) was measured and explained based on the maps stored in the ECU of the engine.
- A significant increase of the fuel temperatures was observed with the B70 blend. It was necessary to install a heat exchanger in the fuel return line, in order to keep fuel at acceptable temperatures (less than 50 °C).
- The effect of the B70 on NO<sub>x</sub> emissions was less pronounced and more complex. NO<sub>x</sub> reduction was only observed at medium-to-high loads. Again, this can be explained based on the modification by the ECU of certain fuel injection parameters for the B70 combustion.
- Reduced PM emissions and smoke opacity was observed by a qualitative comparison of the soot collected on Pallflex filters from undiluted exhaust gas sampled directly from the exhaust line for the total duration of each test. Again, this is in line with what is known from the literature.
- Comparative test results in transient mode were also carried out and assessed, with B70 and B0 fuel.
- The decreased volume heating value of the biodiesel explains the deterioration in engine performance during speed transients at high loads.
- The effect of the B70 blend on the dynamics of the main fuel injection parameters (common rail pressure, pilot and main injection advance and duration) was measured and explained based on the ECU maps and control strategy.
- Certain improvements are suggested to the ECU maps that could allow engine operation at high biodiesel blends without significant loss in engine performance or deterioration in transient mode emissions. The maximum fuel delivery per stroke is proposed to extend by about 10%.

- Continued operation of the engine with the specific, high biodiesel fuel blend, resulted in the failure of the high pressure fuel pump. Based on this experience, it was decided to continue the tests with lower percentage of biodiesel blending.
- In the second part of this thesis, the experiments were shifted to a single-cylinder, conventional high speed Diesel engine, with lower biodiesel blends (B0, B20, B40). The objectives in this part were to study the effect of biodiesel to the conventional injection and combustion, and especially to the behavior of the Diesel Particulate Filter in loading and regeneration mode.
- Decreased air to fuel ratio values overall were measured with the B20 and even more decreased with the B40 blends, as expected. This decrease was extended also to the medium-to-high load range. It is explained by the associated drop in engine efficiency.
- The effect of the decreased volume heating value of the biodiesel on the brake specific fuel consumption was confirmed. Engine efficiency was observed to change with biodiesel, presumably due to the low injection pressures (200 bar) and larger droplet sizes that delay fuel burning rate.
- The effect of the B20 to B100 blends on the injection behavior was assessed by means of flow visualization and LDV measurements of droplet velocity and size distributions, at 200 bar and 10 bar injection pressures at ambient temperature and pressure conditions.
- Reduced PM emissions and smoke opacity was again observed by a qualitative and quantitative comparison of the soot collected on Pallflex filters from undiluted exhaust gas sampled directly from the exhaust line. This is in line with what is known from the literature.
- Special emphasis was given to the study of the loading and regeneration behavior of a small-size, unit Diesel Particulate Filter installed on the single cylinder engine. Comparative test results in loading and regeneration mode were carried out and assessed, with B0, B20 and B40 fuel, assisted by 50 ppm DPX9 Ceria fuel additive. The 1-D regeneration propagation along the filter was captured by means of infrared thermography.
- The most important observation made in the loading and regeneration experiments with the conventional, low pressure injection engine, is the quite favorable effects on particulate (mass and number) emissions, filter loading and regeneration behavior even with the B20 fuel, without any modification to the engine and injection system control.
- The observed benefits as regards the DPF extend also to the faster evolution of regeneration and the lower overall filter wall temperatures with favorable effects on the filter durability.
- As a general conclusion, it should be emphasized that the production and use of biodiesel in Thessaly, that was an important motivating force behind this thesis, remains a valid option today, in view of the increasing fuel prices, the significant fuel needs of the agricultural operations and the resulting good profitability of energy crops. The use of low –to- medium percentage biodiesel blends will be a workable solution both for the common rail engines of modern agricultural tractors and the wide variety of older equipment that is and will be in use for many years to come.

## 11. References

1. BIOFRAC, *EUR 22066 Final report of the Biofuels Research Advisory Council* [http://ec.europa.eu/research/energy/pdf/biofuels\\_vision\\_2030\\_en.pdf](http://ec.europa.eu/research/energy/pdf/biofuels_vision_2030_en.pdf). 2007.
2. European, *Biofuels Technology Platform: Strategic Research Agenda & Strategic Deployment Document* <http://cordis.europa.eu/technology-platforms/pdf/biofuels.pdf>. 2008.
3. FIE, *Diesel Fuel Injection Equipment Manufacturers Common Position Statement: FAME Fuels as a Replacement or Extender for Diesel Fuels* [http://www.greenfuels.org/biodiesel/res/2004\\_10\\_FAME\\_Statement.pdf](http://www.greenfuels.org/biodiesel/res/2004_10_FAME_Statement.pdf). 2004.
4. Agarwal, A.K., *Biofuels (alcohols and biodiesel) applications as fuels for internal combustion engines*. Progress in Energy and Combustion Science, 2007. **33**(3): p. 233-271.
5. Bouaid, A., M. Martinez, and J. Aracil, *Production of biodiesel from bioethanol and Brassica carinata oil: Oxidation stability study*. Bioresource Technology, 2009. **100**(7): p. 2234-2239.
6. Xin, J., H. Imahara, and S. Saka, *Oxidation stability of biodiesel fuel as prepared by supercritical methanol*. Fuel, 2008. **87**(10-11): p. 1807-1813.
7. Graboski, M. and R. McCormick, *Combustion of fat and vegetable oil derived fuels in diesel engines*. Prog Energy Combust Sci, 1998. **24**: p. 125-164.
8. Lapuerta, M., O. Armas, and J. Rodriguez-Fernandez, *Effect of biodiesel fuels on diesel engine emissions*. Progress in Energy and Combustion Science, 2008. **34**(2): p. 198-223.
9. McCormick, R., et al., *Effects of biodiesel blends on vehicle emissions,*, in *Milestone Report NREL/MP-540-40544*. 2006, National Renewable Energy Laboratory.
10. Tsolakis, A., et al., *Engine performance and emissions of a diesel engine operating on diesel-RME (rapeseed methyl ester) blends with EGR (exhaust gas recirculation)*. Energy, 2007. **32**(11): p. 2072-2080.
11. Wu, F., et al., *A study on emission performance of a diesel engine fueled with five typical methyl ester biodiesels*. Atmospheric Environment, 2009. **43**(7): p. 1481-1485.
12. Wu, F., et al., *A study on emission performance of a diesel engine fueled with five typical methyl ester biodiesels*. Atmospheric Environment, 2009. **In Press, Corrected Proof**.
13. Asad, U. and M. Zheng, *Fast heat release characterization of a diesel engine*. International Journal of Thermal Sciences, 2008. **47**(12): p. 1688-1700.
14. EU, *DIRECTIVE 2003/30/EC OF THE EUROPEAN PARLIAMENT AND OF THE COUNCIL*. 2003, of 8 May 2003 on the promotion of the use of biofuels or other renewable fuels for transport.
15. Gallagher, E., *The Gallagher Review of the indirect effects of biofuels production*. July 2008.
16. Nigam, P.O. and A. Singh, *Production of liquid biofuels from renewable resources*. Process in Energy and Combustion Science, 2011. **37**: p. 52-68.
17. EPA, *420-P-02-001 A comprehensive analysis of biodiesel impacts on exhaust emissions*. 2002, Assessment and Standards Division (Office of Transportation and Air Quality)
18. Lance, M.J., et al., *Biofuels impact on DPF durability*. 2011, Oak Ridge National Laboratory.
19. Thomton, M.J., et al., *Impacts of biodiesel fuel blends oil dilution on light-duty diesel engine operation*. 2009.
20. Kotrba, R., *Understanding the post-injection problem*, in *Biodiesel Magazine*. 2008.
21. Bown, I. and Lubrizol. *Interactions between biofuels and lubricants and effects on engine oil durability*. in *SMMT*. 2008. London.
22. EPA, *The effect of cetane number increase due to additives on NO<sub>x</sub> emissions from heavy-duty highway engines*, in *EPA-420-R-03-002*. 2003: Assessment and Standards Division (Office of Transportation and Air Quality of the US Environmental Protection Agency).
23. EU, *New European Driving Cycle (NEDC)*. 1998, Directive 98/69/EC of the European Parliament.
24. *Regulation No 83 of the Economic Commission for Europe of the United Nations (UN/ECE), uniform provisions concerning the approval of vehicles with regard to the emission of pollutants according to engine fuel requirements*. 2006, Official Journal of European Union. p. 223-395.
25. Dieselnets, *Emission Standards: European Union Cars and Light Trucks*. 2012, [www.dieselnets.com](http://www.dieselnets.com).

26. Fontaras, G., et al., *Effects of low concentration biodiesel blend application on modern passenger cars. Part 1: Feedstock impact on regulated pollutants, fuel consumption and particle emissions*. Environmental Pollution, 2010. **158**(6): p. 1451-1460.
27. Al-Riffai, P., B. Dimaranan, and D. Laborde, *Global Trade and Environmental Impact Study of the EU Biofuels Mandate*. March 2010.
28. FIE, *Diesel Fuel Injection Equipment Manufacturers Common Position Statement: FAME Fuels as a Replacement or Extender for Diesel Fuels*. 2004.
29. Zhang, Y. and A.L. Boehman, *Impact of biodiesel on NO<sub>x</sub> emissions in a common rail direct injection diesel engine*. Energy & Fuels, 2007. **21**: p. 2003-2012.
30. Tompkins, B.T., et al., *Efficiency considerations for the use of blended biofuel in diesel engines*. Applied Energy, 2012. **Article in press**, <http://dx.doi.org/10.1016/j.apenergy.2012.03.025>.
31. Tan, P., et al., *Exhaust emissions from a light-duty diesel engine with Jatropha biodiesel fuel*. Energy, 2012. **39**: p. 356-362.
32. Puhan, S., et al., *Performance and emission study of Mahua oil (Madhuca indica oil) ethyl ester in a 4-stroke natural aspirated direct injection diesel engine*. Renewable Energy, 2005. **30**: p. 1269–1278.
33. Armas O, et al., *Efecto del biodiesel procedente de aceites vegetales usados sobre las emisiones y prestaciones de un motor diesel*, in *Anales del XVI Congreso Nacional de Ingenieria Mecanica*. 2004: Leon, Spain.
34. Lapuerta, M., et al., *Composition and size of diesel particulate emissions from a commercial European engine tested with present and future fuels*. IMechE, 2003. **217**(Part D): p. 907–19.
35. Lapuerta, M., O. Armas, and R. Ballesteros. *Diesel particulate emissions from biofuels derived from Spanish vegetable oils*. 2002: SAE paper 2002-01-1657.
36. Senatore A, et al. *A comparative analysis of combustion process in DI Diesel engine fueled with biodiesel and diesel fuel*. 2000: SAE paper 2000-01-0691.
37. Alam M, et al. *Combustion and emissions performance of low sulfur, ultra low sulfur and biodiesel blends in a DI diesel engine*. 2004: SAE paper 2004-01-3024.
38. Szybist, J., et al., *Fuel Process Technology Evaluation of formulation strategies to eliminate the biodiesel NO<sub>x</sub> effect.*, 2005. **86**: p. 1109–26.
39. Boehman, A., J. Song, and M. Alam, *Impact of biodiesel blending on diesel soot and the regeneration of particulate filters*. Energy Fuels, 2005. **19**: p. 1857–64.
40. Tat ME, *Investigation of oxides of nitrogen emissions from biodiesel-fueled engines*. PhD thesis. 2003, Iowa State University.
41. Lapuerta, M., et al., *Effect of the alcohol type used in the production of waste cooking oil biodiesel on diesel performance and emissions*. Fuel, 2008. **87**(15-16): p. 3161-3169.
42. Rodriguez-Anton, L.M., et al., *Volumetric properties at high pressure of waste oil methyl ester compared with diesel oil*. Fuel, 2008. **87**(10-11): p. 1934-1940.
43. Leung, D.Y.C., Y. Luo, and T.L. Chan, *Optimization of exhaust emissions of a diesel engine fuelled with biodiesel*. Energy and Fuels, 2006. **20**(3): p. 1015-1023.
44. Yamane, K., A. Ueta, and Y. Shimamoto, *Influence of physical and chemical properties of biodiesel fuels on injection, combustion and exhaust emission characteristics in a direct injection compression ignition engine*. Int J Engine Res, 2004. **4**: p. 249–261.
45. Rakopoulos, C.D., et al. *Operational and environmental evaluation of diesel engines burning oxygen-enriched intake air or oxygen-enriched fuels: a review*. 2004: SAE paper 2004-01-2924.
46. Rakopoulos, D.C., et al., *Effects of ethanol-diesel fuel blends on the performance and exhaust emissions of heavy duty DI diesel engine*. Energy Conversion and Management, 2008. **49**(11): p. 3155-3162.
47. Kousoulidou, M., et al., *Impact of biodiesel application at various blending ratios on passenger cars of different fueling technologies*. Fuel, 2012. **92**: p. 88-94.
48. Renault, *DDCR Diesel Injection - Fault finding - Diagnostics*, D.K.D.D.C.R.I. (DDCR), Editor. 2007.
49. Catania, A.E., et al., *Experimental investigation of dynamics effects on multiple - injection common rail system performance*. Journal of Engineering for Gas Turbines and Power, 2008. **130**(032806): p. 1-13.

50. Bianchi, G.M., et al., *A numerical and experimental study towards possible improvements of common rail injectors*. SAE paper 2002. **2002-01-0500**.
51. Ubertini, S., *Injection pressure fluctuations model applied to a multidimensional code for diesel engines simulation*. Journal of Engineering for Gas Turbines and Power, 2006. **128**: p. 694-701.
52. Watson, N. and M.S. Janota, *Turbocharging the Internal Combustion Engine*. 1982, London and Basingstoke: THE MACMILLAN PRESS LTD.
53. Horlock, J.H. and D.E. Winterbone, eds. *The Thermodynamics and Gas Dynamics of Internal-Combustion Engines*. Vol. II. 1986, Oxford University Press, USA.
54. Brace, C.J., et al., *Transient investigation of two variable geometry turbochargers for passenger vehicle diesel engines*. SAE Technical Paper No. 1999-01-1241.
55. Benajes, J., et al., *Modelling of turbocharged diesel engines in transient operation. Part 1: Insight into the relevant physical phenomena*. Proceedings of the Institution of Mechanical Engineers, Part D: Journal of Automobile Engineering, 2002. **216**(5): p. 431-441.
56. Payri, F., et al., *Modelling of turbocharged diesel engines in transient operation. Part 2: Wave action models for calculating the transient operation in a high speed direct injection engine*. Proceedings of the Institution of Mechanical Engineers, Part D: Journal of Automobile Engineering, 2002. **216**(6): p. 479-493.
57. Zhang, Z.H., et al., *Experimental investigation on regulated and unregulated emissions of a diesel/methanol compound combustion engine with and without diesel oxidation catalyst*. Science of The Total Environment. **408**(4): p. 865-872.
58. McDonald, J.F., et al., *Emission characteristics for Soy methyl ester fuels in an IDI compression ignition engine*. SAE paper no. 950400, 1995.
59. Sinha, S. and A.K. Agarwal, *Combustion characteristics of rice bran oil derived biodiesel in a transportation diesel engine*. SAE paper no. 2005-01-1730, 2005.
60. Yamane, K., et al., *Characteristics of DPF for diesel engine fueled with biodiesel fuel – First Report: Self-regeneration behavior on vehicle road test and engine bench rig test*. SAE Technical Paper No. 2004-01-1883.
61. Williams, A., et al., *Effect of biodiesel blends on diesel particulate filter performance*. SAE Technical Paper No. 2006-01-3280.
62. Song, J., et al., *Examination of the oxidation behavior of biodiesel soot*. Combustion and Flame, 2006. **146**(4): p. 589-604.
63. Boehman, A.L., J. Song, and M. Alam, *Impact of biodiesel blending on diesel soot and the regeneration of particulate filters*. Energy and Fuels, 2005. **19**(5): p. 1857-1864.
64. Peterson, A., et al., *Impact of biodiesel emission products from a multi-cylinder direct injection diesel engine on particulate filter performance*. SAE Technical Paper No. 2009-01-1184.
65. Müller, J.O., et al., *Diesel engine exhaust emission: Oxidative behavior and microstructure of black smoke soot particulate*. Environmental Science and Technology, 2006. **40**: p. 1231-1236.
66. Zhu, J., et al., *Effects of engine operating conditions on morphology, microstructure and fractal geometry of light-duty diesel engine particulates*. Proceedings of the Combustion Institute, 2005. **30**: p. 2781-2789.
67. Stanmore, B.R., J.F. Brilhac, and P. Gilot, *The oxidation of soot: a Review of experiments, mechanisms and models*. Carbon, 2001. **39**: p. 2247-2268.
68. Kostoglou, M., A.G. Konstandopoulos, and H. Burtscher, *Size distribution dynamics of fuel-borne catalytic ceria nanoparticles*. Aerosol Science, 2007. **38**: p. 604-611.
69. Bissett, E.J. and F. Shadman, *THERMAL REGENERATION OF DIESEL-PARTICULATE MONOLITHIC FILTERS*. AIChE Journal, 1985. **31**(5): p. 753-758.
70. Koltsakis, G.C. and A.M. Stamatelos, *Catalytic automotive exhaust aftertreatment*. Progress in Energy and Combustion Science, 1997. **23**(1): p. 1-39.
71. Koltsakis, G.C. and A.M. Stamatelos, *Modes of Catalytic Regeneration in Diesel Particulate Filters*. Industrial and Engineering Chemistry Research, 1997. **36**(10): p. 4155-4165.
72. Koltsakis, G.C. and A.M. Stamatelos, *Modeling Catalytic Regeneration of Wall-Flow Particulate Filters*. Industrial and Engineering Chemistry Research, 1996. **35**(1): p. 2-13.

73. Koltsakis, G.C. and A.M. Stamatelos, *Modeling Thermal Regeneration of Wall-Flow Diesel Particulate Traps*. AIChE Journal, 1996. **42**(6): p. 1662-1672.
74. Stratakis, G.A. and A.M. Stamatelos, *Thermogravimetric analysis of soot emitted by a modern diesel engine run on catalyst-doped fuel*. Combustion and Flame, 2003. **132**(1-2): p. 157-169.
75. Stratakis, G.A., *Experimental Investigation of Catalytic Soot Oxidation and Pressure-Drop Characteristics in Wall-Flow Diesel Particulate Filters*, PhD Thesis, in Mechanical Engineering Department. 2004, University of Thessaly: Volos.
76. Lu, T., C. Cheunq, and Z. Huang, *Investigation on particulate oxidation from a DI diesel engine fueled with three fuels*. Aerosol Science & Technology, 2012.
77. Jung, H., D.B. Kittelson, and M.R. Zachariah, *Characteristics of SME biodiesel-fueled diesel particle emissions and the kinetics of oxidation*. Environmental Science and Technology, 2006. **40**(16): p. 4949-4956.
78. Strzelec, A., T.T. J., and D.C. S. *Impact of biodiesel on the oxidation kinetics and morphology of diesel particulate*. in *7th US National Technical Meeting of the Combustion Institute*. 2011. Atlanta, GA.
79. Suh, H.K., H.G. Roh, and G.S. Lee, *Spray and combustion characteristics of biodiesel/diesel blended fuel in a direct injection common-rail diesel engine*. ASME Journal of Engineering for Gas Turbines and Power, 2008. **130**(032807): p. 1-9.
80. Brenn, G. and A. Frohn, *Collision and coalescence of droplets of various liquids*. Journal of Aerosol Science, 1989. **20**(8): p. 1027-1030.
81. Orme, M., *Experiments on droplet collisions, bounce, coalescence and disruption*. Progress in Energy and Combustion Science, 1997. **23**(1): p. 65-79.97.
82. Brenn, G. and A. Frohn, *Collision and merging of two equal droplets of propanol*. Experiments in Fluids, 1989. **7**(7): p. 441-446.
83. Jiang, Y., A. Umemura, and C.K. Law, *An experimental investigation on the collision behaviour of hydrocarbon droplets*. Journal of Fluid Mechanics, 1992. **234**: p. 171-190.
84. Martinelli, L., F.V. Bracco, and R.D. Reitz, *Comparisons of computed and measured dense spray jets*. AIAA Progress in Astronautics and Aeronautics, 1984. **95**: p. 484-512.
85. Hiroyasu, H. and T. Kadota, *Fuel droplet size distribution in Diesel combustion chamber*. SAE (740715), 1974.
86. Lee, D.W. and R.C. Spencer, *Preliminary photomicrographic studies of fuel sprays*. NACA TN 424, in 32, N.A.C.f. Aeronautics, Editor. 1932: Washington.
87. Lane, W.R., *Shatter of drops in streams of air*. Industrial and Engineering Chemistry, 1951. **43**(6): p. 1312-1317.
88. Giffen, E., *The atomization of liquid fuels*. 1953, London: Chapman & Hall Ltd.
89. Krzeczkowski, S.A., *Measurement of liquid droplet disintegration mechanisms*. International Journal of Multiphase Flow, 1980. **6**: p. 227-239.
90. Lefebvre, A.H., *Atomization and sprays*. 1989, London: Hemisphere Publishing Corporation, Taylor and Francis.
91. Hinze, J.O., *Fundamentals of the hydrodynamic mechanism of splitting in dispersion processes*. Aiche Journal 1995. **1**: p. 289-295.
92. Hsiang, L.P. and G.M. Faeth, *Drop deformation and breakup due to shock wave and steady disturbances*. International Journal of Multiphase Flow, 1993. **21**(4): p. 545-560.
93. Gelfand, B.E., *Droplet breakup phenomena in flows with velocity lag*. Progress in Energy and Combustion Science, 1996. **22**(3): p. 201-265.
94. Chin, J.S., *An engineering calculation method for turbine fuel droplet evaporation at critical conditions with finite liquid diffusivity*. AIAA, 95-0494, 1995.
95. Reitz, R. and Diwakar, *Modeling atomization processes in high-pressure vaporizing sprays*. Atomization and Spray Technology, 1987. **3**: p. 309-337.
96. O'Rourke, P.J. and A.A. Amsden, *The TAB method for numerical calculation of spray droplet breakup*. 1987. **SAE paper No. 872089**.
97. Reitz, R.D. and F.B. Bracco, *On the dependence of spray angle and another spray parameters on nozzle design and operating conditions*. 1979. **SAE paper No. 790494**.
98. Reitz, R.D. and R. Diwakar, *Structure of high-pressure fuel sprays*. 1987. **SAE paper No. 870598**.



99. Bertoli, C. and M. Migliaccio, *A finite conductivity model for Diesel spray evaporation computations*. International Journal of Heat & Fluid Flow, 1999. **20**: p. 552-561.
100. Ibrahim, E.A., H.Q. Yang, and A.J. Prezwkas, *Modeling of spray droplets deformation and breakup*. AIAA Journal of Propulsion and Power, 1993. **9**(4): p. 652-654.
101. R. Bosch, G., *Dieselmotor - Management. 4. Auflage*. 2004, Wiesbaden: Vieweg Verlag.
102. EU, *EN-14214, Fatty acid methyl esters (FAME) for diesel engines—requirements and test methods*. 2003.
103. Jääskeläinen, H., *Biodiesel Standards & Properties*, in *DieselNet Technology Guide » Alternative Diesel Fuels » Biodiesel*. Revision 2007.07b, www.dieselnet.com.
104. DieselNet, *Appendix: Biodiesel Composition And Properties of Components*, in *DieselNet Technology Guide » Alternative Diesel Fuels » Biodiesel*. Revision 2007.07, www.dieselnet.com.
105. Knothe, G., “*Designer” Biodiesel: Optimizing Fatty Ester Composition to Improve Fuel Properties*. Fuel, 2008(22): p. 1358-1364.
106. Demetriades L, et al., *RIP A6—Production of biofuels in Thessaly: Engine tests with biodiesel mixtures*. 2008: Volos.
107. Castellon-Elizondo, E., G. Lutz, and G. Mata-Segreda, *The soft-solid model for liquids. Application to biodiesel and other materials of technological interest*. Physical Organic Chemistry, 2006. **19**: p. 744-747.
108. VDI, *Waermeatlas*. 2002: Springer Verlag.
109. Kegl, B., *Effects of biodiesel on emissions of a bus diesel*. Bioresource Technology, 2007. **99**(4): p. 863-873.
110. BorgWarner Inc. *Biodiesel sensor*. 2011 [cited 2011 08.03.2011]; Available from: www.beru.com/.
111. Knothe, G., A. Matheaus, and T.W. Ryan, *Cetane numbers of branched and straight-chain fatty esters determined in an ignition quality tester*. Fuel, 2003. **82**(8): p. 971-975.
112. Murphy, M., J. Taylor, and R. McCormick, *Compendium of Experimental Cetane Number Data*. NREL/SR-540-36805. 2004.
113. Szybist, J.P., et al., *Biodiesel combustion, emissions and emission control*. Fuel Processing Technology, 2007. **88**(7): p. 679-691.
114. Heinnoi, K., et al., *Activity of prototype catalysts on exhaust emissions from biodiesel fuelled engines*. SAE Paper No. 2008-01-2514.
115. Kousoulidou, M., et al., *Evaluation of Biodiesel blends on the performance and emissions of a common rail light duty engine and vehicle* SAE Paper No. 2009-01-0692.
116. Czerwinski, J., et al., *A modern HD diesel engine with rapeseed oil, DPF and SCR*. SAE Paper No. 2008-01-1382.
117. Tziourtzioumis, D., et al., *Experimental investigation of the effect of a B70 biodiesel blend on a common rail, passenger car Diesel engine*. Proceedings of the Institution of Mechanical Engineers, 2009. **223**(Part D: Journal of Automobile Engineering): p. 685-701.
118. EU, *EN 14214:2008 Automotive fuels - Fatty acid methylesters (FAME) for diesel engines - Requirements and test methods*. 2008.
119. Catalano, L., V.A. Tondolo, and A. Dadone, *Dynamic rise of pressure in the common rail fuel injection system*. SAE paper 2002. **2002-01-0210**.
120. Wijetunge, R.S., et al., *Dynamic Behaviour of a High Speed Direct Injection Diesel Engine*. SAE Technical Paper No. 1999-01-0829.
121. Kennedy, M.P., *Transient compensation of EGR and boost in an engine using accelerator pedal rate data; US 6985808*. 2006, US Patent Office: USA.
122. Benajes, J., et al., *Influence of injection conditions and exhaust gas recirculation in a high-speed direct-injection diesel engine operating with a late split injection*. Proceedings of the Institution of Mechanical Engineers, Part D: Journal of Automobile Engineering, 2008. **222**(4): p. 629-641.
123. Liu, Y., F. Lu, and R.D. Reitz, *The use of non-parametric regression to investigate the sensitivities of high-speed direct injection diesel emissions and fuel consumption to engine parameters*. International Journal of Engine Research, 2006. **7**: p. 167-180.
124. Szybist, J.P., S.R. Kirby, and A.L. Boehman, *NO<sub>x</sub> emissions of alternative diesel fuels: A comparative analysis of biodiesel and FT diesel*. Energy and Fuels, 2005. **19**(4): p. 1484-1492.

125. Graboski, M.S. and R.L. McCormick, *Combustion of fat and vegetable oil derived fuels in diesel engines*. Progress in Energy and Combustion Science, 1998. **24**(2): p. 125-164.
126. Peterson, C.L. and D.L. Reece. *Emissions testing with blends of esters of rapeseed oil fuel with and without a catalytic converter*. 1996: SAE paper 961114.
127. Choi, C.Y., G.R. Bower, and R.D. Reitz. *Effects of biodiesel blended fuels and multiple injections on DI diesel engines*. 1997: SAE paper 970218.
128. Tat, M.E. and J.H. Van Gerpen. *Physical properties and composition detection of biodiesel-diesel fuel blends 2002*. ASAE meeting presentation 026084.
129. Scholl, K.W. and S.C. Sonrenson. *Combustion of soybean oil methyl ester in a direct injection diesel engine*. 1993: SAE paper 930934.
130. Rakopoulos, C.D., et al., *Comparative performance and emissions study of a direct injection Diesel engine using blends of Diesel fuel with vegetable oils or bio-diesels of various origins*. Energy Conversion and Management, 2006. **47**(18-19): p. 3272-3287.
131. Heywood, J., B., *Internal Combustion Engines Fundamentals*. 1988: McGraw-Hill, Inc.
132. Tat, M.E. and J.H. Van Gerpen, *Measurement of biodiesel speed of sound and its impact on injection timing*. NREL/SR-510-31462. 2003, Nat Renew Energy Lab.
133. Gamma Technologies Inc, *Help Navigator*. VERSION v.7.0. 2009.
134. Grech, N., et al., *Effect of combustor geometry on performance of airblast atomizer under sub-atomizer conditions*. Engineering Applications of Computational Fluid Mechanics, 2012. **6**(2): p. 203-213.
135. Mueller, C.J., et al., *Effects of oxygenates on soot processes in DI diesel engines: experimental and numerical simulations*. SAE Technical Paper No. 2003-01-1791.
136. Haas, M.J., et al., *Engine performance of biodiesel fuel prepared from soybean soapstock: a high quality renewable fuel produced from a waste feedstock*. Energy Fuels, 2001. **15**: p. 1207-1212.
137. Last, R.J., M. Krueger, and M. Duernholz. *Emissions and performance characteristics of a 4-stroke, direct injected diesel engine fueled with blends of biodiesel and low sulfur diesel fuel*. 1995. SAE paper 950054.
138. Lapuerta, M., et al. *Fuel formulation effects on passenger car diesel engine particulate emissions and composition*. 2000: SAE paper 2000-01-1850.
139. Armas, O., J. Hernandez, and C. MD, *Reduction of diesel smoke opacity from vegetable oil methyl esters during transient operation*. Fuel 2006. **85**: p. 2427-2438.
140. Xue, J., T.E. Grift, and A.C. Hansen, *Effect of biodiesel on engine performance and emission*. Renewable and Sustainable Energy Reviews, 2011. **15**: p. 1098-1116.
141. FLIR, *ThermaCam Reseacher Professional 2.8 SR3*. 2007.
142. Schmidt, N., et al., *Detailed diesel exhaust particulate characterization and DPF regeneration behavior measurements for two different regeneration systems*. SAE Technical paper No. 2007-01-1063.
143. Haralampous, O.A., G.C. Koltsakis, and Z.C. Samaras, *Partial regenerations in diesel particulate filters*. SAE Technical paper No. 2003-01-1881.
144. Martirosyan, K.S., K. Chen, and D. Luss, *Behavior features of soot combustion in diesel particulate filter*. Chemical Engineering Science, 2010. **65**: p. 42-46.
145. Chen, K., K.S. Martirosyan, and D. Luss, *Counter-intuitive temperature excursions during regeneration of a diesel particulate filter*. AIChE, 2011. **57**(8): p. 2229-2236.
146. Herz, R.K. and R.M. Sinkevitch, *Reactors for investigation of soot combustion on filter surfaces*. Carbon, 1986. **4**(24): p. 457-462.
147. McCabe, R.W. and R.M. Sinkevitch, *A laboratory combustion study of diesel particulates containing metal additives*. SAE Technical Paper No. 860011, 1986.
148. Hanamura, K., et al., *Visualization of combustion phenomena in regeneration of diesel particulate filter*. SAE Technical Paper No. 2003-01-0836
149. An, H., C. Kilroy, and P.J. McGinn, *An examination of microwave heating to enhance diesel soot combustion*. Thermochemica Acta, 2005. **435**(1): p. 57-63.
150. Gallant, T. *Experimental diesel particulate filter capabilities at PNNL*. in *DEER Conference*. 2006. Chicago, IL.

151. Stratakis, G.A., G.S. Konstantas, and A.M. Stamatelos, *Experimental investigation of the role of soot volatile organic fraction in the regeneration of diesel filters*. Proceedings of the Institution of Mechanical Engineers, Part D: Journal of Automobile Engineering, 2003. **217**(4): p. 307-317.
152. FLIR, *Thermacam S45 User's Manual*. 2006.
153. Stratakis, G.A., D.L. Psarianos, and A.M. Stamatelos, *Experimental investigation of the pressure drop in porous ceramic Diesel Particulate Filters*. Proceedings of the Institution of Mechanical Engineers, Part D: Journal of Automobile Engineering, 2002. **216**: p. 773-784.
154. Chen, K., K.S. Martirosyan, and D. Luss, *Hot zones formation during regeneration of diesel particulate filters*. AIChE, 2011. **57**(2): p. 497-506.
155. Chen, K. and D. Luss, *Temperature excursions in diesel particulate filters: Response to shift to idle*. Ind. Eng. Chem. Res, 2011. **50**: p. 832-842.
156. Chen, K., K.S. Martirosyan, and D. Luss, *Temperature excursions during soot combustion in a diesel particulate filter (DPF)*. Ind. Eng. Chem. Res, 2010. **49**: p. 10358-10363.
157. Blanchard, G., et al., *Passenger car series application of a new Diesel Particulate Filter system using a new ceria-based fuel-borne catalyst: From the engine test bench to european vehicle certification*. SAE Technical Paper No. 2002-01-2781.
158. Stratakis, G.A., G.N. Pontikakis, and A.M. Stamatelos, *Experimental validation of a fuel additive assisted regeneration model in silicon carbide diesel filters*. Proceedings of the Institution of Mechanical Engineers, Part D: Journal of Automobile Engineering, 2004. **218**(7): p. 729-744.
159. Fukuda, K., et al., *Impact study of high biodiesel blends on performance of exhaust after treatment systems*. SAE Paper No. 2008-01-2494.
160. Pontikakis, G., *CATWALL\_v4r3b User Manual*. 2004: Volos.
161. Pontikakis, G., *Modeling, Reaction Schemes and Kinetic Parameter Estimation in Automotive Catalytic Converters and Diesel Particulate Filters*. PhD Thesis, in Mechanical Engineering Department. 2003, University of Thessaly: Volos.
162. Pontikakis, G. and A. Stamatelos, *Three-dimensional catalytic regeneration modeling of SiC diesel particulate filters*. Journal of Engineering for Gas Turbines and Power, 2006. **128**(2): p. 421-433.
163. DieselNet, *Biodiesel—Mono Alkyl Esters*, in *DieselNet Technology Guide » Alternative Diesel Fuels*. Revision 2007.07, www.dieselnet.com.
164. ASTM, *D 6751-03, Standard specification for biodiesel (B100) blend stock for distillate fuels*. 2003.
165. ASTM, *D7467 - 10 Standard specification for Diesel Fuel Oil, Biodiesel Blend (B6 to B20)*. 2010.
166. Kline, K.L., et al., *Biofuel feedstock assessment for selected countries*, O.R.N. LABORATORY, Editor. 2008.
167. Fazal, M.A., A.S.M.A. Haseed, and H.H. Masjuki, *Biodiesel feasibility study: An evaluation of material compatibility; performance; emission and engine durability*. Renewable and Sustainable Energy Reviews, 2011. **15**: p. 1314-1324.
168. Agarwal, A.K., J. Bijwe, and L.M. Das, *Wear assessment in a biodiesel fuelled compression ignition engine*. ASME J. Eng. Gas Turbines Power, 2003. **125**: p. 820-826.
169. FIE, *Fuel Requirements for Diesel Fuel Injection Systems Diesel Fuel Injection Equipment Manufacturers Common Position Statement 2009*.
170. Tung, S.C. and M.L. McMillan, *Automotive tribology overview of current advances and challenges for the future*. Tribol. Int., 2004. **37**: p. 517-536.
171. Corso, S. and R. Adamo, *The effect of diesel soot on reactivity of oil additives and valve train materials*. SAE Paper No. 841369, 1984.
172. Gautam, M., et al., *Effect of diesel soot contaminated oil on engine wear-investigation of novel oil formulations*. Tribol. Int., 1999. **32**: p. 687-699.
173. Nagai, L., et al., *Soot and valve train wear in passenger car diesel engines*. SAE Paper No. 831757, 1983.
174. Berbeizer, L., J. Martin, and P.H. Kasper, *The role of carbon in lubricated mild wear*. 1986.
175. Priest, M. and C.M. Taylor, *Automobile Engine Tribology-Approaching the surface*. Wear, 2000. **241**: p. 193-203.
176. Dong, W.P., et al., *Topographic features of cylinders liners-An application of three dimensional characterization techniques*. Tribol. Int., 1995. **28**(7): p. 453-463.

177. Kjer, T., *Wear rate and concentration of wear particles in lubricating oil*. *Wear*, 1981. **67**: p. 217-226.
178. Agarwal, A.K. and L.M. Das, *Biodiesel development and characteristics for use as a fuel in compression ignition engine*. *Trans. ASME: J. Eng. Gas Turbines Power*, 2001. **123**: p. 440-447.
179. Zieba-Palus, J., *Examination of used motor oils by Flame AAS for criminalistic purposes: A diagnostic study*. *Forensic Sci. Int.*, 1988. **91**: p. 171-179.
180. Kalam, M.A. and H.H. Masjuki, *Biodiesel from palm oil - An analysis of its properties and potential*. *Biomass Bioenergy*, 2002. **23**: p. 471-479.
181. Kaufman, K.R. and M. Ziejewski, *Sunflower methyl esters for direct injected diesel engines*. *Trans. ASAE*, 1984. **27**: p. 1626-1633.
182. Kenneth, P., et al., *100,000-mile evaluation of transit buses operated on biodiesel blends (B20)*. SAE Technical Paper No. 2006-01-3253.
183. Kearney, T. and J. Benton, *Final report: Air force biodiesel demonstration program at Scott AFB*. 2002.
184. Chase, C.L., et al., *A 322,000 kilometer (200,000 Mile) over the road test with HySEE biodiesel in a heavy duty truck*. SAE Technical Paper No. 2000-01-2647.
185. Clark, S.J., et al., *Methyl and esthyl soybean esters as renewable fuels for diesel engines*. *J. Am. Oil Chem. Soc*, 1984. **61**(10): p. 1632-1643.
186. Fraer, R., et al., *Operating experience and teardown analysis for engines operated on biodiesel blends (B20)*. Paper No, SAE 2005-01-3641, 2005.
187. Higelin, P. and A. Charlet, *The use of sunflower oil as Diesel fuel for DI engines*.
188. *Fosseen manufacturing and development. 1000 h durability testing DDC 6V-92TA DDEC II engine*, in *Final Report to National Biodiesel Board Contract No. 214-1*, 27 January 1995.
189. *Truckers complain that biodiesel fuel is clogging engine filters*, in *PTSA weekly update*. 2005. p. p.7.
190. *Minnesota halts 2% biodiesel requirement through Jan 13*, in *Clogging triggers suspension*. 2005, The OilSpot News by DTN.
191. IntelliStick, I. 2008 [cited 2009 17/05/2008]; Available from: [www.intellistick.com](http://www.intellistick.com).
192. Okamoto, B., *Biodiesel fleet durability study*. July 2010, California Air Resources Board.
193. Kegl, B., *Numerical analysis of injection characteristics using biodiesel fuel*. *Fuel*, 2006. **85**: p. 2377-2387.
194. Wu, Z., Z. Zhu, and Z. Huang, *An experimental study on the spray structure of oxygenated fuel using laser-based visualization and particle image velocimetry*. *Fuel*, 2006. **85**: p. 1458-1464.
195. Ramadhas, A.S., S. Jayaraj, and C. Muraleedharan, *Use of vegetable as IC engine fuels - A review*. *Renewable Energy*, 2004. **29**: p. 727-742.
196. Lee, C.S. and S.W. Park, *An experimental and numerical study on fuel atomization characteristics of high-pressure diesel injection sprays*. *Fuel*, 2002. **81**: p. 2417-2423.
197. Knight, B.E., *Communication on the performance of a type of swirl atomizer*. *Proc. I. Mech. Eng.*, 1955. **104**.
198. Hiroyasu, H. and T. Kadota, *Fuel droplet size distribution in a Diesel combustion chamber*. SAE paper no. 740715, 1974.
199. El-Kotb, M.M., *Fuel atomization for spray modeling*. *Prog. Energy Comb. Sci.*, 1982. **8**: p. 61.
200. Borman, G.L. and K.W. Ragland, *Combustion Engineering*. 1998, McGraw-Hill Science/Engineering/Math.
201. TSI, *Software manual*. 2007.
202. Lee, C.S. and R.D. Reitz, *Effect of liquid properties on the breakup mechanism of high-speed liquid drops*. *Atomization Sprays*, 2001. **11**: p. 1-19.

# CURRICULUM VITAE

## **Dimitrios N. Tziourtzioumis**

Laboratory of Thermodynamics and Thermal Engines  
Department of Mechanical Engineering  
University of Thessaly, GR-383 34, Volos Tel. +30 2421074053  
Email: [dimtziour@mie.uth.gr](mailto:dimtziour@mie.uth.gr)

## **EDUCATION**

- 2003 - 2008:** Diploma in Mechanical Engineering. Grade: 8.33/10  
University of Thessaly, Volos, Greece  
Thesis Title: Simulation of the flow field of an air furnace assisted by CFD and Infrared Thermography.  
Thesis Advisor: Prof. A.M. Stamatelos
- 2010:** MS in Mechanical Engineering  
University of Thessaly, Volos, Greece  
Thesis title "State of the Art Design and Analysis Methods in Industry".  
Grade: 9.24/10  
Thesis Title: Simulation and experimental validation of steady state operation of a turbocharged, common rail HDI Diesel engine running on biodiesel blends.  
Thesis Advisor: Prof. A.M. Stamatelos
- 2008 - 2012:** Ph.D. in Mechanical Engineering  
University of Thessaly, Volos, Greece  
Department of Mechanical Engineering  
Thesis Title: Modeling and Experimental Investigation of the steady state and transient operation of a Common Rail, High Pressure Injection Diesel Engine fuelled by high percentage biodiesel blends.  
Research Advisor: Prof. A.M. Stamatelos

## **PROFESSIONAL EXPERIENCE**

- 2005 – today:** Research engineer in the Laboratory of Thermodynamics and Thermal Engines – Department of Mechanical Engineering, University of Thessaly
- February 2010 -**
- July 2010:** "Energy Performance of Buildings" Seminars – Seminar Speaker

## **TEACHING EXPERIENCE**

### Teaching Assistant – Undergraduate courses

University of Thessaly, Department of Mechanical Engineering

- Internal Combustion Engines (spring semester 2007-2012)
- Heating- Refrigeration-Air Conditioning Engineering (fall semester 2007-2011)

TEI-Technological Educational Institute of Larissa

- Internal Combustion Engines I (spring semester 2011-2012)

## Teaching Assistant – Postgraduate courses

University of Thessaly, Department of Mechanical Engineering

- Measuring Techniques and Instrumentation in the Thermal Sciences (spring semester 2007-2010)

## **AREAS OF INTEREST**

- Automotive exhaust gas aftertreatment modeling for Diesel Engines (Diesel oxidation catalysts, diesel particulate filters)
- Fuel Injection – Laser Doppler Velocimetry technique
- HVAC engineering
- Infrared Thermography - Engineering Applications

## **JOURNAL PUBLICATIONS**

1. D. Tziourtzioumis, A. Stamatelos: Effects of a B70 biodiesel blend on the ECU and fuel system operation during steady-state and transient performance of a Common Rail Diesel Engine. *Energy Conversion and Management*, (2012), 60: 56-67.
2. D. Tziourtzioumis, L. Demetriades, O. Zogou and A. Stamatelos: Experimental investigation of the effect of a B70 biodiesel blend on a common rail, passenger car Diesel engine. *Proceedings of the Institution of Mechanical Engineers, Vol.223 Part D: Journal of Automobile Engineering*, (2009), 685-701.
3. D. Tziourtzioumis and A. Stamatelos, Design Improvements in a 30,000 kcal/h Air Furnace, Assisted by CFD and Infrared Thermography. *The Open Fuels & Energy Science Journal*, 2008, 1, 79-90 <http://www.bentham.org/open/toefj/openaccess2.htm>.

## **CONFERENCE PUBLICATIONS**

1. D. Tziourtzioumis, A. Stamatelos: Effect of biodiesel blends on the regeneration behavior of Diesel Particulate Filters. TAP Conference 2012, November 26-27 November 2012, Thessaloniki, Greece. (Abstract Submission)
2. D. Tziourtzioumis, A. Stamatelos: Effects of a B70 biodiesel blend on the ECU and fuel system operation during steady-state and transient performance of a Common Rail Diesel Engine. ECOS 2011 International Conference on Efficiency, Cost, Optimization, Simulation and Environmental Impact of Energy Systems, July 4-7 2011, Novi Sad, Serbia.

## **HONORS AND AWARDS**

“A.S. Onassis” Foundation, Doctoral Scholarship. No. G ZSF 056/2009-2010  
Heraclitus II Doctoral Scholarship (2011) (not accepted)

## **LANGUAGES**

English, French



Onassis  
Foundation